2022 OPAL

Optics, Photonics and Lasers:

Proceedings of the 5th International Conference on Optics, Photonics and Lasers (OPAL' 2022)

18-20 May 2022

Tenerife (Canary Islands), Spain

Edited by Sergey Y. Yurish

IFSA

Optics, Photonics and Lasers:

Proceedings of the 5th International Conference on Optics, Photonics and Lasers (OPAL' 2022)

18-20 May 2022

Tenerife (Canary Islands), Spain

Edited by Sergey Y. Yurish

IFSA Publishing

Sergey Y. Yurish, *Editor*
Optics, Photonics and Lasers
OPAL' 2022 Conference Proceedings

E-mail (for orders and customer service enquires): ifsa.books@sensorsportal.com

Visit our Home Page on http://www.sensorsportal.com

ISBN: 978-84-09-40460-5
BN-20220513-XX
BIC: TTB

Contents

Foreword **6**

Superhydrophobic Polycarbonate Fabrication for Antibacterial Applications **7**
S. Sohrabi, H. Pazokian, B. Ghafary, M. Mollabashi, and M. Montazeralghaem

Electrically Controlled Multiferroic Photonic Grating **9**
Ramaz Khomeriki

Near Infrared Diffused Reflectance on Tissue Simulating Phantoms for Optical Applications **12**
P. Demosthenous and M. Baer

Infrared Spectroscopic Application using an Integrating Sphere for Measuring Vapor Ethanol **15**
P. Demosthenous and M. Baer

Water-repellent Coatings Based on Anodized Aluminum under Femtosecond Laser Ablation **18**
A. M. Rodin, O.Myronyuk, D.Baklan, G.Vasyliev and E.Vanagas

Laser Fabrication of Different Crystals by Pulsed Bessel Beams **21**
A. Kuriakose, M. Bollani P. Di Trapani and O. Jedrkiewicz

High-speed Wavelength Division Multiplexing Transmission over SI-Polymer Fibers **24**
Ulrich H. P. Fischer, Mladen Jóncic

Combining Bright-field and Second Harmonic Generation Microscopy for the Characterization of Thyroid Nodules **26**
R. Hristu, L. G. Eftimie, R. Glogojeanu, S. G. Stanciu and G. A. Stanciu

Measurement of Transonic Airflow in a Compressor Blade Cascade by Spatial Carrier Interferometry **28**
P. Psota, G. Cubreli and D. Šimurda

Efficient Optomechanical Mode-Shape Mapping of Micromechanical Devices in the Presence of Crosstalk **32**
D. Hoch, K.-J. Haas, L. Moller J. Röwe T. Sommer, P. Soubelet, J. J. Finley and M. Poot

Synthesis of Adjacent Stokes Spectra in a Two-stage Transient Stimulated Raman Chirped-pulse Amplifier **34**
P.Mackonis, A.Petrulenas and A. M.Rodin

Bipolar Organic Semiconductors based on Carbazole and Diphenyl Imidazole as Deep-blue OLED Emitters and Hosts for Sky-blue, Green and Red PhOLEDs **37**
O. Bezvikonnyi, V. Andruleviciene, D. Volyniuk, R. Keruckiene, K. Vaiciulaityte, E. Urbonas, J. V. Grazulevicius

Generation of Femtosecond Pulses up to 3 µm by Combining OPCPA with Transient Stimulated Raman Amplification **39**
A. Petrulenas, P. Mackonis and A. M. Rodin

High Temperature Characterization of a Femtosecond Laser Micromachined Fiber in-line Fabry-Pérot Pressure Sensor **42**
Wendy Tomboza, Romain Cotillard, Nicolas Roussel, Minh Chau Phan Huy Géraud Bouwmans, Guillaume Laffont

Comparison of Various Sublimation Matte Coating Sprays for the Optical 3D Scanning with a Focus on the Quality of 3D Scans **45**
J. Franke, T. Koutecký and D. Koutný

Preparing Satellites for Active Debris Removal and Ranging **48**
C. Phipps and C. Bonnal

Quantum Dot Coupling into Hybrid InP-Si Waveguide Modes for on-chip Integrated Photonics **51**
P. Mrowiński, G. Sęk, M. Syperek

Characterization and Comparison of CubeSat and Drone Platform Jitter Effects on Laser Beam Pointing Stability **53**
Femi Ishola, Alberto Carrasco-Casado, Phuc V. Trinh, Koichi Shiratama, Hirokazu Masui, Rodrigo Cordova, Yasushi Munemasa, Mengu Cho, Tetsuharu Fuse, Hiroyuki Tsuji, Morio Toyoshima

High Type A Refractive Index Change by Multi-scan Cumulative Inscriptions in Photosensitive Glasses **60**
L. Loi, T. Guérineau, S. Danto, T. Cardinal, Y. Petit, and L. Canioni

Volume Gratings for the Recording of a Waveguide on Photopolymers **62**
C. Neipp, J. C. Bravo-Francés, J. J. Sirvent-Verdú, M. Morales-Vidal, T. Lloret, D. Puerto, S. Gallego

Near-field Probes based on Nanocones and Nanopyramides **65**
D. Pudis, A. Kuzma, P. Maniakova, M. Feiler, D. Jandura and M. Goraus

Application of Transparent Machine Learning Method for Skin Lesions Classification from Multispectral Reflectance Images **67**
D. Bliznuks, K. Bolochko, E. V. Plorina, A. Lihachev, I. Lihacova

Single SiGe Quantum Dot Coupled to Bichromatic Photonic Crystal Cavities for Potential Applications as Single Telecom Photon Emitters **72**
Thanavorn Poempool, Johannes Aberl, Marco Clementi, Lukas Spindlberger, Lada Vukušić, Matteo Galli, Dario Gerace, Friedrich Schäffler, Moritz Brehm and Thomas Fromherz

Propagation of Azimuthally Polarized Bessel-Gaussian Beam through Helical Axicon **74**
Ibrahim G. H. Loqman Abdu A. Alkelly and Hassan T. Alahsab

Recent Design Evolution and New Trends of Hollow Core Optical Fibers **79**
W. Belardi, A. Pastre, S. Plus, R. Habert, K. Baudelle, L. Bigot, G. Bouwmans, P. J. Sazio, P. Jaworki, P. Koziol, G. Dudzik and K. Krzempek

Polymer-based Inverted Pyramids for SERS **81**
I. Lettrichova, D. Jandura, P. Gaso, D. Pudis and A. Kuzma

Polymer Inverted Refractive-Index-Contrast Grating Prepared by Laser Lithography on Si Substrate **83**
D. Jandura, P. Gaso, J. Suffczyński, T. Czyszanowski and D. Pudis

Nonlinear Upconversion Effect for Enhancement of Curing Depths in Laser-Assisted 3D Printing of Photopolymers **85**
A. Zhakeyev and J. Marques-Hueso

Performance Evaluation of a Network Cluster Operating in the Solar-blind UV-C Band under a Non-Line-of-Sight Regime **87**
N. Raptis, G. Pekridis, K. Krilakis, K. Panoliaskos, E. Roditi and D. Syvridis

Preparation and Investigation of a Nanostructured Tuneable Hybrid Mirror for a High-Energy Tamm Plasmon State Generation **94**
A. Belosludtsev, O. Buchnev, A. Fedotov

Optical Computation of a Spin Glass Dynamics with Adaptive Optics **96**
Marco Leonetti, Luca Leuzzi, Erik Hörmann, Giorgio Parisi, and Giancarlo Ruocco

Bulk Dirac Semimetal for the Exploration of Terahertz OptoelectronicDevices **100**
Tony Mathew Blessan, C. Venkateswaran and N. Yogesh

Laser Processing by Ultrafast Bursts of Pulses **103**
A. Žemaitis, M. Gaidys, P. Gečys and M. Gedvilas

Highly Sensitive Plasmonic Sensor Device made of Au Nanoantennas on SiO_2 Nanopillar Arrays **106**
P. Venugopalan and S. Kumar

Temporal Talbot Effect in Birefringent Optical Filters for Multiplying Pulse Repetition Rates **108**
Youcef Driouche, Rachid Hamdi, Leila Graini, Abderezzaq Halassi, Badr-Eddine Benkelfat

Tests and Developments of a NIR laser CO_2 Sensor based on Dense-pattern Multipass Gas Cell **111**
F. Defossez, J. Jacquemin, R. Vallon, B. Parvitte, V. Zeninari

Birefringent Pulse Shaper Using Non-identical Crystals **113**
Youcef Driouche, Rachid Hamdi, Leila Graini, Abderezzaq Halassi, Badr-Eddine Benkelfat

1DPhC-based Resonant Cavity for Optical Fiber Sensing **116**
J. Durisova, T. Mizera, R. Kanok, P. Hlubina, D. Pudis, P. Gaso, D. Jandura

Anti-squeezing Noise in Continuous-variable Quantum Communication 118
V. C. Usenko, A. Nag Oruganti and I. Derkach

Development of Efficient Clad-pumped Fiber Optical Amplifiers for Telecommunication Systems 120
J. Grube, A. Supe, K. Zakis, S. Olonkins, A. Udalcovs, R. Murnieks, U. Senkans, D. Prigunovs, L. Gegere, E. Elsts, I. Lukosevics, O. Ozolins, S. Spolitis, V. Bobrovs

Optomechanical Inertial Sensing and Displacement Interferometry 123
F. Guzman, A. S. Hines, A. Nelson, and Y. Zhang

Machine Learning Methods applied to Vibrational Spectroscopy: New Horizons 125
D. Sharma, and N. Jaggi

Foreword

On behalf of the OPAL' 2022 Organizing Committee, I introduce with pleasure these proceedings devoted to contributions from the 5th International Conference on Optics, Photonics and Lasers (OPAL' 2020). The conference is organized by the International Frequency Sensor Association (IFSA) in technical cooperation with our media partners: Institute of Physics (IOP), UK, MDPI Photonics (ISSN 2304-6732) and MDPI Chemosensors (ISSN 2227-9040) journals, Switzerland.

In keeping with tradition begun in 2018 in Barcelona, Spain the Series of Conference attracts researchers and practitioners in the related fields, from around the world including 2 keynote speakers from Germany and India.

The conference proceedings contains all papers of regular and keynote presentations. We hope that these proceedings will give readers an excellent overview of important and diversity topics discussed at the conference.

We thank all authors for submitting their latest work, thus contributing to the excellent technical contents of the Conference. Especially, we would like to thank the individuals and organizations that worked together diligently to make this Conference a success, and to the members of the International Program Committee for the thorough and careful review of the papers. It is important to point out that the great majority of the efforts in organizing the technical program of the Conference came from volunteers.

Prof., Dr. Sergey Y. Yurish
OPAL' 2022 Chairman

(003)

Superhydrophobic Polycarbonate Fabrication for Antibacterial Applications

S. Sohrabi [1], H. Pazokian [2], B. Ghafary [1], M. Mollabashi [1] and M. Montazeralghaem [2]
[1] Iran University of Science and Technology, Physics Department, Tehran, Iran
[2] Photonics and Quantum Technology Research School, Nuclear Science and Technology Research Institute, Tehran, Iran
Tel.: + 989194325260
E-mail: s.sorabiiust@gmail.com

Summary: In this paper, effect of excimer laser irradiation on the wettability of polycarbonate at the fluency close to the ablation threshold (F_{th}) with different number of pulses was investigated. The samples were irradiated by an excimer laser at the fluency of 30 mJ/cm^2 with the wavelength of 248 nm and the pulse duration of about 25 ns. The contact angle of the irradiated samples were realized by sessile drop method. With high number of pulses, the irradiated sample shows superhydrophobicity property. The superhydrophobic fabricated surface was tested for bacterial adhesion by gram staining method. Microscopic images and Field Emission Scanning Electron Microscopy (FESEM) were used for adhered bacteria detection after washing the samples with phosphate buffer solution (PBS).

Keywords: Antibacterial surface, Excimer laser, Superhydrophobicity, Polycarbonate, Wettability.

1. Introduction

Bacterial attachment to surfaces and subsequent biofilm formation is critical problem in the world affect human health and life including food processing, medicine, dentistry and water treatment [1, 2].

Multiple physical aspects of the material including wettability, roughness, surface charge and energy have been considered to influence on the bacterial adhesion rate, but wettability is reported to be the most relevant parameter for bacterial adhesion control [3]. Superhydrophobic surfaces have been reported to minimize adhered bacteria due to their micro-nano structures [4, 5]. There are several approaches to fabricate superhydrophobic-antibacterial surfaces. Laser processing can fabricate suitable periodic micro-nano structures on the surface and turn it into a super-hydrophobic one. The super-hydrophicity of the surface leads to antibacterial properties and it can be used in various industries such as medicine.

In this paper, 248 nm KrF laser processing of polycarbonate surface is demonstrated. Due to laser processing, at fluences close to the ablation threshold with high number of pulses, the surface is changed to super hydrophobic one.

2. Experimental Method

2.1. Experimental Work

Polycarbonate was cut into length and width of 1cm × 1cm with the thickness of 1mm. the samples were washed with alcohol and water to be clean before laser processing.

The fluency for the single pulse ablation threshold of PC samples in 248 nm was obtained to be about 40 mJ/cm^2 .Samples were irradiated by a KrF laser at the fluency of 30 mJ/cm^2 with various number of pulses. The contact angle of the pristine and irradiated samples were realized by sessile drop method.

2.2. Bacterial Adhesion

The superhydrophobic fabricated sample and the pristine were tested for E-Coli bacteria adhesion with gram staining method. The samples were examined after PBS wash. Field Emission Scanning Electron Microscopy (FESEM) was used to ensure adhered bacteria rate of the superhydrophobic sample.

3. Results and Discussion and Measurement

Fig. 1 shows the microscopic images of the water contact angle of the samples irradiated at the fluency of 30 mJ/cm^2 with 1000, 2000 and 5000 number of pulses. As it can be understood from the figure, the sample irradiated with 5000 pulses, is changed to a superhydrophobic surface, while the others are turned into hydrophilic ones.

Fig. 1. Microscopic image of the water drop on the sample irradiated at the fluency of 30 mJ/cm^2 with a) 5000; b) 2000, and c) 1000 pulses.

The superhydrophobic sample was tested for checking bacterial adhesion resistance ability.

Fig. 2 shows the microscopic images of the adhered E-Coli bacteria after bacterial test and PBS washing of the pristine and the irradiated sample with 5000 pulses as a superhydrophobic specimen. Adhered bacteria can be seen on the pristine sample in the figure, while there is no bacterium on the superhydrophobic sample.

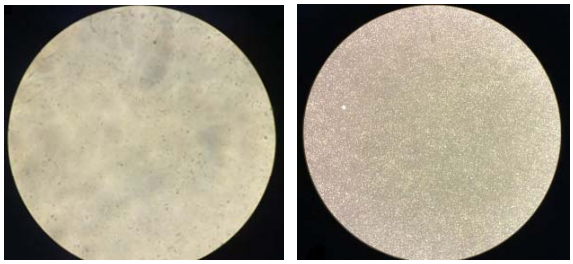

Fig. 2. Microscopic images of left) untreated and right) the sample irradiated at the fluency of 30 mJ/cm^2 with 5000 number of pulses. The microscopic images are one hundred times larger than the original.

To ensure that no bacterium is adhered to the superhydrophobic sample, FESEM images were taken. Fig. 3 shows the FESEM images of the irradiated-superhydrophobic sample at different magnifications.

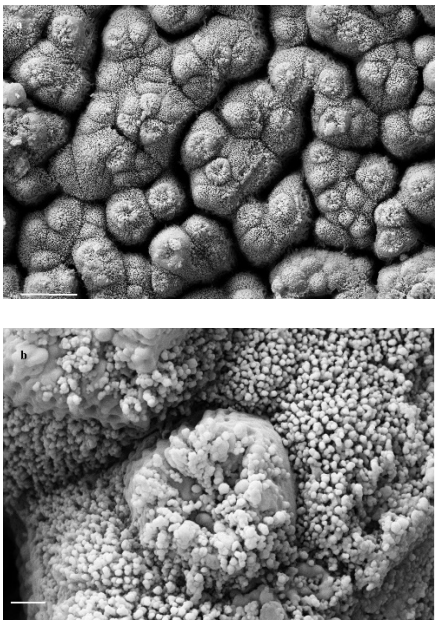

Fig. 3. FESEM images of the sample irradiated at the fluency of 30 mJ/cm^2 with 5000 number of pulses after bacterial test at different magnification. Marked scale bar is about a) 4 micron, and b) 400 nm

As is shown in Fig. 3, Double-scale micro-nano structures are created on the sample irradiated at the fluency of 30 mJ/cm^2 with 5000 number of pulses and no E-Coli bacterium is adhered to the sample. Double scale roughness structures are the most effective morphologies to fabricate an artificial superhydrophobic surface [6]. Air-trapping between the fabricated structures is considered to be responsible for reducing bacterial adhesion to the superhydrophobic surfaces due to decreasing the effective contact area of bacteria and the solid surface [7].

It is important to note that, laser treating of the sample at the fluency of close to the ablation threshold with high number of pulses leading hierarchical micro/nano structures, while low number of pulses are not enough to create suitable structures to change the surface to the superhydrophobic one and no significant structures can be seen in the SEM images of these surfaces (not shown).

4. Conclusions

PC polymer was irradiated with an excimer laser at the fluency of close to the ablation threshold. The effect of the laser irradiation on its wettability was investigated. It was shown that the irradiated sample at the fluency of 30 mJ/cm^2 with 5000 number of pulses, was turned into the superhydrophobic surface. Bacterial adhesion on the superhydrophobic sample was examined. The formation of double-scale micro-nano structures are supposed to be the most important factor affect the superhydrophobicity and antibacterial properties of the sample irradiated at this fluency and with high number of pulses.

References

[1]. G. Feng, Y. Cheng, S.-Y. Wang, D. A. Borca-Tasciuc, R. W. Worobo, and C. I. Moraru, Bacterial attachment and biofilm formation on surfaces are reduced by small-diameter nanoscale pores: how small is small enough?, *npj Biofilms and Microbiomes*, Vol. 1, No. 1, 2015, pp. 1-9.

[2]. Y. Cheng, G. Feng, and C. I. Moraru, Micro-and nanotopography sensitive bacterial attachment mechanisms: a review, *Frontiers in Microbiology*, 2019 p. 191.

[3]. T. Hemmatian, H. Lee, and J. Kim, Bacteria adhesion of textiles influenced by wettability and pore characteristics of fibrous substrates, *Polymers*, Vol. 13, No. 2, 2021, p. 223.

[4]. Y. Yuan, M. P. Hays, P. R. Hardwidge, and J. Kim, Surface characteristics influencing bacterial adhesion to polymeric substrates, *RSC Advances*, Vol. 7, No. 23, 2017, pp. 14254-14261.

[5]. X. Zhang, L. Wang, and E. Levänen, Superhydrophobic surfaces for the reduction of bacterial adhesion, *RSC Advances*, Vol. 3, No. 30, 2013, pp. 12003-12020.

[6]. Y. Yoon, D. Kim, and J.-B. Lee, Hierarchical micro/nano structures for super-hydrophobic surfaces and super-lyophobic surface against liquid metal, *Micro and Nano Systems Letters*, Vol. 2, No. 1, 2014, pp. 1-18.

[7]. Y. Yuan, M. P. Hays, P. R. Hardwidge, and J. Kim, Surface characteristics influencing bacterial adhesion to polymeric substrates, *RSC Advances*, Vol. 7, No. 23, 2017, pp. 14254-14261.

(004)

Electrically Controlled Multiferroic Photonic Grating

Ramaz Khomeriki
Physics Department, Tbilisi State University, 3 Chavchavadze, 0128 Tbilisi, Georgia
Tel.: + 995595397216
E-mail: khomeriki@hotmail.com

Summary: Single phase multiferroic with easy plane magnetic anisotropy and Dzyaloshinskii-Moriya type electro-magnetic coupling is considered. Static electric field causes the establishment of helically ordered ground state and it is shown that this structure acts as a periodic potential for light propagation through the multiferroic. The corresponding magnon-photonic band-gap spectrum is calculated and the possibility of light trapping while driving inside the photonic gap is numerically revieled.

Keywords: Helical, Multiferroic, Light matter interaction.

1. Introduction

Here, we demonstrate how multiferroics properties lead to formation of photonic nanoscale grating. Particularly, as it is shown below, Dzyaloshinskii-Moriya type antisymmetric exchange mechanism in multiferroic materials [1, 2] is responsible for appearance of effective electrical polarization, which can couple with external electric field. The presence of corresponding term in the model Hamiltonian induces the establishment of helical ground state for magnetic spins in the sample; the helicity index is proportional to the magnitude of static electric field. The analysis of coupled matter-wave equations shows that mentioned helical structure acts as a periodic potential (grating) for propagation of electromagnetic waves at visible light frequencies. Electric field could be used for manipulation of light pulses as well as suggesting wide choice of light induced and electrically controlled spintronics setups.

2. The Model

We consider a model of one-dimensional classical spin chain along the x axis with a single phase multiferroicity see Fig. 1. The Hamiltonian of classical spin system including both ferromagnetic symmetric and type antisymmetric exchange terms and subjected to the external electric $\boldsymbol{E}$ and magnetic $\boldsymbol{H}$ fields reads as follows:

$$\hat{H} = \sum_n [-J\boldsymbol{S}_n\boldsymbol{S}_{n+1} + K_2(\boldsymbol{S}_n^z)^2 - \boldsymbol{H}_n\boldsymbol{S}_n - \boldsymbol{E}_n\boldsymbol{P}_n], \quad (1)$$

where J stands for a nearest neighboring spin exchage constant, K_2 is an easy axis anisotropy constant and polarization vector

$$\boldsymbol{P}_n = g_{EM}\left[\boldsymbol{e}_x \times [\boldsymbol{S}_n \times \boldsymbol{S}_{n+1}]\right] \quad (2)$$

comes from Dzyaloshinskii-Moriya type antisymmetric exchange mechanism between neighbouring spins situated in n-th and $n+1$-th sites, respectively, $\boldsymbol{e}_x$ is an unit vector along spin chain direction x and g_{EM} is electromagnetic coupling constant. Then it is straightforward to write down the matter equations complemented with Maxwell equations as follows:

$$-\frac{1}{c}\frac{d}{dt}[\boldsymbol{H}_n + 4\pi\boldsymbol{S}_n] = [\nabla \times \boldsymbol{E}]_n, \quad \frac{d\boldsymbol{S}_n}{dt} = \gamma\left[\boldsymbol{S}_n \times \frac{\partial \hat{H}}{\partial \boldsymbol{S}_n}\boldsymbol{H}\right]$$
$$\frac{1}{c}\frac{d}{dt}[\boldsymbol{E}_n + 4\pi\boldsymbol{P}_n] = [\nabla \times \boldsymbol{H}]_n \quad (3)$$

where γ stands for gyromagnetic ratio. Introducing now normalized radiation fields $\boldsymbol{f}$ and $\boldsymbol{h}$ via the following relations $\boldsymbol{E} = \boldsymbol{e}_y E_0^y + S_0\boldsymbol{f}$, $\boldsymbol{H} = S_0\boldsymbol{h}$ and determining spin deviations from ground state configuration as $S_n^z = S_0 m_n^z$, $S_n^x + iS_n^y = S_0 e^{iQn}[1 + m_n^x + im_n^y]$, we will linearize set of Eqs. (3) and as a first result get the identities: $m_n^x = f_n^x = h_n^x = 0$. Next we introduce magnetic field induction vector $\boldsymbol{B}_n = \boldsymbol{H}_n + 4\pi\boldsymbol{S}_n$ and its normalized version $\boldsymbol{B}_n = S_0\boldsymbol{b}_n$ and proceed in momentum repesentation of matter-wave vector set getting following coupled equations:

$$\frac{d^2 b_k^y}{dt^2} = -c^2k^2\left[b_k^y + 4i\pi\frac{\gamma S_0}{cQ}\left(b_{k-Q}^z + b_{k+Q}^z\right)\right]$$
$$\frac{d^2 b_k^z}{dt^2} = -c^2k^2\left[b_k^z - 4i\pi\frac{\gamma S_0}{cQ}\left(b_{k-Q}^y + b_{k+Q}^y\right)\right]$$

Introducing now a combination $\Phi_k = b_k^y + ib_k^z$ we finally arrive to the characteristic equation for light propagation in periodic potential:

$$\frac{d^2\Phi_k}{dt^2} = -c^2k^2\Phi_k - 4\pi c^2k^2\frac{\gamma S_0}{cQ}\left(\Phi_{k-Q} + \Phi_{k+Q}\right) \quad (4)$$

which implies the size of first gap in the photonic spectrum as $\Delta = 2\pi\gamma S_0$.

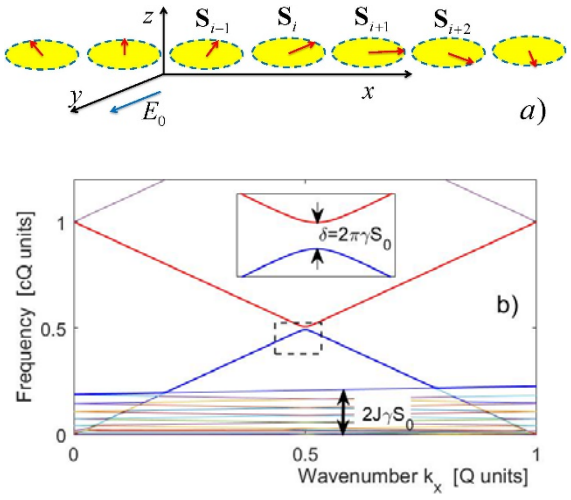

Fig. 1. a) Schematics for easy plane ferromagnetic spin chain along x axis. z stands for anisotropy axis and static uniform electric field $\boldsymbol{E}_0$ is directed along y axis. Arrows' directions represent helical ground state ordering. (b) Band-gap spectrum of magnon-photonic excitations appearing after linearization of initial matter wave equations (3). Blue and red curves represent first two photonic bands and inset shows enlarged view of photonic band-gap Lower lying magnonic excitation bandwidth is $2J\gamma S_0$.

3. Numerical Simulations

We proceed with numerical simulations on the initial set of matter-wave equations (3) choosing operating frequency ω in the visible light spectrum. Then we adjust external homogeneous static electric field E_0^y such that the operation frequency is situated within the photonic band-gap. As far as bandgap is located at $cQ/2$ and helicity index is defined from energy minimization as $Q = g_{EM}E_0^y/J$, the above scenario is realized for $E_0^y = 2J\omega/cg_{EM}$. Choosing that value for the external electric field, we form helical lattice initial ground state (with helicity index Q) in two pieces of the chain separated by a free space. In the middle of the free space we place a radiation source with a frequency ω and gradually increasing radiation amplitude in order to guarantee coherent radiation effect. At ultimate ends of the sample we employ completely absorbing boundary conditions. As seen from Fig. 2a the light is trapped and exponentially decaying profile across the sample is monitored. Now if we will keep the radiation frequency the same and slightly change static electric field, this will change helical order and shift the whole spectrum. As a result, radiation frequency appears to be out from the gap and light is freely released as it is seen in Fig. 2b. This is very convenient way for controlling the grating.

From set of coupled equations (4) it is possible to derive approximate dispersion relations near the photonic band gap. Indeed, as well established, in vicinity of the gap, i.e. when photon wavenumber $k \cong Q/2$ one can reduce (4) to two coupled equations for the harmonics k and k-Q. Then making trivial diagonalization one gets the following dispersion relations for the two photonic bands (blue and red curves in Fig. 1b):

$$\omega \cong \frac{cQ}{2}\sqrt{1 \pm 4\sqrt{\frac{\Delta k^2}{Q^2} + \left(\frac{\pi\gamma S_0}{cQ}\right)^2}}$$

where $\Delta k = k - Q/2$. Now if we fix light source frequency inside the gap, $\omega = cQ/2$, from (5) it immediately follows that wavenumber detuning is purely imaginary $\Delta k = i\pi\gamma S_0/c$ and for the parameter values given above localization length is approximately $\Lambda = 1/|\Delta k| \approx 10^{-5}$ m, which coincides pretty well with the direct numerical simulations presented in Fig. 2a.

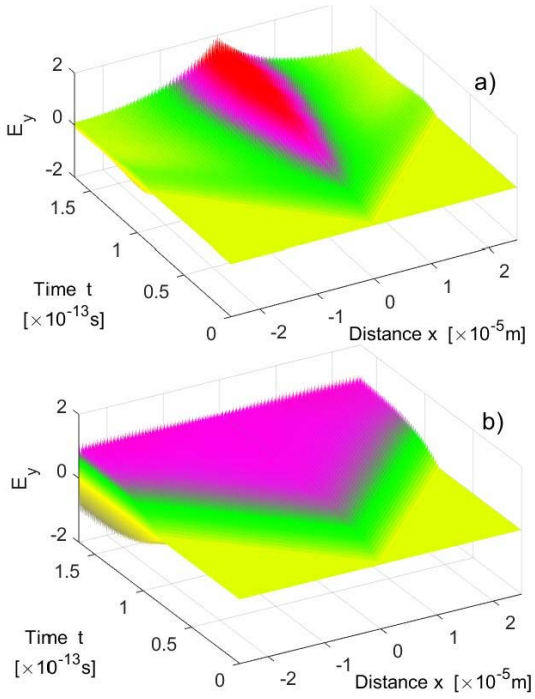

Fig. 2. Results of numerical simulations on initial set of matter-wave equations (3). We choose source light frequency in the visible spectrum $\omega/2\pi = 5 \cdot 10^{14}$ Hz and apply different static electric fields: in (a) electric field induces helical ground state with helicity index $Q = 2\omega/c$ and this causes light trapping inside the multiferroic lattice, while in (b) source frequency is kept the same and electric field is changed by 10%, resulting light complete release.

4. Conclusions

Concluding, it should be mentioned once again that magneto-Electric coupling in the Multiferroic materials allow control of the magnetic order and associated transport properties by an external electric field, which uniquely defines the spacing of the periodic potential. At the same time one can manipulate amplitude of the potential by applying static magnetic field along easy-plane anisotropy axis z that results in appearance of nonzero precession angle and helicity will be tilted out of plane by angle θ proportional to the magnetic field. This itself will cause the renormalization of easy plane magnetization $S_0 \to S_0 \cos\theta$ and as a consequence amplitude of the

periodic potential as well as a photonic bad-gap value $\Delta = 2\pi\gamma S_0$ will be decreased. All the mentioned facts promise to open new avenues for light and spin control presumably at low-energy consumption.

Acknowledgements

This work was supported by Shota Rustaveli National Science Foundation of Georgia (SRNSFG) [grant number FR-19-4049].

References

[1]. J. Liang, Q. Cui, H.n Yang, Electrically switchable Rashba-type Dzyaloshinskii-Moriya interaction and skyrmion in 2-dimensional magnetoelectric multiferroics, *Phys. Rev. B,* Vol. 102, 2020, pp. 220409(R)

[2]. D. Pantel, S. Goetze, D. Hesse, M. Alexe, Reversible electrical switching of spin polarization in multiferroic tunnel junctions, *Nat. Mater.,* Vol. 11, 2012, pp. 289-295.

(005)

Near Infrared Diffused Reflectance on Tissue Simulating Phantoms for Optical Applications

P. Demosthenous [1] and M. Baer [2]
[1] Cyprus Research & Innovation Center Ltd (CyRIC), 72, 28th Octovriou Ave, Engomi, 2414 Nicosia, Cyprus
[2] Institute of Microwaves and Photonics (LHFT) and Erlangen Graduate School for Advanced Optical Technologies (SAOT), Cauerstr. 9, 91058 Erlangen, Germany
Tel.: + 357 22-282828
E-mail: p.demosthenous@cyric.eu

Summary: We demonstrate a series of experiments that examine near infrared (NIR) diffused reflectance on low-cost optical tissue phantoms compose of water, gelatin, and/or titanium dioxide (TiO_2) powder. Such samples are commonly used in optical applications to simulate human tissue, where TiO_2 powder is used as the scattering agent. The experiments use a NIR Distributed Feedback Laser (DFB) at spectral around 2.274μm, where water presents relative low absorption coefficient compared to other substances such Ethanol that could provide blood alcohol concentration (BAC) measurements. The results demonstrate a fusibility study on using diffused reflectance on tissue phantoms in comparison to finger measurements, for optical applications similar to the optical detection of exogenous substances on human body.

Keywords: Near infrared, Diffused reflectance, Tissue phantoms, Distributed feedback laser, Blood alcohol concentration.

1. Introduction

This paper examines the fusibility on detecting Ethanol on human body, for determine blood alcohol concentration (BAC), by using NIR diffused reflectance on tissue phantoms in comparison to finger measurements. The optical setup uses an integrating sphere for the efficient collection of the diffused light from the sample, and at the same time examines the fusibility of a touch-based oriented detection.

2. Materials and Methods

The experiments use an Integration sphere that is known to be beneficial in some spectroscopic applications, especially in scattered/diffused reflectance or transmittance measurements [1]. Moreover, integrating spheres are used to enhance the collection of backscattered light in non-invasive sensing applications such as, finger photo plethysmography for determine blood constituents [2], and quantum cascade laser spectroscopy for glucose sensing [3]. In order to examine near infrared (NIR) diffused reflectance on simulating tissues, the experiments use, low-cost optical tissue phantoms [4] composing of water, gelatin, and/or titanium dioxide (TiO_2) powder. Such samples are commonly used in optical applications to simulate human tissue.

3. Measurement of Tissue Phantoms

3.1. Sample Preparation

Gelatin samples were prepared within glass chemistry vials that are transparent to NIR light. The dry components (gelatin, TiO_2) were filled into the glass vials and shaked. Then the water was added quickly, to prevent clogging of the gelatin. The mixture was shaken until the gelatin was soaked with water. Then the mixture was heated in the microwave at full power. To prevent the TiO_2 powder to settle down, the vial was placed in a custom-made sample-shake carousel until the mixture reaches a semi-solid consistency. When preparing samples with ethanol, the ethanol is added to the mixture after cooking. This prevents the ethanol from evaporating and changing its concentration in the mixture.

3.2. The Optical Setup

The optical setup for the measurements uses the Thorlabs NIR integrating sphere (IS200-4) in combination with Sacher DFB Laser (2.274μm) and Roithner RW-16 LED at roughly 1.6 μm (Fig. 1).

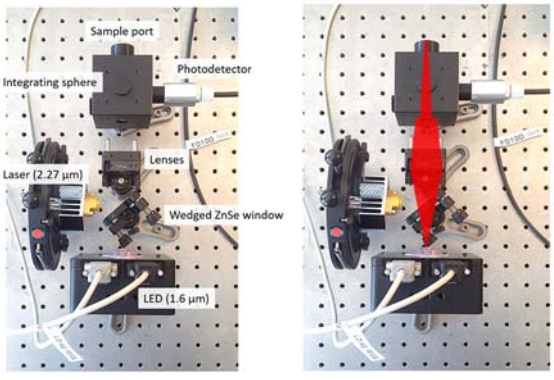

Fig. 1. Optical setup, which combines two NIR light sources (left). Beam path for the LED light source (right).

DFB Laser at 2.274 μm corresponds to an absorption peak of Ethanol, while 1.6 μm LED has been chosen for baseline measurements where ethanol and water absorption is low. Both light sources are

combined using a wedged ZnSe window. As neither the Laser nor the LED are perfectly collimated, two lenses, f1=80 mm and f2=100 mm, are used to collimate/focus the light within the integrating sphere. The setup is aligned in a way that the light that enters the integrating sphere completely, leaves the integrating sphere at the opposite port.

3.3. Ethanol samples with gelatin and TiO_2

For the measurements with ethanol samples, two samples with 17% ethanol and two samples with only water have been prepared using the proposed method. Each of these samples has been measured twice. Further, a measurement with the sample port open has been conducted. The results of the detected light intensities are presented in Fig. 2. The signal processing uses simultaneous signal acquisition by synchronous detection of orthogonal frequency components algorithm [5]. The ratio of the Laser and LED intensity is also shown in Fig. 3. The diffuse reflectance of the samples is rather weak, but comparable to a finger as will be shown in the next section. Unfortunately, there is no significant difference between the samples with and without ethanol. Therefore, there is an obvious limitation on getting lower limits of detection for BAC measurements.

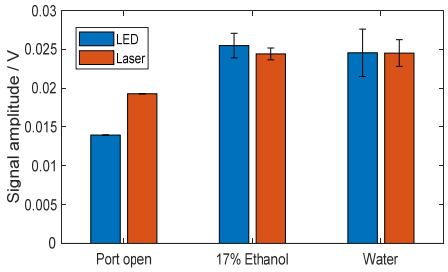

Fig. 2. Measurement of gelatin samples with TiO_2, with and without ethanol.

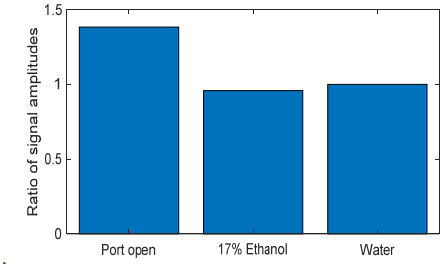

Fig. 3. Ratio of the Laser and LED signal amplitude.

4. Measurement of Finger 'Sample'

As a final experiment, similar measurements have been conducted, but this time on a real finger 'sample'. The sample port was covered with a thin glass plate and diverse prepared fingers have been pressed against the glass plate: a) Dry finger; b) Finger soaked for >5 min in pure ethanol; c) Finger soaked for >5 min in water. In addition, a measurement with the plain glass plate was done. The results are given in Fig 4 and Fig. 5. Worthy of note is the little difference between all measurements which proves that such touch-based systems lead to quite repeatable results. Unfortunately, there is again a very little difference between the finger soaked in ethanol and the finger soaked in water, similarly to the measurement that uses gelatin tissue phantoms.

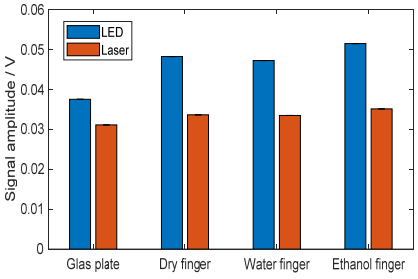

Fig. 4. Measurement of dry finger, water, and Ethanol-soaked finger.

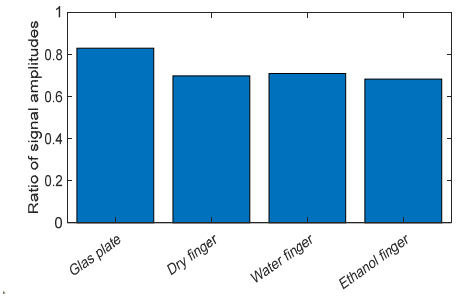

Fig. 5. Laser & LED signal amplitude ratio of Fig. 4.

5. Conclusions

Although the repeatability of these experiments was quite promising, a differentiation between ethanol concentrations in tissue phantoms and a finger is hardly possible via diffused reflectance.

Acknowledgements

The work was supported by the Project POST-DOC/0718/0186 which is co-financed by the European Regional Development Fund and the Republic of Cyprus through the Research and Innovation Foundation.

References

[1]. L. M. Hanssen, K. A. Snail, Handbook of Vibrational Spectroscopy: Integrating spheres for mid-and near-infrared reflection spectroscopy, *John Wiley & Sons Ltd*, 2002.

[2]. T. Yamakoshi, J. Lee, K. Matsumura, Y. Yamakoshi, P. Rolfe, D. Kiyohara, KI. Yamakoshi, Integrating sphere finger-photoplethysmography: preliminary

investigation towards practical non-invasive measurement of blood constituents, *PloS One*, Vol. 10, Issue 12, 2015, p.e0143506.

[3]. A. Werth, S. Liakat, A. Dong, C. M. Woods, C. F. Gmachl, Implementation of an integrating sphere for the enhancement of noninvasive glucose detection using quantum cascade laser spectroscopy, *Applied Physics B*, Vol. 124, Issue 5, 2018, pp. 1-7.

[4]. L. Ntombela, B. Adeleye, N. Chetty, Low-cost fabrication of optical tissue phantoms for use in biomedical imaging, *Heliyon*, Vol. 6, Issue 3, 2020, p. e03602.

[5]. M. Baer, B. Schmauss, P. Demosthenous, Simultaneous Signal Acquisition by Synchronous Detection of Orthogonal Frequency Components, in *Proceedings of the Sensor and Measurement Science International Conference (SMSI 2021)*, 3-6 May 2021, pp. 254-255.

(006)

Infrared Spectroscopic Application using an Integrating Sphere for Measuring Vapor Ethanol

P. Demosthenous [1] and M. Baer [2]
[1] Cyprus Research & Innovation Center Ltd (CyRIC), 72, 28th Octovriou Ave, Engomi, 2414 Nicosia, Cyprus
[2] Institute of Microwaves and Photonics (LHFT) and Erlangen Graduate School for Advanced Optical Technologies (SAOT), Cauerstr. 9, 91058 Erlangen, Germany
Tel.: + 357 22-282828
E-mail: p.demosthenous@cyric.eu

Summary: We demonstrate a near infrared (NIR) spectroscopic application for measuring vapor ethanol within the internal of an integrating sphere. The optical setup uses a NIR distributed feedback laser (DFB) at 2274 nm wavelength, where Ethanol presents high absorption coefficient. The measurements show a discrimination of different concentration of vapor ethanol with remarkable low noise level.

Keywords: Near infrared, Integrating sphere, Distributed feedback laser, Vapor ethanol.

1. Introduction

Integration spheres are known to be beneficial in some spectroscopic applications, especially in scattered reflectance or transmittance measurements [1]. Moreover, integrating spheres are beneficial in gas sensing applications, as they easily increase the effective optical path length from the light source to the detector. Hence, the interaction length between light and gas sample becomes higher [2]. In the work presented here, an integrating sphere is used to measure ethanol vapor in air, with a distributed feedback laser (DFB) at 2274 nm wavelength, which is close to an absorption band of ethanol.

2. Measuring Vapor Ethanol

In order to measure different concentrations of vapor ethanol that exist within the internal an integrating sphere, the setup shown in Fig. 1 was used. Cotton wool samples immersed in ethanol solutions of defined concentrations (0.00 %, 9.38 %, 18.75 %, 37.50 %) were used, one at a time, to provide the vapor ethanol within the sphere. During the sample preparation, ten minutes were needed until the cotton wool was fully soaked with liquid. To clean the integrating sphere from remaining ethanol vapors after each sample mounting, the integrating sphere was flushed with fresh air after each measurement. This was done using a little air pump for several minutes through the sample port, while no sample was mounted. Specifically, the procedure protocol for the measurement of different ethanol concentrations was as follows: 1.sample port closed for 5 min, 2.sample port open and measurement of reference for 3 min, 3.sample mounted and measurement of vapor ethanol for 5 min, 4.ventilation of integrating sphere with air pump for 3 min, 5.repetition of step 2-4 for all ethanol concentrations, 6.sample port open for 3 min to get an idea of the overall drift, 7.sample port closed (>5 min).

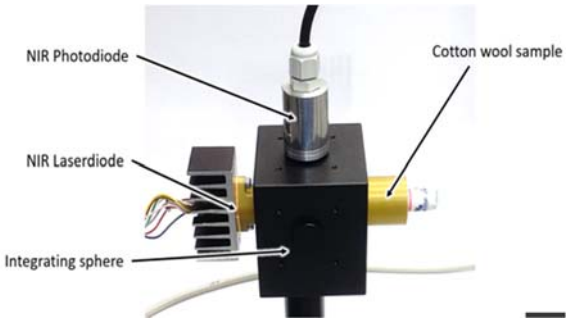

Fig. 1. Optical setup for measuring different vapor ethanol concentrations using NIR.

Before running any test with this setup, an Allan-Werle measurement has been conducted to confirm that the setup works and is sufficiently stable. For the Allan-Werle measurements all ports of the integrating sphere were closed except those for the Laser and the detector. The used light source was the Sacher Laser (DFB-2274-002) because ethanol shows high absorption at its wavelength (2.274um). The achieved Allen-Werle plot is depicted in Fig. 2. The minimum can be found at roughly 4 sec of integration time, where the noise level in general is acceptable low.

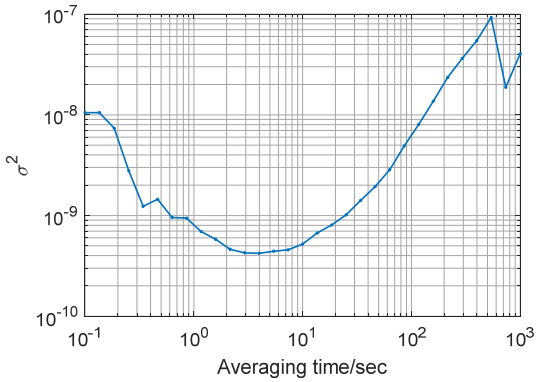

Fig. 2. Allan-Werle variance of the optical setup.

The result of the experiment that follows the measurement procedure stated above, is shown in Fig. 3. It is noticeable, that there is almost no difference between the sample port opened and the sample mounted. Thus, it can be concluded that the sample absorbs almost all of the light, no matter if ethanol is present or not, this is something that verifies the absorption peak at ~2.3 um of cotton sample [3]. However, with increasing ethanol concentration, a difference in the signal shape over time can be determined.

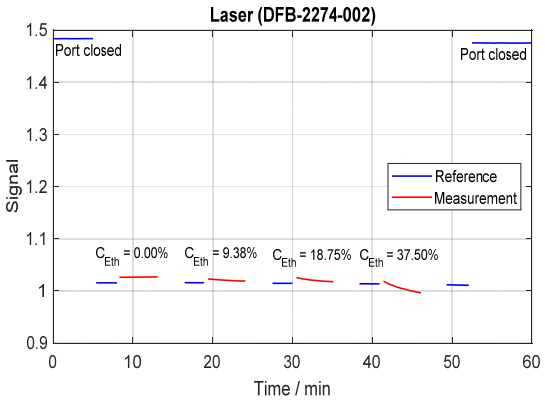

Fig. 3. Measurement result for different vapor ethanol concentrations.

Fig. 4 shows the excerpt of each concentration measurement (red lines in Fig. 3) referenced to the reference level (blue lines in Fig. 3) taken right before. It can be seen that the signal level right after the sample has been mounted does not give any information on the actual ethanol concentration of the sample. However, over time, the signal level decreases. This effect is stronger for samples with higher ethanol concentration, where ethanol vapor fills the integrating sphere and leads to higher light absorption due to multiple reflections within the integrating sphere, resulting to a decrease of the detected signal level.

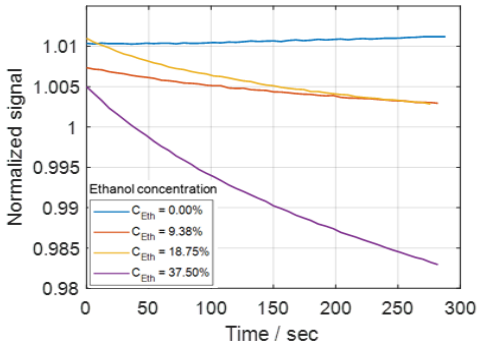

Fig. 4. Excerpt graph from measurement results in Fig. 3.

As discussed, the initial signal value after the sample is mounted does not give any information on the ethanol concentration on the sample. However, the initial value of the graphs in Fig. 4 have been used as baseline and shifted to 1 (Fig. 5). It is possible to distinguish between different ethanol concentrations and it is remarkable, that the noise level is quite low. The slight signal increase of the 0% ethanol measurement originates either from any kind of drift in the setup or from the fact that humidity in the integrating sphere increases over time. The former however appears more reasonable, because there is no good explanation why increasing humidity should increase and not decrease the light intensity. From that, we conclude, that the optical setup, the used electrical components, and the signal processing software [4] are well suited for this type of application. From the graphs in Fig. 5 one can estimate that the limit of detection for this method is in the range of 5%vol ethanol concentration.

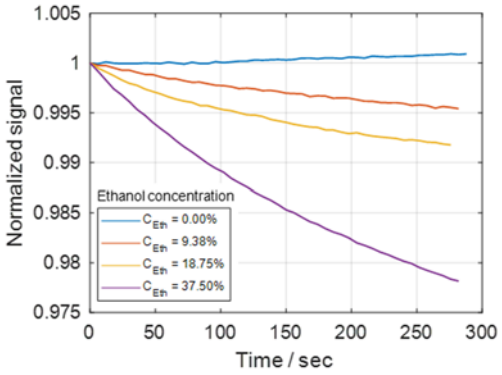

Fig. 5. Measurement results from Fig. 3, normalized and baseline corrected.

3. Conclusions

It has been demonstrated that is possible to distinguish between different vapor ethanol concentrations existing within the internal of an integrating sphere, with a limit of detection at around 5 %vol ethanol.

Acknowledgements

The work was supported by the Project POST-DOC/0718/0186 which is co-financed by the European Regional Development Fund and the Republic of Cyprus through the Research and Innovation Foundation.

References

[1]. L. M. Hanssen, K. A. Snail, Handbook of Vibrational Spectroscopy: Integrating spheres for mid-and near-infrared reflection spectroscopy, *John Wiley & Sons Ltd*, 2002.

[2]. S. Tranchart, I. H. Bachir, J. L. Destombes, Sensitive trace gas detection with near-infrared laser diodes and

an integrating sphere, *Applied Optics*, Vol. 35, Issue 36, 1996, pp. 7070-7074.

[3]. Y. Liu, C. Delhom, B. T. Campbell, and V. Martin, Application of near infrared spectroscopy in cotton fiber micronaire measurement, *Information Processing in Agriculture*, Vol. 3, Issue 1, 2016, pp. 30-35.

[4]. M. Baer, B. Schmauss, P. Demosthenous, Simultaneous Signal Acquisition by Synchronous Detection of Orthogonal Frequency Components, in *Proceedings of the Sensor and Measurement Science International Conference (SMSI 2021),* 3-6 May 2021, pp. 254-255.

(007)

Water-repellent Coatings Based on Anodized Aluminum under Femtosecond Laser Ablation

A. M. Rodin [1], O. Myronyuk [2], D. Baklan [2], G. Vasyliev [2] and E. Vanagas [1,3]
[1] Solid State Laser laboratory, Center for Physical Sciences and Technology,
Savanorių 231, LT-02300 Vilnius, Lithuania
[2] National Technical University of Ukraine 'Igor Sikorsky Kyiv Polytechnic Institute',
37, Prospect Peremogy 21, 03056 Kyiv, Ukraine
[3] Evana Technologies Ltd, Mokslininkų 2, LT-08412 Vilnius, Lithuania
Tel.: + 370 60140057
E-mail: aleksej.rodin@ftmc.lt

Summary: Hierarchical structures are formed on the surface of anodized aluminum, in which the microlevel in the form of a mesh and dot patterns was obtained by femtosecond laser ablation followed by polymethylhydrosiloxane, and the nanolevel was achieved by a pre-hydrophobized pyrogenic silica coating. The use of the Zisman Plot to determine the critical energy of surface wetting showed that the decrease in the values of the contact angle with a decrease in the surface tension of the mixture occurs stepwise: the first stage is observed at a surface tension below 44 mN/m, and the second at 42–38 mN/m. It is shown that the mesh structure is more stable than the dot structure.

Keywords: Ultrafast laser-matter interaction, Femtosecond laser ablation, Water repellent coatings, Anodized aluminium.

1. Introduction

Although superhydrophobicity has long been known from lotus leaves, it was first described in 1964 and has been the subject of >11000 papers to date. The superhydrophobicity is determined by the microstructure and nanoscale of the material surface, the form-factor or shape of the texture and the intrinsic hydrophobicity of the material. Superhydrophobic coatings can be used to obtain anti-icing [1], self-cleaning [2] and anti-corrosion properties [3].

Depending on the type of substrate, lithography, electrospinning, vapor deposition, template methods, electrochemical synthesis and sol-gel processing can be used to create a hydrophobic surface [4]. Laser ablation of aluminum is more efficient than chemical etching, plasma spray and chemical vapor deposition while ultrashot laser pulses open the way to hierarchical micro-nanoscale textures [5]. In addition, femtosecond lasers create smoother and sharper micro-nanoscale hierarchical structures that increase hydrophobicity [6].

Although hydrophobization sometimes occurs spontaneously, organosilicon compounds that react with the functional groups of the oxide layer are used to speed up the process. Surface interaction reactions are described in the literature [7]. For aluminum, these organosilicon compounds are able to react with the oxide layer, more precisely, with the functional groups of this layer. The widespread use of superhydrophobic materials is limited by the lack of cost-effective, fast and scalable technology for texturing and hydrophobization.

We have studied the formation of textures by a commercial femtosecond laser in a thick oxide layer on an aluminum surface in combination with a widely available polymethylhydride siloxane.

2. Experiment

2.1. Samples Preparation and Laser Treatment

Industrial grade 6060 alloy 2 mm thick aluminum plates and polymethylhydridesiloxane (XIAMETER MHX 1107, Dow Chemical) to hydrophobize their surface were used.

Anodizing was carried out for 60 min at a current density of 2 A/dm^2 in a 2.4 M H_2SO_4, temperature of the solution during the anodizing process was maintained at no more than 10°C.

The mesh (~28×16 μm^2) and void (Ø11–22×46 μm) textures were formed with a *Light Conversion* "Carbide" laser integrated into a "Freezer01" tool from *Evana Technologies*.

2.2. Chemical Surface Modification

After laser treatment, cleaning with compressed air and washing with water, 0.0788 g of a 0.05% solution of polymethylhydrogen siloxane (PMHS) in xylene was applied stepwise and dried for 10 min at 80 °C. The nanocoating (a solution of 3.75 wt.% Aerosil R 972 and 1.25 wt.% of acrylic resin Pliolite AC 80, 95 wt.% xylene) was applied with an airbrush and dried for 20 min at 80 °C [8].

2.3. Characterization

The values of the contact angle from distilled water were measured by the sessile drop method. The critical

surface tension was determined by the water-ethanol mixture at various concentrations by the sessile drop method. The Zisman plot method was used to determine the surface energy and describe the wettability of the obtained coatings [9].

To characterize the surface of the samples and determine the contact angle, was used an optical microscope with a built-in digital camera Delta Optical HCDE-50 and the corresponding ScopeTek View software. For data reproducibility, five points were measured on each sample.

Scanning electron microscope Selmi REM-106 was used to obtain electron microscopy images. Infrared spectra of the surface of the samples, namely coatings of alumina, polymethylhydridesiloxane and coatings of aluminum oxide treated with polymethylhydridesiloxane, were obtained on a Nicolet 4700 FTIR spectrophotometer. The spectrum was recorded in the range 400–4000 cm^{-1} by the attenuated total reflection (ATR) method.

3. Results and Discussion

The structure of the layer after laser ablation of aluminum oxide (Fig. 1) differs from the structures without prior anodization. The edges of the recesses on the surfaces are flat, and the space between the formed elements retains an unchanged fairly flat structure.

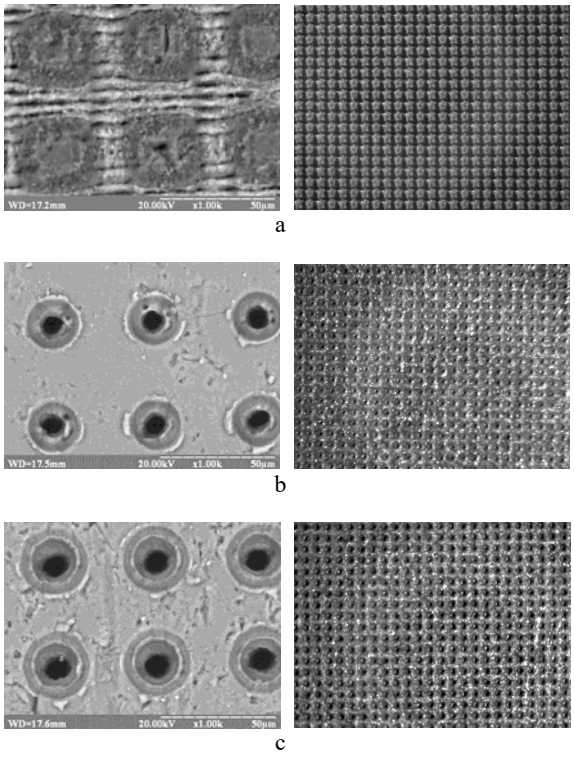

Fig. 1. Surface structure of samples under SEM (left) and under an optical (right) microscopes.

The anodized surface is initially hydrophilic, so the applied water drop disappears in the pores due to the capillary effect. The hydrophilicity of the layer does not change with time as it does when texturing pure aluminium. The use of hydridesiloxanes allows to increase the hydrophobicity of the aluminum oxide surface due to interaction with surface hydroxyl groups [10]. Such reactions can proceed at room temperature, which is important for scaling up the technology.

To determine the effective degree of water repellency, the contact angle was measured (Fig. 2) after applying a 0.05 % solution in xylene to the surface of textured samples, drying and removing residues.

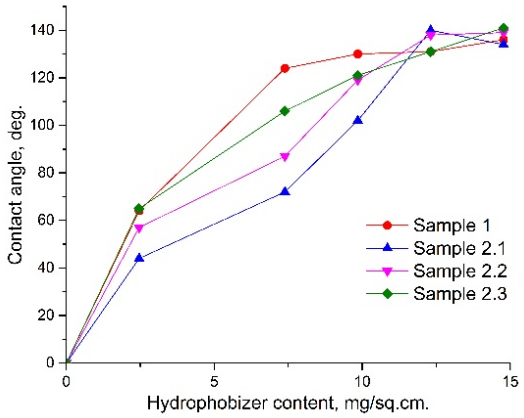

Fig. 2. Determination of the effective concentration of the modifier for hydrophobization of samples.

As can be seen, an increase in hydrophobicity due to the formation of a coating occurs even at low concentrations of the modifier, but this state is metastable. A stable effect is achieved at concentrations 7.5–12 mg/cm^2 depending on the texture. Values >130° are achieved with a further increase in the content of the water repellent. It is obvious that the amounts of polymethylhydrosiloxane consumed are much higher than those required for the formation of a monomolecular layer.

The surface of the plates was studied by IR-spectroscopy. The textured surface spectrum is characteristic of anodized alumina, except for the absence of a broad peak of adsorbed water, which can be explained by the rather low specific surface area of the material. The spectrum of the treated surface confirms the assumption that there is a significant amount of unbound polymer on it, possibly due to the formation of van der Waals interactions or hydrogen bonds between the surface and the siloxane.

The treatment of textured surfaces with polymethylhydridesiloxane increases hydrophobicity, close to theoretically predicted by the Cassie law, but such surfaces are not superhydrophobic. To achieve the latter, a layer of 66% hydrophobic fumed silica and 33 wt.% styrene acrylate in xylene solution was pneumatically sprayed [1].

As can be seen from Table 1, the microstructure after laser ablation plays the role of a basis for a

nanostructure capable of increasing the contact angle by 7–12°, i.e. to the superhydrophobic level.

Table 1. Static water contact angle values on different surfaces.

Sample	PMHS treated, WCA, degrees	Silica treated, WCA, degrees
1	132 ± 1	141 ± 1
2.1	125 ± 1	136 ± 1
2.2	132 ± 1	139 ± 1
2.3	134 ± 1	145 ± 1
Silica glass treatment	-	126 ± 1

To determine the critical wetting energy by the Zisman method, our results were presented as the dependence of the surface wetting angle and surface tension on the respective mixture.

4. Conclusions

Two types of high-contrast microstructures were recorded with a femtosecond laser on the surface of an anodized alumina layer, then treated with polymethylhydridesiloxane to achieve contact angles from 125° to 134°.

It is shown that hydrophobization under atmospheric conditions requires an excess of polysiloxane, part of which remains on the surface in an unbound state. The use of fumed silica with hydrophobized particles to organize the nanolevel of the hierarchical structure makes it possible to increase the contact angle to 136–145°. It has been established two values of the critical surface energy for the nano- and microlevels: <44 mN/m and 33–35 mN/m, which corresponds to a stepwise transition from Cassie to Wentzel state. At the same time, the second values for a structure with columns are lower than for a structure with holes. Thus, the oxide layer is an excellent substrate for microstructures, but the nanostructures necessary for water-repellent properties are provided by the nanocomposite layer.

Acknowledgements

This project has received funding from the Research Council of Lithuania, agreement S-LU-22-3 (Lithuania-Ukraine programme) and S-MIP-21-30.

References

[1]. L. B. Boinovich, A. M. Emelyanenko, V. K. Ivanov, A. S. Pashinin, Durable Icephobic Coating for Stainless Steel, *ACS Applied Materials & Interfaces*, 5, 7, 2013, pp. 2549-2554.

[2]. Y. B. Park, H. Im, M. Im, and Y. K. Choi, Self-cleaning effect of highly water-repellent microshell structures for solar cell applications, *Journal of Materials Chemistry*, 21, 3, 2011 pp. 633-636.

[3]. J. Jeevahan, M. Chandrasekaran, G. Britto Joseph, R. B. Durairaj, G. Mageshwaran, Superhydrophobic surfaces: a review on fundamentals, applications, and challenges. *Journal of Coatings Technology and Research*, 15, 2, 2018, pp. 231-250.

[4]. K. Manoharan, S. Bhattacharya, Superhydrophobic surfaces review: Functional application, fabrication techniques and limitations, *Journal of Micromanufacturing*, 2, 1, 2019, pp. 59-78.

[5]. G. Yuan, Y. Liu, C. V. Ngo, C. Guo, Rapid fabrication of anti-corrosion and self-healing superhydrophobic aluminum surfaces through environmentally friendly femtosecond laser processing, *Optics Express*, 28, 24, 2020, pp. 35636-35650.

[6]. B. Li, M. Zhou, W. Zhang, G. Amoako, C. Gao, Comparison of structures and hydrophobicity of femtosecond and nanosecond laser-etched surfaces on silicon, *Applied Surface Science*, 263, 2012, pp. 45-49.

[7]. P. Rodič, B. Kapun, M. Panjan, I. Milošev, Easy and Fast Fabrication of Self-Cleaning and Anti-Icing Perfluoroalkyl Silane Film on Aluminium, *Coatings*, 10, 3, 2020, p. 234.

[8]. B. P. Da Costa Neto, A. L. M. L. da Mata, M. V. Lopes, B. Rossi-Bergmann, M. I. Ré, Preparation and evaluation of chitosan–hydrophobic silica composite microspheres: Role of hydrophobic silica in modifying their properties, *Powder Technology*, 255, 2014, pp. 109-119.

[9]. S. Ebnesajjad, C. F. Ebnesajjad, Surface treatment of materials for adhesive bonding, *Elsevier*, 2014.

[10]. O. Myronyuk, D. Baklan, L. Nudchenko, Evaluation of the surface energy of dispersed aluminium oxide using owens-wendt theory, *Technology Audit and Production Reserves*, Vol. 2, No. 1(52), 2020, pp. 25-27.

(009)

Laser Fabrication of Different Crystals by Pulsed Bessel Beams

A. Kuriakose [1, 2], M. Bollani [3], P. Di Trapani [1] and O. Jedrkiewicz [2]
[1] Dipartimento di Scienza e Alta Tecnologia, Università dell'Insubria, Via Valleggio 11, 22100 Como, Italy
[2] Istituto di Fotonica e Nanotecnologie (IFN)-CNR, Udr di Como, Via Valleggio 11, 22100 Como, Italy
[3] Istituto di Fotonica e Nanotecnologie (IFN)-CNR, L-NESS, Via Anzani 42, 22100 Como, Italy
E-mail: akuriakose@studenti.uninsubria.it

Abstract: Ultrafast laser micromachining in diamond and sapphire has been realized using finite energy Bessel beams. The hardness of diamond and crack formation in sapphire have been addressed and tackled using different optimization techniques. In-bulk microstructures (graphitic wires in the case of diamond) can be formed without the need of sample translation and opportunely tailored by a suitable choice of the Bessel pulse parameters. Through-holes of hundred micrometer size can be generated, optimized and compared in both crystals.

Keywords: Laser micromachining, Bessel beams, Diamond, Sapphire, Micro through-holes.

1. Introduction

Ultrafast laser micromaching in crystals using femtosecond and picosecond pulses has emerged as one of the most efficient and precise techniques for microfabrication of transparent materials thanks to the minimization of heat transfer during the nonlinear absorption process [1]. Moreover, non-conventional beams have attracted interest in laser micromachining of crystals, dielectrics and semiconductor thin films. In particular, the non-diffracting nature of Bessel beams [2] makes the latter a great choice for in-bulk modifications without the need for sample translation along its thickness.

Diamond is composed of carbon atoms arranged in a crystalline structure and is featured by exceptional properties such as the highest thermal conductivity, high mechanical hardness and good biocompatibility [3]. Owing to its great physical properties such as scratch resistance, superior hardness, tensile strength, and wide spectral range transparency, sapphire is widely used in optoelectronic industries such as the substrate layer for Light Emitting Diodes, for integrated optical and microfluidic devices, touchscreens, micromechanical devices and optical windows [4].

In this work, we present the effect of Bessel beam bulk machining on two different kinds of crystals namely monocrystalline synthetic HPHT diamond (300 μm thick) and CVD diamond (500 μm thick), and monocrystalline c-plane sapphire (430 μm thick). We address the different types of challenges during the microfabrication: hardness and graphitic formation in the case of diamond, and the presence of cracks in sapphire. By using the most apt laser parameters, micrometer-thick graphitic wires are drawn in diamond. Finally, we are able to drill through-holes in both crystals.

2. Laser Micromachining in Diamond

2.1. Generation of Graphitic Microwires

In-bulk micromachining studies have been performed by means of a 20-Hz Ti:Sapphire amplified laser system delivering 40-fs transform-limited pulses (stretchable till picosecond regime) at 800 nm wavelength by injecting the beam orthogonally to the sample thickness. By using a finite energy Bessel beam featured by an elongated focal zone larger than the sample thickness in multiple pulse regime, graphitic lines are generated without any sample translation across the whole material bulk because of the laser-matter interaction and the consequent modification of the crystalline structure (Fig. 1). In this work, we will highlight the role of pulse duration, number of pulses and pulse energy, for a given Bessel beam geometry, in generating tailored graphitic thin micro-lines for conductivity applications. We will also define a different laser machining regime that leads to strong in bulk-ablation, essential for the generation of through-holes.

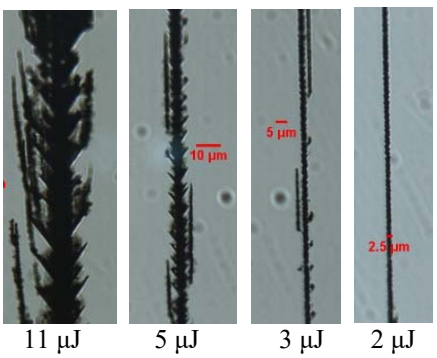

Fig. 1. Evolution of graphitic microwires with respect to pulse energy at 1 ps pulse duration.

2.2. Generation of Micro Through-holes

Through-holes in thick diamond samples can be realized by means of a micro-drilling process based on a trepanning-like technique [5] using Bessel beams. The number of machining passes, pulse energy and number of path encircling of the laser beam injected from the sample top, can be set up such that holes of any desired radius can be generated irrespective of the hardness but with a lower threshold radius limit given by the sample thickness. We present clean through-holes obtained in 300 μm bulk diamond serving as building blocks for microfluidic applications (Fig. 2).

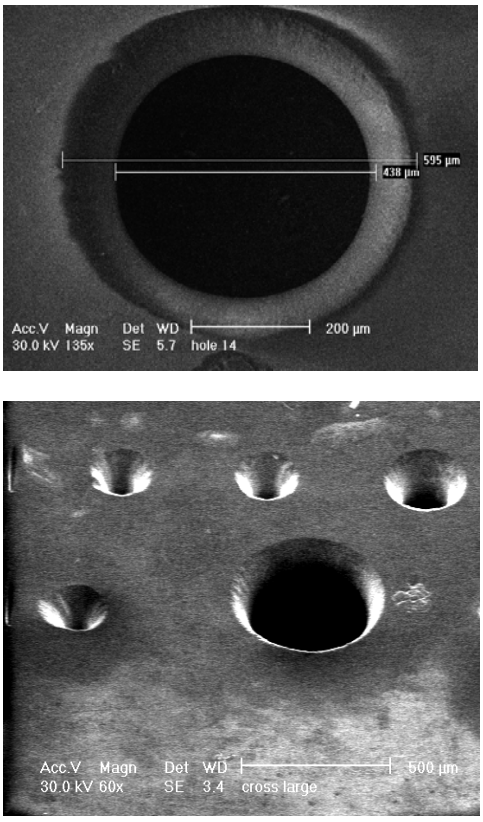

Fig. 2. SEM images of holes in diamond: Hole for microfluidic applications (top) and holes with different radii (bottom).

3. Laser Micromachining in Sapphire

3.1. Generation of Crack-less Microstructures

Bessel beam micromachining studies have been performed in sapphire both in single shot and in multiple shot, highlighting a different response of this crystal to the laser-matter interaction with respect to diamond. In the literature, it has been noted that the crack formation in sapphire depends on the pulse duration of the laser beam. While it is less evident in the femtosecond regime, it is highly pronounced with picosecond duration pulses [4]. This effect is particularly observable on the top surface of the sapphire sample. In our work, we show that by using a lower cone angle than that reported in the literature, we are able to prevent the formation of surface cracks when injecting the beam orthogonally through the whole sample thickness even in the picosecond regime.

3.2 Generation of Micro Through-holes

The Bessel beam drilling technique has been successfully applied here for the first time on sapphire. We will show that by suitably tailoring the laser beam parameters it is possible generate, on a 430 μm thick sapphire sample, through-holes which have negligible crack and very low taper angle which, to our knowledge, have never been reported before by using Bessel beams (Fig. 3). While different pulse energies and durations are explored, we demonstrate that a final optimization of the generated hole can be achieved by using on the top surface sample, a 60 μm thick layer of Kapton Polyimide, featured by the same refractive index as that of sapphire.

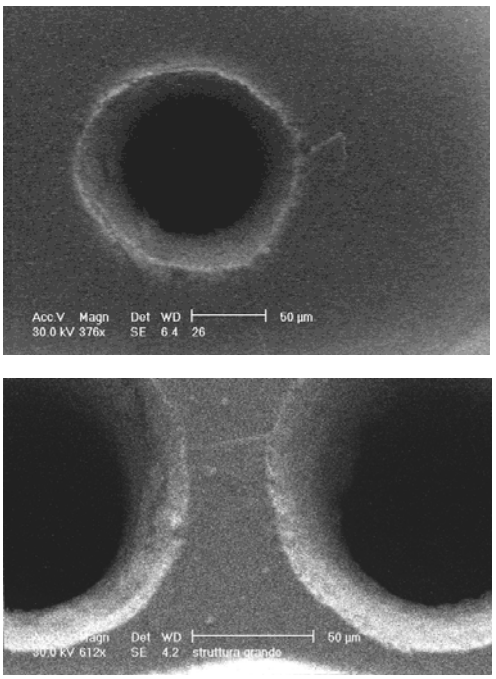

Fig. 3. SEM images of through holes in sapphire: Hole at most ambient parameters (top) and crack-less twin holes (bottom).

4. Conclusions

The laser microfabrication technique with finite energy ultrafast Bessel beams has been implemented to address various challenges while micromachining two different crystals. Various tailorable microstructures are generated with least amount of additional damages so that they can be used for different applications. In particular, we show the possibility to drill through-holes of hundred micrometer size in both crystals.

Acknowledgements

This project has received funding from the European Union's Horizon 2020 research and innovation programme under the Marie Skłodowska-Curie grant agreement No. 956387

References

[1]. R. R. Gattass, E. Mazur, Femtosecond Laser Micromachining in Transparent Materials, *Nature Photonics*, Vol. 2, Issue 4, 2008, pp. 219-225.

[2]. J. Durnin, J. J. Miceli, Jr., J. H. Eberly, Diffraction-free beams*, Physical Review Letters*, Vol. 58, Issue 15, 1987, pp. 1499-1501.

[3]. S. Kumar, S. M. Eaton, M. Bollani, B. Sotillo, A.Chiappini, M. Ferrari, R. Ramponi, P. Di Trapani, O. Jedrkiewicz, Laser surface structuring of diamond with ultrashort Bessel beams, *Scientific Report*s, Vol. 8, 2018, p. 14021.

[4]. T. Liu, H. Wei, J. Wu, J. Lu, Y. Zhang, Modulation of crack formation inside single-crystal sapphire using ultrafast laser Bessel beams, *Optics & Laser Technology*, Vol. 136, 2021, p. 106778.

[5]. O. Jedrkiewicz, D. Valetti, P. Di Trapani, Etching and drilling of through-holes in glass by means of picosecond Bessel beams, *SN Applied Sciences,* Vol. 1, 2019, p. 1267.

(010)

High-speed Wavelength Division Multiplexing Transmission over SI-Polymer Fibers

Ulrich H. P. Fischer and Mladen Jóncic
Harz University of Applied Sciences, Friedrichstr. 57, 38855 Wernigerode, Germany,
Tel.: +49-(0)3943-659351, fax : +49-(0)3943-659399
E-mail: ufischer@hs-harz.de

Summary: In short-range communication 1 mm PMMA SI-POF established itself as a reasonable alternative to the traditional data communication media such as glass fibers, copper cables and wireless systems. Due to multiple advantages such as a large core diameter, tolerance to fiber facet damages and low installation costs, the SI-POF is already applied in industrial automation, automotive industry and in-house/office networks. The commercial systems with SI-POF use a single channel for data transmission. Utilization of several optical carriers for parallel transmission of data channels over a single fiber, known as WDM, represents another alternative to increase the capacity of SI-POF link. To experimentally demonstrate the feasibility and potential of a high-speed POF WDM concept, a four-channel data transmission setup was realized. In addition, the record 14.77 Gb/s data rates employing the offline-processed DMT modulation were demonstrated over 50 m SI-POF, respectively, at the BER=10^{-3}. Compared to the fastest single-wavelength systems, two times higher transmission capacity was achieved.

Keywords: Polymeric optical fibers, WDM transmission, WDM multiplex, WDM demultiplex, WDM over POF.

1. Introduction

Having its origin in the 1960's as well as the silica glass fiber, the polymer optical fiber (POF) stayed long in the shadow of the huge development and success of glass fiber communications. However, the advances in POF technology and the growing need for high-speed short-range communication networks make POF nowadays gain more and more in importance. The key advantage of POF is a large core diameter. It makes POF tolerant to the fiber facet damages and relaxes the alignment tolerances, thus also reducing the installation costs. A comprehensive overview on various POFs is given in [1].

Three major application sectors of SI-POF data communication technology are industrial automation, automotive industry and in-house/office networks. The bus systems such as Profibus (1.5 Mbit/s, 60 m) and industrial Fast Ethernet (100 Mbit/s, 50 m) are typical applications and since 2013 also the Gigabit Ethernet transceivers (1 Gb/s) are available on the market enabling the transmission of broadband services over 50 m SI-POF [2].

1.1. Capacity Extension by WDM Technology

Complying with any of the hitherto developments, utilization of several optical carriers for parallel transmission of data channels over a single fiber represents another alternative to increase the transmission capacity of SI-POF. The technique is well known as wavelength division multiplexing (WDM).

The principle of WDM is shown in Fig. 1. Since different wavelengths λ_1–λ_N do not interfere with each other in a linear medium, they can be used to simultaneously carry the data signals over a single fiber. The most frequently mentioned motivation for POF WDM is to increase the transmission capacity of SI-POF link compared to the single-wavelength systems.

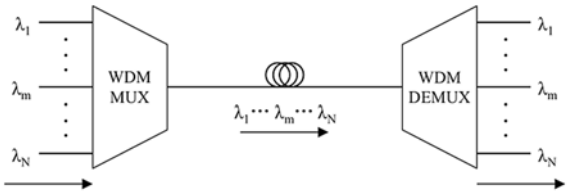

Fig. 1. Principle of WDM: MUX - Multiplexer, DEMUX – Demultiplexer.

In the early attempts, the LED-based POF systems exploiting WDM technology could not provide sufficient capacity [3, 4]. Only recently, supported by the advance in the visible laser diode technology, the record-breaking POF WDM transmission experiments, including the work of the author, were performed [5, 6, 8].

2. Four-channel POF WDM Transmission Experiments

The data transmission setup is shown in Fig. 2. It comprised an Agilent N4903A bit error rate tester (BERT), four butt-coupled edge-emitting laser diodes, multiplexing POF coupler, 50/100 m SI-POF link, interference-based POF demultiplexer, optical receivers and Agilent 86100B sampling oscilloscope.

To combine the optical signals (MUX) with different wavelengths onto the SI-POF link, a Comcore 4×1 fused POF coupler was used. For direct launching with 405 nm (DL-5146-101S), 450 nm, 515 nm and 639 nm laser diodes, the IL between any of four input (laser coupled) ports and the output port was 8-9 dB.

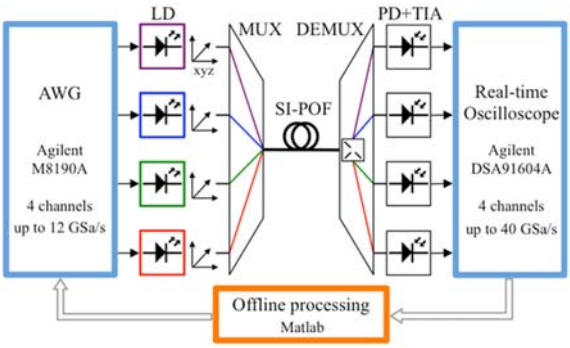

Fig. 2. Experimental setup for the measurements employing offline-processes DMT modulation: LD – laser diode; MUX – multiplexer; DEMUX – demultiplexer; PD – photodiode; TIA – transimpedance amplifier.

The experimental setup for the measurements employing the offline-processed DMT modulation is shown in Fig. 2. It comprised the four-channel Agilent M8190A AWG, four butt-coupled edge-emitting laser diodes, four-legged multiplexing POF bundle, SI-POF link of two different lengths (50, 100m), interference-based POF demultiplexer, optical receivers, four-channel Agilent DSA91604A real-time oscilloscope and computer with a software for offline signal processing.

2.1. Experimental Results

To estimate the quality of the WDM channels and allocate the number of bits per subcarrier, four DMT pilot signals with 256 subcarriers, each loaded with 16-QAM, were simultaneously transmitted over four channels. In 50 m and 100 m experiments the bandwidth occupied by the pilot signals was initially set to 1 GHz and 500 MHz respectively.

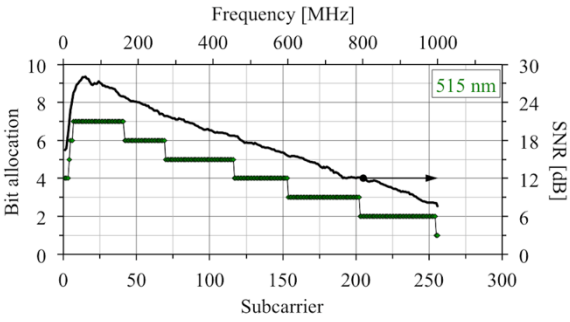

Fig. 3. Measured example SNR per subcarrier before bit-loading (solid black curve) and bit-loading scheme obtained on the basis of Chow's rate adaptive bit-loading algorithm (curve with markers) for the 515 nm channel in 50m POF experiment.

After deduction of the DMT transmission overhead, the data rates transmitted in the individual WDM channels were 3.26 Gb/s (405 nm channel), 3.90 Gb/s (450 nm channel), 4.08 Gb/s (515 nm channel) and 3.53 Gb/s (639 nm channel). The total averaged BER in each channel was 10^{-3} allowing the FEC with 7% overhead. A measured example of the Bandwidth of the subcarrier behavior of the green Channel at 515nm is depicted in Fig. 3. Therefore, an aggregate bit rate of 14.77 Gb/s achieved at the BER=10^{-3} corresponded to 13.8 Gb/s information bits at the BER<10^{-9}. The realized system provided 2.3 times more capacity than the fastest 50 m single-wavelength system known from literature, which operated at 650 nm [9].

4. Conclusions

In this work it was shown, that WDM transmission over POF realised a huge extension of overall data rates within one fiber over 50 m. The 14.77 Gb/s data transmission based on the offline-processed DMT modulation was demonstrated over 50 m SI-POF at the BER=10^{-3}. That is the second highest transmission capacity ever achieved over 50 m SI-POF.
Enabling higher WDM data rates, it will be possible to reach data rates for POF WDM Systems with up to 40 Gbit/s with 16 WDM channels.

References

[1] W. D. [Ziemann08] O. Ziemann, J. Krauser, P. E. Zamzow, *POF Handbook – Optical Short Range Transmission Systems. , 2008.* Springer Verlag Berlin Heidelberg, 2008.

[2] K. L. Johnson, W. Hogan, M. M. Dummer, and C. Steidl, Advances in High-Speed Red Vcsel Performance, *Adv. Opt. Technol.*, Vol. 2012, pp. 5–10, 2012.

[3] P. J. Pinzón, I. Pérez, and C. Vázquez, Visible WDM System for Real-Time Multi-Gb/s Bidirectional Transmission over 50-m SI-POF, *IEEE Photonics Technol. Lett.*, Vol. 28, no. 15, 2016.

[4] X. Li *et al.*, 11 Gb/s WDM transmission over SI-POF using violet, blue and green µlEDs, in Proceedings of *Optical Fiber Communications Conference and Exhibition (OFC 2016)*, 2016.

[5] and U. S. [Kruglov14] R. Kruglov, J. Vinogradov, S. Loquai, O. Ziemann, C.-A. Bunge, T. Hager, 21.4 Gb/s discrete multitone transmission over 50-m SI-POF employing 6-channel WDM, in Proceedings of the *OFC/NFOEC*, 2014, p. Paper Th2A.2.

[6] M. Joncic *et al.*, Four-Channel WDM Transmission Over 50-m SI-POF at 14.77 Gb/s Using DMT Modulation, *Photonics Technol. Lett. IEEE2*, Vol. 26, no. 13, pp. 1328–1331, 2014.

[7] M. Jončić *et al.*, Four-Channel WDM Transmission via 1-mm Si-POF Employing DMT Modulation, in Proceedings of the *POF Conference 2014*, 2014, p. 8.

[8] I. Yahav, N. Sheffi, Y. Biofcic, and D. Sadot, Multi-Gigabit Spatial-Division Multiplexing Transmission over Multicore Plastic Optical Fiber, *J. Light. Technol.*, vol. 39, no. 8, April 2022, pp. 2296–2304.

[9] O. Z. [Vinogradov11] J. Vinogradov, R. Kruglov, S. Loquai, Multi gigabit transmission with blue, green and red laser diodes, in Proceedings of the *20th International Conference on Plastic Optical Fibers*, 2011, pp. 467–470.

(011)

Combining Bright-field and Second Harmonic Generation Microscopy for the Characterization of Thyroid Nodules

R. Hristu [1], L. G. Eftimie [2], R. Glogojeanu [3], S. G. Stanciu [1] and G. A. Stanciu [1]
[1] Center for Microscopy-Microanalysis and Information Processing, University Politehnica of Bucharest, 313 Splaiul Independentei, 060042, Bucharest, Romania
[2] Central University Emergency Military Hospital, Pathology Department, 134 Calea Plevnei, 010825 Bucharest, Romania
[3] Department of Special Motricity and Medical Recovery, The National University of Physical Education and Sports, Bucharest, Romania
E-mail: radu.hristu@upb.ro

Summary: Thyroid carcinomas represent a challenging problem as their differentiation from the much more frequent benign pathologies can be sometimes difficult. Microscopic assessment of hematoxylin and eosin-stained tissue sections represents the current gold standard in thyroid pathology diagnosis. Quantitative second harmonic generation microscopy is gaining momentum in the investigation of fixed tissue sections, fresh tissue or even for *in vivo* experiments and provides images with high specificity to collagen within tissue samples. Automatic image analysis methods which can be used to differentiate between malignant and benign thyroid nodules are of paramount importance for addressing thyroid pathologies. We demonstrate here that the combination of bright-field microscopy and second harmonic generation imaging with image features extraction can be used to differentiate between capsules surrounding malignant and benign thyroid nodules. Our results indicate that second harmonic generation microscopy can complement traditional histopathological imaging to provide suitable data for thyroid nodule classification.

Keywords: Second harmonic generation microscopy, Bright-field microscopy, Collagen capsule, Thyroid nodule, Image features extraction.

1. Introduction

Thyroid nodules, although very common, have no symptoms in most of the cases. They are the clinical manifestations of different pathologies, both benign (e.g., follicular adenoma) as well as malignant (e.g., papillary or follicular thyroid carcinomas). The gold standard in thyroid cancer diagnosis is visualizing hematoxylin and eosin (H&E) stained thyroid tissue with bright field microscopy. However, the disadvantage of morphological interpretation of tissue by standard histopathology is significant inter-observer variability [1].

Qualitative evaluation of H&E-stained tissue sections is often sufficient for routine diagnostic purposes, but the advent of digital image analysis techniques and their evolution over the past years [2] has raised the possibility that objective quantification of microscopic image features will gain importance in providing data for clinical diagnostic purposes.

Laser scanning microscopy using nonlinear optical effects (e.g. two-photon excitation and second harmonic generation) have been proven to be useful tools in tissue imaging. Second harmonic generation (SHG) is a label-free, investigation method [3] which was successfully used to date for imaging collagen, myosin and tubulin. The success of SHG microscopy in the field of biomedical research relies on the quantification of collagen organization using different methods [4]. One of these methods is polarization-resolved SHG (PSHG) microscopy [5] which can provide information unavailable from intensity measurements alone.

2. Materials and Methods

Thyroid tissue samples were prepared according to standard histology protocols (stained with H&E). The slides were imaged with a bright-field Aperio LV1 IVD Whole Slide Scanner (Leica Biosystems) using a 20X objective lens. Regions of interest selected on the collagen capsule surrounding thyroid nodules were cropped from the whole slide images (WSI) and were further used for PSHG microscopy imaging.

PSHG images were acquired using a Leica TCS-SP confocal laser scanning microscope modified for NLO imaging [6]. The excitation source was a Ti:Sapphire laser (Chameleon Ultra II, Coherent) tuned at 860 nm. The input excitation laser beam was linearly polarized. A 40× magnification and 0.75 numerical aperture (NA) objective was used for focusing the laser beam on the sample and to collect the backscattered SHG (BSHG). The SHG signals were collected in the forward direction (FSHG) using a 0.9 NA condenser lens.

In order to extract the features to characterize collagen in bright-field WSI, prior to the analysis, the image tiles were converted to 8-bit images using different strategies: the intensity of the RGB image (*8b*), a weighted conversion (*8bw*), selection of the red channel (*RED*), and color deconvolution to extract the eosin channel (*EOSIN*).

Image features were extracted from both bright-field and PSHG microscopy images using standard histogram characterization, the gray-level co-occurrence matrix (GLCM), Helmholtz and fractal analysis (Fig. 1).

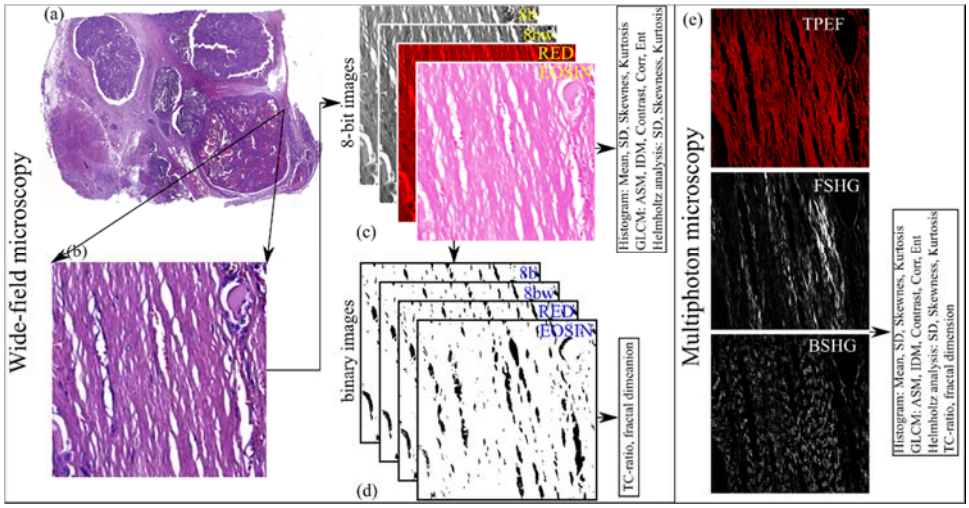

Fig. 1. Schematic representation of the feature extraction protocol. From the WSI (a) image tiles are cropped; (b) around the nodule capsule; (c) Four RGB to 8-bit conversion strategies are considered (i.e., 8b, 8bw, RED, EOSIN). Histogram, GLCM and Helmholtz analysis features are extracted from the 8-bit images; (d) 8-bit images are further binarized to extract TC-ratio and fractal features; (e) Feature extraction from SHG images.

3. Results

The statistical analysis performed on the features extracted from the WSI patches demonstrates that the histogram and the texture analysis performed by GLCM provide reliable features which can discriminate between the considered collagen thyroid nodule capsules. On the other hand, unsatisfactory results were provided by the TC-ratio and fractal dimension, which were extracted from binary images. Finally, the Helmholtz analysis which can determine local direction of structures in the images retrieved features which are not suitable to detect differences between microscopic image tiles acquired on thyroid nodule capsules.

A broader perspective of the extracted image features can be attained when using a Fisher score which is one of the most widely used supervised feature selection methods. We compute the Fisher score for features extracted from each of the four strategies to obtain the 8-bit image from WSIs. The irrelevant and/or redundant features were excluded based on the Fisher score, keeping only features with Fisher score values above the average Fisher score for all the features.

From the entire set of tested parameters, histogram skewness and kurtosis, GLCM (IDM, ASM), fractal dimension and SD in Helmholtz analysis provided statistically significant differences between benign and malignant nodule capsules on PSHG images.

4. Conclusions

The present study demonstrates that combining bright-field microscopy and second harmonic generation imaging with image feature extraction may be used to provide complementary information to the current histopathology procedures involving thyroid nodule diagnosis. The statistical and classification potential analysis demonstrate that thyroid nodule capsule features can be considered as good candidates to provide diagnostic cues.

Acknowledgements

This work was supported by the Romanian Executive Agency for Higher Education, Research, Development and Innovation Funding (UEFISCDI) under the grant PN-III-P1-1.1-TE-2019-1756 (SHGThyPath).

References

[1] R. V. Lloyd, et. al., Observer variation in the diagnosis of follicular variant of papillary thyroid carcinoma, *American Journal of Surgical Pathology*, Vol. 28, Issue 10, 2004, pp. 1336–1340.

[2] S.W. Jahn, et. al., Digital pathology: advantages, limitations and emerging perspectives, *Journal of Clinical Medicine*, Vol. 9, Issue 11, 2020, pp. 3697.

[3] X. Chen, et. al., Second harmonic generation microscopy for quantitative analysis of collagen fibrillar structure, *Nature Protocols*, Vol. 7, Issue 4, 2012, pp. 654-669.

[4] R. Hristu, et. al., Quantitative second harmonic generation microscopy for the structural characterization of capsular collagen in thyroid neoplasms, *Biomedical Optics Express*, Vol. 9, Issue 8, 2018, pp. 3923-3936.

[5] R. Hristu, et. al., Pixel-level angular quantification of capsular collagen in second harmonic generation microscopy images of encapsulated thyroid nodules, *Journal of Biophotonics*, Vol. 13, Issue 12, 2020.

[6] R. Hristu, et. al., Influence of hematoxylin and eosin staining on the quantitative analysis of second harmonic generation imaging of fixed tissue sections, *Biomedical Optics Express*, Vol. 12, Issue 9, 2021, 5829–5843.

(013)

Measurement of Transonic Airflow in a Compressor Blade Cascade by Spatial Carrier Interferometry

P. Psota [1], G. Cubreli [1] and D. Šimurda [2]
[1] Technical University of Liberec, Faculty of Mechatronics, Informatics and Interdisciplinary Studies, Institute of New Technologies and Applied Informatics (NTI), Studentská 2, 461 17 Liberec 1, Czech Republic
[2] Institute of Thermomechanics of the Czech Academy of Sciences, v. v. i., Dolejškova 1402/5, 182 00 Praha, Czech Republic
E-mail: pavel.psota@tul.cz

Summary: In this paper we introduce a robust, portable, high-speed and high-resolution interferometric method that can be easily applied in a wind tunnel facility providing very accurate results with high spatial resolution in almost real time. The method was used for investigation of high-speed flow in planar compressor blade cascade.

Keywords: High-speed, Interferometry, Transonic flow, Compressible flow, Shock waves, Wind tunnel.

1. Introduction

Increasing turbine efficiency is forcing the development of new ultra-long and thin turbine blades that operate at transonic to supersonic flow rates. These long blades in the last low-pressure stages of turbines are very prone to self-excited oscillations due to flow, the so-called blade flutter, which leads to high-cycle fatigue and potentially catastrophic blade breakage. An identical problem arises in the first stages of compressors of large aircraft engines. The blade flutter is currently the most difficult design problem in terms of guaranteeing the safety and operational reliability of large turbomachines. Such phenomena must be accurately measured in order to provide necessary feedback to design more efficient turbomachines and improve the computational models used in numerical flow simulations.

Due to the presence of density gradients, the compressible fluid flow is well suitable for an investigation using optical methods which are sensitive either to the refractive index - interferometry, or to a refractive index gradient (schlieren [1], shadowgraph [2]) that are very sensitive but difficult to quantify.

This paper presents interferometric technique [3] for research of compressible fluid flow in a wind tunnel facility. The technique has been developed in order to enhance understanding of the blade flutter phenomenon in turbomachines, in particular for transonic flow conditions. The developed technique is sensitive and accurate yet easy to use under conditions typical for aerodynamic labs.

The interferometer employs a high-speed camera [4] in order to avoid blurring, fiber optics and available "of-the-shelf" optics and optomechanics. A single-shot quantitative data processing based on spatial carrier interferometry (SCI) and Fourier analysis allows for almost real-time quantitative processing [5]. The method was used for investigation of high-speed flow in planar blade cascades, namely for studying dynamic events during transonic and supersonic blade flutter.

2. Spatial Carrier Interferometry

Digital interferometry is an accurate and full-field measurement method that is sensitive to the change in the phase of an optical wave. Superposition of two coherent waves generates an interference pattern. Introducing a tilt between reference and object arms in interferometer results in SCI. Assuming the tilt in x-direction only, the captured interference pattern on a CCD or CMOS camera sensor can be expressed as

$$I(x,y) = A(x,y) + B(x,y)\cos(\varphi(x,y) + 2\pi f_0 x), \quad (1)$$

where f_0 denotes spatial carrier frequency due to the tilted wave, A stands for additional term and B is the signal modulation.

Such interference pattern is further Fourier transformed and spatially filtered to select the portion of the signal around the spatial frequency f_0. Bandwidth of the band-pass filter influences the lateral resolution of measurements. An inverse Fourier transform results in complex field C_F and hence the interference phase can be calculated as:

$$\varphi(x,y) = \arctan\left(\frac{Im\big(C_F(x,y)\big)}{Re\big(C_F(x,y)\big)}\right). \quad (2)$$

Let us assume a phase measurement at steady/reference state without presence of fluid flow resulting in the complex field C_{F0}. Such measurement carries information about interferometer optical aberrations including aberrations introduced by e.g. optical windows of the wind tunnel experiment... Other measurements performed with the presence of a

phenomenon (C_{F1}) can be related to the reference state by the interference phase:

$$\Delta\varphi(x,y) = \\ = \arctan\left(\frac{Im\left(C_{F1}(x,y)C^*_{F0}(x,y)\right)}{Re\left(C_{F1}(x,y)C^*_{F0}(x,y)\right)}\right) \quad (3)$$

in order to suppress undesired optical aberration. The interference phase can be used to determine the desired physical quantity such as temperature [6], shape [7], refractive index [8], vibration amplitudes [9] or density/ isentropic Mach number [3] as in this particular case.

To apply SCI, a fiber based Mach Zehnder interferometer was built, see Fig. 1. A laser beam was generated by a pigtailed single-frequency distributed feedback laser (LAS) of the wavelength λ=773 nm and the fiber output power of 38 mW. The laser beam was split using a fibersplitter (FBS) into the reference wave (R) and the object wave (O). The reference wave was guided by an optical fiber to the non-polarizing beamsplitter (NBS), while the free-space object wave passed through a collimating imaging lens LC, which sent light through the test section of a transonic wind tunnel (TS), before passing through a lens LT1. Lenses LT1 and LT2 acted as a beam expander with magnification of Mag≈0.18 as well as an imaging system. Both reference and object waves were recombined by the beamsplitter (NBS) and collimated by LT2. The object wave impinged normally the digital camera sensor (HSC) while the reference wave was tilted in order to introduce the spatial carrier frequency f_0.

The intensity interference pattern *I* (interferogram) of both superposed beams was captured by a Phototron FASTCAM Mini WX100 high-speed camera having resolution of 2048×2048 pixels (10μm×10μm pixel size) with a frame rate of 1080fps. The exposure time 10μs was set in order to avoid blur of the interference pattern while keeping its sufficient brightness. After data processing based on the Fourier transform, optical phases for both steady state and airflow were retrieved using (2) and the interference phase was computed (3).

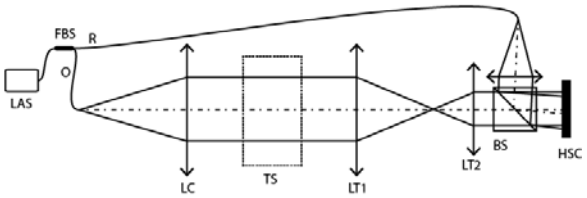

Fig. 1. SCI arrangements: LAS – laser, FBS – fiber beam-splitter, LC – collimating lens, TS – test section, LT1, LT2 – lenses, BS – beam splitter, HSC – high-speed camera, R – reference wave, O – object wave.

3. Compressor Blade Cascade Measurement

A planar compressor blade cascade with five blades was mounted in the test section of a transonic wind tunnel (see Fig. 2). The blades have a chord length of 120 mm, span L=160 mm (i.e. aspect ratio of 1.33) and maximum thickness 5.94 mm. The cascade stagger angle is 41.5°. During measurements, the flow velocity is monitored using Prandtl probe at the inlet of the test section and two rows of static pressure taps on the test section sidewall upstream and downstream of the blade cascade. Inlet Mach number of the airflow was set to be M_{in}=1.

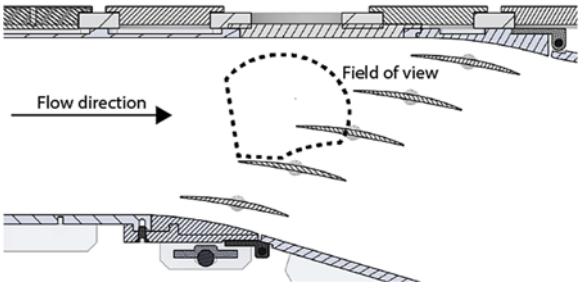

Fig. 2. The blade cascade with interferometer's field of view.

The test section is mounted in a suction-type high-speed modular wind tunnel of the Institute of Thermomechanics of the Czech Academy of Sciences, see Fig. 3. The wind tunnel consists of a free atmospheric entry, dryers and filters, contraction leading to the test section and exit parts with control and safety valves connected to a high-volume vacuum chamber.

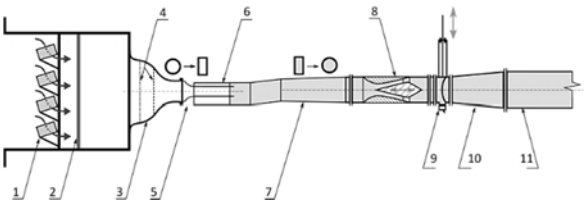

Fig. 3. Schematic of the wind tunnel: 1 - silica-gel dryer, 2 - pebble and cloth filter, 3 - circular contraction, 4 - honeycomb and screen, 5 - contraction and cross section change insert, 6 - test section, 7 - diffuser and cross section change insert, 8 - control nozzle, 9 - quick acting valve, 10 - diffuser, 11 - pipe connection to vacuum chamber.

The measured interference pattern (Fig. 4a) is processed in order to retrieve the interference phase (Fig. 4b). The interference phase is then spatially unwrapped and linked to density (Fig. 4c) using

$$\rho(x,y) = \rho_{ref}(x_0,y_0) + \frac{\Delta\varphi(x,y)\lambda}{2\pi LK}. \quad (4)$$

In (4), L denotes the wind tunnel testing section width, K is the Gladstone-Dale constant and ρ_{ref} is the reference density calculated from a static pressure sensor located in the position (x_0,y_0). For the case of isentropic compressible flow of ideal gas, the measured density ρ(x,y) can be further linked with the

isentropic Mach number (Fig. 4d) by the following equation:

$$M_i(x,y) = \sqrt{\frac{2}{\kappa-1} \cdot \left(\left(\frac{\rho_{in}}{\rho(x,y)} \right)^{\kappa-1} - 1 \right)}, \qquad (5)$$

where ρ_{in} is the inlet air density and κ=1.4 denotes the heat capacity ratio for an ideal diatomic gas.
The spatial resolution 150 μm is in our particular case determined by the bandwidth of the applied band-pass filter.

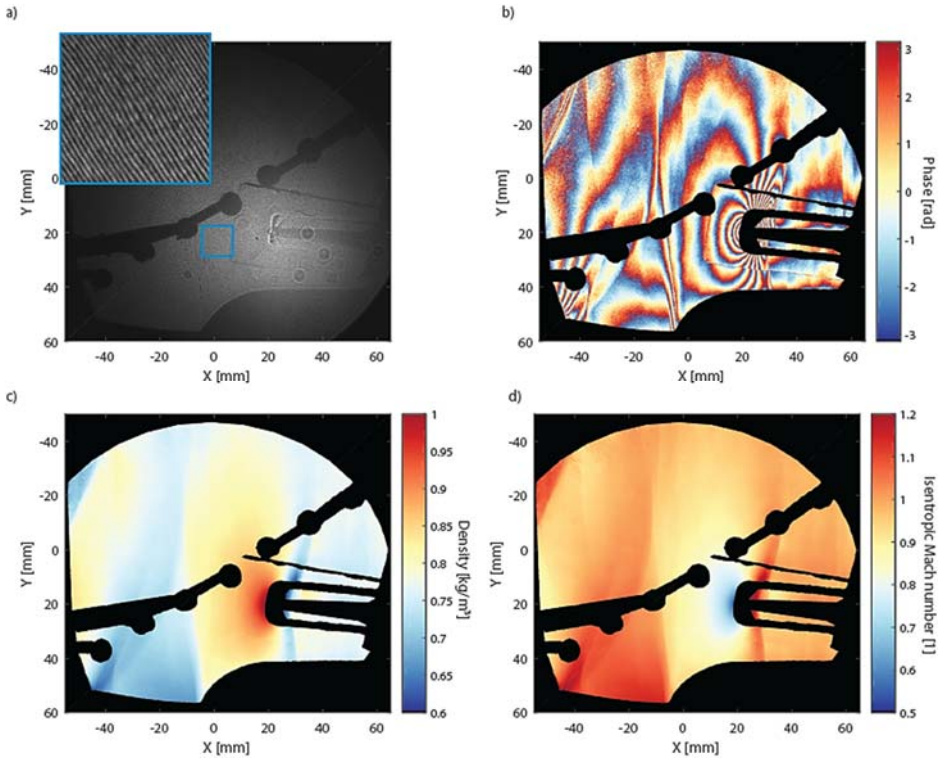

Fig. 4. a) Interference pattern; b) Wrapped phase; c) Density distribution; d) Isentropic mach number.

4. Conclusions

This paper presents a very effective technique for investigating compressible fluid flow. The developed interferometric technique is very sensitive and accurate yet easy to use even under pretty harsh environmental conditions (vibrations, flow instability, etc.) typical for aerodynamic labs. The interferometer employs a high-speed camera, fiber optics and available "off-the-shelf" optics and optomechanics. The interferometer consists of an illumination and a sensing unit, each weighing less than 5kg. An optical fiber delivers reference wave from the illumination to the sensing unit while the object wave emitted from the illumination unit propagates through a measured volume into the sensing unit. Both waves are superposed and an interference pattern is captured by the high-speed camera. The construction of the interferometer together with the fiber optics ensure high compactness and portability of the system. Moreover, a single-shot quantitative data processing based on introducing a spatial carrier frequency and processing in Fourier domain allows for almost real-time quantitative processing suitable also for very fast evolving phenomena. The interferometer has been successfully applied to measure airflow through a blade cascade and results are used to better understand the blade flutter.

Acknowledgements

This research was supported by the Ministry of Education, Youth and Sports of the Czech Republic – program Inter-Excellence, project No. LTAUSA19036.

References

[1]. M. Passmann, S., F. Joos, Focusing Schlieren Visualization of Transonic Turbine Tip-Leakage Flows, *International Journal of Turbomachinery, Propulsion and Power*, Vol. 5, Issue 1, 2020.
[2]. M. Hijikuro, M. Anyoji, M. Hijikuro, M. Anyoji, Application of Optical Flow Analysis to Shadowgraph Images of Impinging Jet, *Journal of Flow Control, Measurement & Visualization*, Vol. 8, Issue 4, 2020, pp. 173–187.
[3]. P. Psota G. Cubreli, J. Hala, D. Simurda, P. Sidlof, J. Kredba, M. Stasik, V. Ledl, M. Jiranek, M. Luxa, J. Lepicovsky, Characterization of supersonic compressible fluid flow using high-speed interferometry, *Sensors*, Vol 21, Issue 23, 2021.

[4]. H. Tang, P. Razavi, K. Pooladvand, P. Psota, N. Maftoon, J. J. Rosowski, C. Furlong, J. T. Cheng, High-Speed Holographic Shape and Full-Field Displacement Measurements of the Tympanic Membrane in Normal and Experimentally Simulated Pathological Ears, *Applied Sciences*, Vol 9, Issue 14, 2019.

[5]. P. Psota, P. Dancova, G. Cubreli, V. Ledl, T. Vit, R. Dolecek, O. Matousek, Development and application of spatial carrier interferometry for whole field real-time investigation of temperatures in liquid media, *Int. J. Therm. Sci.*, Vol. 145, 2019, 106029.

[6]. Ledl, V., T. Vit, R. Dolecek & P. Psota, Digital holografic interferometry used for identification of 2d temperature field, *Experimental Fluid Mechanics*, 2010, pp. 354-359.

[7]. Psota, P., H. M. Tang, K. Pooladvand, C. Furlong, J. J. Rosowski, J. T. Cheng & V. Ledl, Multiple angle digital holography for the shape measurement of the unpainted tympanic membrane, *Optics Express*, 28, 2020, pp. 24614-24628.

[8]. Mokry, P., P. Psota, K. Steiger, J. Vaclavik, R. Dolecek, D. Vapenka & V. Ledl, Ferroelectric domain pattern in barium titanate single crystals studied by means of digital holographic microscopy, *Journal of Physics D-Applied Physics*, 49, 25, 2016, 255307.

[9]. Psota, P., P. Mokry, V. Ledl, M. Stasik, O. Matousek & J. Kredba, Absolute and pixel-wise measurements of vibration amplitudes using time-averaged digital holography, *Optics and Lasers in Engineering*, 121, 2019, pp. 236-245.

(014)

Efficient Optomechanical Mode-Shape Mapping of Micromechanical Devices in the Presence of Crosstalk

D. Hoch [1,2,3], K.-J. Haas [1], L. Moller [1], J. Röwe [1], T. Sommer [1,2], P. Soubelet [1,4], J. J. Finley [1,2,4] and M. Poot [1,2,3]
[1] Department of Physics, Technical University of Munich, 85748 Garching, Germany
[2] Munich Center for Quantum Science and Technology (MCQST), 80799 Munich, Germany
[3] Institute for Advanced Study, Technical University of Munich, 85748 Garching, Germany
[4] Walter Schottky Institute, Technical University of Munich, 85748 Garching, Germany
E-mail: menno.poot@tum.de

Summary: Visualizing eigenmodes is crucial for understanding the dynamics of state-of-the-art micromechanical devices. A method is established to map modes of mechanical structures optically. The fast and robust method, based on parallel modified phase-lock loops, is illustrated with a silicon nitride membrane, where it outperformed three alternative approaches. Crosstalk, however, remained a problem so far. To solve this, the phase-lock loop is equipped with crosstalk compensation and it is shown that now also in the presence of strong crosstalk, where resonances and phase responses are distorted, accurate maps are obtained.

Keywords: Optomechanics, Mode-mapping, MEMS, Phase-lock loop, Silicon-nitride, Membrane, Crosstalk.

1. Introduction

With the rapid developments in opto- and electromechanical systems, efficient methods for mode mapping are instrumental. A number of techniques to visualize mechanical modes have been developed, including optical interferometry, heterodyne detection, dark field imaging, and force microscopy. However, most of these have one or more drawbacks, such as poor sensitivity, lack of phase information, low spatial resolution, or long measurement times. We experimentally demonstrate a method that combines the high sensitivity of the optical interferometric techniques with demodulation and frequency tracking to offer rapid and robust imaging of multiple modes simultaneously [1], which now even works in the presence of severe crosstalk.

2. Mode Mapping

2.1 Setup and Sample

The method can be used with a wide variety of resonators and readout and excitation schemes; its use is illustrated with interferometric measurements of the local position of a square Si_3N_4 membrane that is driven using a piezo. By focussing light of a HeNe laser with a 10× objective onto the membrane, measuring the reflected light enables sensitive displacement detection with a lateral resolution of a few micrometers. The lowest flexural modes are at a few MHz, and their quality factors are ~ 10^5. From the observed frequencies, certain modes can be identified unambiguously, but for degenerate modes that is not possible, and their mode profile has to be visualized.

2.2. Comparison between Different Methods

The easiest method is to drive the mode resonantly at f_0 and to record the response while scanning over the membrane. However, especially for high-quality resonators, drift of the frequency will result in inaccurate mode maps [1]. A way to circumvent this is to use a phase-lock loop (PLL) that adjusts the driving frequency in order to keep the measured phase $\phi=\angle Z$ at the set point ϕ_{setpoint}, tracking f_0. However, this causes problems e.g. when crossing nodal lines. This is solved by taking a modulo π of the error signal e_j and by only updating the frequency when the signal $|Z|$ exceeds a threshold Z_{min}:

$$\begin{aligned} e_j &= \phi - \phi_{\text{setpoint}} \mod \pi \\ f_{n+1} &= f_1 + Pe_n + I\sum_{j=1}^{n} e_j \text{ for } |\boldsymbol{Z}| > \boldsymbol{Z}_{\min} \end{aligned} \quad (1)$$

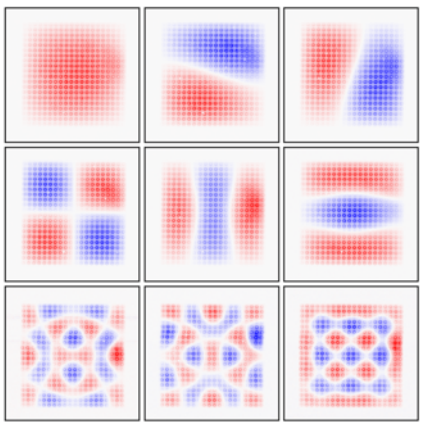

Fig. 1. Top row: measured mode maps for the (1,1), (1,2) and (2,1) mode of a 375×375μm square SiN membrane. Middle: (2,2), (3,1) and (1,3) modes. Bottom: superpositions of the (1,7), (7,1) and (5,5) modes.

2.3. Mode Maps of Square Membranes

With this improved PLL method, the modes can be mapped accurately and efficiently. Fig. 1 shows the 6 lowest modes of the membrane, as well as a triplet near 7.3 MHz (bottom) which are superpositions of the degenerate (1,7), (7,1) and (5,5) modes. The accuracy of the method even allows quantitative fitting of their coefficients [1].

3. Mapping in the Presence of Strong Crosstalk

The method works well for resonances in the low MHz range. However, when going to higher frequencies, e.g. by using smaller and thus stiffer resonators, a new challenge appears: the distortion of the resonances by crosstalk. The crosstalk is – in addition to the mechanical transduction - a second pathway from excitation to detection, and is in our setup electrical in nature.

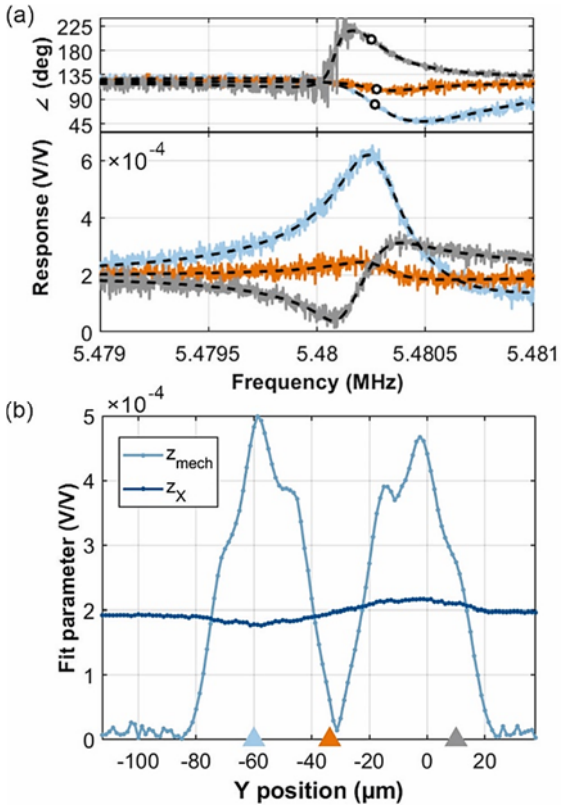

Fig. 2. (a) Measured response of the (2,2) mode of 103×103 μm membrane at three different locations with fits using Eq. (1). The circles indicate the phase ∠Z(ω_0). (b) extracted values for the mechanical and crosstalk contributions vs position on the membrane. The locations of the traces of (a) are indicated by the triangles.

3.1. Resonances

The driven responses in Fig. 2a display Fano-like resonances and it is not possible to find a phase where the PLL can lock to. The resonances are fitted using the harmonic oscillator response functions with crosstalk included:

$$Z(\omega) = z_{\mathrm{mech}} e^{i\alpha} \frac{\omega_0 \gamma}{\omega_0^2 - \omega^2 + i\omega\gamma} + z_X e^{i\phi_X} \qquad (2)$$

From this, the mechanical and the crosstalk contributions are determined and plotted vs. the position over the membrane in Fig. 2b. The crosstalk z_X is similar in magnitude as the mechanical signal z_{mech} and this, despite the inclusion of the mod π operation, prevents a direct application of the PLL [1].

3.2. Crosstalk Compensation and Maps

Eq. (2) shows that the PLL should use ∠{Z - $z_X \cdot \exp(i\phi_X)$} instead of ∠Z directly. With this insight, the phase is locked and mode maps are acquired (Fig. 3). After subtraction of the crosstalk, an accurate map of e.g. the (2,2) mode is obtained, showing clearly straight nodal lines in white and equal amplitudes of the anti-nodes.

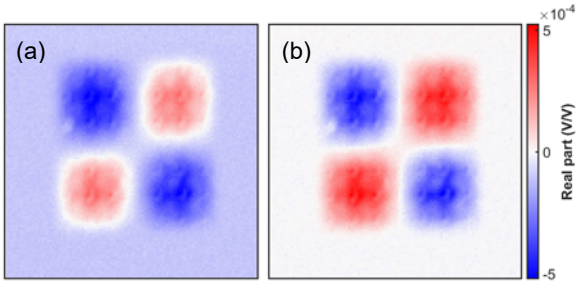

Fig. 3. Measured map of the (2,2) mode with crosstalk compensation in the PLL. Both the response before (a), and after (b) crosstalk subtraction are shown.

4. Conclusions

A powerful method to visualize the eigenmodes of mechanical resonators is demonstrated. It is shown that with the modified PLL, modes with regions without a strong response or with sign changes can be mapped, now even in the presence of strong crosstalk.

Acknowledgements

Funded by the German Research Foundation (DFG) [EXC-2111-390814868] and TUM-IAS, funded by the German Excellence Initiative and the European Union Seventh Framework Programme [grant agreement 291763]. We thank X. Yao for assistance with the nanofabrication and L. Rosendahl, E. Lebedev, and A. Yadav for help with the setup and measurements.

References

[1]. D. Hoch, K.-J. Haas, L. Moller, T. Sommer, P. Soubelet, J. J. Finley and M. Poot. Efficient Optomechanical Mode-Shape Mapping of Micromechanical Devices, *Micromachines,* Vol. 12, 2021, 880.

(015)

Synthesis of Adjacent Stokes Spectra in a Two-stage Transient Stimulated Raman Chirped-pulse Amplifier

P. Mackonis, A. Petrulenas and A. M. Rodin
Solid State Laser laboratory, Center for Physical Sciences and Technology,
Savanorių 231, LT-02300 Vilnius, Lithuania
Tel.:+37067025050
E-mail: paulius.mackonis@ftmc.lt

Summary: The synthesis of adjacent overlapped Stokes spectra in two stages of transient stimulated Raman chirped-pulse amplifier, tuned respectively to the vibrational mode 901 and 767 cm^{-1} of a potassium gadolinium tungstate [$KGd(WO_4)_2$] crystal is demonstrated. The contribution of the spatio-temporal overlap of seed and pump pulses, as well as self-phase modulation, was investigated. The non-collinear configuration allows the composite bandwidth at the central wavelength of 1120 nm to be increased by a factor of 23 compared to the pump pulse bandwidth of 1.6 nm. After reaching a conversion efficiency of 35% in the second stage, the compressibility of a chirped Stokes pulse with a tailored spectrum was investigated.

Keywords: Stimulated Raman scattering, Ultrafast lasers, Supercontinuum generation, Spectrum synthesis, Pulse compression.

1. Introduction

Recent studies have shown that increasing the wavelength of the driving femtosecond laser pulses through nonlinear conversion makes it possible to generate higher photon energy attosecond X-ray pulses [1], improve the efficiency of THz generation [2] and confine more energy in a single filament for gas sensing [3]. Stimulated Raman scattering (SRS) is an alternative to the widely used Optical Parametric Chirped Pulse Amplification (OPCPA) for generating intense SWIR pulses, eliminating phase matching limitations, exceeding OPCPA efficiency, and providing high temporal contrast. However, broadband excitation pulses were still implied to achieve pulse width of less than 100 fs, and no gain in peak power at the Stokes wavelength occurred until recent experiments on Transient Stimulated Raman Chirped pulse Amplification (TSRCPA) in KGW pumped with 1.2 ps transform-limited pulses [4]. Developing this concept, we first investigate the synthesis of the composite spectrum obtained from two successive TSRCPA stages tuned to vibrational modes at 767 and 901 cm^{-1} of a KGW crystal, respectively. A record 23-fold increase in the composite spectral bandwidth of amplified Stokes pulses compared to pump pulses and a conversion efficiency of 35% in the output TSRCPA stage were achieved experimentally. The possibility of compression of amplified pulses is also presented.

2. Experiment

The Yb:YAG chirped-pulse amplifier [5] used in the experiments delivered 1.2 ps (FWHM) transform-limited pulses with an energy of 20 mJ at a repetition rate of 100 Hz (Fig. 1). A small part (~12 μJ) of the laser pulse energy was directed to an undoped YAG rod 15 mm long to obtain stable supercontinuum (SC) pulses in the wavelength range from 1050 to 2400 nm [6]. These SC pulses were used to seed the first TSRCPA stage. Laser pulses with energies up to 2.5 mJ after passing through optical delay lines were used to pump two successive TSRCPA stages based on N_p-cut KGW crystals 30 mm and 15 mm long, tuned to vibrational modes at 901 (N_m-axis) and 767 cm^{-1} (N_g-axis), respectively. To reveal the features of TSRCPA in collinear and noncollinear configurations, seed and pump pulses were combined in KGW crystals at a small angle or propagated collinear at constant beam diameters. The possibility of compression of amplified pulses was tested using SF11 prisms with an apex angle of 59° spaced 2.1 m apart to compensate for the positive dispersion in YAG and KGW crystals.

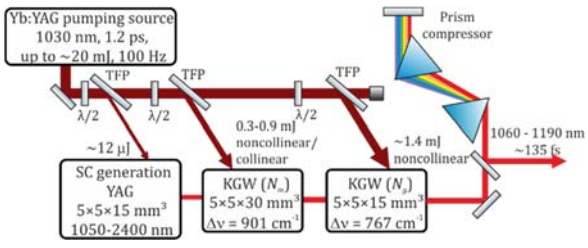

Fig. 1. Experimental setup for investigation of transient stimulated Raman chirped-pulse amplification (TSRCPA).

3. Results and Discussion

For the noncollinear configuration, an efficient amplification of the SC was observed in the first TSRCPA stage at a pump energy of 0.4 mJ (15 GW/cm^2) for N_m excitation. The use of SC seed lowered the SRS threshold by ~50 %. At higher pump intensities, second-order Stokes and anti-Stokes

radiation appeared, which led to saturation of the conversion efficiency and, at the same time, distortion of the amplified beam.

The iris aperture made it possible to separate the clear Gaussian central spot with a 30% energy loss. In the noncollinear case, the generated unwanted SRS and pump beams propagated in the same direction and were spatially separated from the amplified seed.

The study also revealed that the bandwidth and output energy of amplified pulses in the noncollinear configuration strongly depend on the location of the spatial overlap of the seed and pump pulses along the KGW crystal. Since the pump pulse propagates along the crystal, the acquired SPM is large enough to affect the bandwidth of the Stokes pulse. The widest spectrum was observed when the interacting pulses overlapped in the middle of a 30 mm KGW crystal. In this case, the Stokes pulse also reaches its maximum energy, and the SPM of the amplified pulse introduces additional spectral broadening. In addition, the greatest spectral broadening was achieved with the optimal delay between the seed and pump pulses, when the best gain is observed. With an increase in the pump energy, the amplified Stokes predominantly broadens towards shorter wavelengths, since in transient SRS, the Stokes pulse is formed at the trailing edge of the pump pulse. Consequently, a more significant spectral broadening to the short-wavelength range was observed. This asymmetric broadening was convenient for further spectral synthesis at the second TSRCPA stage, in which the spectrum of the first stage should overlap with the adjacent Stokes corresponding to 767 cm^{-1}.

The second TSRCPA stage was tuned to the adjacent vibrational mode of the KGW crystal at 767 cm^{-1}, which made it possible to synthesize an extremely wide tailored spectral bandwidth of ~38 nm (Fig. 2(a) – solid black line) corresponding to a transform-limited 50 fs pulse (Fig. 2(b) – dotted line) at the central wavelength of 1120 nm. A conversion efficiency of 35% was achieved at a pump pulse energy of 1.4 mJ, corresponding to 30 GW/cm^2.

To achieve the shortest pulse width, the distance between the two prisms was varied experimentally. The resulting temporal quality was mediocre, with large pedestals and side pulses. Nevertheless, the shortest pulse width of 135 fs (FWHM) was achieved (Fig. 2(b) – solid line), which is ~9 times shorter than the pump. Indeed, with passive compression, the phase modulation is still clearly visible (Fig. 2(b) – dashed line), therefore, to approach the sub-100 fs pulse width, it is necessary to use active phase control, i.e. acousto-optic programmable dispersive filter (AOPDF).

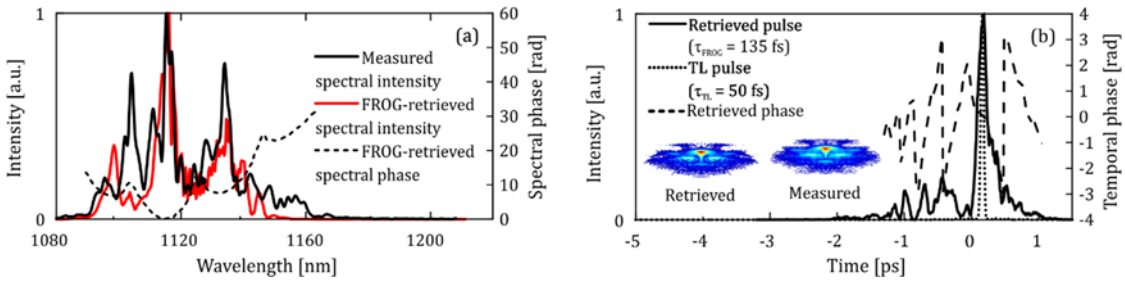

Fig. 2 (a) Synthesized spectrum after two TSRCPA stages (solid black), FROG-retrieved spectral intensity profile (solid red), and its spectral phase (dashed) before compression; (b) temporal profile (solid) of amplified pulse after compression retrieved from the SHG-FROG measurement, compared to transform-limited pulse calculated from the measured spectrum (dotted) and the retrieved temporal phase (dashed). τ_{TL} – transform limited pulse width.

4. Conclusions

TSRCPA demonstrates the efficient amplification of ultrashort laser pulses with an extremely wide spectral bandwidth. For a selected single vibrational mode at 901 cm^{-1} in a KGW crystal, TSRCPA was investigated in different amplifier configurations under transient excitation with transform-limited 1.2 ps pump pulses. The noncollinear configuration made it possible to increase the second-order Stokes threshold and ensure a higher optimal pump and amplified Stokes pulse energy, as well as a better quality of the amplified Stokes beam. In this case, the amplification of two adjacent vibrational Stokes components in successive TSRCPA stages provides a 23-fold increase in the composite bandwidth of amplified Stokes pulses compared to pump pulses with a maximum conversion efficiency of 35 %. As a result, a spectral bandwidth of 38 nm was achieved at a central wavelength of 1120 nm. Despite the modulated spectral phase of the synthesized pulse, compression of the amplified Stokes pulses to 135 fs was experimentally obtained. In the visible and near-infrared spectral region, a promising method for controlling the bandwidth of high-energy, few-optical-cycle laser pulses in a neonfilled hollow-core fibre [7] is also available.

Acknowledgements

This work was supported by Research Council of Lithuania under the grant S-MIP-21-30. Two authors thank for NATO SPS G5734 fellowships.

References

[1]. M.-C. Chen, P. Arpin, T. Popmintchev, M. Gerrity, B. Zhang, M. Seaberg, D. Popmintchev, M. M. Murnane and H. C. Kapteyn, Bright, coherent, ultrafast soft x-ray harmonics spanning the water window from a tabletop light source, *Physical Review Letters,* Vol. 105, 2010, pp. 173901.

[2]. M. Clerici, M. Peccianti, B.E. Schmidt, L. Caspani, M. Shalaby, M. Giguère, A. Lotti, A. Couairon, F. Légaré, T. Ozaki, D. Faccio and R. Morandotti, Wavelength Scaling of Terahertz Generation by Gas Ionization, *Physical Review Letters,* Vol. 110, 2013, pp. 253901.

[3]. V. Shumakova, S. Ališauskas, P. Malevich, A. A. Voronin, A. V. Mitrofanov, D. A. Sidorov-Biryukov, A.M. Zheltikov, D. Kartashov, A. Baltuška and A. Pugžlys, Chirp-controlled filamentation and formation of light bullets in the mid-IR, *Optics Letters,* Vol. 44, 2019, pp. 2173.

[4]. P. Mackonis, A. Petrulenas, A. M. Rodin, V. Girdauskas and A. Michailovas, Two-stage transient stimulated Raman chirped-pulse amplification in $KGd(WO_4)_2$ with compression to 145 fs, *Optics Letters,* Vol. 45, 2020, pp. 6627.

[5]. P. Mackonis and A. M. Rodin, Laser with 1.2 ps, 20 mJ pulses at 100 Hz based on CPA with a low doping level Yb:YAG rods for seeding and pumping of OPCPA, *Optics Express,* Vol. 28, 2020, pp. 1261.

[6]. P. Mackonis, A. Petrulenas, V. Girdauskas and A.M Rodin, Stable 1100 – 2400 nm supercontinuum in YAG with picosecond pumping for simplified OPCPA, in *Proceedings of the Conference on Lasers and Electro-Optics Europe and European Quantum Electronics Conference, OSA Technical Digest (Optical Society of America)*, 2019, paper ca_p_43.

[7]. W. Tawfik, A method for controlling the bandwidth of high-energy, few-optical-cycle laser pulses tunable from the visible to the near-infrared, *Ukrainian Journal of Physical Optics,* Vol. 16, 2015, pp. 147.

(016)

Bipolar Organic Semiconductors based on Carbazole and Diphenyl Imidazole as Deep-blue OLED Emitters and Hosts for Sky-blue, Green and Red PhOLEDs

O. Bezvikonnyi, V. Andruleviciene, D. Volyniuk, R. Keruckiene, K. Vaiciulaityte, E. Urbonas and J. V. Grazulevicius
[1] Department of Polymer Chemistry and Technology, Kaunas University of Technology,
K. Barsausko g. 59, LT- 51423, Kaunas, Lithuania
Tel.: +370(37)300192
E-mail: oleksandr.bezvikonnyi@gmail.com

Summary: New organic semiconducting compounds based on carbazole and diphenyl imidazole moieties were designed, synthesized and investigated. The thermal, photophysical and electroluminescent properties of the derivatives were examined. The compounds exhibited narrow blue emission. Additional low-energy emission band appeared in the spectra of the solid-state samples of the compounds under continuous photoexcitation and interaction with oxygen. The compounds were utilized as deep-blue emitters of prompt fluorescent organic light emitting diodes. 1931 CIE color space coordinates of (0.16, 0.08) and external quantum efficiency of 1.1% were reached for OLED based on one of the compounds. Additionally, the series of sky-blue, green and red phosphorescent organic light emitting diodes were fabricated utilizing the studied compounds as host matrixes for phosphorescent emitters due to the appropriate charge transport characteristics and energy levels of the first triplet excited state above 3 eV. The charge carrier drift mobility of holes exceeded 10^{-4} $cm^2/V \cdot s$ at electric field of ca. $6.4 \cdot 10^5$ V/cm. The maximum external quantum efficiency values of up to ca. 8% were obtained for the most effective OLED containing the studied compound.

Keywords: Imidazole, Carbazole, Deep-blue emitter, HLCT, OLED, PhOLED host.

1. Introduction

The technology of organic light emitting diodes (OLED) is rapidly expanding. The development of stable and highly emissive OLED requires the search and application of fluorophores with restricted intermolecular interactions, and sufficient charge transport and charge balance [1]. The issue of the stability and efficiency of blue emission remains the biggest problem of the technology.

The limit of internal quantum efficiency (IQE) is 25 % for prompt fluorescent OLEDs. Utilization of tripet excitons in electroluminescence by use of phosphorescent emitters is way to reach 100 % of IQE [2]. The search of host materials with suitable properties is in high demand for the field of phosphorescent OLEDs. The main issue with the approach is the use of expensive earth-rare metals. The theoretical expansion of IQE limit to 100 % is also possible due to a hot exciton up-conversion via reverse intersystem crossing between singlet and triplet hybridized local charge transfer states (HLCT) states.

2. State-of-the-art

Carbazole ring can be easily substituted with various acceptor moieties like imidazole [3]. These materials exhibit suitable bipolar charge transport characteristics, triplet energies, and relatively high photoluminescence quantum efficiencies. It was reported recently that blue emitters can be also approached as hosts optoelectronic devices of different color of emission [4]. Because of highly twisted structure and conformations, imidazole-based donor-acceptor emitters often have HLCT emissive states. Imidazole-based HLCT hosts were also reported highlighting the possibility of triplet energy harvesting in host materials [5, 6].

3. Results and Discussions

Here, we present multifunctional derivatives of carbazole and imidazole syntesized by simple one-pot condensation reaction. The spectral peaks of their tetrahydrofuran (THF) solutions are located at ca. 400 nm. The Lippert-Mataga plots revelead that the solvatochromic effect occurs due to HLCT states stimulated by the structural elements of the compounds. The investigation of phosporesence revealed the triplet energies are in the range of 3.1-3.18 eV suitable for electronic excitation energy transfer to many of emitters. The ring-opening reaction of the imidazole during the interactions with oxygen under UV-irradiation is detected. Using the time-of-flight technique it was discovered that the hole drift mobilities in the thin films of the compounds are ranging from 10^{-5} cm^2/Vs to 10^{-4} cm^2/Vs at electric field of $6.4 \cdot 10^5$ V/cm.

Their properties enable the compounds as emitters and hosts for OLEDs avoiding the photochemical oxidation of the imidazole ring by the fabrication of devices in deoxygenated medium by thermal vacuum

deposition technique (Table 1). The prompt fluorescent OLEDs based on doping-free emitting layers of the compounds exhibit deep-blue electroluminescence with 1931 CIE coordinates of c.a. (0.17, 0.14) (Fig. 1).

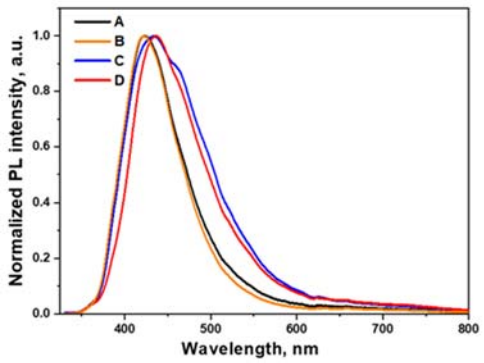

Fig. 1. EL spectra of A-D OLEDs based on emitting doping-free layers of 1-4 (Table 1)

4. Conclusions

Photophysical and electrochemical properties of the series of newly designed and synthesized derivatives of diphenyl imidazole and carbazole were evaluated. Attachment of the second imidazole ring to the structure leads to the improvement of thermal stability and increase of glass transition temperature. The compounds were also utilized as hosts for sky-blue, green and red phosphorescent OLEDs reaching 7.6, 8.3 and 6.4% of external quantum efficiency, respectively.

Acknowledgements

This research was funded by the European Social Fund under the No 09.3.3-LMT-K-712 "Development of Competences of Scientists, other Researchers and Students through Practical Research Activities" measure (Project No 09.3.3-LMT-K-712-19-0136).

Table 1. Electroluminescent properties of OLEDs.

Device	Emitting layer (EML)	λ_{em}, nm	CIE, xy	V_{on}, V	Max. Brightness, cd/m^2	Max. Current efficiency, cd/A	Max. Power efficiency, lm/W	Max. EQE, %
Doping-free blue fluorescent devices ITO/MoO_3/NPB/EML/TSPO1/TPBi/LiF/Al								
A	**1**	420	(0.17, 0.09)	4.0	840	0.7	0.38	0.9
B	**2**	418	(0.16, 0.08)	4.1	1030	0.8	0.42	1.1
C	**3**	431	(0.17, 0.15)	4.8	1350	0.9	0.43	0.8
D	**4**	437	(0.17, 0.14)	4.0	1430	0.8	0.41	0.6
Green phosphorescent devices ITO/m-MTDATA/EML/Bphen/LiF/Al								
E	$Ir(ppy)_3$:**1**	422	(0.21, 0.17)	5.2	5580	2.7	1.1	2.5
F	$Ir(ppy)_3$:**2**	510	(0.27, 0.58)	3.7	4630	3.5	1.6	0.97
G	$Ir(ppy)_3$:**3**	510	(0.29, 0.60)	3.1	24600	3.1	13.7	8.3
H	$Ir(ppy)_3$:**4**	510	(0.25, 0.39)	3.9	5800	1.9	1.1	0.74
Red phosphorescent devices ITO/MoO_3/NPB/EML/TSPO1/TPBi/LiF/Al								
I	$(piq)_2Ir(acac)$:**1**	625	(0.56, 0.29)	4.4	5700	2.7	0.9	3.0
J	$(piq)_2Ir(acac)$:**2**	625	(0.59, 0.29)	4.0	4800	2.6	1.4	2.7
K	$(piq)_2Ir(acac)$:**3**	632	(0.67, 0.32)	3.2	8400	4.4	3.3	6.4
L	$(piq)_2Ir(acac)$:**4**	629	(0.63, 0.31)	3.3	4700	3.9	1.7	4.5
Sky-blue phosphorescent devices ITO/HAT-CN/NPB/EML/TSPO1/TPBi/LiF/Al								
M	FIrpic:**3**	475	(0.15, 0.36)	3.2	3300	17.9	17.6	7.6

References

[1]. J. H. Jou, S. Kumar, A. Agrawal, T. H. Li, S. Sahoo, Approaches for fabricating high efficiency organic light emitting diodes, *Journal of Materials Chemistry C.,* Vol. 3, 2015, pp. 2974-3002.

[2]. K. S. Yook, J. Y. Lee, Organic materials for deep blue phosphorescent organic light-emitting diodes, *Advanced Materials*, Vol. 24, 2012, pp. 3169-3190.

[3]. A. P. Kulkarni, C. J. Tonzola, A. Babel, S. A. Jenekhe, Electron transport materials for organic light-emitting diodes, *Chemistry of Materials*, Vol. 16, 2004, pp. 4556–4573.

[4]. Y. M. Chen, W. Y. Hung, H. W. You, A. Chaskar, H. C. Ting, H. F. Chen, K. T. Wong, Y. H. Liu, Carbazole-benzimidazole hybrid bipolar host materials for highly efficient green and blue phosphorescent OLEDs, *Journal of Materials Chemistry*, Vol. 21, 2011, pp. 14971-14978.

[5]. L. Chen, S. Zhang, H. Li, R. Chen, L. Jin, K. Yuan, H. Li, P. Lu, B. Yang, W. Huang, Breaking the Efficiency Limit of Fluorescent OLEDs by Hybridized Local and Charge-Transfer Host Materials, *The Journal of Physical Chemistry Letters*, Vol. 9, 2018, pp. 5240–5245.

[6]. X. Ouyang, X. L. Li, L. Ai, D. Mi, Z. Ge, S. J. Su, Novel "hot exciton" blue fluorophores for high performance fluorescent/phosphorescent hybrid white organic light-emitting diodes with superhigh phosphorescent dopant concentration and improved efficiency roll-off, *ACS Applied Materials & Interfaces*, Vol. 7, 2015, pp. 7869–7877.

(017)

Generation of Femtosecond Pulses up to 3 μm by Combining OPCPA with Transient Stimulated Raman Amplification

A. Petrulenas, P. Mackonis and A.M. Rodin
Solid State Laser laboratory, Center for Physical Sciences and Technology,
Savanoriu 231, LT-02300 Vilnius, Lithuania
Tel.: +37067094170
E-mail: augustinas.petrulenas@ftmc.lt

Summary: We present a 3-stage OPCPA in the wavelength range of 1800 – 2300 nm based on BiBO crystals pumped by picosecond Yb:YAG laser pulses. The maximum signal energy reaches >2 mJ at a conversion efficiency of ~30%. The spectral bandwith of the amplified signal ~100 nm at the central wavelength of ~1.9 μm corresponds to a transform-limited pulse width of ~30 fs. After the third OPCPA stage, the pulse is compressed to 65 fs in a ZnSe plate 30 mm long. The possibilities of further compression of amplified pulses, as well as filamentation of output pulses in air or compressed gas, are discussed.

Keywords: Supercontinuum, OPCPA, Filamentation, SWIR, Mid-IR, Pulse compression.

1. Introduction

Few-cycle short-wave infrared (SWIR) pulses are useful for research in strong field physics and nonlinear optics, since an increase in the wavelength of the driving laser radiation makes it possible to generate higher photon energy atosecond X-ray pulses [1], as well as to improve the efficiency of THz generation [2].

Wide bandwidth SWIR-MIR pulses covering many important molecular vibrations are useful for remote sensing and LIDAR [3]. Laser beam filamentation is a highly nonlinear process that occurs when self-focusing due to the optical Kerr effect is balanced by diffraction, plasma defocusing, and other nonlinear mechanisms. The laser peak power needs to be above the critical power, which scales with the laser wavelength as λ^2, in order to reach the filamentation regime. The filamentation of SWIR-MIR radiation in air is useful for the direct detection of biochemicals and air pollutants with resonant fingerprints of common molecules such as H_2O, CO_2, CO, and NH_4.

Optical parametric chirped pulse amplification (OPCPA) has been successfully applied to generate intense ultrashort pulses in the SWIR range. The widest OPCPA bandwidth at 2 μm is achieved when pumped at 1 μm in a degenerate OPCPA (DOPA) configuration in type-I phase-matching Bismuth Borate (BiBO) or similar crystals. In this case, the spectra of the signal and idler are identical and opposite to the pump polarization. In a collinear configuration of overlapping pump and signal, it is impossible to distinguish the signal pulse from the idler at the output, which leads to interference and instability of the amplified pulses. On the other hand, a small non-collinear angle (0 – 2°) between the pump and the signal does not lead to a significant change in the phase matching bandwidth, but allows a spatial distinction between the idler and signal.

One of the possible implementations of SWIR OPCPA layouts is based on using a small portion of the pump laser energy to generate a supercontinuum (SC) up to 2.5 μm, which forms a seed for amplification in one or more OPCPA stages. However, at present, the output pulse energy in such systems does not reach the mJ level. In this work, we present a non-collinear amplification of white light supercontinuum seed pulses in three degenerate OPCPA (DOPA) stages based on bismuth triborate (BIBO) crystals up to 2 mJ in the wavelength range of 1.8 – 2.3 μm. The possibility of using amplified pulses after compression for filamentation in air or compressed gas will also be discussed.

2. Experiment

The self-made pump source (Fig. 1) was based on a two-stage double-pass chirped-pulse amplifier with a low doping level Yb:YAG rods. It provides 1.2 ps transform-limited pulses with an energy of 20 mJ at 100 Hz [4]. A small portion with an energy of 12 μJ and 7 μJ was split off to excite stable SC in a 15 mm and 130 mm YAG rod respectively [5]. SC pulses in the range 1850 – 2300 nm with positive or negative group delay dispersions (GDD) were amplified in three successive non-collinear OPCPA stages operating near degeneracy. Positive chirped pulses up to ~500 fs were obtained in a 5 mm thick AR-coated ZnSe plate and a 15 mm YAG. OPCPA stages were based on BiBO crystals (Type-I, phase matching angle $\theta = 8°$). Finally, the amplified signal pulses were compressed using ZnSe or glass plates to produce negative or positive chirped pulses.

Compressed pulses were directed for filamentation and excitation of rotational stimulated Raman scattering in a gas cell.

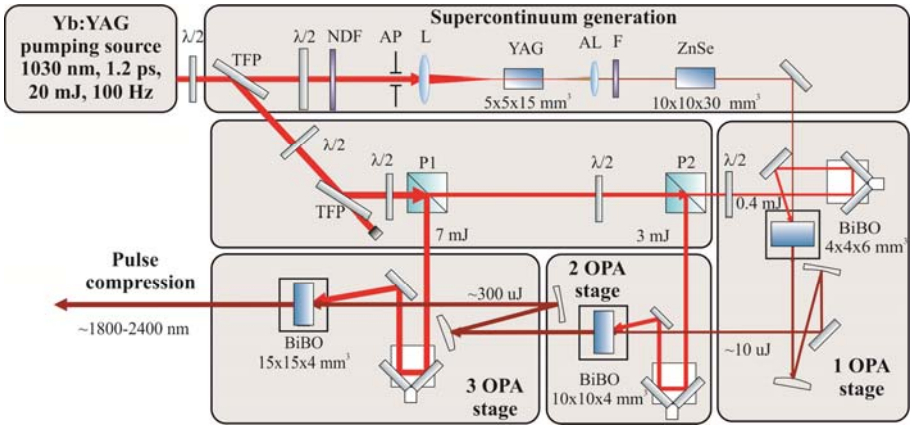

Fig. 1. Experimental layout of SC amplification in three OPCPA stages based on BiBO crystals. TFP – thin-film poliarizer, AL – achromatic lens, F – long-pass filter, YAG – yttrium aluminum garnet, NDF – neutral density filter.

3. Results

In the first OPCPA stage, the best conversion efficiency of ~3 % was observed in a BiBO crystal 6 mm long at a pump intensity of 60 GW/cm^2. At the second OPCPA stage, with signal amplification in a BiBO crystal 4 mm and 6 mm long, 10 % efficiency was achieved at a pump intensity of 40 GW/cm^2. After two OPCPA stages, the signal amplified to 220 µJ. Finally, in the third OPCPA stage using a 4 mm long BiBO crystal, ~30 % conversion efficiency and output pulses with an energy greater than 2 mJ at a center wavelength of 2.05 µm, supporting transform-limited (TL) pulse width of ~30 fs have been achieved (Fig. 2-left).

After carefully evaluating the GDD, the first pulse compression experiments of amplified negatively chirped broadband IR SC were carried out using a 30 mm long ZnSe crystal.

Because of the high n_2, a small portion of the amplified signal was directed to ZnSe and compressed to ~66 fs (Fig. 2 – right). On the other hand, amplifiend in OPCPA signal pulses with positive GDD will be compressed in glass to reach 40 GW peak power. This has been shown to be sufficient to generate filaments in high-pressure gas cells (e.g. N_2), which makes it possible to significantly expand the spectrum to wavelengths exceeding 3 µm due to the excitation of rotational stimulated Raman scattering.

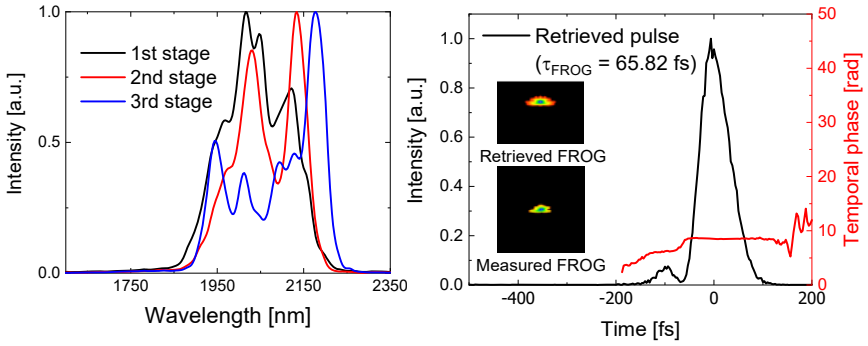

Fig. 2. Left – the spectra of the amplified signal after each OPCPA stage. Right – temporal profile of compressed pulse retrieved from SHG-FROG measurement and retrieved temporal phase.

4. Conclusions

We have developed OPCPA in the SWIR wavelength range of 1.8 – 2.3 µm. With the optimal length of BiBO crystals, the conversion efficiency of ~30 % and the output energy of ~2 mJ were achieved after three OPCPA stages. The amplified signal pulses were compressed to 66 fs in a ZnSe plate. The possibilities of filamentation of ultrashort SWIR pulses in a gas cell will be discussed.

Acknowledgment

This research was sponsored by Research Council of Lithuania under contract S-MIP-21-30. Two authors of the work are also grateful for partial financial support from NATO Science for Peace and Security Programme under grant G5734 “HOSTITUNOP: Tuned optical sensors for detection and identification of airborne hostile agents”.

References

[1]. W. Holgado, C. Hernández-García, B. Alonso, M. Miranda, F. Silva, O. Varela, J. Hernandez-Toro, L. Plaja, H. Crespo, and I.J. Sola, Tunable high-harmonic generation by chromatic focusing of few-cycle laser pulses, *Physics Review A,* Vol. 95, Issue 6, 2017, pp. 063823.

[2]. X. Ren, J. Li, Y. Yin, K. Zhao, A. Chew, Y. Wang, S. Hu, Y. Cheng, E. Cunningham, Y. Wu, M. Chini, and Z. Chang, Time-resolved dynamics in N_2O_4 probed using high harmonic generation, *Journal of Optics*, Vol. 322, Issue 5905, 2008, pp. 1207-1211.

[3]. M. J. Thorpe and J. Ye, Cavity-enhanced direct frequency comb spectroscopy, *Applied Physics B,* Vol. 91, Issue 3, 2008, pp. 397–414.

[4]. P. Mackonis and A. M. Rodin, Laser with 1.2 ps, 20 mJ pulses at 100 Hz based on CPA with a low doping level Yb:YAG rods for seeding and pumping of OPCPA, *Optics Express*, Vol. 28, Issue 2, 2020, pp. 1261-1268.

[5]. P. Mackonis, A. Petrulenas, V. Girdauskas, and A. M. Rodin, Stable 1100 – 2400 nm supercontinuum in YAG with picosecond pumping for simplified OPCPA, in *Proceedings of the Conference on Lasers and Electro-Optics Europe and European Quantum Electronics Conference*, 2019, Paper ca_p_43.

(019)

High Temperature Characterization of a Femtosecond Laser Micromachined Fiber in-line Fabry-Pérot Pressure Sensor

Wendy Tomboza [1,2,3], Romain Cotillard [2], Nicolas Roussel [2], Minh Chau Phan Huy [1] Géraud Bouwmans [3] and Guillaume Laffont [2]

[1] Safran Tech, Safran Sensing Systems Applications and Research, Rue des Jeunes Bois, Châteaufort, 78114 Magny-Les-Hameaux, France

[2] CEA List, 91190, Saclay, France

[3] Univ. Lille, CNRS, UMR 8523 - PhLAM - Physique des Lasers Atomes et Molécules

E-mail: wendy.tomboza@safrangroup.com

Summary: In this work, a femtosecond laser micromachined Fiber Fabry-Pérot Interferometer (FFPI) pressure sensor is presented. In order to extend the temperature stability above 700°C, a series of thermal annealing cycles is applied. Thanks to these annealings, the temperature response of the proposed FPI is extended further to 900 °C with a good thermal repeatability and a sensitivity stabilization to 0.61 pm/°C. Pressure measurement are also presented from 0 to 100 bar at room temperature and shows good linear response.

Keywords: Fiber-optic sensor, Laser machining, Fabry-Pérot, Pressure sensor.

1. Introduction

Optical Fiber Sensors based on Fiber Fabry-Pérot interferometers (FFPI) are one of the most widespread solutions for pressure monitoring. For aeronautical applications and especially for aircraft engines monitoring, such sensors require robustness at temperature above 500 °C, with pressure resolution less than 1 bar. Many methods have been developed to fabricate fiber optic pressure sensors. Those include the use of silica capillary [1-2], photonic crystal fiber [3-5], cleaving and splicing and laser welding manufacturing process [6-9]. However, those sensors involve time consuming manual assembling and hence cannot be easily considered for industrialization with good reproducibility. To improve fabrication efficiency and stability, laser-machined FFPI sensors have been developed and tested over high temperature conditions [10-13]. However, because of the relaxation of fiber's internal stresses coming from the drawing process of the optical fiber [14], the maximum operational temperature is often limited to ~ 700 °C.

In this paper, we propose a femtosecond laser machined Fabry-Pérot fiber sensor for pressure measurement at high temperature (up to 900 °C). It has the advantages of a compact and robust structure obtained from a straightforward fabrication process. The proposed structure is diaphragm-free in order to minimize the influence of pollution due to combustion gases or any other mechanical source of degradation of the membrane.

2. Description of the Sensor Structure

The fiber in-line Fabry-Pérot sensor is based on a spherical air cavity of length L1. As shown in Fig. 1(a), the device contains two reflecting diopters (M1 silica/air interface and M2 air/silica interface), resulting in a two-beam interference.

When pressure is applied, the length of the air cavity will change. Resolving the variation of the cavity from the spectral shift of the interferogram can provide the pressure.

The fabrication process consists of several steps. First, a single mode fiber (Corning SMF28) is cleaved and fixed vertically on a computer controlled high-precision 3D translation stage. Then, a femtosecond laser is focused on the center of the fiber tip in order to create a micro hole at its surface and centered on the fiber's core. The length of the Fabry-Pérot cavity can be adjusted by changing the depth of the micro hole. The femtosecond laser used in this experiment is a frequency-doubled Yb-based laser emitting at 515 nm. The energy per pulse and the repetition rate are 1.3 µJ and 2 kHz respectively. The fs-light pulses are focused on the fiber tip through a Cassegrain microscope objective (x36, NA=0.5). The laser power is adjusted by mean of a variable attenuator.

The micromachined fiber is then spliced to another SMF using a Fujikura 70S splicer to form a sealed spherical air cavity. Fusion splicing parameters, based on multimode fiber splicing parameters, are adjusted in order to avoid the collapsing of the cavity. An example of micromachined sensor is presented in Fig. 1 (b).

3. Experimental Results and Discussion

In order to measure the temperature response, a sensor having a cavity length of 52.6 µm is placed in a high temperature vertical tubular furnace. The output spectrum of the sensor is recorded using a tunable laser (Tunics-Plus), a fiber circulator and a component tester (Yenista CT400). The sensor is first heated from 30 °C

to 900 °C (with ~40 °C/min slope rate), then, the annealing temperature is gradually reduced to room temperature to avoid reintroduction of new thermal stresses into the fiber microstructure. The same procedure is repeated for three other cycles. The cavity length change under temperature is mainly induced by thermal expansion of the cavity.

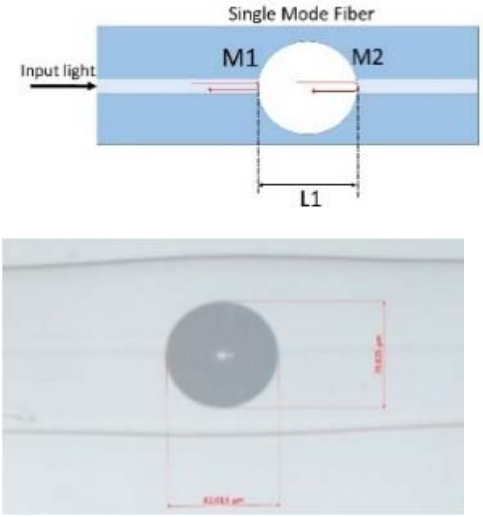

Fig. 1. (a) Schematic of the proposed pressure transducer; (b) Microscope image of the fiber in-line transducer.

The temperature response of the FFPI is measured by tracking a single peak on the reflection spectrum (presented on the Fig. 2 inset). Fig. 2 shows the relationship between the dip wavelength shift and the annealing temperature for each thermal treatment. During the first cycle of annealing process, the interference dip of the FFPI shifts monotonically towards longer wavelength as the temperature increases from 30 °C to 700 °C, indicating linear temperature response with a sensitivity of 0.96 pm/°C. However, beyond 700 °C the dip wavelength shift deviates from the linear trend. This may be due to the thermal relaxation of residual stress in the fiber structure. In the other cycles, the linear range of the sensor is extended to 900 °C and the temperature sensitivity decreases and converges to 0.61 pm/°C.

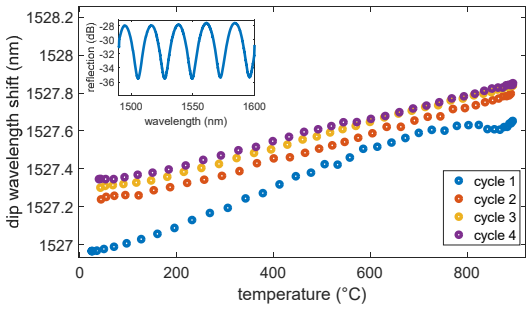

Fig. 2. Dip wavelength shift as a function of temperature in the different thermal annealing cycle. Inset: reflection spectrum of the sensor.

The pressure sensitivity of the FFPI sensor is characterized. The relationship between the dip wavelength shift of the sensor reflection spectrum and applied pressure is given by [10]:

$$\Delta\lambda = \frac{(1-2\mu)R_0^2}{E(R_0^2 - R^2)}\lambda_0 \Delta P \qquad (1)$$

where R_0 is the radius of the fiber, R is the radius of the cavity, λ_0 is the the dip wavelength, μ is the Poisson coefficient and E is the Young modulus.

The sensor (with a cavity length of 79.6 µm) is sealed in a pressure chamber where the air pressure is supplied using compressed nitrogen gas cylinder and controlled by a numerical manometer. The resolution of the manometer and the precision of the pressure output are 100 mbar and 0.1 %FS respectively. The sensor exhibits good linear response over pressure as shown in Fig. 3. Based on a linear fitting of the curve, the sensitivity of the sensor is calculated to be 2.8 pm/bar. The calculated theoretical sensitivity is 2.2 pm/bar which is close to the experimental value. Given a wavelength measurement resolution of 1 pm of the spectrometer, the resolution of the pressure sensor is estimated to 0.3 bar.

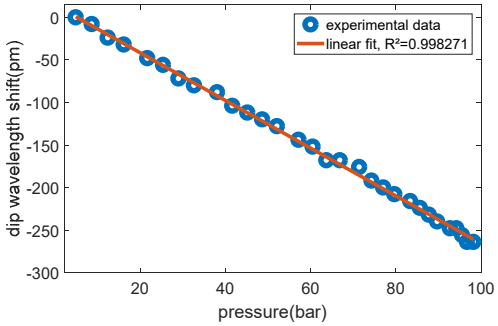

Fig. 3. Dip wavelength shift as a function of pressure.

4. Conclusions

A simple in-fiber air-cavity FFPI transducer is demonstrated for high temperature and pressure and its thermal stabilization obtained after four thermal annealing cycles up to 900 °C. The stabilized FFPI transducer shows desirable linear performance over a wide range of temperature from 30 °C to 900 °C, with a temperature sensitivity of 0.61 pm/°C. The sensor also exhibits a good linear pressure response from 0 to 100 bar with a pressure sensitivity of 2.8 pm/bar. The proposed FFPI pressure sensor is a potential candidate for high-temperature and high-pressure measurements in aeronautical fields. The actual performances of the proposed device are promising for future aircraft engine test bed experiments.

In order to decouple the effect of temperature and pressure, a temperature compensation structure, based on a femtosecond laser-inscribed point-by-point void-based Fiber Bragg Grating in series with the Fiber Fabry-Pérot cavity will be proposed. By using a

temperature discrimination method based on 2D sensitivity matrix, it will be possible to measure both temperature and pressure under severe temperature conditions.

References

[1]. B. Xu, C. Wang, D. N. Wang, Y. Liu, and Y. Li, Fiber-tip gas pressure sensor based on dual capillaries, *Opt. Express*, Vol. 23, No. 18, 2015, p. 23484.

[2]. Co, Y. Liu, Y. Liao, C. Lang, Y. Li, and S. Qu, Simple fiber-optic sensor for simultaneous and sensitive measurement of high pressure and high temperature based on the silica capillary tube, *Opt. Express*, Vol. 27, No. 18, 2019, p. 25777.

[3]. M. Quan, J. Tian, and Y. Yao, Ultra-high sensitivity Fabry–Perot interferometer gas refractive index fiber sensor based on photonic crystal fiber and Vernier effect, *Opt. Lett.*, Vol. 40, No. 21, 2015, p. 4891.

[4]. C. Wu, H. Y. Fu, K. K. Qureshi, B.-O. Guan, and H. Y. Tam, High-pressure and high-temperature characteristics of a Fabry–Perot interferometer based on photonic crystal fiber, *Opt. Lett.*, Vol. 36, No. 3, 2011, p. 412.

[5]. Y. Jiao, X. Dong, Q. Fu, Z. Li, J. Tian, and Y. Yao, Open-cavity Fabry-Perot interferometer pressure and temperature fiber sensor based on photonic crystal fiber, in *Proceedings of the 16th Int. Conf. Opt. Commun. Networks (ICOCN' 2017)*, Vol. 2017, pp. 1–3.

[6]. H. Liang *et al.*, Diaphragm-free fiber-optic fabry-perot interferometric gas pressure sensor for high temperature application, *Sensors (Switzerland)*, Vol. 18, No. 4, 2018.

[7]. W. Wang *et al.*, Adhesive-free bonding homogenous fused-silica Fabry–Perot optical fiber low pressure sensor in harsh environments by CO2 laser welding, *Opt. Commun.*, Vol. 435, No. November 2018, 2019, pp. 97–101.

[8]. X. Chen, X. Tong, C. Zhang, C. Deng, Y. Mao, and S. Chen, High-precision optical fiber Fabry–Perot composite sensor for pressure and temperature, *Opt. Commun.*, Vol. 506, No. July 2021, 2022, p. 127580.

[9]. X. Zhou, Q. Yu, and W. Peng, Fiber-optic Fabry–Perot pressure sensor for down-hole application, *Opt. Lasers Eng.*, Vol. 121, No. October 2018, 2019, pp. 289–299.

[10]. Z. Ran, S. Liu, Q. Liu, Y. Wang, H. Bao, and Y. Rao, Novel high-temperature fiber-optic pressure sensor based on etched PCF F-P interferometer micromachined by a 157-nm laser, *IEEE Sens. J.*, Vol. 15, No. 7, 2015, pp. 3955–3958.

[11]. Y. Zhang, L. Yuan, X. Lan, A. Kaur, J. Huang, and H. Xiao, High-temperature fiber-optic Fabry–Perot interferometric pressure sensor fabricated by femtosecond laser: erratum, *Opt. Lett.*, Vol. 39, No. 1, 2014, p. 17.

[12]. B. Xu, Y. Liu, Y. Liu, D. Jia, and C. Jiang, Optical fiber fabry-pérot interferometer based on an air cavity for gas pressure sensing, *IEEE Photonics J.*, Vol. 9, No. 2, 2017, pp. 1–9.

[13]. Z. Ran *et al.*, Miniature fiber-optic tip high pressure sensors micromachined by 157 nm laser, *IEEE Sens. J.*, Vol. 11, No. 5, 2011, pp. 1103–1106.

[14]. Q. Tian, H. Yang, K. S. Lim, Y. He, H. Ahmad, and X. Liu, Temperature and strain response of in-fiber air-cavity Fabry-Perot interferometer under extreme temperature condition, *Optik (Stuttg).*, Vol. 220, June 2020, p. 165034.

(020)

Comparison of Various Sublimation Matte Coating Sprays for the Optical 3D Scanning with a Focus on the Quality of 3D Scans

J. Franke [1], T. Koutecký [1] and D. Koutný [1]
[1] Brno University of Technology, Faculty of Mechanical Engineering, Institute of Machine and Industrial Design, Technická 2896/2, 616 69 Brno, Czech Republic
Tel.: +420 541 144 927
E-mail: Jakub.Franke@vut.cz

Abstract: Comparison of sublimation matting sprays Aesub Blue, Reflecon Tarnish 11HC and Attblime AB6 for optical 3D scanning is shown in this work. The work shows their matting ability on a high reflexive Si-wafer, effect on the 3D scanning results and sublimation time under elevated temperature. Coatings were deposited by automated system to ensure uniform conditions for each sample. The spray movement speed and spray axial distance were set as constant. The work shows that all used sprays created coatings with considerable thickness which can affect a 3D scanning accuracy. The best scan quality was ensured by 4 layers of Aesub Blue, 1 layer of Reflecon Tarnish 11HC and 2 layers of Attblime AB6. The best coating efficiency was offered by Reflecon Tarnish 11HC. The sublimation time at the temperature of 26.6 °C was about 28 minutes for Aesub Blue, 43 minutes for Reflecon Tarnish 11HC and 136 minutes for Attblime AB6.

Keywords: Optical 3D scanning, matte coating, sublimation spray

1. Introduction

1.1. State of the Art

3D scanning is nowadays common method for parts digitization for geometry and dimension inspection or reverse engineering. Active optical scanners that work with a projection and capturing of reflected light patterns or lines are frequently used. However, these scanners have problems with scanning of specular, translucent, transparent or dark surfaces. In the work of Wang and Feng [1], 3D scanning of the opaque reflective surface was performed by a laser stripe scanner. It was mentioned there that the light reflection from the reflective surface can be composed of the diffuse lobe, specular lobe and specular spike, where the specular components are problematic. The light reflection on the translucent surface was described e.g. in the work of Chen [2]. In this case, the light can penetrate the surface and can be scattered under the surface. It can result in incorrect depth coordinate computation. 3D scanning of the transparent surfaces is another challenge. In this case, conventional active optical scanners fail completely. The difficulty of scanning such surfaces is coupled with the light behavior on the transparent surface where several light transport phenomena can occur, as it was stated e.g. in the work of Morris and Kutulakos [3]. The problem of the dark surfaces is that they absorb the light. All these problematic surfaces negatively influence 3D scanning quality and amount of the scanned data.

Temporary matte coatings are used to improve optical properties of problematic surfaces. The coating improves light reflection from the scanned surface to the sensor of the scanner leading to better scan quality and higher amount of scanned data. Chalk sprays or titanium dioxide powders are commonly used materials [4–6]. Their disadvantage is that they remain on the object after 3D scanning. A cleaning must be performed if the scanned object has to be used for some further application.

A newly available sublimation scanning sprays can eliminate the need for the cleaning [7–9]. These sprays do not contain any pigment and they are able to vanish from the scanned surface over time. Sublimation sprays are relatively new in the field of 3D scanning and there is no research addressing the sublimation sprays for 3D scanning purposes. There is no exact information about their effects on the 3D scan quality or sublimation times.

1.2. Objective of the Work

The aim of this work is to study the effect of three different sublimation matting sprays on the 3D scan quality and also show their real sublimation time at elevated temperature.

2. Materials and Methods

Sublimation sprays Aesub Blue (Scanningspray Vertriebs UG), Reflecon Tarnish 11HC (MR Chemie GmbH) and Attblime AB6 (Graichen Produktions- und Vertriebs GmbH) were used as coating materials. An automated spraying system (see Fig. 1) was used to ensure uniform deposition conditions. The speed of spray movement and spray axial distance were set as constant ($V = 800$ mm/s, $Z = 175$ mm). The coatings were deposited with 1, 2, 4 and 6 layers. Coatings were measured 2 minutes after their deposition to eliminate their temperature and time dependent behavior.

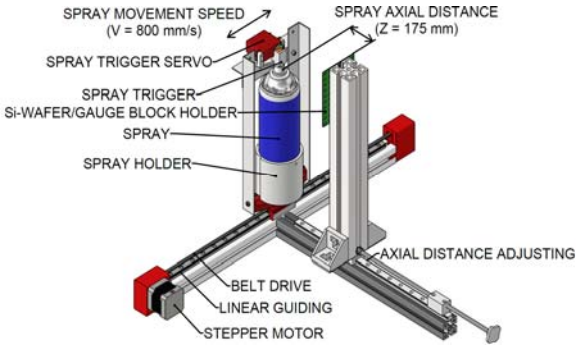

Fig. 1. Automated spraying system scheme.

2.1. Coated Objects

A highly reflexive Si-wafer (15 × 15 × 0.5 mm) was used for the analysis of the surface overlap by the coating, for analysis of the matting efficiency and for the sublimation time measurement.

A white ceramic gauge block with nominal dimension of 30 mm (30 × 35 × 9 mm) was used for the measurement of the coating thickness.

2.2. 3D Scanning

Atos III Triple Scan (GOM GmbH) was used for 3D scanning, see scanning details in the Table 1.

Table 1. 3D scanning details.

Parameter	Si-wafer	Gauge block
Measuring volume (mm)	MV60 (60×45×35)	MV170 (170×130×130)
Point distance	0.017 mm	0.055 mm
Exposure time	50 ms	70 ms
Polygonization	Standard	
Scanning orientation	Non-tilted	Tilted by 45°
Scanning automation	Lift and rotation table	
Ambient temperature	21.8 ± 0.7 °C	

2.3. Coating Analysis

The Si-wafer overlap by the coating was measured by ImageJ software in the images taken by the optical microscope Olympus SZX7 (Olympus). A magnification was set to 1.

The coating matting efficiency was analysed on the scanned data in the software GOM Inspect (GOM GmbH). A standard deviation (*Sigma*) of the captured point cloud against the theoretical fitting plane defined by the scanned surface of the Si-wafer was measured. A size of the scanned area was also measured. The size of the analysed area was 12 × 12 mm.

Coating thickness measurement was done on 3D scans in the software GOM Inspect using the *Projected Point Distance* function. The gauge block was coated in the middle of the surface defining its nominal dimension. Width of the coated area was 15 mm. Sides of the surface remained uncoated which was achieved using a clamping mask during the coating deposition. Uncoated surface defined zero reference plane from which the coating thickness was measured.

3. Results

From the Fig. 2 *left*, it is clear that Reflecon Tarnish 11HC created the highest coverage after one spray pass. The lowest coverage had Aesub Blue. It was coupled with a volumetric flow rate of the sprays. Lack of the Si-wafer overlap led to the reduction of scanned area.

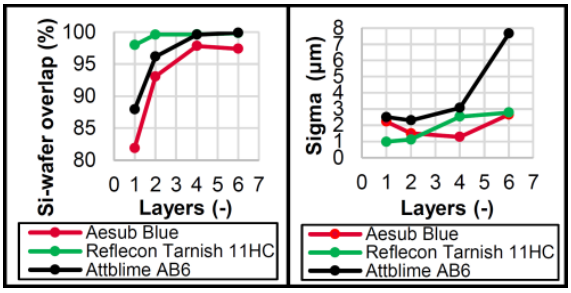

Fig. 2. Dependence of the average Si-wafer overlap (*left*) and average *Sigma* value (*right*) on coating layers.

Aesub Blue ensured the best 3D scan quality at 4 coating layers (*Sigma = 1.27 µm*), Reflecon Tarnish 11HC at 1 layer (*Sigma = 0.99 µm*) and Attblime AB6 at 2 layers (*Sigma = 2.31 µm*), see Fig. 2 *right*. In these cases, the control area of the Si-wafer was captured completely. A higher number of layers resulted in higher *Sigma* which was probably affected by the coating microstructure. It was the most significant in the case of Attblime spray indicating a high irregularity of its coatings.

The experiments with the gauge block showed that even 1 layer coating was detectable by the 3D scanner for all tested sprays. The average 1 layer coating thicknesses with standard deviations are stated in the Table 2. The thickest coating was created by Reflecon Tarnish 11HC which was coupled with its high coverage ability. In the Table 2, the 1 layer coating sublimation time at the temperature of 26.6 ± 0.6 °C is also stated. The values represent the time of complete disappearance.

Table 2. Coatings thicknesses and sublimation times.

Spray	1 layer	
	Thickness (µm)	Sublimation time (min)
Aesub Blue	17.76 ± 1.58	28 ± 9
Reflecon Tarnish 11HC	27.78 ± 0.47	43 ± 11
Attblime AB6	21.46 ± 2.75	136 ± 26

4. Conclusion

- All sprays created coatings with a considerable thickness which can affect scanned geometry
- Too many coating layers can negatively affect the 3D scan quality
- Reflecon Tarnish 11HC offered the best coating efficiency
- Aesub Blue created coatings with the lowest thickness with the shortest sublimation time
- Attblime AB6 had the longest sublimation times

Acknowledgement

This work was supported by faculty specific research project no. FSI-S-20-6296.

References

[1]. Wang, Y. and H.-Y. Feng, Modeling outlier formation in scanning reflective surfaces using a laser stripe scanner, *Measurement: Journal of the International Measurement Confederation*, 2014, 57, pp. 108–121.

[2]. Chen, T., H. P. A. Lensch, C. Fuchs and H. P. Seidel, Polarization and phase-shifting for 3D scanning of translucent objects. in *Proceedings of the IEEE Conference on Computer Vision and Pattern Recognition*, 2007, p. 1–8.

[3]. Morris, N. J. W. and K. N. Kutulakos, Reconstructing the surface of inhomogeneous transparent scenes by scatter-trace photography, in *Proceedings of the IEEE 11th International Conference on Computer Vision*. 2007, p. 1–8.

[4]. Paloušek, D., M. Omasta, D. Koutný, J. Bednář, T. Koutecký and F. Dokoupil, Effect of matte coating on 3D optical measurement accuracy, *Optical Materials*, 2015, 40, pp. 1–9.

[5]. Hruboš, D., T. Koutecký and D. Paloušek, An experimental study for determination of an application method and TiO2 powder to ensure the thinnest matte coating layer for 3D optical scanning, *Measurement: Journal of the International Measurement Confederation*, 2019, 136, pp. 42–49.

[6]. Franke, J., T. Koutecký, M. Malý, M. Kalina and D. Koutný, Study of process parameters of the atomizer-based spray gun for the application of a temporary matte coating for 3D scanning purposes, *Materials Chemistry and Physics*, 2022, 282, p. 125950.

[7]. AESUB. Products, *3D Scanning sprays*, Available: https://aesub.com/en/products/

[8]. MR Chemie GMBH, Reflecon® Tarnish - Type 1 - Volatile Scanning Sprays, *Products*, Available: https://www.mr-chemie.de/en/type-1-volatile-scanningsprays/

[9]. Graichen Produktions- und Vertriebs GMBH, *Attblime,* Available: https://attblime.com/?lang=en

(021)

Preparing Satellites for Active Debris Removal and Ranging

C. Phipps [1] and C. Bonnal [2]
[1] Photonic Associates, LLC, 200A Ojo de la Vaca, Santa Fe, NM, USA
[2] CNES, Direction des Lanceurs, 52 rue Jacques Hilairet, 75612 Paris Cedex, France
Tel.: +1-215-358-4360, fax: +1-505-466-3877
E-mail: crphipps@aol.com

Summary: In this paper we present three technical improvements that will better prepare satellites for their later removal prior to launch, in accordance with international agreements such as the IADC Space Debris Mitigation Guidelines, which ensure that satellites are designed to re-enter within 25 years. Space debris are non-functional satellites orbiting the Earth, such as abandoned second stage rockets, nanosatellites (most of which have no onboard propulsion) and collision fragments including those from deliberate destruction. Just-in-time Collision Avoidance (JCA) can prevent anticipated collisions. It requires far more precise orbit parameters for debris than we have now. The main tool we will use is ultra-precise laser ranging from an orbiting ranging station, which can operate up to 500 km range from a debris, provided it has good optical cross-sections. To enhance cross-sections, we would install 1-cm optical corner cubes on each satellite, four around its equator and two at its poles so that one or more will always be visible. We compare pulsed and frequency-chirped CW lasers in this regard. To better optimize energetic efficiency of laser propulsion to nudge satellites away from a predicted collision, we suggest the Thomson scattering technique, which permits simultaneously measuring the change of target velocity and the plume exhaust velocity, which can be combined to calculate this efficiency in real time.

Keywords: Laser ranging, Just in time collision avoidance, Picosecond laser, Thomson scattering, Chirped-frequency CW laser.

1. Introduction

We have discussed laser Active Debris Removal (ADR) extensively, including precise ranging [1, 2] sufficient to reduce false collision alarms from 100/year to 0.02/year. In those works, we assumed the laser pulse originating from a spaceborne laser station scatters off a target satellite into PI sterradians. At 1000 km range, the ranging system needed a 50 mJ, 100 ps pulsed laser and 75cm diameter optical aperture to attain adequate signal to noise (S/N) ratio. In this paper, we discuss prelaunch satellite modifications that can permit low power CW lasers to be used for ranging. A second (high power) pulsed laser is needed for the ultimate "laser nudging" operation to prevent subsequent predicted collisions.

2. Pre-launch Preparation

We propose two simple preparations for new satellites which will permit dramatic improvements in system performance in (JCA) by enhancing their laser signal cross sections and improving control of thrust direction in the "nudging" operation. Nudging is done with a system similar to that in [3]. We will show that just 250 mW CW in a suitably "chirped" 1064 nm beam will provide adequate S/N at a range up to 500 km in this case.

2.1. Chirped CW Laser

Fig. 1 illustrates our laser pulse format. For this idea, we are indebted to a very well written thesis [4]. Fig. 2 shows the laser transmit/receive path.

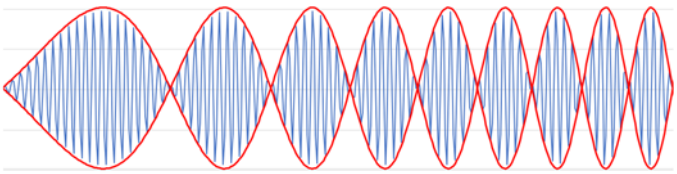

Fig. 1. Amplitude-modulated optical wave with chirped modulation frequency

The Fig. 1 waveform is described by Eq. (1) with

$$E = \sin(\omega_1 t)\sin(\omega_2(1+bt)t), \qquad (1)$$

where ω_1 is the optical wave, and $\omega_2(1+bt)$ is the linearly chirped amplitude modulation. We will not be able to perform direct operations on the optical wave without a complex optical interferometer. However, we can cross-correlate the returning (time-reversed) AM modulation pattern (shown in red) with a copy of that for the outgoing wave, then select the peak to determine range. The optical frequency is 282 THz. The chirped modulation frequency covers a 5 GHz

band. Then the spacial resolution c/(4B) =1.5 cm. Chirped laser pulse duration is 10 ms at 250 mW at 1064 nm, giving a 2.5 mJ transmitted pulse energy. This precision is equal to our results with the 50 mJ, 100 ps pulsed laser source we discussed in [1] for ordinary satellite surfaces without corner cubes.

With 1-cm corner cubes installed, this chirped CW pulse gives a signal to noise ratio (S/N) = 970k and an electric signal 6.3k larger than detector dark current. The beat frequency between the returned and outgoing wave is [4]

$$f_B = 2Bz/(c\tau) \quad (2)$$

where τ is the 10 ms CW pulse duration. If τ = 10 ms and z = 500 km, Eq. (2) gives 1.7 GHz for f_B.

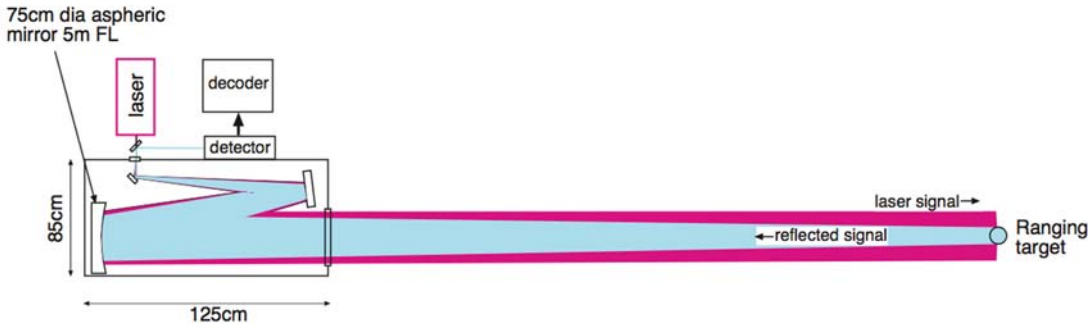

Fig. 2. Laser transmit/receive path to target, and detector. Range is up to 500km.

2.2. Corner Cubes

We will install six 1-cm corner cube reflectors on each satellite, 4 around its equator and 2 at its poles so that one or more will always be visible for any satellite orientation. An open corner cube reflector returns a ray directly to its source, within a field of view of about ±45° [5].

2.3. Controlling thrust Direction

We will install specially designed "fuel patches" on new satellites, containing an array of hemispherical fuel dots [Fig. 3] to give a net impulse vector approximately parallel to the incident laser beam for a 120° range of laser incidence angles with 100 ps pulses. This feature occurs because the incident beam is at ablation threshold for perpendicular incidence on the fuel dots, but below it at other angles. Using this technique, we can better control the laser thrust vector.

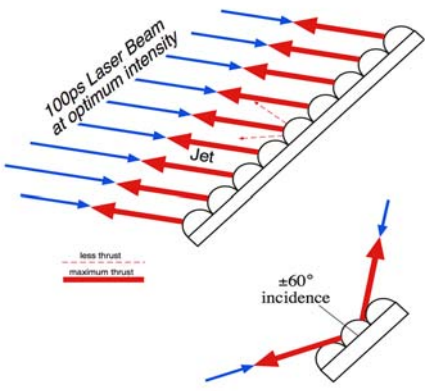

Fig. 3. Illustration of "fuel patch".

2.4. Thomson Scattering

With precise orbital parameters obtained with the Fig. 2 system for all tracked debris, we can predict collisions that will occur. Then, a different, high energy laser system is used to nudge one member of the collision pair a week in advance to avoid the collision [2]. Doppler shift of the return signal gives the change of target velocity produced by our "nudging laser." This gives C_m, the delivered momentum per incident laser joule. The Thomson scattering technique [6] can be applied with a small pulsed laser to separately determine ion velocity in the target plume. Simultaneous measurement of C_m and v_E (plume exhaust velocity) gives ablation kinetic efficiency η_{AB} in real time [Eq. (3)]. Laser parameters can then be dithered to optimize η_{AB}.

$$\eta_{AB} = C_m v_E / 2 \quad (3)$$

3. Conclusions

We have outlined two pre-launch satellite preparations that can improve our ability to track and propel them, and a third technique for optimizing laser propulsion kinetic efficiency in real time.

References

[1]. C. Bonnal, D. McKnight, C. Phipps, C. Dupont, S. Missonier, L. Lequette, M. Merle and S. Rommelaere, Just in time collision avoidance – a review" *Acta Astronautica,* 170, 2020, pp. 637-651.

[2]. C. Phipps and C. Bonnal, A spaceborne, pulsed UV laser system for re-entering or nudging LEO debris, and re-orbiting GEO debris, *Acta Astronautica,* 118, 2016, pp. 224-236.

[3]. C. Phipps, L'ADROIT – A spaceborne ultraviolet laser system for space debris clearing, *Acta Astronautica,* 104, 2014, pp. 243-255.
[4]. P. Adany, Simplified homodyne detector for FM chirped lidar, B. S. Thesis, *University of Kansas,* 2007.
[5]. S. Somerstein, J. Fuller and R. Kennedy, Retroreflector field of view properties for open and solid cube corners, *SPIE Proceedings,* 1168, 1989.
[6]. C. Phipps, and D. Bershader, Measurement of Nonisotropic Electron Velocity Distributions by Laser Scattering, in Dynamics of Ionized Gases (M. J. Lighthill, I. Imai, and H. Sato, Eds.), *University of Tokyo Press*, 1973.

(022)

Quantum Dot Coupling into Hybrid InP-Si Waveguide Modes for on-chip Integrated Photonics

P. Mrowiński, G. Sęk and M. Syperek
Department of Experimental Physics, Faculty of Fundamental Problems of Technology,
Wrocław University of Science and Technology, Wybrzeże Wyspiańskiego 27, 50-370 Wrocław, Poland
Tel.: + 48 71 320 29 86
E-mail: pawel.mrowinski@pwr.edu.pl

Summary: These studies show coupling efficiency between emission from a point source, presumably an InAs quantum dot, embedded in the InP waveguide to propagating modes of the hybrid InP-Si waveguide system on the SiO_2 platform. The coupling efficiency is estimated to 80 %. This knowledge is important for a hybrid on-chip integration of III-V quantum dot emitters operating in the third-telecom spectral window at 1550 nm placed at a common Si-based platform towards photonic integrated circuits.

Keywords: Quantum dot, Waveguide, Si, Nanoaphotonics, FDTD.

1. Introduction

In this work, we investigate the coupling of propagating photonic modes in a hybrid structure composed of coupled InP and silicon-on-insulator (SOI) waveguides (WGs) with the perspective for future quantum photonic integrated circuits utilizing InAs/InP quantum dot (QD) as non-classical photons source. Such a hybrid semiconductor system can be realized in a direct wafer bonding technique, which has been used to integrate GaAs and Si_3N_4 WGs [1] and other III-V materials with SOI substrates [2, 3]. Our theoretical studies employed the FDTD method implemented in Lumierical - commercially-available FDTD solver [4], which is a powerful tool for optimization of variety of nanophotonic and optoelectronic devices [5–8].

2. Hybrid InP-Si Waveguide System – FDTD Simulations

We create our model structure within the Lumerical 3D CAD environment. The model is consistent with the fabrication and processing steps that are planned for the integration of epitaxially grown InP wafer containing a layer of InAs QDs with a SOI wafer and subsequent WGs fabrication. Due to the processing requirements, a hybrid WG is composed of coupled Si and InP WGs, where the Si WG has width equal to or larger than the width of InP WG. We set the Si WG width to 1.75 µm and height of 0.22 µm, and tune the InP WG width in the range of 0.5 to 1.75 µm, keeping its height at 0.58 µm, see Fig. 1a). First, we perform calculations of the mode structure in this system taking refractive indexes of n(InP) = 3.167, n(Si) = 3.475, $n(SiO_2)$ = 1.444 at the photon wavelength of 1.55 µm [9]. In Fig. 1b) the real part of the effective refractive index (n_{eff}) is presented in function of the InP WG width. First, we observe an increase of the n_{eff} and the number of confined modes with increasing the InP WG width. Second, we notice that the excess loss of the modes characterized by Re(n_eff) > 2.0, are in a range from 5.1×10^{-4} to 6.6×10^{-4} db/cm, which states that they differ slightly in terms of propagation length and all the modes could be considered in the evaluation of the dipole (quantum dot) coupling.

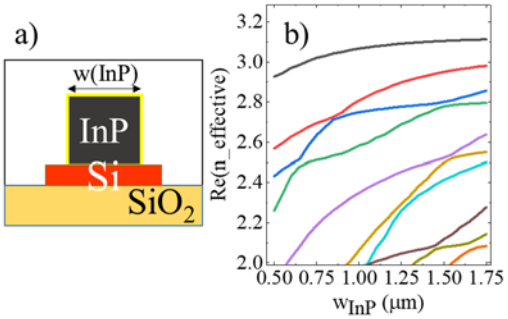

Fig. 1. a) Sketch of the coupled hybrid InP-Si waveguide system on a SiO_2 platfom; b) Real part of the complex effective refractive index for the confined modes versus the InP WG width.

The mode structure of the InP WG with the width of 1.25 µm is demonstrated in Fig. 2. The QD placed in the center of the InP WG plays the role of a point source modelled as an electric dipole with its linearly polarized dipole moment oriented in-plane and perpendicular to the WG main axis. The coupling efficiency of the QD-emitted EM field to the propagating WG mode is evaluated as an overlap of the EM field distribution with the mode's field distribution at a faraway distance from the source. Here we set the distance to 15 µm (convergence is obtained at ~10 µm) due to limitations of the numerical engine. The evaluated QD EM-field coupling to all propagating modes is demonstrated in Fig. 2b) with the highest coupling efficiency of 0.38 for the #3 mode and

0.11 for the #1 fundamental mode. The total coupling to all propagating modes is about 0.80.

In Fig. 2b) (middle panel), we demonstrate the TE fraction of a given mode, which allows to distinguish between the TE-like and TM-like mode charater. As the QD EM-field coupling depends both on the polarization of the propagated mode field and the position of the QD, we found that the third TE-like mode is the dominant one and mimics a Gauss mode. This knowledge can be used for further analysis related to the geometry of the InP WG, seeking the best conditons securing the most effective coupling between, e.g. tapered InP WG and the Si WG.

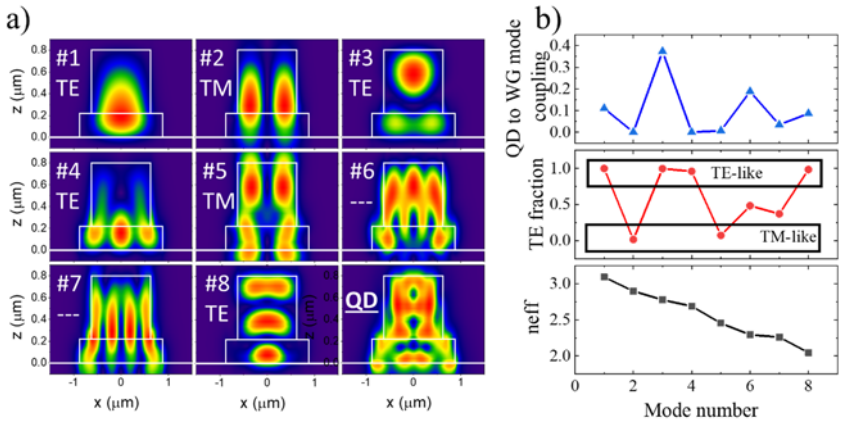

Fig. 2. a) Electric field distrbution of the modes confined in the coupled hybrid InP-Si waveguide on SiO_2 and the dipole generated field (bottom-right panel). b) Results of the evaluated mode-dipole emission coupling efficiency (upper panel), mode character given by TE fraction (middle panel) and effective refractive index (lower panel) for modes #1-#8.

3. Conclusions

We conclude that the coupled hybird InP-Si-waveguide system consisting of a single InAs quantum dot embedded directly in the InP waveguide can be successfully utilized for photonics integrated circuits, as it provides nearly 80% coupling of quantum dot emission to propagating waveguide modes. This conclusion is made based on the observed multimode character of the waveguide that support four TE-like modes strongly localized in the InP WG.

Acknowledgements

We acknowledge financial support from the National Science Centre (Poland) within Project No. 2020/39/D/ST5/02952.

References

[1]. M. I. Davanço, J. Liu, L. Sapienza, C. Z. Zhang, J. V. De Miranda Cardoso, V. Verma, R. P. Mirin, S. W. Nam, L. Liu, and K. Srinivasan, *Nat. Commun*., 8, 2017, 889.
[2]. G. C. Park, W. Xue, A. Taghizadeh, E. Semenova, K. Yvind, J. Mørk, and I. S. Chung, *Laser Photonics Rev.,* 9, 2015, L11.
[3]. A. Sakanas, E. Semenova, L. Ottaviano, J. Mørk, and K. Yvind, *Microelectron. Eng*., 214, 2019, 93.
[4]. Http://www.lumerical.com/tcad-products/fdtd/,, n.d..
[5]. P. Mrowiński, M. Emmerling, C. Schneider, J. P. Reithmaier, J. Misiewicz, S. Höfling, and G. Sęk, *Phys. Rev. B,* 97, 2018, 165427.
[6]. P. Mrowiński and G. Sęk, *Phys. B Condens. Matter,* 562, 2019, 141.
[7]. A. Ghimire, E. Shafran, and J. M. Gerton, *Sci. Rep.,* 4, 2014, 6456.
[8]. L. Yang, H. Wang, Y. Fang, and Z. Li, *ACS Nano,* 10, 2016, 1580.
[9]. In Handb. Opt. Constants Solids, *Elsevier*, 1998, p. iv.

(023)

Characterization and Comparison of CubeSat and Drone Platform Jitter Effects on Laser Beam Pointing Stability

Femi Ishola [1], Alberto Carrasco-Casado [1], Phuc V. Trinh [1], Koichi Shiratama [1], Hirokazu Masui [2], Rodrigo Cordova [2], Yasushi Munemasa [1], Mengu Cho [2], Tetsuharu Fuse [1], Hiroyuki Tsuji [1] and Morio Toyoshima [1]

[1] National Institute of Information and Communications Technology (NICT), 4-2-1 Nukui-Kitamachi, Koganei, Tokyo 184-8795, Japan

[2] Kyushu Institute of Technology, 1-1 Sensui Cho, Tobata, Kitakyushu, Fukuoka, 804-8550 Japan

E-mail: femi@nict.go.jp

Summary: Adaption of laser-communication terminals into airborne and lean-satellite platforms is now a vogue, made possible due to the advancements in lightweight components and compactness of onboard electro-optical transceivers and control systems. This enables more secured and higher data-transmission rates beyond multiple Gigabit/second on CubeSats and drones compared to Megabit/second rates offered by similar radio-transceivers form factors. However, laser-transmission links require a very stringent beam-pointing stability, because they are easily perturbed by attitude variations and micro-vibrations generated by the host platform's propulsion system or other mechanically active subsystems in proximity with the transmitter's optical head. Severe line-of-sight jitter causes the downlink laser beam to drift from the targeted receiving system's field-of-view, inducing pointing errors, increasing signal outage probability and loss of information. We experimentally examine the platform jitter generated by the propellers of a hexacopter drone during ground operation and the attitude-control unit's reaction wheels in a 6U CubeSat structure. We determined the vibration spectrum unique to these platforms and accordingly prescribe requirements for applicable optical fine pointing and disturbance isolation or suppression systems needed to achieve a high-fidelity laser-communication link.

Keywords: Laser communications, Platform jitter, Beam-pointing stability, Drone, CubeSat.

1. Introduction

Small satellites and Unmanned Aerial Vehicles (UAVs) are projected to play crucial roles in the evolution of next-generation 6G communication systems. Due to the increasing demand of higher data transmission rates, it becomes imperative to adapt free-space optical (FSO)/laser communication (lasercom) links within existing RF networks [1]. Laser beams have higher directivity, suitable for long distance and high-capacity signal transmission. However, this makes it also susceptible to beam pointing instability especially when the platform has persistent mechanical disturbances and continuous attitude variations. Nowadays, commonly used drones are the rotary-wing propeller type aircrafts that generates substantial high-frequency mechanical jitter and audible sound from take-off to landing. Similarly, orbit-bound CubeSats have the same problem with microvibrations generated by the reaction wheels used for attitude control.

Careful consideration of the impact of platform microvibrations is a good reason to have sufficient margin for pointing losses in the optical link budget design. Microvibrations or jitter are generally defined as structurally transmitted force disturbances generated from components such as servomotors, reaction wheel assembly (RWA), drive mechanisms and appendages of the platform. The CubeSat's RWA is the chief source of jitter on the platform which perturb the hosted optical instrument or lasercom payload line-of-sight pointing stability. Static and dynamic imbalances, bearing friction, manufacturing or factory errors and operational degradation are responsible for the RWA jitter. Static imbalance is the misalignment of the wheel's center of gravity (CoG) from its main rotating axis while dynamic imbalance is defined as the cross product of the wheel's inertia caused by angular deviation of the principal inertia with respect to the spin axis. While most COTS RWA and drone propeller manufacturers seldom provide full jitter data [2], it is essential to characterize the device micro-vibrations to estimate the impacts of a lasercom payload and possible mitigation measures. In this paper, we describe the results of practical jitter experiments aiming to characterize the impact of a CubeSat's RWA and drone's propeller unwanted force propagation on a laser beam pointing setup. An historical perspective of the development microvibration analysis is presented in section 2. The methodology of conducted experiments, the results, and the platform comparison are described and jitter mitigation measures are discussed in section 3. We summarized the importance of the study in section 4.

2. Microvibration Analysis

Drones are highly mechanically active airborne platforms, with significant vibrations and shock produced by the multiple brushless motor driven propellers. The vibrations are transmitted through the entire structural system in a fashion peculiar to the drone's airframe design. Not much material is available on disturbance characterization of rotary-wings, multi-rotor drones [3, 4] as they have diversed

configuration and aerodynamic designs. External factors such as weather, wind speed, and air turbulence contributes to the vibration pattern in drones.

Reaction wheel technology is currently well developed and extensively adopted in satellite platforms for communication, imaging and remote sensing applications. RWA jitter is modelled analytically, empirically or a combination of both. Origin of RWA disturbance modelling efforts dates back to the 1970s with early mathematical/analytical approaches taking shape in the 90s while empirical modelling method was developed in the early 2000s [5]. The empirical modelling was first created for RWA vibration assessments of the Hubble Space Telescope [6]. It is a more robust scheme that make use of parameters recorded from a reaction wheel test or experiment. In the empirical approach, the steady-state jitter force or torque $J(t)$, having an amplitude A_i, (N^2/Hz) is proportional to the square of the RWA speed, Ω (Hz) and contains discrete harmonics (n).

$$J(t) = \sum_{i=1}^{n} A_i \Omega^2 \sin(2\pi h_i \Omega t + \phi_i) \qquad (1)$$

where h_i is the harmonic coefficient and ϕ_i is the phase of the harmonic with values range from 0 to 2π. Equation 1 provide insights to the nature of the microvibration forces and torques with respect to the speed of the RWA. Typically, different RWA produces different jitter patterns therefore it is essential to characterize the particular RWA in use at every given case. The power spectral density P_j of the RWA disturbance force is related to the root-mean-square (RMS) line-of-sight pointing error of the platform [7]:

$$P_J(f) = \sum_{i=1}^{n} \frac{F_i^2(\Omega)}{2} \delta(h_i \Omega - f) \qquad (2)$$

3. Description of Experiments

3.1. CubeSat RWA Jitter Experiment

We assembled an experimental test-bed at the Kyushu Institute of Technology's Centre for Nanosatellite Testing (CeNT) to determine the spectrum of jitter induced by the MAI-400 integrated attitude determination and control system (ADCS) unit's reaction wheel, with a line-of-sight laser transmitter in a 6U CubeSat structure as shown in Fig. 1. The axial acceleration and gyroscope data from the ADCS internal sensors where obtained via an XBee radio interface between the MAI-400 and a laptop computer. In order to monitor the effects of the vibrations at different RWA speed, an optical beam position sensing system was incorporated at the receiving end. The RWA speed was incremented in steps starting from off position to its full capacity (10,000RPM) to study the impact on the magnitude of force projected to the optical components as well as the resultant instability of the laser beam. The unit's internal accelerometer and gyroscope simultaneously recorded the dynamics at each steps. The recorded accelerometer and gyroscope data are shown in Figs. 5 - 7.

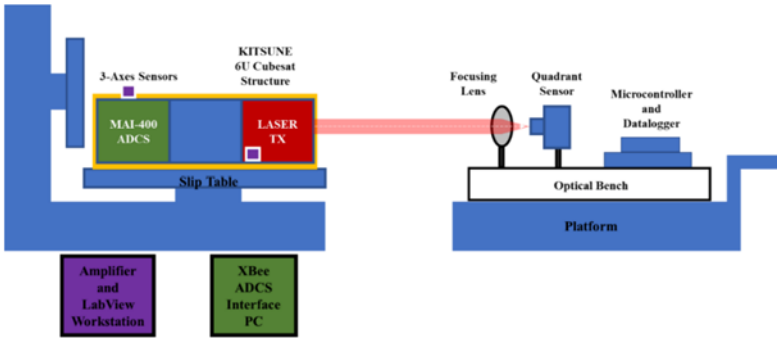

Fig. 1. 6U CubeSat ADCS jitter measurement setup.

Fig. 2. (a) Drone with mounted Lasercom Module; (b) Ad-hoc optical receiving system.

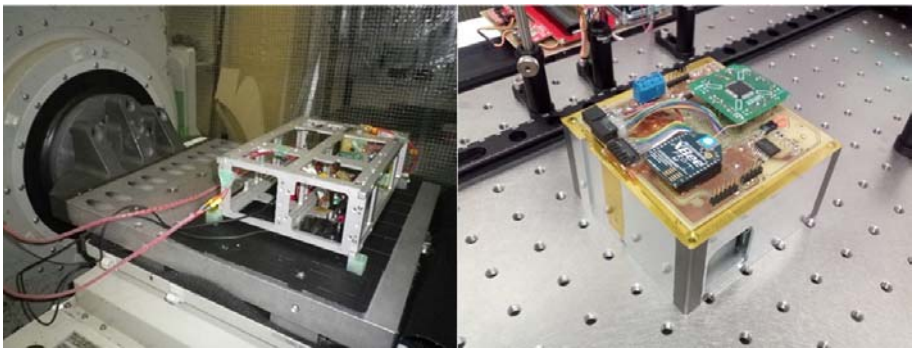

Fig. 3. (a) CubeSat structure placed on slip table (b) MAI-400 ADCS Module.

Fig. 4. (a) Lasercom module with downlink laser beam switched on (b) Footprint of the laser beam at the receiver.

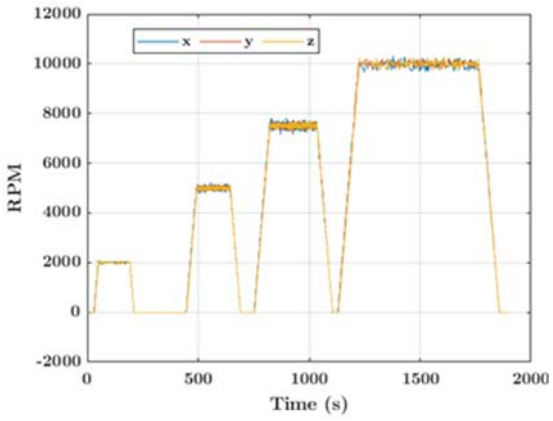

Fig. 5. (a) CubeSat Reaction Wheel Tachometer profile.

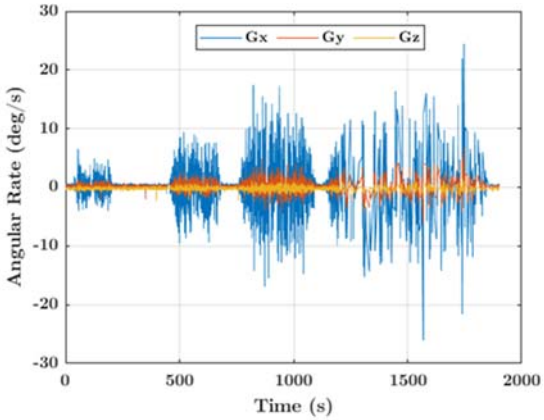

Fig. 6. ADCS module internal Gyroscope data.

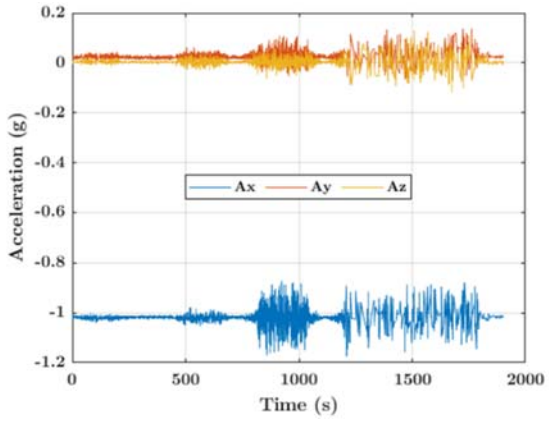

Fig. 7. ADCS module internal Accelerometer data.

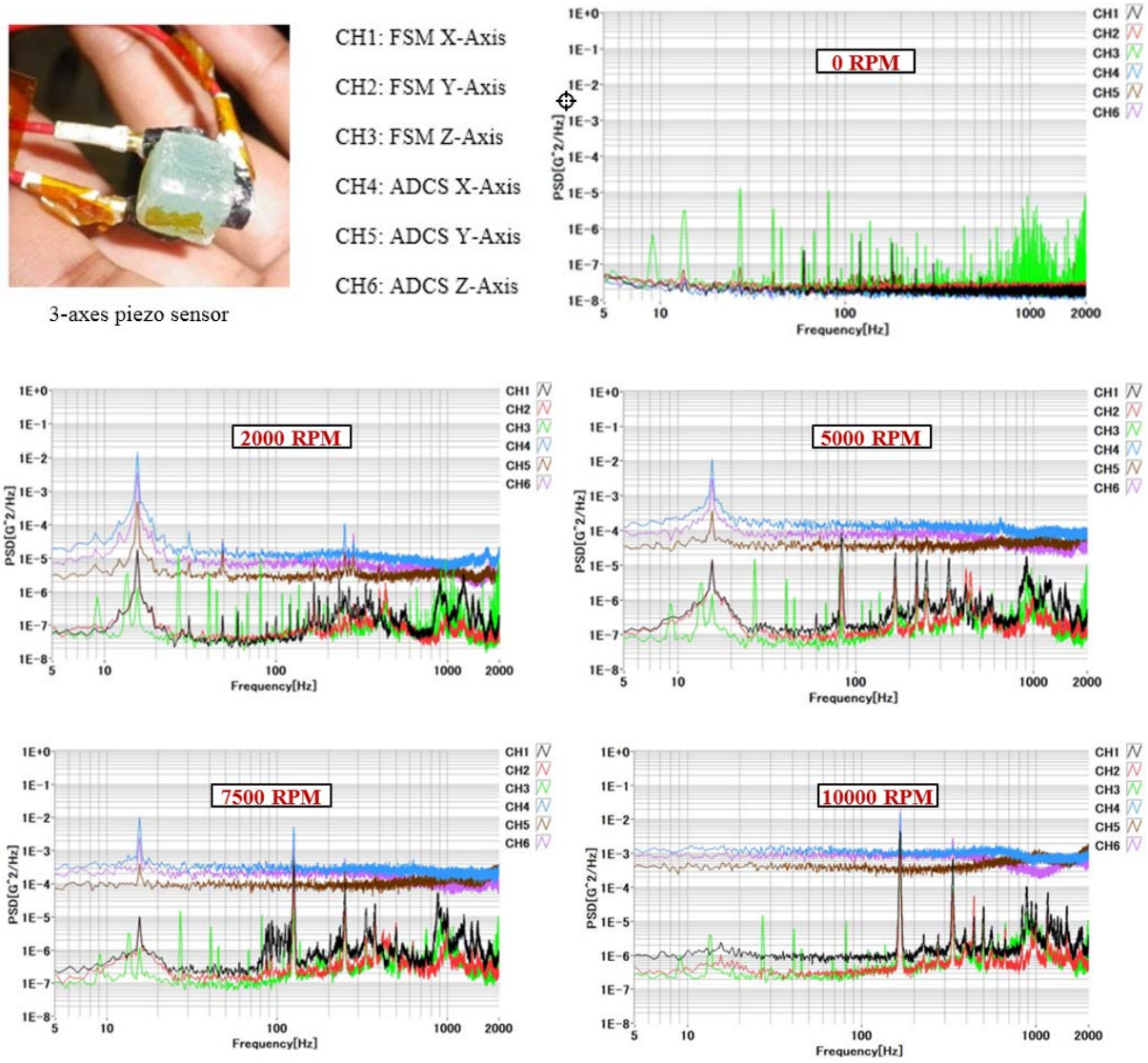

Fig. 8. Vibration spectrum at ADCS and FSM locations during different reaction wheel speeds

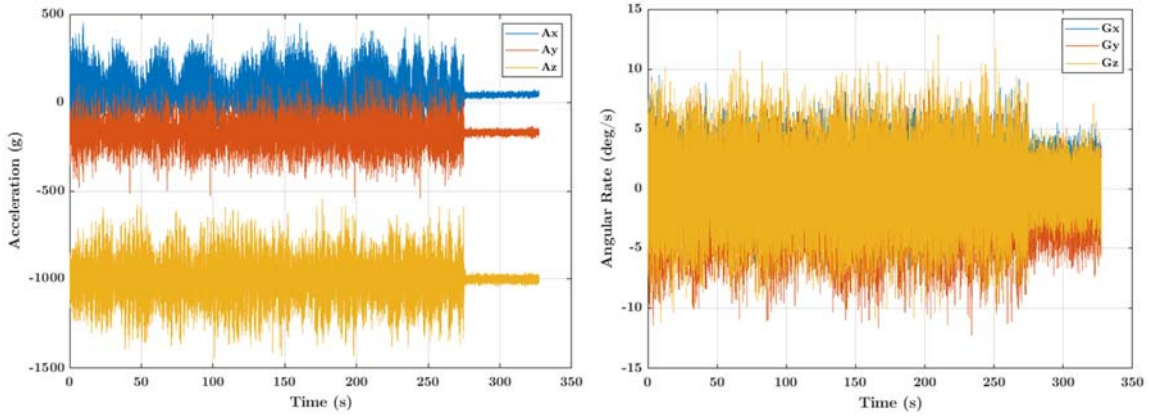

Fig. 9. (a) Drone accelerometer data with gimbal smooth tracking mode activated (b) Drone gyroscope data with gimbal smooth tracking mode activated.

Three-axes external piezo accelerometers were mounted on various locations at the structure and the ADCS unit, connected to a pre-charge amplifier. The pre-charge amplifier converted the piezo-electric type accelerometer high impedance charge input into a low impedance voltage signal fed into a data acquisition

system [8]. Piezo-electric sensors are an excellent choice for jitter measurement and characterization [9] given their high resolution, very high frequency response and wide dynamic range. Two units of the 3-axes piezo sensors were used (shown in Fig. 8), one at the Fine Steering Mirror (FSM) location and the other one close to the reaction wheel.

3.2. Drone Jitter Experiment

CubeSats and UAVs/drones are both very attractive for lasercom terminal adaption because they are low-cost, rapid manufacturing time and suitable for several application scenarios. Drone propellers are an active vibration sources that needs to be damped in order to host sensitive optical payloads such as LiDAR and lasercom terminals. In the framework of the NICT-Kyutech collaborations, we conducted a drone jitter experiment at the NICT's Space Communication Systems Laboratory in Tokyo, utilizing the DJI M600 Pro Hexacopter fitted with a lasercom module and an active Ronin-MX gimbal stabilizer. As shown in Fig. 2, the drone was firmly fixed to the ground the entire duration and separated from the ad-hoc receiving system by 15 meters direct line-of-light. The gimbal was stabilized while the propellers where operated at full speed. Accelerometer and gyroscope sensor in the lasercom module recorded the vibrations of the platform while a laser position sensor at the receiver monitored the displacement of the beam footprint at the receiver.

3.3. Platforms Comparison

In this study, we collected both vibrational data using attitude sensors as well as optical detector to monitor the impact of the disturbances on the direct line-of-sight beam pointing at the receiver. This combination offers a unique discernment of the similarities and differences between the two platforms. The DJI M600 pro drone uses six E2000 propulsion motor drive, each attached to a twin blade foldable propeller providing up to 30,600 g thrust. During flight, the microvibrations generated on the drone are a resultant effect of the propeller motion, wind speed, drone structural configuration, appendages and movements of the gimbal/payload. The drone propulsion system generates much stronger force and torque, therefore much beam instability was observed at the receiver optical position measurement device as shown in Fig 10 and 11. Despite activating stabilization function of the drone gimbal, drifting of the laser beam could still be seen, indicating high frequency jitter in the system. The maximum speed of the CubeSat RWA was 10,000 RPM but the force amplitudes were quiet lower. CubeSats operate at longer link range compared to drone, hence the effect of the micro-disturbances are very well pronounced because of the diverging beam and its footprint size at the receiver. Amateur drones are typically permitted to fly at 100 meters altitude but the communication range could be up to few kilometres for an horizontal link.

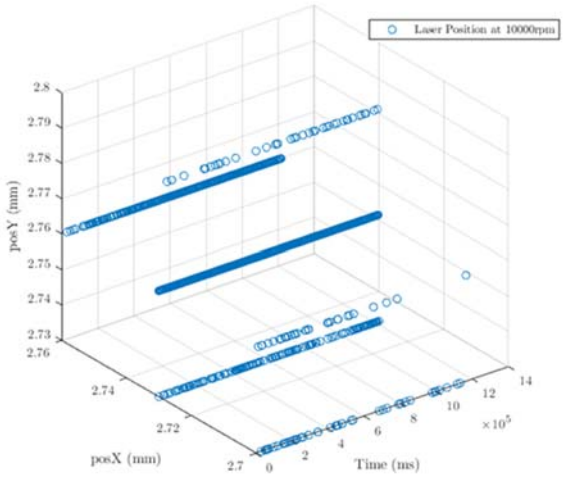

Fig. 10. CubeSat laser beam drift at the receiver.

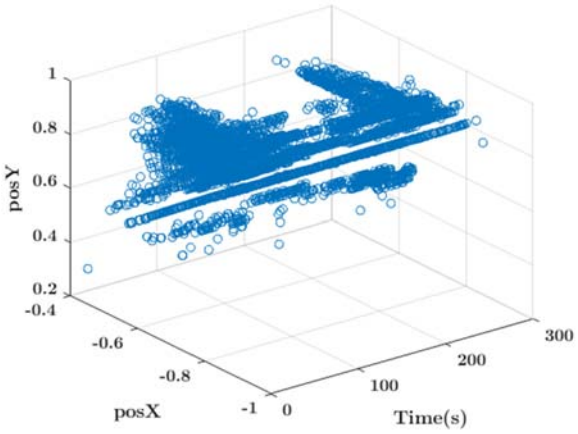

Fig. 11. Drone Laser beam drift at the receiver.

3.4. Jitter Mitigation Measures

Microvibrations must be damped or isolated to achieve a high performing optical system on a platform susceptible to internal or externally generated disturbances. The simplest approach is to locate the laser optical-head as far away as possible from the dominant jitter source (RWA). Careful and compact arrangement of the platform subsystems and minimization of flanges and appendages on the structure is a passive means of reducing the impact of micro-vibrations in lasercom systems. However, high-frequency disturbances are easily transmissible and can permeate through the entire structural system which therefore necessitates more proactive countermeasures. A self-tuning feed-forward jitter compensation strategy applicable to laser link was described by Skormin et. al [10, 11]. The method featured coupling the output of an accelerometer to an electrical RLC circuit for jitter signal reconstruction

and utilization in the feed-forward control system. However, the drawback with feed-forward control scheme is that set-points tracking of the controlled variable is not always guaranteed [12], because the controller takes action ahead of time before the jitter can disrupt the actuation device (e.g. Fine Steering Mirror). Lasercom nodes usually require an initial search and scan using a beacon beam to orient and align the optical heads. Jitter interference is noticeable in the link acquisition and beam scanning procedures (raster, spiral etc.) between for example, a microsatellite having ADCS module and a receiver. [13, 14] suggested interpolation algorithm to alter the scanning beam by compensating for the platform vibrations. A dual-beam scan method was proposed by [15] as more advantageous compared to the single-scan because it provide double speed and more resilient against the scan beam jitter. The ASTERIA (Arcsecond Space Telescope Enabling Research in Astrophysics) 6U imaging CubeSat [16-18] featured an active jitter mitigation system providing pointing stability of up to 0.5arcsecond for precision photometry application; a two-axis piezo-electric positioning stage, implementing fine pointing by taking reference directional information from an onboard CMOS star tracker. Such a system can be applied to a lasercom payload to provide very good laser beam pointing stability. However, piezo-electric actuators often demand high voltages and have limited field of regard compared to more flexible option of using micro-electro mechanical (MEMS) FSMs.

4. Conclusions

The need for multi-platform compatible optical communication transceivers is driven by demand for low-cost, mass produced, ready-to-fly COTS lasercom solution that can support ubitiquous multi-layer laser and hybrid (plus RF) communication network. A cross-platform lasercom terminal that is adaptable to both drone and CubeSat platforms must be capable of operating within the baseline performance despite differences in spectrum and amplitude of jitter experienced in the two cases. We have characterized the microvibartion experienced in a 6U CubeSat with an integrated ADCS module and a heavy-lift hexacopter drone. Determination of the peak and harmonic vibrational frequencies are important requirements to implementing an active fine pointing system with sufficient bandwidth. Since different platform gives different vibrational profiles, it is an indispensable task to conduct the kind of experiments described in this paper in a bid to achieve a high quality and reliable laser communication link.

Acknowledgements

The work reported in this paper was facilitated by the NICT-Kyutech matching research fund.

References

[1]. F. Ishola and M. Cho, Experimental Study on Photodiode Array Sensor Aided MEMS Fine Steering Mirror Control for Laser Communication Platforms, *IEEE Access*, Vol. 9, 2021, pp. 100197–100207.

[2]. J. Shields *et al.*, Characterization of CubeSat Reaction Wheel Assemblies, *Journal of Small Satellites*, Vol. 6, No. 1, 2017, pp. 565–580.

[3]. J. Verbeke and S. Debruyne, Vibration analysis of a UAV multirotor frame, in *Proceedings of the International Conference on Noise and Vibration Engineering (ISMA 2016)*, 2016, pp. 2329–2337. Accessed: Apr. 28, 2022. [Online]. Available: https://lirias.kuleuven.be/retrieve/403821

[4]. C. Ge, K. Dunno, M. A. Singh, L. Yuan, and L.-X. Lu, Development of a Drone's Vibration, Shock, and Atmospheric Profiles, *Applied Sciences*, Vol. 11, No. 11, Art. No. 11, Jan. 2021.

[5]. C. J. Dennehy, A Survey of Reaction Wheel Disturbances Modelling Approaches for Spacecraft Line-of-Sight Jitter Performance Analysis, Sep. 2019, p. 13.

[6]. Rebecca A. Masterson, Development and validation of empirical and analytical reaction wheel disturbance models, Thesis, *Massachusetts Institute of Technology*, 1999. Accessed: Sep. 02, 2021. [Online]. Available: https://dspace.mit.edu/handle/1721.1/80018

[7]. J. Shields *et al.*, Characterization of CubeSat Reaction Wheel Assemblies, *Journal of Small Satellites*, Vol. 6, No. 1, 2017, Art. No. 1.

[8]. F. Ishola, Free-Space Optical Communications for Resource-Limited Small Satellites, *Kyushu Institute of Technology,* Kitakyushu, Japan, 2021. [Online]. Available: https://bit.ly/3Kg1TDb

[9]. B. Zwolinski, C. Cavalloni, and M. Dumont, Measuring Considerations for Jitter Characterization on Small Satellite Reaction Wheels, in *Proceedings of the International Sensor and Measurement Science Conference (SMSI 2020),* 2020, p. 67-68.

[10]. V. A. Skormin, M. A. Tascillo, and D. J. Nicholson, A jitter rejection technique in a satellite-based laser communication system, in *Proceedings of the IEEE National Aerospace and Electronics Conference (NAECON 1993)*, Dayton, OH, USA, 1993, pp. 1107–1115.

[11]. V. A. Skormin, M. A. Tasullo, and T. E. Busch, Demonstration of jitter rejection technique for free-space laser communication, *SPIE Proceedings, Vol. 2123: Free-Space Laser Communication Technologies VI,* pp. 381–392.

[12]. R. Singh, Model-based control system design and evaluation for continuous tablet manufacturing processes (via direct compaction, via roller compaction, via wet granulation), in *Computer Aided Chemical Engineering*, Vol. 41. Chapter 13, R. Singh and Z. Yuan, Eds., *Elsevier*, 2018, pp. 317–351.

[13]. M. Scheinfeild, N. S. Kopeika, and R. Melamed, Acquisition system for microsatellites laser communication in space, in *Free-Space Laser Communication Technologies XII*, May 2000, Vol. 3932, pp. 166–175.

[14]. X. Zhi, Y. Ai, and M. Lu, Acquisition methods for microsatellite laser communication in space, in *Wireless and Mobile Communications II*, August 2002, Vol. 4911, pp. 372–379.

[15]. G. Hechenblaikner, Analysis of performance and robustness against jitter of various search methods for

acquiring optical links in space, *Appl. Opt.*, Vol. 60, No. 13, May 2021, Art. No. 13.

[16]. M. Smith *et al.*, On-Orbit Results and Lessons Learned from the ASTERIA Space Telescope Mission, in *Proceedings of the 32nd Annual AIAA/USU Conference on Small Satellites,* 2018, pp. 1-20.

[17]. C. Pong, On-Orbit Performance & Operation of the Attitude & Pointing Control Subsystems on ASTERIA, in *Proceedings of the 32nd Annual AIAA/USU Conference on Small Satellites*, 2018, p. 20.

[18]. M. Knapp *et al.*, Demonstrating High-precision Photometry with a CubeSat: ASTERIA Observations of 55 Cancri e, *The Astronomical Journal*, Vol. 160, No. 1, Art. No. 1, June 2020.

(024)

High Type A Refractive Index Change by Multi-scan Cumulative Inscriptions in Photosensitive Glasses

L. Loi [1,*], T. Guérineau [2], S. Danto [2], T. Cardinal [2], Y. Petit [1,2] and L. Canioni [1]
[1] Université de Bordeaux, CNRS, CEA, CELIA, UMR 5107, 351 Cours de la Libération, 33405 Talence, France
[2] Université de Bordeaux, CNRS, IPB, ICMCB, UMR 5026,
87 Avenue du Dr. A. Schweitzer, 33608 Pessac, France
E-mail: laura.loi@u-bordeaux.fr

Summary: In femtosecond laser inscription, the multi-scan technique has already proved to increase the refractive index change associated to the embedded structures for both low and high repetition rate regimes. However, for the latter case, the thermal effects induced by the subsequent absorption of the laser pulses tend to tightly narrow the DLW window for smooth type I material modifications, making it difficult to control the refractive index change. On the other hand, femtosecond laser inscription of silver-sustained (type A) refractive structures in silver-containing glasses with high repetition rate was recently shown to occur in an athermal regime. The present work shows that this remarkable athermal regime, in combination with the multi-scan technique, enables for achieving high type A refractive index changes, up to 1.3×10^{-2}, in a commercial silver-containing glass.

Keywords: Direct laser writing, Multi-scan laser inscription, High refractive index change, Ultrafast laser-matter interaction, Athermal regime, Type A refractive index modifications, Laser induced silver clusters, Photosensitive media.

1. Introduction

Since the first demonstration of femtosecond laser inscription in fused silica [1], many techniques have been exploited to achieve three-dimensional material structuring for the fabrication of waveguides and of more complex optical devices. In this regard, Direct Laser Writing is a well-known technique that allows for the fine control of the localized energy deposition and associated material modification. Femtosecond laser focusing in glasses leads to different types of material modifications: Type I, the only one associated with smooth refractive index contrast compatible with low-loss waveguiding applications, while Type II and Type III correspond to nanogratings and voids creation, respectively. In 2017, our group demonstrated the existence of a new type of refractive index change in silver-containing glasses, labeled Type A, which is not related to matrix modifications. Indeed, such a new type appears at a different laser irradiation regime, and it is sustained by the photo-induced creation of molecular silver clusters, such new chemical species providing new chemical bonds associated to intense UV absorption bands and broadband VIS fluorescence emission [2, 3]. Femtosecond laser inscription generally takes place in two regimes: at low repetition rate (from 1 kHz to 250 kHz) and high pulse energy, or at high repetition rate (above 1 MHz) and low pulse energy. The difference between these two regimes lies on the thermal management during the pulse-to-pulse energy deposition during the laser pulses train irradiation. Indeed, in the case of low repetition rate, the large time scale between successive pulses allows for heat diffusion out of the interaction voxel, preventing thermal accumulation. Laser induced modifications are, thus, smooth but the associated refractive index change is rather weak, up to 3×10^{-3} in fused silica. In the high repetition rate regimes, instead, the resulting absorption of focused laser pulses increases the temperature of the glass above the glass transition temperature in the interaction voxel, inducing the glass matrix to locally melt and quickly quench. Due to heat diffusion, the induced material modifications show a profile with radial symmetry associated to dimensions larger than that of the interaction voxel. The associated refractive index change is higher than that obtained in the low repetition rate regime, however, it might be positive, negative or show both behaviors, depending on the writing parameters and the glass composition.

Remarkably, the inscription of Type A refractive index modifications takes place in an athermal regime, despite the use of a high repetition rate laser source. Indeed, a comparison study between Type I and Type A refractive index modification demonstrated that the laser irradiance necessary to activate the clustering of silver species is much lower than that required in the inscription of Type I material modifications [4]. Moreover, Type A refractive index change is always positive and localized at the regions where silver clusters are photo-induced, allowing for inscription of features with dimensions down to 100 nm and thus overcoming the diffraction limit. This smooth and positive refractive index change was demonstrated to support light guiding, enabling the fabrication of optical components such as waveguides, couplers, beam splitters and refractive index sensors [5].

In the present work the inscription of Type A refractive index modifications is performed in combination with the multi-scan technique. Such technique has been widely adopted in literature in order to increase the induced refractive index change in both femtosecond laser inscription regimes. In the case of low repetition rate, the work of Lapointe et al.

reported on increasing the refractive index contrast from 1.4×10^{-3} to 9×10^{-3} after 500 consecutive laser scans on the same position, in the case of short pulse duration (65 fs) [6]. In the high repetition rate regime, the thermal effects originated in the many-pulse absorption make it difficult to control the refractive index increase while performing the multi-scan technique. Indeed, as reported in the work of Graf *et al.*, the heat accumulation leads to the formation of pearl-chained waveguides with high propagation losses [7].

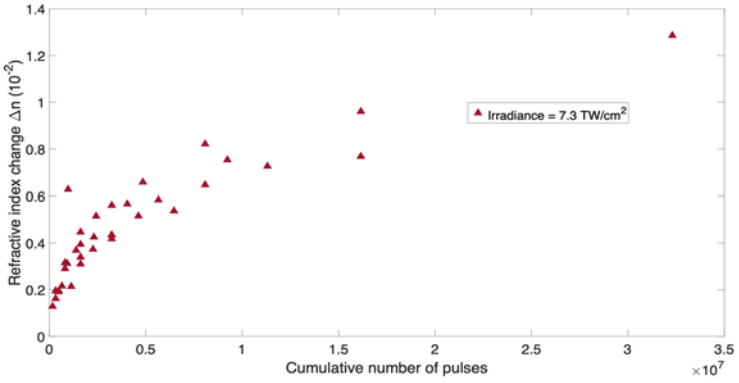

Fig. 1. Refractive index change Δn as a function of the cumulated number of absorbed laser pulses in a 10 MHz high repetition rate but still athermal regime.

2. Experimental Setup and Results

The present study benefits from the counter-intuitive athermal inscription of Type A modifications in a gallo-phosphate glass photosensitized with silver ions by means of a KGW:Yb femtosecond oscillator (up to 2.6 W, 9.8 MHz, 400 fs FWHM at 1030 nm) and the multi-scan technique. For each structure, the consecutive laser scans are repeated *in loco* a different number of times. Each structure is then imaged using the Sid4BIO device (Phasics) in order to extract the Optical Path Difference (OPD) profiles induced by the laser-induced silver clusters. Finally, by diving the OPD by the thickness of each structure, the dependence of the refractive index change Δn on the different number of laser scans is extracted. Remarkably high and smooth refractive index changes up to 1.3×10^{-2} are achieved (see Fig. 1). The reported results demonstrate that such high refractive index change is directly dependent on the number of cumulative absorbed laser pulses, *i.e.* the number $N_p = N_{scan}.\varphi.f_{rep}/v$ of pulses irradiated during the inscription of N_{scan} laser scans, at a given writing speed v, for a laser source with f_{rep} repetition rate and focused beam diameter φ.

3. Conclusion

The multi-scan cumulative femtosecond laser inscription of Type A refractive index modifications in photosensitive glasses tailored with silver ions is carried out in an athermal regime. This remarkable condition allows to achieve high induced refractive index change whose amplitude is directly related to the cumulative number of absorbed pulses.

References

[1]. K. M. Davis, K. Miura, N. Sugimoto, and K. Hirao, Writing waveguides in glass with a femtosecond laser, *Optics Letters,* 21, 1997, pp. 1729-1731.

[2]. A. Abou Khalil, J. P. Bérubé, S. Danto et al., Direct laser writing of a new type of waveguides in silver containing glasses, *Scientific Reports,* 7, 2017, 11124.

[3]. M. Bellec, A. Royon, B. Bousquet, K. Bourhis, M. Treguer, T. Cardinal, M. Richardson, and L. Canioni, Beat the diffraction limit in 3D direct laser writing in photosensitive glass, *Opt. Expr.*, 17, 2009, pp. 10304-10318.

[4]. A. Abou Khalil, J. P. Bérubé, S. Danto, T. Cardinal, Y. Petit, L. Canioni, and R. Vallée, Comparative study between the standard type I and the type A femtosecond laser induced refractive index change in silver containing glasses, *Opt. Mater. Express,* 9, 2019, pp. 2640-2651.

[5]. A. Abou Khalil, Philippe Lalanne, Jean-Philippe Bérubé, Yannick Petit, Réal Vallée, and Lionel Canioni, Femtosecond laser writing of near-surface waveguides for refractive-index sensing, *Opt. Express,* 27, 2019, pp. 31130-31143.

[6]. J. Lapointe, J. P. Bérubé, S. Pouliot, and R. Vallée, Control and enhancement of photo-induced refractive index modifications in fused silica, *OSA Continuum*, 3, 2020, pp. 2851-2862.

[7]. R. Graf, A. Fernandez, M. Dubov, H. Brueckner, B. Chichkov, and A. Apolonski, Pearl-chain waveguides written at MHz repetition rate, *Appl. Phys. B*, 87, 2007, pp. 21-27.

(025)

Volume Gratings for the Recording of a Waveguide on Photopolymers

C. Neipp [1], J. C. Bravo-Francés [1], J. J. Sirvent-Verdú [1], M. Morales-Vidal [2], T. Lloret [2], D. Puerto [1] and S. Gallego [1]

[1] Dept. of Physics, Systems Engineering, Signal Theory, University of Alicante, Spain
[2] Dept. of Optics, University of Alicante, Spain
Tel.: (+34) 96 590 3682
E-mail: cristian@ua.es

Summary: In this work we present an application of volume transmission gratings for the coupling of light inside and outside a holographic waveguide. The volume gratings were recorded on photopolymer, since they have demonstrated great advantages over other materials. The gratings were fabricated with a spatial frequency of 1700 lines/mm so as to couple light inside the glass substrate under total reflection condition. The results demonstrate the efficiency of this device to be used in augmented reality applications, for example as see-through glasses.

Keywords: Waveguides, Photopolymers, Diffraction gratings, Holography, Volume holographic elements.

1. Introduction

It is a fact that augmented reality or virtual reality has taken on importance in society. Augmented Reality devices usually consist of a headset and a display system to show the user the virtual information that is added to the real one. In the particular case of the application of these concepts to the fabrication of see-through systems, these have been very welcomed by the general public, since they possess the advantage of being hands-free and have high privacy character.

For the fabrication of these devices planar waveguide technology with holographic optical elements has been widely used [1-3]. The system to be developed consists mainly of three parts: two holographic optical elements coupling the input light to the waveguide and also extracting the light from the substrate, and the glass that acts as a substrate for the holographic material acting as a waveguide by the phenomenon of total internal reflection. In this particular work the two holographic elements used are simple volume gratings recorded on photopolymer material.

The use of photopolymers for the recording of the holographic optical elements is due to the fact that these materials possess important characteristics such as low price, self-processing capability and a high versatility that, offer significant advantages over conventional wet-type recording materials [4].

2. Theoretical Device

In order to fabricate an holographic waveguide on photopolymers using volume gratings, two holographic optical elements must be recorded at a certain distance between them. The first hologram couples the light to the waveguide in total reflection condition, while the second hologram couples the beam out of the waveguide. In order to work as couplers the transmission holographic gratings should couple the incident light between air and the glass substrate accomplishing total internal reflection. Fig. 1 shows the configuration of the gratings; the diffracted beam must form the critical angle (total internal reflection) with respect to the normal of the glass substrate. $\vec{k}_r$ and $\vec{k}_o$ are the propagation vectors of the reference (incident) and object (diffracted) beam respectively, $\vec{K}$ is the grating vector and θ_g is the critical angle inside the photopolymer.

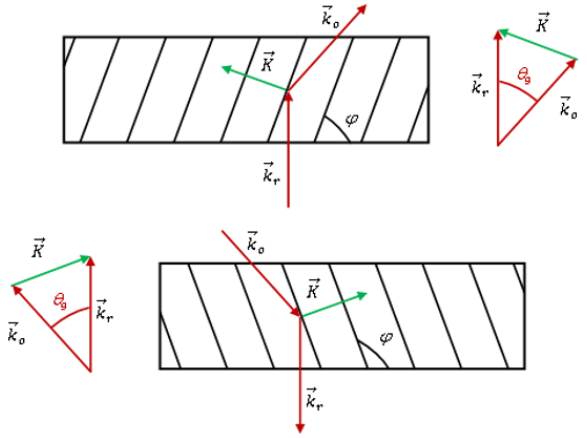

Fig. 1. Volume gratings used for wave coupling.

The grating vector is defined as:

$$\vec{K} = \vec{k}_r - \vec{k}_o, \tag{1}$$

And it is related to the spatial frequency, *f*, and the period of the grating, Λ, by:

$$\left|\vec{K}\right| = 2\pi f = \frac{2\pi}{\Lambda}, \tag{2}$$

The angle φ formed by the interference fringes with the substrate can be calculated by using:

$$\varphi = \operatorname{atan}\left(\frac{K_y}{K_x}\right) - \frac{\pi}{2}, \tag{3}$$

Using equations (1)-(3) it is possible to design the diffraction gratings needed to create the waveguide according to the requirements of the device.

In Fig. 2 we represent a scheme of the recording and reconstructing geometry.

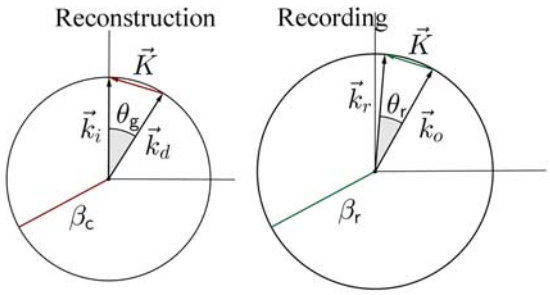

Fig. 2. Recording and reconstruction Geometry.

3. Experimental Setup

The proposed waveguide is recorded on the photopolymer material using a wavelength of 532 nm, and it is reconstructed by using a He-Ne laser, 632.8 nm, giving a propagation angle inside the layer higher of 41.5°, to obtain total reflection inside the substrate and guide the light.

Polyvinyl-alcohol acrylamide based photopolymer was used for the recording of the waveguides. The particular chemical composition used in our experiments can be described as: polyvinylalcohol, 25 ml (8 % w/v), as the binder to give physical consistence to the layer and acrylamide as main monomer, 0.84 g, with functionality one. The crosslinker added to the solution is N, N'-Methylene-Bis-Acrylamide, 0.25 g, with functionality two, and the radical generator is triethanolamine, 2 mL. The last component of PVAA photopolymer is the dye, we use yellowish eosin, 0.7 ml (0.8 % w/v), which presents good absorption at 532 nm (Nd-YVO4 laser), the recording intensity, and no absorption at 632 nm (He-Ne laser), the guided light.

The experimental device is an asymmetric transmission holographic setup. A Nd:YAG laser tuned at a wavelength of 532 nm was used to record diffraction gratings by means of continuous laser exposure. The laser beam was split into two secondary beams with an intensity ratio of 2.5:1. The diameter of these beams was increased to 1 cm using a spatial filter and collimating lens, while spatial filtering was ensured. The working intensity at 532 nm was 2.5 mW/cm^2 and 1.0 mW/cm^2 for up and down arms. Slanted gratings of 1700 lines/mm were recorded; to do this, the reference beam formed an angle to the normal of −4.8 º, whereas the object beam formed an angle of 68º. We monitored in real time the diffraction grating using red light (λ = 633 nm which the dyes do not absorb) using close to normal incidence (0.3º). After recording, the sample was rotated to record the angular response around the first Bragg condition. In Fig. 3 the experimental setup is shown.

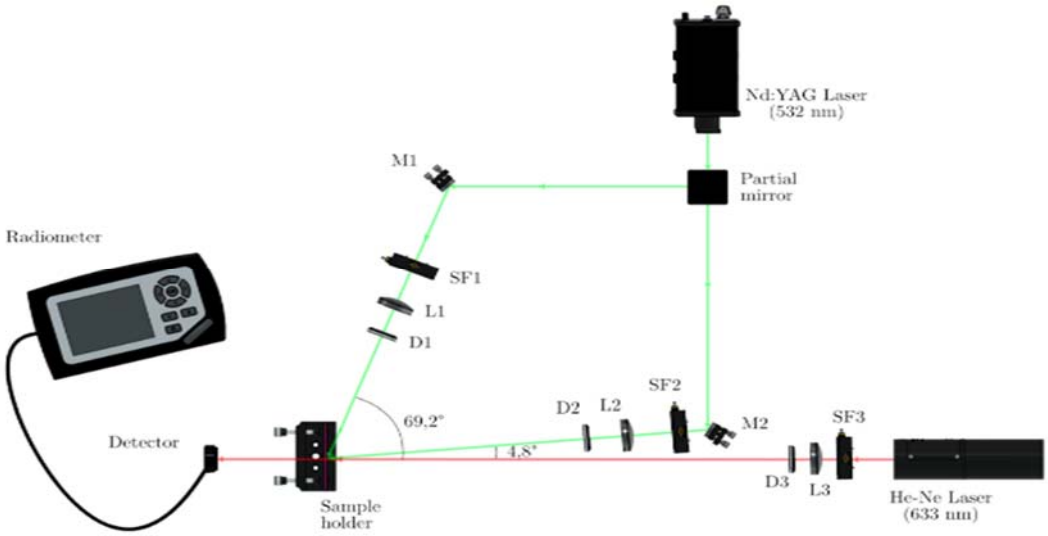

Fig. 3. Experimental setup.

4. Results and Discussion

Fig. 4 shows the transmission efficiency as a function of the angle for a slanted transmission grating recorded on photopolymer material. The spatial frequency of the gratings is of 1700 lines/mm and as can be seen from the figure a high diffraction efficiency of 70% was achieved. On the other hand in Fig. 4 a waveguide fabricated on photopolymer material by using two volume transmission diffraction gratings is presents; where two facts must be pointed out, the ability of the waveguide to propagate light by total internal reflection, and the efficiency of the two volume gratings to couple light inside and outside the waveguide.

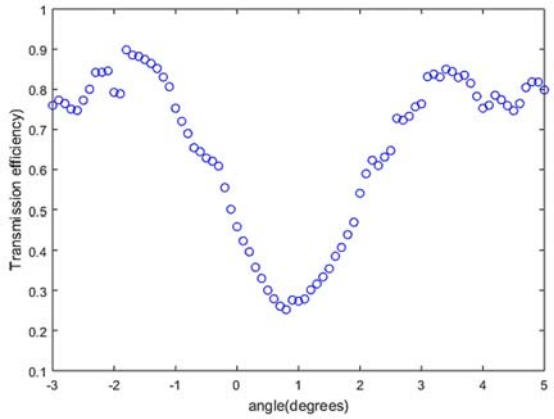

Fig. 4. Transmission efficiency of a volume grating with a spatial frequency of 1700 lines/mm.

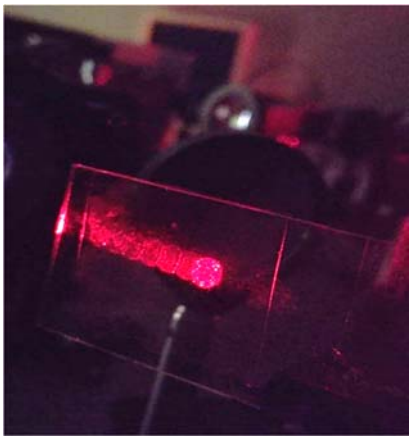

Fig. 5. Waveguide recorded on photopolymer.

5. Conclusions

In this work we have presented an application of volume transmission gratings for the coupling of light inside and outside a holographic waveguide. The volume gratings were recorded on photopolymer, and were fabricated with a spatial frequency of 1700 lines/mm so as to couple light inside the glass substrate under total reflection condition. The volume gratings recorded show a diffraction efficiency of 70 % and the waveguide fabricated demonstrates the efficiency of this device to be used in augmented reality applications, for example as see-through glasses.

Acknowledgements

This work was supported by the by 'Generalitat Valenciana' of Spain (projects PROMETEO /2021/006, IDIFEDER/2021/014, cofunded by European Union through the FEDER Programme, and CDEIGENT/2018/024), by the Ministerio de Ciencia e Innovación of Spain (project PID2019-106601RB-I00), and by the University of Alicante (project UATALENTO18-10).

References

[1]. H. J. Coufal, D. Psaltis, G. T. Sincerbox, (Eds.), Holographic Data Storage, *Springer–Verlag*, 2000.
[2]. J. Guo, Y. Tu, L. Yang, L.Wang, B. Wang, Design of a multiplexing grating for color holographic waveguide, *Optical Engineering*, Vol. 54, 2015, pp. 125105-125105.
[3]. N. Zhang, J. Liu, Han, J.; X. Li, F. Yang, X. Wang, B. Hu, Y. Wang, Improved holographic waveguide display system, *Applied Optics*, Vol. 54, 2015, pp. 3645-3649.
[4]. J.-A. Piao, G. Li, M.-L. Piao, N. Kim, Full color holographic optical element fabrication for waveguide-type head mounted display using photopolymer, *Journal of the Optical Society of Korea*, Vol. 17, 2013, pp. 242-248.

(026)

Near-field Probes based on Nanocones and Nanopyramides

D. Pudis [1, 2], A. Kuzma [3, 4], P. Maniakova [1], M. Feiler [3], D. Jandura [1] and M. Goraus [1]
[1] Dept. of Physics, Faculty of Electrical Engineering and Information Technology, University of Žilina, Univerzitná 1, 010 26 Žilina, Slovakia
[2] University Science Park of the University of Zilina, Zilina, Slovakia
[3] Faculty of Electrical Engineering and Information Technology, Institute of Electronics and Photonics, Slovak University of Technology in Bratislava, Bratislava, Slovakia
[4] International Laser Center, Bratislava, Slovakia
Tel.: + 4215132300
E-mail: dusan.pudis@feit.uniza.sk

Summary: The unique properties of metal-dielectric nanoprobes are caused by resonant properties of conductive nanosystems due to the surface plasmon polaritons arising at metal-dielectric interface. The motivation of this paper is to prepare novel design of near-field probes using three dimensional laser lithography. We focused on design and fabrication of metal-dielectric nanocones and nanopyramids. The nanoprobes based on IP-Dip polymer and coated by gold were theoretically proposed and experimentally verified in different geometries. Simulated and measured near-field profiles document well resolutions and favor prepared nanoprobes for fully integration on optical fiber as a final probes for highly resolved near-filed imaging.

Keywords: Near-field probes, 3D laser lithography, IP-Dip polymer.

1. Introduction

The subwavelength confined and enhanced optical fields push the limits in optical characterization, manipulation and processing on the nanometer scale. Also characterization of the optical field on the subwavelength nanoscale still remains a challenge. Near-field analysis was successfully used in some special cases how to resolve subwavelength radiation sources and nanoantennas [1]. There were presented many of original concepts of near-field probes attacking the tenths of nanometers resolution [2-4]. Near-field probes are key element of the near-field microscopy achieving subwavelength resolution of optical fields. Their quality and optical imaging depends on the resolution of the near-field probe. Majority of these probes is based on metal-dielectric interface and mostly they were prepared or integrated at the facet or end of optical fibers [3, 4]. The unique properties of metal-dielectric nanoprobes are caused by resonant properties of conductive nanosystems due to the surface plasmon polaritons arising at metal-dielectric interface [5].

Generally, the motivation to prepare novel design of near-field probes increases especially by introducing submicrometer three dimensional (3D) lithography. The experiences with the 3D fabrication of submicrometer structures we used for development of different nanoprobes, especially focused on the nanocones (NC's) and nanopyramids (NP's). The nanoprobes based on IP-Dip polymer and coated by gold were theoretically proposed and experimentally verified in different geometries.

2. Experimental and Results

We focused on the fabrication of two basic types of nanostructures: i) nanocones and ii) nanopyramids. Nanostructures for probes were designed as the metal-dielectric NC's and NP's with base of 10 μm and different height of 5 and 6 μm. Dielectric part consists of IP-Dip polymer (n = 1.52 at 780 nm unexposed) and the metallic gold layer. For the fabrication of the nanostructures, we used a commercial 3D laser lithography system Photonic Professional GT from Nanoscribe GmbH working on principle of two-photon absorption in the volume of polymer. High quality NC's and NP's were prepared and documented by scanning electron microscope (SEM) (Fig. 1).

A series of simulations of a NP's and NC's of 5 μm height show strongly focused radiation from the tip of NC's and NP's (Fig. 2) if they are excited by different wavelengths of 420 nm, 530 nm and 625 nm.

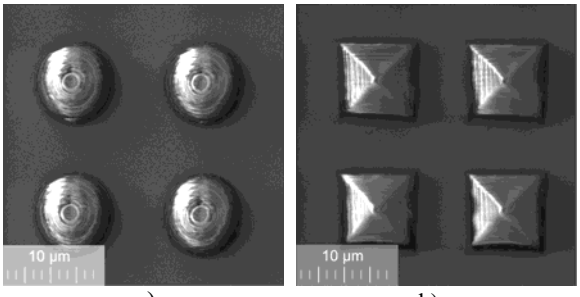

a) b)

Fig. 1. SEM images of metal coated a) NC's and b) NP's.

The circular symmetry of the NC causes weak halo effect that is more blurred with increasing wavelength of radiation. The edges of the NP result in a diffraction effect, which generally reduces the focus of radiation above the tip of the NP.

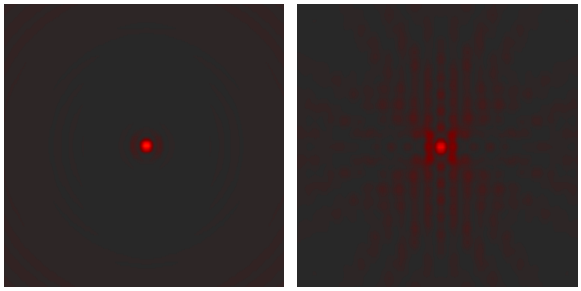

a) b)

Fig. 2. Simulated near-field intensity 8x8 μm^2 of a) NC, and b) NP, excited by wavelength of 530 nm.

Fig. 3 summarizes profiles of 5 μm high NC from the point of near-field intensity and the resolution calculated as Full width at half maximum (FWHM). Near-field intensity shows considerable increase of the signal for the excitation wavelength of 625 nm in comparison to the 420 nm. The FWHM is significantly smaller just for the 420 nm excitation wavelength and achieves only 195 nm.

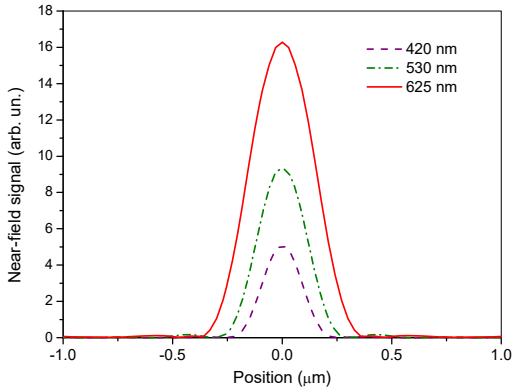

Fig. 3. Simulation of near-field profiles for 5 μm high NC at different excitation wavelengths.

The measured near field of NC shows narrow emission with FWHM of 470 nm. The NC produces nearly app. 37 time intensity increasing in the tip of the NC. Effect of the excitation wavelength was investigated at different wavelengths 625, 530 and 420 nm. The longer wavelengths extend the FWHM as is documented in the measured near-field profile (Fig. 4).

4. Conclusions

We presented new concept in fabrication of near-field probes based on 3D laser lithography. We proposed two main designs based on nanopyramide and nanocone structure prepared from IP-Dip polymer and coated with thin gold layer. The near-field emission was simulated and measured by near-field scanning optical microscope in transmission mode using different excitation wavelengths. The analysis revealed narrow emission from nanocones with FWHM of 470 nm. The obtained results are promising for fabrication of polymer based 3D probes for direct integration on optical fibers.

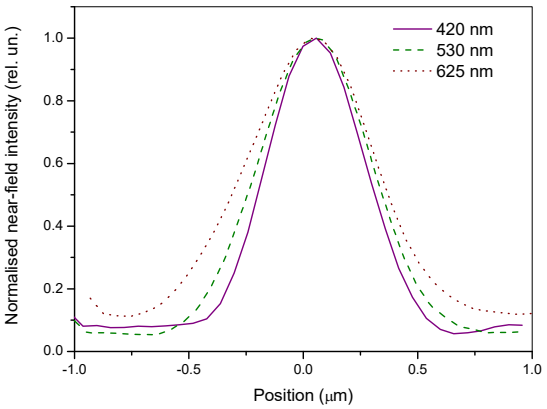

Fig. 4. Normalised near-field profiles of NC excited at different wavelengths.

Acknowledgements

This work was supported by grant agency of Ministry of Education, Science, Research and Sport of the Slovak Republic projects VEGA 1/0677/21, VEGA 1/0363/22, and APVV 20-0264. This publication was realized with support of Operational Program Integrated Infrastructure 2014 - 2020 of the project: Innovative Solutions for Propulsion, Power and Safety Components of Transport Vehicles, code ITMS 313011V334, co-financed by the European Regional Development Fund.

References

[1]. J. N. Farahani et al., Bow-tie optical antenna probes for single-emitter scanning near-field optical microscopy, *Nanotechnology* 18, 125506-1-4 (2007).
[2] S. Kim et al., High external-efficiency nanofocusing for lens-free near-field optical nanoscopy, *Nature Photonics* 13, 636-643 (2019).
[3] I. Kubicova et al., Spatial resolution of apertureless metal-coated fiber tip for NSOM lithography determined by tip-to-tip scan, *Optik* 124, 1971-1973 (2013).
[4] G. Calafiore et al., Campanile Near-Field Probes Fabricated by Nanoimprint Lithography on the Facet of an Optical Fiber, *Scientific Reports* 7, 1651 (2017).
[5] L. Du et al., Mapping plasmonic near-field profiles and interferences by surface-enhanced Raman scattering, *Scientific Reports* 3:3064, 1-6 (2013).

(027)

Application of Transparent Machine Learning Method for Skin Lesions Classification from Multispectral Reflectance Images

D. Bliznuks [1,4], K. Bolochko [1], E. V. Plorina [2,3], A. Lihachev [3,4] and I. Lihacova [3,4]
[1] Riga Technical University, Faculty of Computer Science and Information Technology, Riga, Latvia
[2] Longenesis, LTD, Riga, Latvia
[3] University of Latvia, Institute of Atomic Physics and Spectroscopy, Riga, Latvia
[4] R4U, LTD, Riga, Latvia
E-mail: dmitrijs.bliznuks@rtu.lv

Summary: We propose a transparent machine learning approach for melanoma and nevus classification that can reach high accuracy (97 %) without relying on biophotonic expert knowledge, while also explaining each decision made during the classification process. The proposed approach stands in between empirical/mathematical formulas derived from experts' knowledge and the "black box"-like training of deep neural network models, keeping the best from each. The paper presents a random forest classifier, trained on 140 histologically approved lesions with explanations of extracted non-trivial classification factors (skin vs lesion diffusion properties) and classification decisions. Since the proposed solution can define each feature's importance, it could be further applied for other lesion classifications where it is hard to define exact skin chromophores and develop mathematical formulas for diagnostics.

Keywords: Random forest, Melanoma, Multispectral imaging, Machine learning, Automatic diagnostics.

1. Introduction

Melanoma is a melanocytic tumor that is responsible for most skin cancer-related deaths. By contrast, melanocytic nevi is a very common benign lesion with a clinical picture that frequently may resemble melanoma. Although melanocytic nevi are benign, it is frequently mistakenly suspected as a malignant lesion during visual diagnostics, leading to unnecessary and painful excision. In our previous studies, a multispectral imaging approach using three narrow-band reflectance images for melanoma differentiation from nevus was developed [1, 2]. The diagnostics parameter p' was created, which was empirically defined as a combination of skin formation and the surrounding healthy skin reflection intensities, multiplied by certain coefficients. Reflectance images obtained at narrow spectral bands represent the relative absorption of skin hemoglobin (526 nm, further defined as G), melanin (663 nm, further defined as R), and water (964 nm, further defined as IR) within the skin. Since p' formula coefficients were defined empirically there might be better classification formula. In the previous studies, we concluded that the spectral reflectance imaging approach can distinguish malignant melanomas from benign pigmented and vascular pathologies with 94 % sensitivity and 89% specificity by advanced processing of only three specifically selected spectral band images.

The new trends in melanoma detection involve the use of different Artificial Intelligence (AI) methods like Deep Learning for automatic segmentation and classification of malignant lesions [3]. The accuracy of these solutions may range from 74% to 97.5%. However, the main problem of using Deep Learning methods is that it is not clear what features of the images are considered when classifying a lesion. Moreover, it is not possible to see the inner mechanics of a Neural Network and it is considered a "black box", which makes it harder to certify for medical use. There are some examples below with incorrect features used for training (like a marker on the skin), that would lead to an incorrect diagnosis.

To solve a problem of a "black box" so-called Explainable Artificial Intelligence (XAI) methods are used [10]. As seen in Fig. 1, most explainable methods like Decision Trees require prior expert knowledge and still have low performance due to limitations of expert knowledge, especially in the novel research areas.

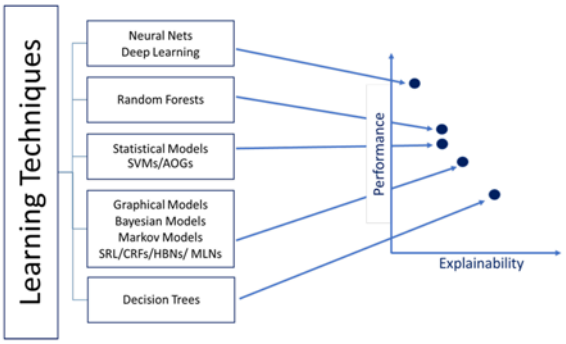

Fig. 1. Performance and Explainability relation of AI methods [10].

Obviously, it is impossible to provide expert knowledge for every diagnostic/classification task. By using AI methods like Deep Learning it is possible to train the neural model by using only data, without an expert in the respective field of knowledge. The downside of using Deep Learning is the low explainability. In the case of medical diagnostics, it can be crucial when the neural model uses incorrect features for training.

To overcome this issue, the XAI uses different methods to understand certain decisions obtained from the neural model. One of the methods [9] is Saliency maps (Fig. 2).

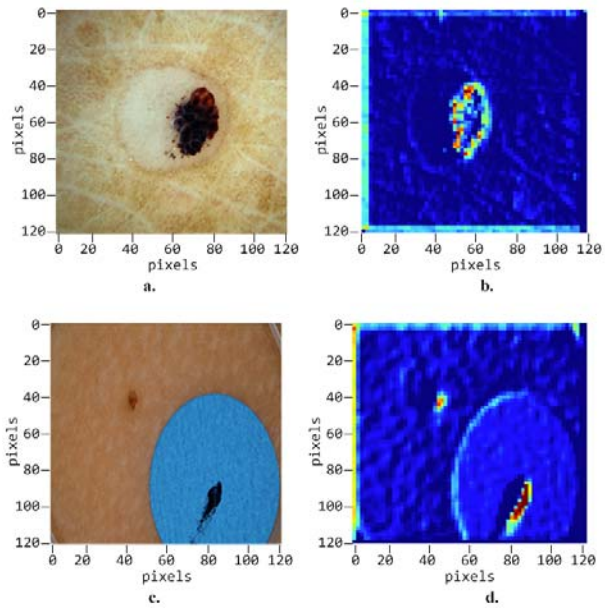

Fig. 2. Saliency map of DL model for classifying skin lesions, 'a.' and 'c.' original skin images, 'b.' and 'd.' - saliency maps, where red color defines high significance on classification and blue - low [8]

In Fig. 2b neural model correctly used pigmented part of the lesion for classification. Whereas on the lower right corner of Fig. 2d Saliency map, the region inside the marker is used to make a diagnostic decision. Therefore such a network can incorrectly classify lesions based only on the marker that was used by a clinician to mark suspicious lesions. Moreover, a Saliency map cannot always provide obvious proof of the correct usage of features (Fig. 3).

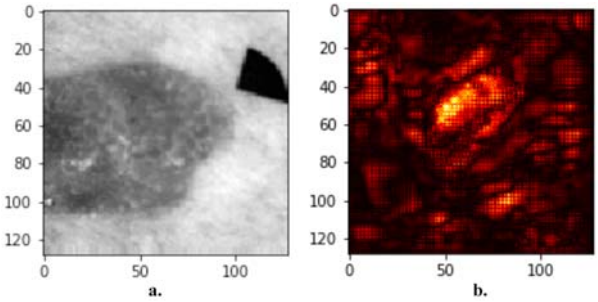

Fig. 3. Original skin lesion image (a) and Saliency map (b) from neural model [8].

By using the saliency map from Fig. 3b it is not possible to unambiguously define the correctness of the neural model. Active regions are unevenly spread inside the lesion as well as on the skin. It might define that texture is used to make classification decisions or just usage of incorrect random areas that are not important for classification.

Shallow methods of Machine Learning, like random forests [4] allow reaching both goals: training automatic classifiers without expert knowledge and allowing explaining automatic decisions for each sample. Additionally, shallow methods may reveal previously unknown features that are used for classifying the lesion as malignant melanoma.

We propose a random forest approach that allows reaching 97 % precision for classifying melanoma (C43) and nevus (D22) on the dataset of 140 real patients' lesions that were histologically approved. Moreover, we prove that the trained model is using meaningful skin features – chromophores. In the next section, we explain the random forest approach and explain the biophotonic meaning of each decision step made by the classification algorithm.

2. Methodology

Random forest [5] - is an ensemble learning method for classification that consists of a multitude of decision trees. The decision tree is a hierarchical structure that is built using the features of a data set. Each node of the decision tree is split according to a measure associated with a subset of the features [6].

The training data consisted of multispectral images containing nevus (D22), melanoma (C43), and skin (SKIN), where each pixel has a certain intensity value. From these intensity values, a total number of 32 features was obtained, where each feature represents a different relation between the selected pixel intensities and means intensities of pixels that belong to the skin in all three spectrums. The accuracy of the classifier depends on the so-called depth of amount of trees and the depth of the classification tree, where each branch of a tree defines the class with a certain probability. To reach 97 % accuracy we used 100 trees with a depth of 8. Train dataset consisted of 80 melanomas and nevi, 40 for validation, and 20 for the test set, with a 50/50 balance of melanoma and nevi. The skin class was on each image taking from 50 % to 80 % of the image area.

After training a random forest classifier it was determined that a total of 5 features is enough to perform reliable classification. Features included the following lesion and skin values: G/R/IR - specific pixel's intensity value in the specific spectral band. SG - average skin intensity value in green spectral band. MEAN_SKIN - average skin value through all spectral skin bands. Fig. 4 shows the visual graph describing each feature's importance.

The most important feature is G/SG which allows separating most of the samples into 3 classes. IR/MEAN_SKIN looks for deeply penetrated lesions that most often lead to late-stage melanoma. As compared to other factors, this is the most specific diagnostics.

Since Random Forest consists of a large number of separate decision trees, it might be difficult to depict all trees on paper. Therefore, we extracted one decision tree with a maximum depth of 8 (Fig. 7) and explained

all the decision steps from a biophotonics point of view. Even with one single tree, the accuracy is more than 94 %.

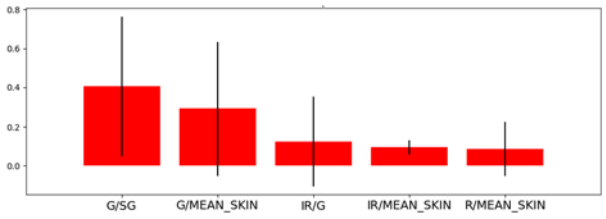

Fig. 4. Feature importance.

On the Fig. 5 confusion matrix is shown for that single tree. Since trained model can define class for each input pixel, matrix can be treated as segmentation quality metric. True label for each pixel was determined by actual lesion class. Since we do not have segmentation of melanocytic region inside each lesion, we cannot calculate Dice Coefficient.

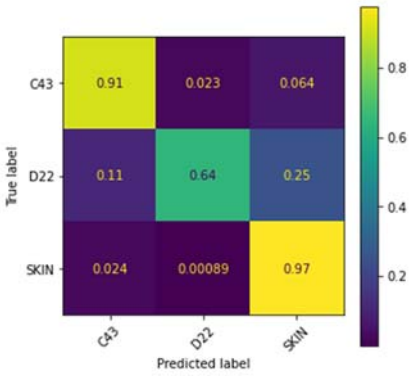

Fig. 5. Confusion matrix per pixel classification (segmentation).

Since the classifier was trained to define the class (nevus, melanoma, and skin) for each pixel, it is possible not only to classify lesions but also to segment the whole skin image. Fig. 6 shows one test image with melanoma regions marked with red, skin with blue, nevi - green and marker (required by clinicians) as black. True histology result is melanoma (C43).

In the center of figure 6 green color appears (class D22), it was approved by dermatologist, that certain areas, similar as marked with green, do not contain melanocytes. Since that lesion area is pigmented, classifier treated them as nevi and not skin that normally is not pigmented.

Total accuracy score of the decision tree is 94.88 % with F1 score value for all classes 86.34 % and weighted F1 score value 94.80 %. Lower scores of per pixel classification are due to some noises around the marker in the original images, as well as the fact that melanoma images may contain values within the lesion that are not melanocytic, as shown in Fig. 6.

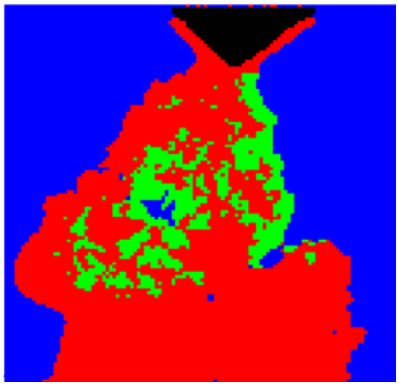

Fig. 6. Processed lesion image with per pixel classification performed (skin – blue, melanoma – red, nevus – green, marker – black is ignored).

Since the main task is to classify the lesion, we used a threshold of 5 % of malignant pixels on the whole image. The resulting accuracy reached 100 % on the test dataset, however, the test dataset was not big enough (10 melanomas and 10 nevi) to make a reliable validation. The larger dataset with multiple cross-validations should be used in future to establish the precise threshold for malignant pixels per image classification.

To check if model's decisions can be described from biophotonic point of view, we will review one tree (Fig. 7), where each branch classifies the data according to the color code, skin class is depicted by purple tones, melanoma class is depicted by orange tones and nevus is depicted by green tones.

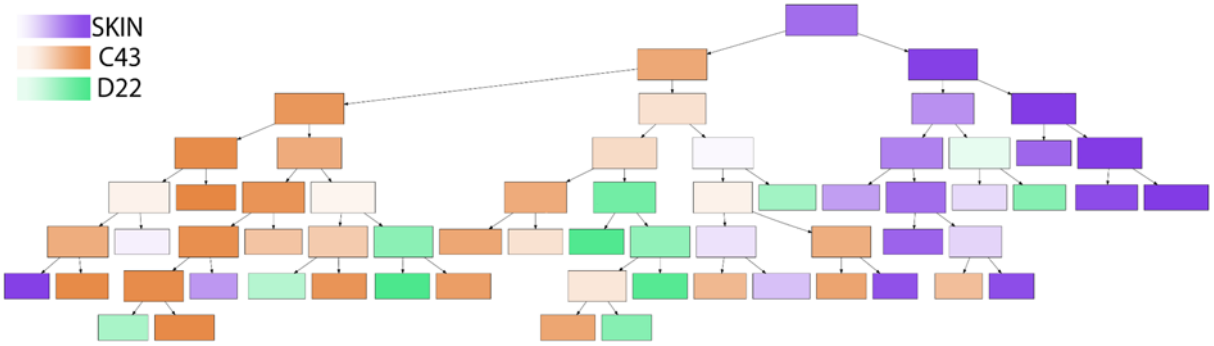

Fig. 7. Extracted one Full Decision Tree from Random Forest lesion classifier.

In every node the decision tree compares one of the features (skin/lesion intensities) to a certain threshold. If the feature is greater than the threshold, the right branch of the tree is considered. If the value is less or equal to the threshold, the left branch of the tree is used. However, some branches lead to redundant classification, while other branches may contain a rule of classification that is based on noise, and, therefore, should not be taken into consideration.

Fig. 8 shows an example of classification redundancy (the rightmost branch of the full decision tree). As can be seen from this example, the branching anyway leads to classifying the data as the skin class, so the best course of action would be to cut the branches of the decision tree that lead to the same classification.

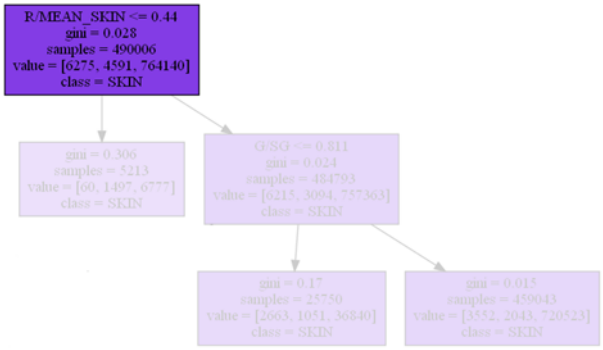

Fig. 8. Example of classification redundancy.

In addition to data redundancy the tree may also be affected by image noise. In this case, the branch considers two classes, however, one class contains a very small number of samples, while the total sample count at the start of the redundant branch is a lot larger. This can be considered an outlier and should not be taken into consideration.

After careful consideration of the tree structure, it can be concluded that the tree may be optimized and reduced, without severely impacting the precision of the classification. Fig. 9 shows the optimized decision tree.

Based on the classification results, we see distinct patterns in clustering samples based on their biophotonic properties. The decision tree divides all samples into three sections: the left section results in classifying most of the values as malign melanoma (C43 - red background), the right section results in classifying most values as skin (SKIN - blue background), while the middle section results in differentiating between all three possible classes, including benign lesion (D22 - green background).

In general, data obtained from random forest classifiers could be characterized as finding hyperpigmented and invasive lesions. At stage Nr.1 the classifier divides lesions into two groups by analysis of G/SG ratio representing pronounced absorption of skin hemoglobin and melanin. At this stage examined images are divided into groups of a) hyperpigmented and highly vascularized lesions and b) lesions with relatively low melanin concentration. Thus, the further classification at steps 2 and 3 will differentiate lesions with low melanin concentration, excluding pigmented melanomas. At steps Nr.4 and Nr.5 the value of high hemoglobin and melanin absorption obtained from lesions divided to the values of surrounding skin obtained at the green and red bands, where infrared is intended to exclude water and hemoglobin absorption. At step Nr.6 (IR/G) the division of lesion reflectance at infrared to the lesion reflection at green will highlight the relative amount of melanin. Since the absorption of hemoglobin in green in comparison to infrared is several orders of magnitude higher. Also should mention the most accurate indicator (IR/Mean_skin) representing the ratio of lesion infrared reflection divided to the skin mean of all reflection bands. The mean reflectance of melanomas in the VIS-NIR range is lower in comparison with nevi.

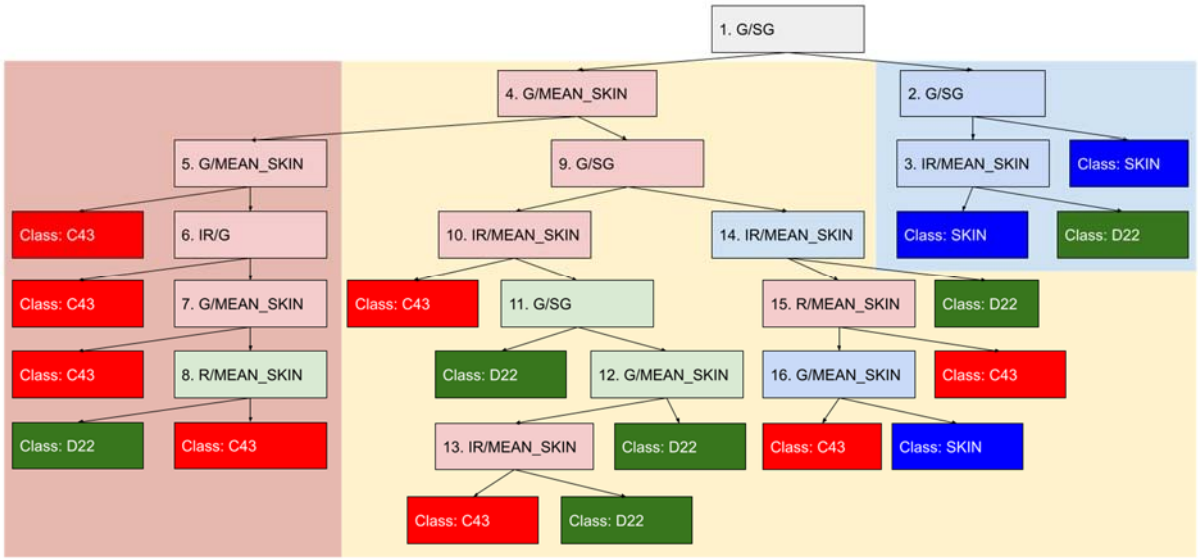

Fig. 9. Optimized Decision Tree from Random Forest lesion classifier.

This corresponds to deeper penetration of optical radiation into the tissues serving information about deeper structures, which could significantly differ between nevi and melanomas. Which apparently demonstrates the presence of melanin and structural changes in the skin's deeper layers. This automatic classifier confirms the recently obtained correlation between melanoma invasion depth and their reflection intensity under infrared illumination [7]. To summarize, the random forest method in the analysis of multispectral reflectance images demonstrates quite logical decisions correlated with skin optical properties.

4. Conclusions

Proposed approach is transparent and comprehensible and therefore may provide additional knowledge about the relations of skin chromophores. This, in turn, reveals a possibility to create accurate machine learning diagnostic algorithms for lesions with unknown biophotonic properties. By using feature importance it is possible to define which spectral bands are most important for diagnostics of specific disease. Future research will test additional spectral bands, including autofluorescence under ultraviolet illumination that would allow distinguish melanoma from seborrheic keratosis. As well as cross validation should be used to approve the high result of lesion classification.

Acknowledgements

This research is funded by the European Regional Development Fund project “Rare skin diseases efficient identification and multi-modal diagnostic system” (agreement No.1.1.1.1/20/A/072) and “Portable Device for Non-contact Early Diagnostics of Skin Cancer (1.1.1.1/16/A/197)”.

References

[1]. I. Diebele, I. Kuzmina, A. Lihachev, J. Kapostinsh, A. Derjabo, L. Valeine, J. Spigulis, Clinical evaluation of melanomas and common nevi by spectral imaging, *Biomed. Opt. Express*, Vol. 3, 2012, pp. 467-472.

[2]. I. Lihacova, K. Bolochko, E. V. Plorina, M. Lange, A. Lihachev, D. Bliznuks, A. Derjabo, A method for skin malformation classification by combining multispectral and skin autofluorescence imaging, *Proc SPIE,* Vol. 10685, 2018, 1068535.

[3]. D. Popescu, M. El-Khatib, H. El-Khatib, L. Ichim, New Trends in Melanoma Detection Using Neural Networks: A Systematic Review, *Sensors*, Vol. 22, 2022, pp. 496.

[4]. S. Chauhan, L. Vig, M. De Filippo De Grazia, M. Corbetta, S. Ahmad, M. Zorzi, A Comparison of Shallow and Deep Learning Methods for Predicting Cognitive Performance of Stroke Patients From MRI Lesion Images, *Frontiers in Neuroinformatics*, Vol. 13, 53, 2019.

[5]. S. Suthaharan, A Cognitive Random Forest: An Intra- and Intercognitive Computing for Big Data Classification Under Cune Condition, in Handbook of Statistics 35, *Elsevier*, Ch. 6., 2016, pp. 207-227.

[6]. A. Navada, A. N. Ansari, S. Patil, B. A. Sonkamble, Overview of use of decision tree algorithms in machine learning, in *Proceedings of the IEEE Control and System Graduate Research Colloquium*, 2011, pp. 37-42.

[7]. S. Bozsányi, N. N. Varga, K. Farkas, A. Bánvölgyi, K. Lőrincz, I. Lihacova, A. Lihachev, E. V. Plorina, Á. Bartha, A. Jobbágy, E. Kuroli, G. Paragh, P. Holló, M. Medvecz, N. Kiss, N. M. Wikonkál, Multispectral Imaging Algorithm Predicts Breslow Thickness of Melanoma. *J. Clin. Med*., Vol. 11, 2022, pp. 189.

[8]. Dmitrijs Bliznuks, Evija Cibulska, Andrey Bondarenko, Yuriy Chizhov, and Ilze Lihacova, Deep learning model deploying on embedded skin cancer diagnostic device, *Proc. SPIE 11585, Biophotonics - Riga 2020*, 115850D, 2020.

[9]. Lapuschkin, S., Wäldchen, S., Binder, A. et al., Unmasking Clever Hans predictors and assessing what machines really learn, *Nat Commun,* 10, 2019, 1096.

[10]. A. Rawal, J. Mccoy, D. Rawat, B. Sadler and R. Amant, Recent Advances in Trustworthy Explainable Artificial Intelligence: Status, Challenges and Perspectives, *IEEE Transactions on Artificial Intelligence*, in print.

(029)

Single SiGe Quantum Dot Coupled to Bichromatic Photonic Crystal Cavities for Potential Applications as Single Telecom Photon Emitters

Thanavorn Poempool [1], Johannes Aberl [1], Marco Clementi [2], Lukas Spindlberger [1], Lada Vukušić [1], Matteo Galli [2], Dario Gerace [2], Friedrich Schäffler [1], Moritz Brehm [1] and Thomas Fromherz [1]

[1] Institute of Semiconductor and Solid State Physics, Johannes Kepler University, A-4040 Linz, Austria
[2] Department of Physics, University of Pavia, 27100 Pavia, Italy
Tel.: +43 732 2468 9602, fax: +43 732 2468 8650
E-mail: thanavorn.poempool@jku.at, thomas.fromherz@jku.at

Summary: To realize scalable, Si-based quantum information technology, CMOS compatible sources controllable on the single-photon level are required. Despite their small radiative efficiencies limited by staggered band alignment, SiGe QDs are promising candidates for such sources due to their telecom-wavelength emission. By deterministically positioning a SiGe QD into a Bichromatic cavity, thanks to its theoretically high-Q factor and small mode volume, the resonant modes emission is strongly enhanced by the Purcell effect. Photoluminescence spectra clearly show cavity-enhanced single QD emission. In addition, preliminary results on recombination and excited state lifetime of the cavity-enhanced QD emission will be reported.

Keywords: SiGe quantum dot, Bichromatic potential, Photonic crystal cavity.

1. Introduction

The search for light emitters, monolithically integrable with Si state-of-the-art electronics, has driven Si photonics research during the last decades. For the realization of scalable, Si-based quantum information technology, CMOS compatible sources controllable on the single-photon level are required. Solid-state quantum dots (QDs) have been shown to be excellently suited for the realization of single-photon emitters [1].

In Si/SiGe system, the indirect bandgap of the bulk materials in combination with the spatial separation of electron and hole in QD states results in long radiative lifetimes and low emission efficiencies [2]. However, perfect control over the QD nucleation site can be achieved in this material system [3] and allows to deterministically Purcell-enhance these efficiencies by QD-aligned photonic crystal cavity (PhC) [4].

2. Experiments and Results

We successfully optimize SiGe QD growth by molecular beam epitaxy to achieve a single QD (SQD) nucleated into a pre-patterned single pit (SP) on SOI substrate (see Fig. 1(a) AFM image). The SP is defined by e-beam lithography together with alignment marks. Aligned to these marks, a PhC centered to the SQD was then patterned onto the existing capped SQD (see Fig. 1(b), showing the PhC and the SQD in an uncapped sample). Here, we implement a bichromatic cavity [5], offering high-Q factors and small mode volume by straightforward design rules and, in addition, allowing a controlled trade-off between high Q-factor and far-field (ff) coupling efficiency [6]. The radiation efficiency is enhanced by such PhC plus the ff optimization, and the observed resonant spectrum shows an intense emission at ~1336 nm wavelength that can be assigned to the SQD emission as shown in the blue line in Fig. 1(c).

The Q-factor, as measured by resonant scattering [5] for this cavity containing the SQD emitter, accounts for as much as ~53,600 and it is limited by the designed ff coupling. Without the cavity perturbation of the ff optimization, a Q-factor as highest as ~104,000 is demonstrated. This value represents the highest so far reported for an SOI-based photonic crystal cavity containing a SiGe QD at its center.

For the resonant SQD emission mode M0, we determine a thermal activation energy of ~160 meV, much larger than observed for the higher-order modes, i.e., M3, which reads ~40 meV as shown in Fig. 2(a). Moreover, the PL mode intensity is measured in dependence of the PL excitation power, and the results are fitted to the empirical power law $I_{PL} \propto P_{exc}^{m}$, where I_{PL} is the integrated PL intensity, P_{exc} is excitation power. As depicted in Fig. 2(b), for the mode M0, the fitting reveals a linear dependence (*m~1.08)* at low excitation power and becomes sub-linear (*m~0.64*) at higher excitation. These exponent values indicate direct recombination of electrons and holes and direct competition between Auger- and non-radiative recombination that is limiting the QD emission efficiency, respectively. For all other modes shown in Fig. 1, this typical QD behavior of the PL intensity on the excitation power is absent, pointing to optical wetting layer transitions as the source for the M1-M4 mode emission, in agreement with the small activation energies observed for them.

Fig. 2(c) shows a semi-logarithmic plot of time-resolved PL measured at 10 K and recorded under a 5 MHz repetition rate with an above-band excitation of 442 nm excitation laser (130 ps pulse width). A single

exponential decay is observed for the average excitation power of 5 µW. The decay time of ~4 ns can be obtained.

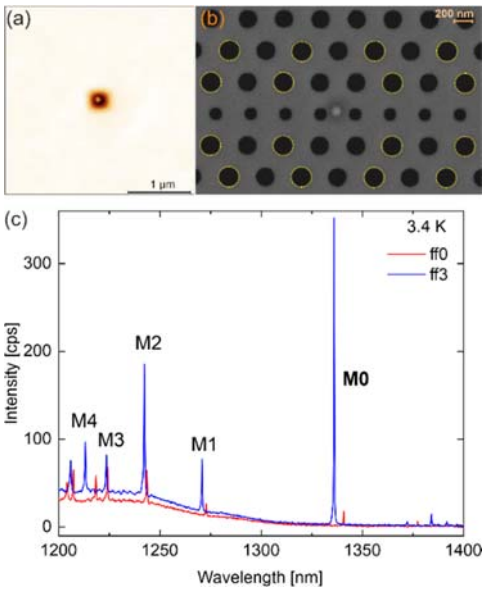

Fig. 1. (a) 3x3 µm² AFM image of uncapped SQD nucleated onto the defined SP; (b) Bichromatic photonic crystal cavity and far-field optimization pattern (yellow circles); (c) Resonance modes are characterized from µ-PL.

5. Conclusions

Our results demonstrate the high relevance of the single SiGe QD coupled to the high-Q cavity for applications such as sources for Si integrated optics and quantum light sources in the telecom wavelength range.

Acknowledgments

(1) Project CUSPIDOR that has received funding from the QuantERA ERA-NET co-fund in Quantum Technologies implemented within the European Union's Horizon 2020, (2) the Austrian Science Foundation FWF under Projects I 3760-N27, FWF_30564NBL (co-founded by the province of Upper Austra), Y1238-N36, and (3) the Linz Institute of Technology (LIT): Grant No. LIT-2019-7-SEE-114.

References

[1]. P. Senellart, *et al*., High-performance semiconductor quantum-dot single-photon sources, *Nature Nanotech*, 12, 2017, pp. 1026–1039.
[2]. L. Tsybeskov, *et al.*, Silicon-Germanium Nano-structures for Light Emitters and On-Chip Optical Interconnects, *Proc. IEEE*, 97, 2009, pp. 1284-1303.
[3]. M. Brehm, *et al.*, Site-controlled and advanced epitaxial Ge/Si quantum dots: fabrication, properties, and applications, Nanotechnology 28, 2017, 392001.
[4]. M. Schatzl, *et al.*, Enhanced Telecom Emission from Single Group-IV Quantum Dots by Precise CMOS-Compatible Positioning in Photonic Crystal Cavities, *ACS Photonics,* 4, 2017, 665.
[5]. A. Simbula, *et al.*, Realization of high-Q/V photonic crystal cavities defined by an effective Aubry-André-Harper bichromatic potential, *APL Photonics*, 2, 2017, 056102.
[6]. S. L. Portalupi, *et al.*, Planar photonic crystal cavities with far-field optimization for high coupling efficiency and quality factor, *Opt. Express*, 18, 2010, pp. 16064–16073 ().
[7]. M. Galli, *et al.*, Light scattering and Fano resonances in high-*Q* photonic crystal nanocavities, *Appl. Phys. Lett.,* 94, 2009, 071101.

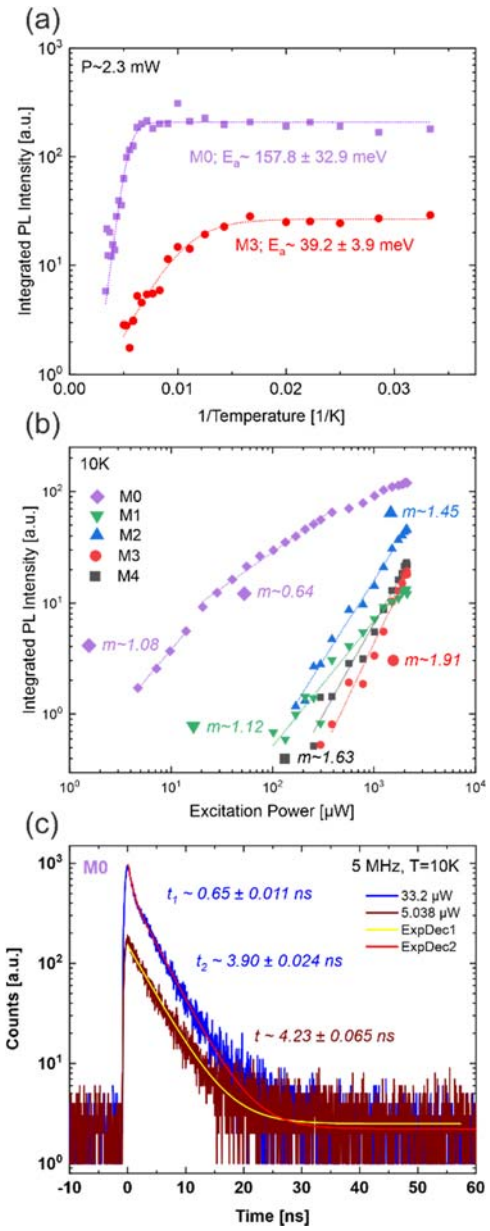

Fig. 2. (a) Arrhenius plot of the modes M0 and M3; (b) Power dependence measurement and their extracted *m* component in the empirical power law; (c) Dynamic decay times of the M0 under different average excitation pulsed intensities.

(030)

Propagation of Azimuthally Polarized Bessel-Gaussian Beam through Helical Axicon

Ibrahim G. H. Loqman [1], Abdu A. Alkelly [1*] and Hassan T. Alahsab [1, 2]
[1] Physics Department, Faculty of Science, Sana'a University, Sana'a, Yemen
[2] Physics Department, Faculty of Applied Science, Dhamar University, Dhamar, Yemen
Tel.: +9677776267057
E-mail: aa_alkelly@yahoo.com

Summary: Propagation properties of azimuthally polarized Bessel-Gaussian (APBG) beams with non-zero order through a helical axicon (HA) are theoretically investigated. The formula of APBG beams field in the focal region are derived by the vector diffraction theory. Numerical results illustrate that the beam and axicon parameters affect the intensity distribution in the focal region very considerably. Super--long transversely polarized focal depth with different shapes are obtained by choosing appropriate values of parameters. We also observed that a focal shift occurs which depends on both axicon parameter and numerical aperture. We expect that focusing APBG beams by HA can be used in optical trapping.

Keywords: Bessel-Gaussian beam, Azimuthal polarization, Helical axicon, Vector diffraction theory.

1. Introduction

A helical axicon is a hybrid of a spiral phase plate, that is an optical element whose thickness increases azimuthally, and of an axicon [1]. It has attracted researchers interest due to its unique characteristics and different applications. It is shown that the helical axicon (HA) can be used to transform Gaussian beam and a plane wave into a vortex beam [2, 3]. The HA also has been used to generate Bessel-Gaussian beams of arbitrary order [4], spiraling Bessel beams with adjustable topological charges from Laguerre-Gaussian beam [5], vortex beams [6, 7] and non-diffracting Bessel beam by conversion high-order Laguerre-Gaussian beam [8]. It is found that the topological charge and axicon parameter can alter the focal pattern in the focal region [9, 10]. A general approximate analytical expressions of the Fresnel diff-raction of Laguerre–Bessel–Gaussian beam by the HA has been derived analytically based on the stationary phase method [11].

Last decades, high order Bessel–Gaussian beams that propagate with stability in both size and intensity have attracted lots of researchers attentions due to their extraordinary properties. Such class of beams propagate without divergence, carrying orbital angular momentum with a helical phase fronts and have the property of self-healing [12 - 15]. These properties have propitiated their application in optical trapping [16, 17], optics communication [18] and generating perfect optical vortices [19]. Recently, focusing of polarized Bessel-Gaussian beams which have either pure azimuthal or pure radial polarization had been studied extensively. A needle of strong longitudinal polarized field with long depth of focus and strong intensity has been obtained by focusing a radially polarized Bessel–Gaussian beams with a high numerical aperture lens and a diffractive optical element [20]. In [21], X. Gao *et. al.* have investigated focusing properties of Bessel–Gaussian beam with radial varying polarization detail. The same group, also, studied the focus shaping of the radially polarized Bessel–Gaussian beam with a sine-azimuthal variation wavefront [22]. Multiple intensity rings, dark hollow have been generated by focusing radial varying polarized Bessel–Gaussian beam with radial phase modulation [14]. It is found that radially polarized laser beams have small focuses and non-propagating longitudinal field components; while azimuthally polarized beams have hollow intensity distributions form [17].

By taking into account the fact that focusing Bessel–Gaussian beams are very important in many applications such as optical trapping [17] and the properties of the HA. To the best of our knowledge, the propagation properties of APBG beam through the HA are investigated for the first time in this work. The propagation properties of focused APBG beams such as depth of focus (DOF) and the full width at half maximum (FWHM) by a linear axicon, that is a special case of the HA when the topological charge of a HA p = 0, are also studied. The theoretical model is introduced in section 2. The numerical results are discussed in section 3. In section 4 the conclusion of results is shown.

2. Theoretical Model

The electric field of the APBG beam $E(\rho,\phi)$, in cylinderical coordinate system (ρ,ϕ,z), at the source plane can be given by

$$E(\rho,\phi) = E(\rho,\phi)\boldsymbol{e_\phi}, \tag{1}$$

where $\boldsymbol{e_\phi}$ is the azimuthal unit vector of the polarized direction and $E(\rho,\phi)$ is the electric field of Bessel-Gaussian beam that is given by [23]

$$E(\rho,\phi) = J_1(\beta\rho)\exp\left(-\frac{\rho^2}{w_0^2}\right)\exp(i\phi), \quad (2)$$

where J_1 is the Bessel function of the first kind of order 1 which is the topological charge of the optical vortex, β is the transverse wave number that indicates the quickness of the fluctuation of Bessel function and w_0 is the beam width. The transmittance of the HA is defined as [6]

$$T = \exp(i\alpha\rho + ip\phi), \quad (3)$$

where α is the axicon parameter that shows the axicon strength and $p = 0, \pm1, \pm2, \ldots$ is a topological charge of the HA. Based on the variable transformation Eq.3 can be rewritten as [9, 10]:

$$T = \exp\left[i\alpha\rho_b\frac{\rho}{\rho_b} + ip\phi\right] = \exp\left[i\alpha\rho_b\frac{\rho}{\rho_b} + ip\phi\right] = \exp\left[i\eta\frac{\sin\theta}{NA} + ip\phi\right] \quad (4)$$

where $\eta = \alpha\rho_b$ is the dimensionless axicon parameter, NA is the numerical aperture and θ is the tangential angle with respect to the optical axis as shown in Fig. 1.

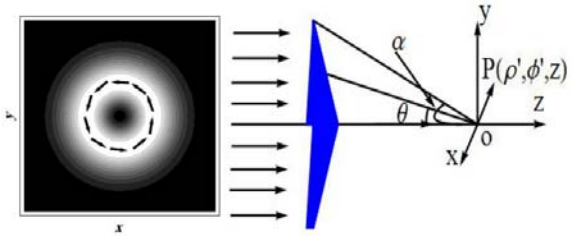

Fig. 1. Scheme for a azimuthally polarized Bessel-Gaussian beam focused by helical axicon.

According to vector diffraction theory, the electric field of APBG beam focused by HA is [24, 25]:

$$\boldsymbol{E}(\rho',\phi',z) = E_{\rho'}\boldsymbol{e_{\rho'}} + E_{\phi'}\boldsymbol{e_{\phi'}} + E_z\boldsymbol{e_z}, \quad (5)$$

where $\boldsymbol{e_{\rho'}}, \boldsymbol{e_{\phi'}}$ and $\boldsymbol{e_z}$ are the radial, azimuthal, and longitudinal unit vectors, respectively. The amplitudes of the three orthogonal components $E_{\rho'}, E_{\phi'}$ and E_z in the focal region are given by

$$\begin{pmatrix} E_{\rho'}(\rho',\phi',z) \\ E_{\phi'}(\rho',\phi',z) \\ E_z(\rho',\phi',z) \end{pmatrix} = -\frac{iA}{\pi}\int_0^{\alpha}\int_0^{2\pi}\sqrt{\cos\theta}E(\theta,\phi) * T(\theta,\phi)\exp[ik(z\cos\theta + \rho'\sin\theta * \cos(\phi-\phi'))] * \begin{pmatrix} -\sin\theta\sin(\phi-\phi') \\ \sin\theta\cos(\phi-\phi') \\ 0 \end{pmatrix} d\phi d\theta, \quad (6)$$

where k is the wave number, $\alpha = \arcsin(NA)$ is the convergence angle corresponding to the radius of the incident optical aperture. The coordinate system is shown in Fig.1. In order to simplify calculation process, Eq.2 can be expressed as [26, 27]

$$E(\theta,\phi,0) = J_1\left(\frac{2\beta_1 sin\theta}{NA}\right)\exp\left[-\left(\frac{\beta_2 sin\theta}{NA}\right)^2\right]\exp(i\phi), \quad (7)$$

where β_1 and β_2 are the ratios of pupil diameter to the beam diameter.

By substituting Eqs. 4 and 7 into Eq. 6 the three orthogonal component of electric field can be obtained as

$$\begin{pmatrix} E_{\rho'}(\rho',\phi',z) \\ E_{\phi'}(\rho',\phi',z) \\ E_z(\rho',\phi',z) \end{pmatrix} = -\frac{iA}{\pi}\int_0^{\alpha}\int_0^{2\pi}\sqrt{\cos\theta} * \exp\left[-\left(\frac{\beta_2\sin\theta}{NA}\right)^2\right] J_1\left(\frac{2\beta_1\sin\theta}{NA}\right)\exp\left[i\eta\frac{\sin\theta}{NA} + \exp(i(+1)\varphi)\right]\exp[ik(\rho'\sin\theta\cos(\phi-\phi'))] \begin{pmatrix} -\sin\theta\sin(\phi-\phi') \\ \sin\theta\cos(\phi-\phi') \\ 0 \end{pmatrix}\exp[ikzcos\theta]d\phi d\theta. \quad (8)$$

The integration with respect to φ can be accomplished by using the following formula:

$$\int_0^{2\pi}\sin(\phi-\phi')\exp[im\phi + it\cos(\phi-\phi')]d\phi = \pi i^m\exp(im\phi')[J_{m+1}(t) + J_{m-1}(t)], \quad (9)$$

and

$$\int_0^{2\pi}\cos(\phi-\phi')\exp[im\phi + it\cos(\phi-\phi')]d\phi = \pi i^{m+1}\exp(im\phi')[J_{m+1}(t) - J_{m-1}(t)]. \quad (10)$$

Therefore, the orthogonal components of the output electric field are given by:

$$\begin{pmatrix} E_{\rho'}(\rho',\phi',z) \\ E_{\phi'}(\rho',\phi',z) \\ E_z(\rho',\phi',z) \end{pmatrix} = i^p A\exp(i(p+1)\phi') \int_0^{\alpha}\sqrt{\cos\theta}J_1\left(\frac{2\beta_1\sin\theta}{NA}\right)\exp\left[-\left(\frac{\beta_2\sin\theta}{NA}\right)^2 + i\eta\frac{\sin\theta}{NA} + ikzcos\theta\right] \begin{pmatrix} -\sin\theta[J_{p+2}(k\rho'sin\theta) + J_p(k\rho'sin\theta)] \\ i\sin\theta[J_{p+2}(k\rho'sin\theta) - J_p(k\rho'sin\theta)] \\ 0 \end{pmatrix} d\theta. \quad (11)$$

The optical intensity is proportional to the modulus square of Eq. 5.

3. Numerical Calculation and Discussion

In this section some numerical calculation will be carried out in order to obtain the properties of propagation APBG beam through helical axicon depending on Eq. 11. It is noticeable that the integral

over the parameter θ could not accomplished analytically; therefore, the numerical integration will be used. In our calculation, we consider A equal unit one and $\lambda = 632.8\ nm$ and the distance unit in figures in this work is the wavelength of the incident beam in vacuum.

Fig. 2 illustrates the intensity distribution of APBG beam with HA for different axicon parameter $\eta = 0, \eta = 2, \eta = 4, \eta = 6, \eta = -2$ and $\eta = -4$ under condition of $\beta_1 = 2$, $\beta_2 = 1$, $p = 1$, and $NA = 0.95$. This figure shows that the intensity distribution vary with respect to axicon parameter. It is clearly shown that the focal hole shape still constant as the axicon parameter changed and the intensity distribution is symmetry about the z axis. For $\eta = 0$ as it is shown in Fig. 1 (a) the focal region is symmetry about z and its center is at $z = 0$. In addition, it can be seen from Fig. 1 (b-d) the generated focal hole region shifts away from the HA on increasing the positive value of the axicon parameter η. In the other hand, the generated focal hole in the focal region shifts toward the HA on decreasing the negative value the axicon parameter as it is shown in Fig. 1 (e and f) that are for $\eta = -2$ and $\eta = -4$, that indicate focal shift phenomenon occurs that means the movement of the center of focal hole. It can be concluded that different HA different focal hole regions for the same incident beam.

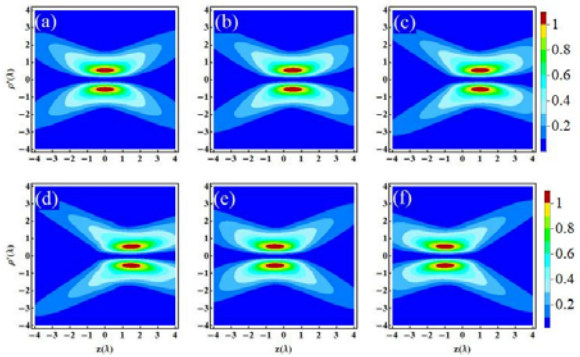

Fig. 2. Intensity distribution of APBG beam with HA under condition $\beta_1 = 2, \beta_2 = 1, p = 1, NA = 0.95$ and (a) $\eta = 0$, (b) $\eta = 2$, (c) $\eta = 4$, (d)$\eta = 6$, (e) $\eta = -2$, (f) $\eta = -4$, respectively.

Fig. 3 exhibits the intensity distribution of APBG beam with a HA for positive and negative different values of topological charge under condition of $\eta = 4$, $\beta_1 = 2$, $\beta_2 = 1$, and $NA = 0.95$. It is shown from Fig.3 (a and f) that the focused APBGB with $p = 0$ and -2 are not hollow and have peaks on the optical axes due to the presence of J_0 that is found in the integrand for both $p = 0$ and -2. In the other hand, the focal hole region is constructed for $p \neq 0$ and -2 as can be seen in Fig. 3 (b, c, d and e). The radius of the focal hole increases as the topological charge either positively increase or negatively decrease. By comparing Fig. 3 (b with e) and Fig. 3 (d with g) it is found that the focal hole region is longer and have smaller radius for negative values of p than positive values. It can be conclude that the HA changes the topological charge of the incident beams and convert it to a non-vortex beam [8,7].

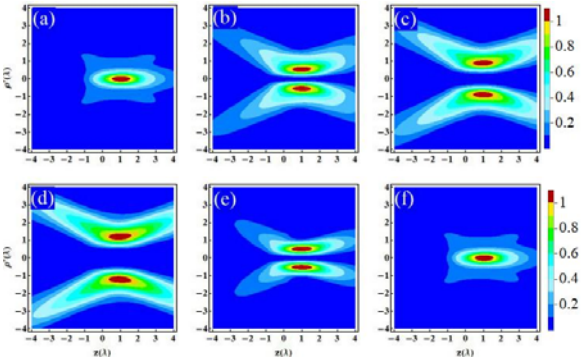

Fig. 3. Intensity distribution of APBG beam with HA under condition $\beta_1 = 2, \beta_2 = 1, \eta = 4, NA = 0.95$ and (a) $p = 0$, (b) $p = 1$, (c) $p = 2$, (d)$p = 3$, (e) $p = -1$ and (f) $p = -2$, respectively.

Now, let the parameters β_1 and β_2 vary to show how the focal hole region change. In Fig. 4 the parameter β_1 increase from 1 to 3.5 for $\beta_2 = 1$ and in Fig. 5 the parameter β_2 increase from 1.5 to 2.5 for $\beta_1 = 3$ the other parameters are $\eta = 2$, $NA = 0.95$, and $p = 1$ for both of them. It is obviously shown that the shape of the focal hole region in these two figures have changed considerably and some novel focal hole patterns are appear including dark hollow focus, multiple intensity ring that can be used to construct optical traps. In addition, the focal hole region shift is not related to the parameters β_1 and β_2 as it is shown from Figs. 3 and 4. In addition, the position of the maximum intensity value change as the values of both parameters β_1 and β_2 change with forming different focal region shapes. Therefore, they can affect the focal pattern considerably and produce some novel focal hole regions that can be used in optical trapping.

The intensity distribution of APBG beams with different values of numerical aperture with $p = 1$ and $p = 0$, that is corresponding to a linear axicon, under condition $\eta = 2$, $\beta_1 = 3$ and $\beta_2 = 3$ are shown in Figs. 6. It can be seen that the intensity distribution in the focal region strongly depend on both the numerical aperture and the topological charge. While a transversely polarized focal hole is formed with $p = 1$ an extended focal spot is formed with $p = 0$. The focal depth considerably extend as the numerical aperture decrease and the focal shift increase, also, that are coincide with our previous work [28]. A super–long focal tube is obtained from focusing APBG beams with small values of numerical aperture. The dependence of both DOF and FWHM of focused APBG beam by a linear axicon on the numerical aperture are illustrated in Fig. 7 under condition of $\eta = 2, \beta_1 = 3, \beta_2 = 3$, and $NA = 0.95$. It is clearly shown that the depth of focus increases considerably

as the NA decreases. The depth of focus equal 48.9λ and 38.6λ for $NA = 0.40$ and $NA = 0.45$, respectively. Moreover, the FWHM is also extend as the numerical aperture decrease.

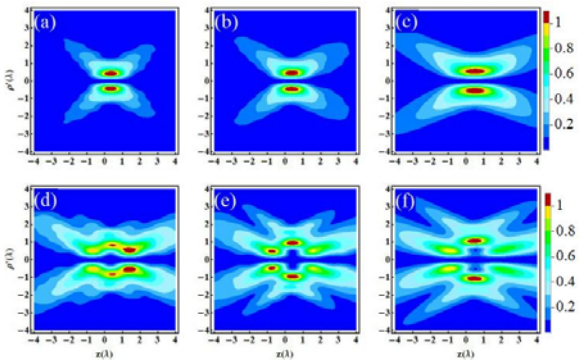

Fig. 4. Intensity distribution of APBG beam with HA under condition $\eta = 2$, $NA = 0.95$, $p = 1$, $\beta_2 = 1$ and (a) $\beta_1 = 1$, (b) $\beta_1 = 1.5$, (c) $\beta_1 = 2$, (d) $\beta_1 = 2.5$, (e)$\beta_1 = 3$, (f) $\beta_1 = 3.5$, respectively.

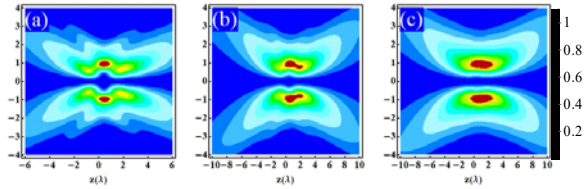

Fig. 5. Intensity distribution of APBG beam with HA under condition $\eta = 4$, $NA = 0.95$ $\beta_1 = 3$ and (a) $\beta_2 = 1.5$, (b) $\beta_2 = 2$, (c) $\beta_2 = 2.5$, respectively.

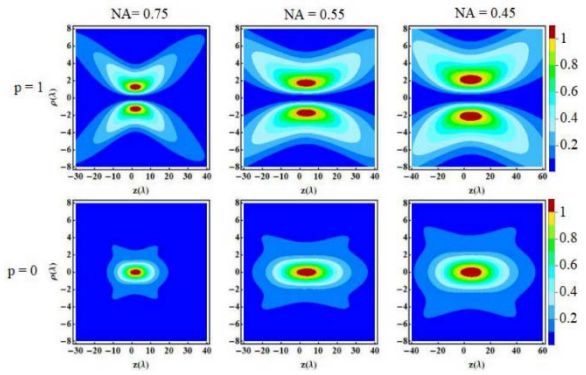

Fig. 6. Intensity distribution of APBG beam with HA under condition $\eta = 2$, $\beta_1 = 3$ and $\beta_2 = 3$ with $p = 0$ and $p = 1$.

4. Conclusions

In summary, by using the vector diffraction theory propagation properties of the azimuthally polarized Bessel-Gaussian beam (APBGB) through helical axicon is numerically investigated. Our numerical results clearly show that the intensity distribution in the focal region of the APBGB can be adjusted considerably by axicon parameter, topological charge of the spiral phase, and beam parameters. A long focal tube has been obtained. We suggest that focusing of APBGB by HA may find application in optical trapping.

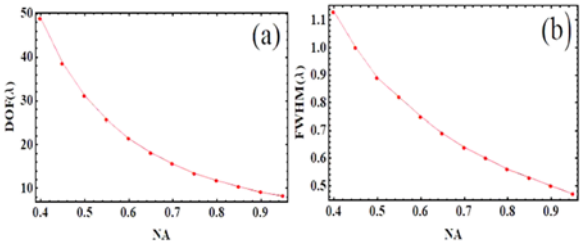

Fig. 7. Depth of focus (DOF) and the full width at half maximum (FWHM) of a focused APBG beam with HA under condition $\eta = 2$, $\beta_1 = 3$, $\beta_2 = 3$ and $p = 0$ that is corresponding to a linear axicon.

References

[1]. S. Khonina, V. Kotlyar, V. Soifer, M. Shinkaryev, G. Uspleniev, Trochoson, *Optics Communications,* Vol. 91, 1992, pp. 158–162.

[2]. V. V. Kotlyar, A. A. Kovalev, R. V. Skidanov, O. Y. Moiseev, V. A. Soifer, Diffraction of a finite-radius plane wave and a Gaussian beam by a helical axicon and a spiral phase plate, *J. Opt. Soc. Am. A*, Vol. 24, Issue 7, 2007, pp. 1955–1964.

[3]. M. Beijersbergen, R. Coerwinkel, M. Kristensen, J. Woerdman. Helical-wavefront laser beams produced with a spiral phaseplate, *Optics Communications,* Vol. 112, 1994, pp. 321–327.

[4]. V. Arrizón, U. Ruiz, D. Aguirre-Olivas, D. Sánchez-de-la Llave, A. S. Ostrovsky, Comparing efficiency and accuracy of the kinoform and the helical axicon as Bessel–Gauss beam generators, *J. Opt. Soc. Am. A*, Vol. 31, Issue 3, 2014, pp. 487–492.

[5]. S. Qiong-Ge, Z. Ke-Ya, F. Guang-Yu, L. Zheng-Jun, L. Shu-Tian, Generalization and propagation of spiraling Bessel beams with a helical axicon, *Chinese Physics B,* Vol. 21, Issue 1, 2012, pp. 014208.

[6]. V. Kotlyar, A. Kovalev, V. Soifer, C. S. Tuvey, J. A. Davis, Sidelobe contrast reduction for optical vortex beams using a helical axicon, *Optics Letters*, Vol. 32, Issue 8, 2007, pp. 921–923.

[7]. S. Topuzoski, L. Janicijevic, Diffraction of Laguerre-Gaussian beam by a helical axicon, *Acta Physica Polonica-Series A General Physics,* Vol. 9, Issue 4, 2009, pp. 557.

[8]. S. Topuzoski, L. Janicijevic, Conversion of high-order laguerre–gaussian beams into Bessel beams of increased, reduced or zeroth order by use of a helical axicon, *Optics Communications,* Vol. 282, Issue 17, 2009, pp. 3426–3432.

[9]. X. Dong, T. Geng, S. Zhuang, Focusing properties of hyperbolic-cosine-Gaussian beams combining a helical axicon, *Optik,* Vol. 124, Issue 18, 2013, pp. 3422–3426.

[10]. G. Wang, Y. Miao, Q. Zhan, G. Sui, R. Zhang, Focusing of linearly polarized Lorentz-Gaussian beam with helical axicon, *Optik,* Vol. 130, Issue 2017, pp. 266–272.

[11]. F. Saad, Z. Hricha, M. Khouilid, A. Belafhal, A theoretical study of the Fresnel diffraction of Laguerre-Bessel-Gaussian beam by a helical axicon, *Optik,* Vol. 149, 2017, pp. 416–422.

[12]. S. Vyas, Y. Kozawa, S. Sato, Self-healing of tightly focused scalar and vector Bessel–Gauss beams at the focal plane, *J. Opt. Soc. Am. A,* Vol. 28, Issue 5, 2011, pp. 837–843.

[13]. S. Zhao, W. Zhang, L. Wang, W. Li, L. Gong, W. Cheng, H. Chen, J. Gruska, Propagation and self-healing properties of Bessel-Gaussian beam carrying orbital angular momentum in an underwater environment, *Scientific Reports,* Vol. 9, Issue 1, 2019, pp. 1–8.

[14]. B. Wu, X. Zeng, Y. Miao, Y. Fan, X. Gao, S. Zhuang, Focal shift of radial varying polarized bessel-gauss beam with radial phase modulation, *Optik,* Vol. 157, 2018, pp. 675–683.

[15]. G. Wu, F. Wang, Y. Cai, Generation and self-healing of a radially polarized Bessel-Gauss beam, *Physical Review A,* Vol. 89, Issue 4, 2014, pp. 043807.

[16]. G. Volpe, G. P. Singh, D. Petrov, Optical tweezers with cylindrical vector beams produced by optical fibers, *Proceedings of SPIE: Optical Trapping and Optical Micromanipulation,* Vol. 5514, 2004, pp. 283–292.

[17]. F. Wu, B. Zhang, Z. Liu, Y. Tang, N. Zhang, Optical trapping forces of a focused azimuthally polarized Bessel-Gaussian beam on a double-layered sphere, *Optics Communications,* Vol. 405, 2017, pp. 96–100.

[18]. F. Zhu, S. Huang, W. Shao, J. Zhang, M. Chen, W. Zhang, J. Zeng, Free-space optical communication link using perfect vortex beams carrying orbital angular momentum (oam), *Optics Communications,* Vol. 396, 2017, pp. 50–57.

[19]. M. K. Karahroudi, B. Parmoon, M. Qasemi, A. Mobashery, H. Saghafifar, Generation of perfect optical vortices using a Bessel–Gaussian beam diffracted by curved fork grating, *Applied Optics,* Vol. 56, Issue 21, 2017, pp. 5817–5823.

[20]. K. Huang, P. Shi, X.-l. Kang, X. Zhang, Y.-p. Li, Design of doe for generating a needle of a strong longitudinally polarized field, *Optics Letters,* Vol. 35, Issue 7, 2010, pp. 965–967.

[21]. X. Gao, R. Fu, H. Shen, X. Dong, T. Geng, S. Zhuang, Focus shaping of Bessel–Gauss beam with radial varying polarization, *Optica Applicata,* Vol. 42, Issue 3, 2012, pp. 481–491.

[22]. X. Gao, D. Zhang, T. Mei, R. Fu, S. Zhuang, Focus shaping of the radially polarized Bessel–Gauss beam with a sine-azimuthal variation wavefront, *Optica Applicata,* Vol. 43, Issue 3, 2013, pp. 567-582.

[23]. F. Gori, G. Guattari, C. Padovani, Bessel-Gauss beams, *Optics Communications,* Vol. 64, Issue 6, 1987, pp. 491–495.

[24]. K. S. Youngworth, T. G. Brown, Focusing of high numerical aperture cylindrical-vector beams, *Optics Express,* Vol. 7, Issue 2, 2000, pp. 77–87.

[25]. S. Sato, Y. Kozawa, Hollow vortex beams, *J. Opt. Soc. Am. A,* Vol. 26, Issue 1, 2009, pp. 142–146.

[26]. E. Y. Yew, C. J. Sheppard, Tight focusing of radially polarized gaussian and Bessel-Gauss beams, *Optics Letters,* Vol. 32, Issue 23, 2007, pp. 3417–3419.

[27]. X. Gao, S. Hu, J.-S. Li, Z.-H. Ding, H.-M. Guo, S.-L. Zhuang, et al., Tunable optical gradient trap by radial varying polarization Bessel–Gauss beam, *Journal of Biomedical Science and Engineering,* Vol. 3, Issue 3, 2010, pp. 304–307.

[28]. A. A. Alkelly, I. G. H. Loqman, H.-M. H. T. Al-Ahsab, Focus shaping of cylindrically polarized vortex beams by a linear axicon, *Electronic Journal of University of Aden for Basic and Applied Sciences,* Vol. 2, Issue 4, 2021, pp. 145–150.

(031)

Recent Design Evolution and New Trends of Hollow Core Optical Fibers

W. Belardi [*1], A. Pastre [1], S. Plus [1], R. Habert [1], K. Baudelle [1], L. Bigot [1], G. Bouwmans [1], P. J. Sazio [2], P. Jaworki [3], P. Koziol [3], G. Dudzik [3] and K. Krzempek [3]

[1] Université de Lille, CNRS, UMR 8523 –PhLAM – Physique des Lasers, Atomes et Molécules, F-59000 Lille, France

[2] Optoelectronics Research Centre, University of Southampton, Southampton, SO17 1BJ, UK

[3] Laser & Fiber Electronics Group, Faculty of Electronics, Wroclaw University of Science and Technology, 50-370 Wroclaw, Poland

Tel.: +33362531617

[*]E-mail: walter.belardi@univ-lille.fr

Summary: The development of hollow core optical fibers based on the antiresonant optical principle is gaining a significant interest within the optical fiber research community due, among others, to their broadband transmission, low attenuation, mid-infrared and ultra-violet operation, as well as their unique ability to handle high optical power. In this work, we will offer an update on our recent activities related to the introduction of novel hollow core fiber designs and the fabrication and development of hollow core fibers with a lateral cut for sensing applications.

Keywords: Fiber design and fabrication, Fiber properties, Microstructured fibers.

1. Introduction

Hollow core optical fibers (HCs) are waveguides capable of efficiently transmitting light in air [1]. In recent years significant interest has developed in HCs with a simplified geometrical structure comprising a limited number of detached tubes within an outer jacket tube [2]. In such Anti-Resonant hollow core Fibers (ARFs), light propagation is allowed by the presence of elements surrounding the central air core which are *anti-resonant* with respect to the transmitted optical wavelength [3] and which have a *negative curvature* of the core boundary [4].

These geometrical characteristics allow for an overlap of less than 0.01 % between the fundamental optical mode travelling within the fiber and the glass within the cladding area [4].

Their most promising advantages are, therefore, directly-linked to the absence of glass material in the fiber core, which, in principle, may be expected to imply, not only lower nonlinearity and dispersion, but also lower attenuation.

This minimal interaction is extremely important in the fields of high power optical beam delivery, HCs made of non-conventional materials, ultraviolet and mid-infrared optical transmission.

Although HCs have attracted the interest of the research community since the dawn of optical fiber technology, and particularly in the last 20 years, their structural design keeps evolving at a fast pace. The large use of numerical or analytical tools, as well as the fabrication and characterization of novel fiber structures are allowing a better understanding on the link between the geometrical properties of HCs and their optical properties.

In this work, we discuss the design evolution and the most recent trends in the development of HC fiber structures. In particular, we will show novel HCs with lower attenuation, reduced bending loss, strong mono-modality, lower dispersion, with an eye at both conventional and un-conventional spectral ranges. We will also discuss how novel HCs can, in principle, be used not only as passive components, but also as amplifiers and active devices.

We will see how these new forms of HCs will adapt to novel applications in the medical field, optical telecommunications, industrial processing, biology, gas sensing, and others.

2. Novel Designs for Light Amplification

Given the low overlap between the guided light and the glass, light amplification in a ARF has been demonstrated by filling the air core with several gas compositions in order to obtain the desired overlap between the pump and signal light and the transmitting medium [5, 6].

In contrast, we explore here the theoretical possibility of achieving light amplification in an unfilled ARF. We discuss in detail a novel geometrical structure for ARFs which comprises both *anti-resonant* and *resonant* elements (Fig. 1), and which is capable of combining a relatively low attenuation with a very much increased level of overlap between the transmitted optical mode and a rare-earth-doped glass within the cladding area.

3. Novel Fibers for Unconventional Spectral Ranges

Mid-infrared silica based HCs have been demonstrated in a number of works. However, silica

glass absorption increases between 3000 and 50000 dB/m in the 4.5-5µm range [7]. This has been, for long time, a major limit to the use of hollow core optical fibers beyond the wavelength of 4.7 µm.

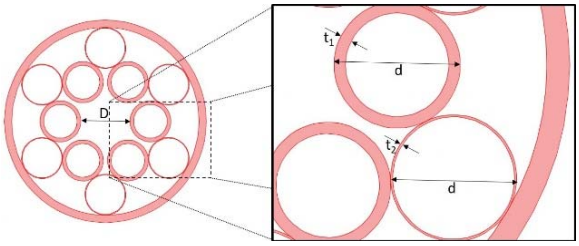

Fig. 1. Hollow core fibers with resonant and antiresonant elements.

Within our work, we update the ultimate limits in the practical use of hollow core fiber technology in the mid-infrared.

We first discuss the last developments on borosilicate based hollow core antiresonant fibers (ARFs) with very large core sizes, while keeping acceptable bending losses for most practical applications [Fig. 2a]. Then we report about the successful fabrication of long and fully handable silica based hollow core optical fibers with minimum attenuation of 0.2 dB/m at 4.7 µm and beyond [Fig. 2B].

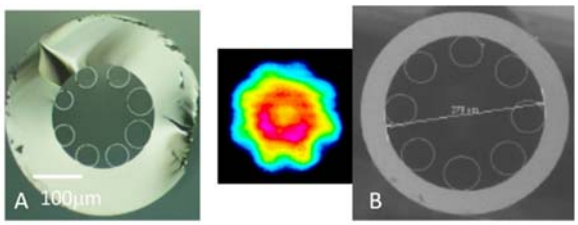

Fig. 2. Hollow core optical fibers for the mid-infrared spectral range: borosilicate based fibers (A) and silica-based fibers (B).

4. Novel Designs for Gas Sensing Applications

We discuss the fabrication of novel optical designs of hollow core optical fibers for sensing applications [Fig. 3A and B]. The lateral cut of HCs is demonstrating great advantages in terms of fast gas optical detection [8]. We discuss the recent improvements in the fabrications of this kind of design as well as the adoption of post-processing techniques for the lateral cutting of these fibers along their length [Fig. 3C].

4. Conclusions

We review recent progresses in the design development and fabrication of novel forms of hollow core optical fibers. These new concepts may reveal extremely useful in the field of optical communication, optical beam delivery as well as gas sensing.

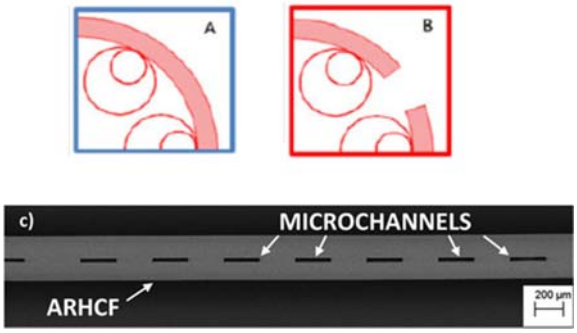

Fig. 3. Design of hollow core optical fibers with a lateral cut (B) and fabrication of side-cutted hollow fibers via a femtosecond laser.

Acknowledgements

This work is supported by the European M-Era,net project GADEIRE.

References

[1]. W. Belardi, Hollow core optical fibers, *MDPI*, 2019.
[2]. W. Belardi, J. C. Knight, Hollow antiresonant fibers with low bending loss, *Optics Express,* Vol. 22, Issue 8, 2014, pp. 10091-10096.
[3]. N. M. Litchinitser, A. K. Abeeluck, C. Headley, B. J. Eggleton, Antiresonant reflecting photonic crystal optical waveguides, *Optics Letters,* Vol. 27, Issue 18, 2002, pp.1592-1594.
[4]. W. Belardi, J. C. Knight, Effect of core boundary curvature on the confinement losses of hollow antiresonant fibers, *Optics Express,* Vol. 21, Issue 19, 2013, pp. 21912-21917.
[5]. P. St. J. Russell, P. Hölzer, W. Chang, A. Abdolvand, J. C. Travers, Hollow-core photonic crystal fibres for gas-based nonlinear optics, *Nature Photonics,* Vol. 8, Issue 4, 2014, pp. 278–286.
[6]. Z. Wang, W. Belardi, F. Yu, W. J. Wadsworth, and J. C. Knight, Efficient diode-pumped mid-infrared emission from acetylene-filled hollow-core fiber, *Opt. Express,*Vol. 22, Issue 18, 2014, pp. 21872-21878.
[7]. R. Kitamura, L. Pilon, and M. Jonasz, *Applied Optics,* Vol. 46, Issue 33, 2007, pp. 8118-8133.
K. Krzempek, P. Koziol, P. Jaworki, and W. Belardi, Antiresonant hollow core fiber-assisted photothermal spectroscopy of nitric oxide at 5.26 µm with parts-per-billion sensitivity, *Sensors and Actuators: B Chemical,* Vol. 345, Art. 130374, 2021, pp. 1-10.

(032)

Polymer-based Inverted Pyramids for SERS

I. Lettrichova [1], D. Jandura [1], P. Gaso [1], D. Pudis [1] and A. Kuzma [2, 3]
[1] University of Zilina, Dept. of Physics, 1 Univerzitna, 010 26 Zilina, Slovakia
[2] Slovak University of Technology in Bratislava, Institute of Electronics and Photonics, 3 Ilkovicova, 812 19 Bratislava, Slovakia
[3] International Laser Center,3 Ilkovicova, 841 04 Bratislava, Slovakia
Tel.: + 421 41 513 23 20
E-mail: lettrichova@fyzika.uniza.sk

Summary: In this paper, special 3D substrate available for Surface-enhanced Raman spectroscopy (SERS) measurements are presented. We prepared gold-coated inverted pyramids patterned in the surface of IP-Dip polymer by direct laser polymerization. SERS structure consists of field of 10x10 inverted pyramids with base of 5 μm and three different depths – 2.5 μm, 4 μm and 6 μm. Afterwards, an Au layer with 4 different thicknesses (10 nm, 20 nm, 30 nm and 40 nm) is evaporated. Transmission, as well as reflection spectra were simulated and measured for characterization of prepared structures. Recently published inverted pyramids in polymethylmetacrylate shows very good qualitative signal enhancement with respect to the commercial silicon-based Klarite SERS substrate.

Keywords: Surface-enhanced Raman spectroscopy, SERS substrate, Polymer-based materials, IP-Dip.

1. Introduction

Surface-enhanced Raman spectroscopy (SERS) is very attractive for the development of selective and sensitive analytical procedures [1]. It combines advantages of vibration-based Raman spectroscopy [2] with signal enhancing techniques. Raman spectroscopy requires little or no sample preparation, it is applicable to many types of hazardous materials, and it can provide fast and accurate identification and quantification. The energy spectrum of molecular vibrations serves as a characteristic and unique fingerprint for the chemical composition of a sample. Unfortunately, Raman scattering is an extremely week effect. For this reason, often signal enhancing techniques are employed for detection methods [3].

2. Surface-enhanced Raman Spectroscopy

The magnitude of Raman scattering can be considerably enhanced, if the scattering molecule is placed near a roughened metal substrate [1], usually silver, gold or copper. Thanks to surface plasmon in nanoscale features of metal surface excited by visible light, strong electromagnetic fields are generated, what leads to enhancement in Raman signal. This enhancement factor is on the order of $10^6 – 10^7$, or in case of resonance as high as $10^{12} – 10^{14}$ [4]. The size, shape and material of nanoscale features must be considered to determine the resonant frequency of the conduction electrons in a metal-dielectric nanostructure.

3. 3D Substrates for SERS

A large variety of different SERS active substrates has been realized for different SERS applications introducing different planar and three dimensional (3D) technologies. Although many 3D methods have been developed for fabricating SERS nanostructures, most involve multiple step technologies. Very promising alternative is single-step process based on direct laser polymerization in a volume of liquid polymers. It leads to exceptional designs of great variability of 3D structures with submicrometer resolution and in combination with metal deposition it brings very effective SERS substrates.

4. Inverted Pyramids in IP-Dip Polymer

In this paper, we present gold-coated inverted pyramids patterned in the surface of IP-Dip polymer that can be directly used as SERS substrate. Nanoscribe Photonic Professional GT laser lithographic system based on direct laser writing was used for structure fabrication. The laser focuses into the volume of IP-Dip photoresist, where two-photon polymerization process arises in the focal spot volume with lateral resolution achieving 200 nm and vertical resolution of 600 nm.

Prepared SERS structure consists of field of 10x10 inverted pyramids with base of 5 μm and three different depths – 2.5 μm, 4 μm and 6 μm. Afterwards, an Au layer with 4 different thicknesses (10 nm, 20 nm, 30 nm and 40 nm) is evaporated.

Transmission, as well as reflection spectra were simulated and measured for characterization of prepared structures.

In the next step, the sample is investigated by micro-Raman measurements using R6G as the probe molecule. The R6G in aqueous solution at concentration of 10^{-2} M is used. The micro-Raman measurements is performed in air at room temperature, in backscattering geometry. Recently published

inverted pyramids in polymethylmetacrylate [5] shows very good qualitative signal enhancement with respect to the commercial silicon-based Klarite SERS substrate [6].

5. Results and Discussion

In the Fig. 1a, there is shown SEM image of Au coated polymer-based inverted pyramids. Inverted pyramids in IP-Dip polymer with a base of 5 µm and depth of 4 µm with Au layer with thickness of 30 nm is shown. The detailed SEM image documents layer-by-layer technology process, where the structure slicing of app. 200 nm can be visible. According to Mu et al., it can lead to surface plasmon polariton resonance formation [7].

The transmission spectrum of the structure presented in Fig. 1a is shown in the Fig. 1b. As the reference, the unpatterned glass substrate with 30 nm Au layer was used. The transmission is a function of wavenumber with minimum at app. 470 nm. The transmission and reflectance measurements and simulation show usability of prepared structures for SERS. Anyway, further simulation and investigation of arrangement, as well as Au layer thickness has to be done in order to enhance the Raman signal for application in SERS.

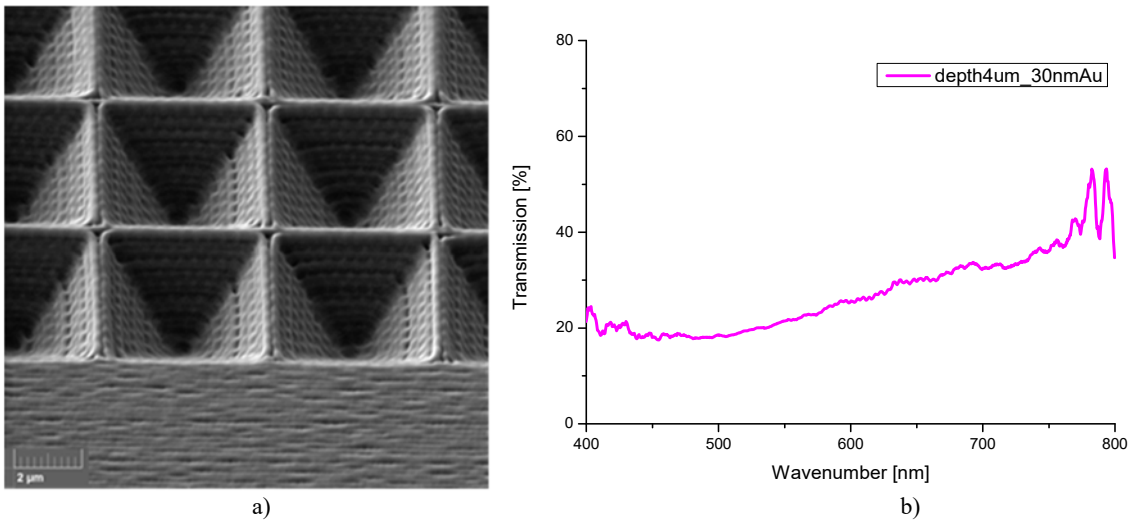

a) b)

Fig. 1. a) Scanning electron microscope image of inverted pyramids in IP-Dip polymer with base of 5 µm and depth of 4 µm with 30 nm Au layer; b) Transmission spectrum of the structure.

Acknowledgements

This work was supported by grant agency of Ministry of Education, Science, Research and Sport of the Slovak Republic projects VEGA 1/0677/21, VEGA 1/0363/22, and APVV 20-0264. This publication was realized with support of Operational Program Integrated Infrastructure 2014 - 2020 of the project: Innovative Solutions for Propulsion, Power and Safety Components of Transport Vehicles, code ITMS 313011V334, co-financed by the European Regional Development Fund.

References

[1]. M. Fleischmann. P. J. Hendra, A. J. McQuillan, Raman spectra of pyridine adsorbed at a silver electrode, *Chemical Physics Letters*, Vol. 26, 1974, pp. 163-166.

[2]. C. V. Raman, K. S. Krishnan, A new type of secondary radiation, *Nature*, Vol. 121, 1928, pp. 501-502.

[3]. P. L. Stiles, J. A. Dieringer, N. C. Shah, R. P. V. Duyne, Surface-Enhanced Raman Spectroscopy, *Annual Review of Analytical Chemistry*, Vol. 1, 2008, pp. 601–626.

[4]. S. Nie, S. R. Emory, Probing single molecules and single nanoparticles by surface enhanced Raman scattering, *Science*, Vol. 275, 1997, pp. 1102-1106.

[5]. S. Z. Oo, S. Siitonen, V. Kontturi, D. A. Eustace, M. D. B. Charlton, Disposable gold coated pyramidal SERS sensor on the plastic platform, *Optics Express*, Vol. 24, Issue 1, 2016, pp. 724-731.

[6]. G. Mcnay, D. Eustace, E. Smith, K. Faulds, D. Graham, Surface-Enhanced Raman Scattering (SERS) and Surface-Enhanced Resonance Raman Scattering (SERRS): A Review of Applications, *Applied Spectroscopy*, Vol. 65, Issue 8, 2011, pp. 825-837.

[6]. Mu, J., Li, J., Li, W., Luo, Q., Gu, Ch, Hollow metallic pyramid plasmonic structures fabricated by direct laser writing and electron beam evaporation. *Microelectronic Eng.*, Vol. 110, 2013, pp. 307-331.

(033)

Polymer Inverted Refractive-Index-Contrast Grating Prepared by Laser Lithography on Si Substrate

D. Jandura [1], P. Gaso [1], J. Suffczyński [2], T. Czyszanowski [3] and D. Pudis [1]
[1] Department of Physics, Faculty of Electrical Engineering and Information Technology, University of Zilina, Univerzitna 1, 01026 Zilina, Slovakia
[2] Institute of Experimental Physics, Faculty of Physics, University of Warsaw, ul. Pasteura 5, 02-093 Warsaw, Poland
[3] Photonics Group, Institute of Physics, Lodz University of Technology, 90-924 Łódź, Poland
E-mail: jandura@fyzika.uniza.sk

Summary: In this paper, we present the simulation and preparation in IP-Dip material of a polymer grating, which is used as a highly reflective and spectrally selective mirror based on Inverted Refractive-Index-Contrast Grating (ICG) geometry. We simulated the power reflectance as a function of the grating parameters and prepared the grating structure in IP-Dip material using three-dimensional (3D) laser lithography according the proposed theoretical design. The morphology of the prepared structures was analyzed using a scanning electron microscope.

Keywords: Grating, Polymer photonics, 3D laser lithography, IP-Dip polymer.

1. Introduction

Nanophotonic devices use a light-matter interaction leading to an enormous improvement of optical properties. This is typically achieved with optical cavities, which trap photons for many optical cycles before the photons escape. This allows, for instance, a photon to interact with an active optical material for a longer time, which is advantageous for many applications [1]. A new class of planar optics has emerged, that is a subwavelength grating surrounded by significantly lower refractive index region, herein referred to as high-contrast gratings (HCGs) [2]. It can be designed to reflect or transmit nearly completely and with a specific optical phase over a broad spectral range and/or various incident beam angles [3]. We focused on a specific concept of the grating with inverted arrangement of refractive index contrast with respect to HCG, known as Inverted Refractive-Index-Contrast Grating (ICG) [4]. This concept is based on low refractive index grating stripes that are implemented on a surface of a high refractive index cladding layer. Recently, great attention was given to polymer materials because of an improvement of the three-dimensional (3D) techniques. 3D Laser lithography has achieved a resolution better than 200 nm allowing the preparation of 3D photonic crystals [5]. In this paper, we focus on the simulation and experimental demonstration of optical properties of polymer grating in IP-Dip material based on ICG geometry using the 3D laser lithography process.

2. ICG Grating Design and Simulation

We proposed ICG grating in IP-Dip polymer and simulated, using Plane Wave Admittance Method [6], the power reflectance as a function of grating parameters as Fig. 1 illustrates. The maximal power reflectance of ICG can be as high as 80%. In analysis, we consider transverse electric (TE) polarization of the electromagnetic (EM) field. In this polarization, the sole electric field component, designated as E_x is parallel to the grating stripes.

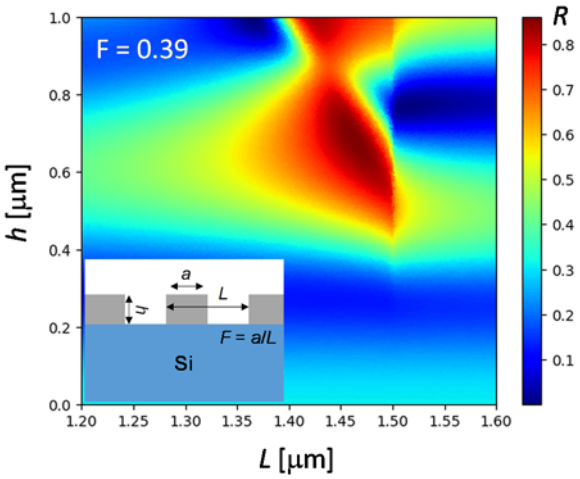

Fig. 1. The simulation of power reflectance represented by colour scale in the domain of grating period L, grating height h when a duty cycle of the grating is $F = 0.39$ and the wavelength is 1500 nm.

3. Fabrication and Analysis of ICG Grating

For preparation, we used a laser lithography system Photonic Professional GT from Nanoscribe GmbH. A femtosecond laser is focused into the volume of an IP-Dip photoresist, where the two-photon polymerization process occurs in the volume focal spot (voxel). In the fabrication process, the IP-Dip

photoresist was deposited on top of the silicon substrate and polymerization by laser writing was realized layer by layer in a single-step process. As the IP-Dip material exhibits a shrinkage effect after polymerization and the development process, the designed dimensions were appropriately oversized. Scanning electron microscope (SEM) image of prepared IP-Dip surface grating on silicon substrate with defined parameters is shown in Fig. 2.

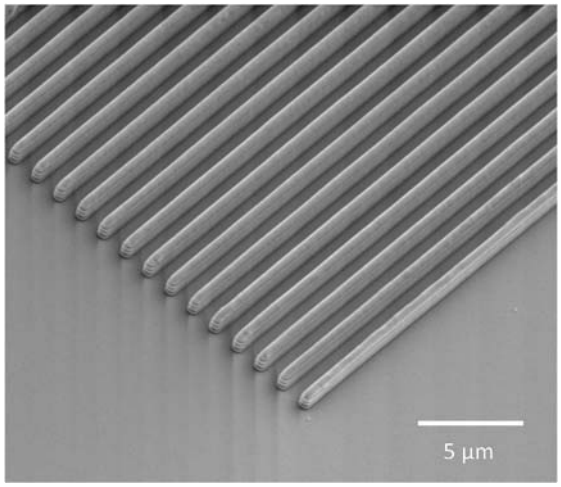

a)

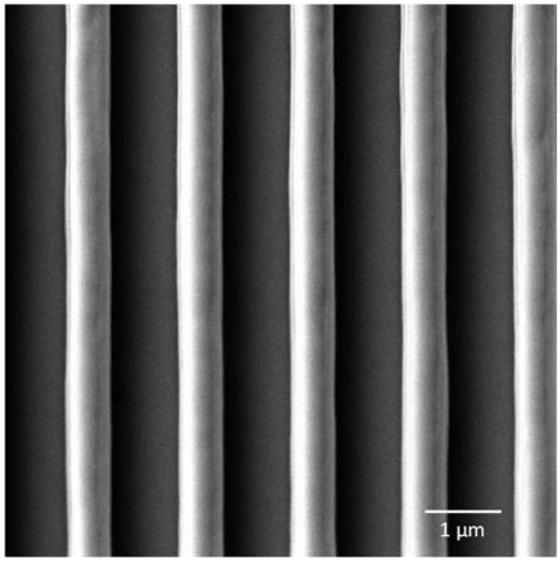

b)

Fig. 2. a) SEM tilted view and b) SEM top view of IP-Dip surface grating with real parameters: L = 1462 nm, h = 688 nm, F = 0.39.

4. Conclusions

In this paper, we have presented the simulation and preparation of the polymer based ICG structure. We proposed grating parameters for an ICG structure in IP-Dip polymer with respect to the simulated power reflectance. The main advantage of the polymer grating compared with semiconductor ICG could be very fast and less demanding preparation and simple application to various hybrid photonic devices, while maintaining such properties as high reflectance, polarization selectivity and a possibility of phase control of the light.

Acknowledgements

This work was supported by the Slovak National Grant Agency under project No. VEGA 1/0363/22 and the Slovak Research and Development Agency under the project No. APVV-20-0264, as well as the Polish National Science Centre within the projects OPUS 2020/39/B/ST7/03502. This paper was supported under the project of Operational Programme Integrated Infrastructure: Independent research and development of technological kits based on wearable electronics products, as tools for raising hygienic standards in a society exposed to the virus causing the COVID-19 disease, ITMS2014+ code 313011ASK8. The project is co-funding by European Regional Development Fund.

References

[1]. A. C. Overvig, S. Shrestha, N. Yu, Dimerized high contrast gratings, *Nanophotonics*, Vol. 7, 2018, pp. 1157-1168.

[2]. C. J. Chang-Hasnain, W. Yang, High-contrast gratings for integrated optoelectronics, *Advances in Optics and Photonics*, Vol. 4, 2012, pp. 379-440.

[3]. M Gębski, M. Dems, A. Szerling, M. Motyka, et al., Monolithic high-index contrast grating: a material independent high-reflectance VCSEL mirror, *Opt. Exp,* Vol. 23, 2015, pp. 11674- 11686.

[4]. E. Pruszynska-Karbownik, L. Zinkiewicz, J. Suffczynski, T. Czyszanowski, Inverted high-contrast gratings, in *Proc. SPIE 11695, High Contrast Metastructures X*, 116951R, 2021.

[5]. P. Urbancová, D. Pudiš, A. Kuzma, M. Goraus, P. Gašo, D. Jandura, IP-Dip-based woodpile structures for VIS and NIR spectral range: complex PBG analysis, *Opt. Mater. Express,* Vol. 9, 2019, pp. 4307-4317.

[6]. M. Dems, R. Kotynski, K. Panajotov, Plane Wave Admittance Method – a novel approach for determining the electromagnetic modes in photonic structures, *Opt. Exp.,* Vol. 13, 2005, pp. 3196-3207.

(034)

Nonlinear Upconversion Effect for Enhancement of Curing Depths in Laser-Assisted 3D Printing of Photopolymers

A. Zhakeyev [1] and J. Marques-Hueso [1]
[1] Heriot-Watt University, Institute of Sensors, Signals and Systems, EH14 4AS, Edinburgh, United Kingdom
Tel.: +44 (0) 131 451 8268, fax: +44 (0) 131 451 4155
E-mail: J.Marques@hw.ac.uk

Summary: Photopolymer resins used in stereolithographic 3D printing are limited to penetration depths of less than 1 mm. Our approach explores the use of near-infrared (NIR) to visible upconversion emissions from lanthanide-based phosphors to initiate photopolymer crosslinking at a much higher depth. This concept relies on the use of invisibility windows and non-linear optical effects to achieve selective crosslinking in photopolymers. NIR-green light UC allows for laser patterning of structures with curing depth of over 1 cm and aspect ratios of over 20:1 in a single pass.

Keywords: Upconversion, Laser patterning, Photopolymerization, Stereolithography, 3D printing

1. Introduction

Unlike subtractive manufacturing processes, additive manufacturing (AM), also known as three-dimensional (3D) printing, can directly produce complex 3D objects, with near-complete design freedom, and shows promise in markets that have high demand for customization, flexibility, design complexity and low transportation costs [1]. 3D printing techniques based on photopolymerization, such as stereolithography (SLA), digital light processing (DLP) and two-photon polymerization (2PP) exhibit high resolution compared to other 3D printing techniques, particularly 2PP, which is capable of fabricating structures with sub 100 nm features [2]. In SLA/DLP techniques, the curing depths are limited to hundreds μm, due to low penetration depths of ultraviolet (UV) and blue light, due to the presence of UV/blue light absorbing photoinitators. It was demonstrated by 2PP, which utilizes two-photon absorption (TPA), where a molecule absorbs two photons at the same time by using a virtual state, that the use long wavelength excitation source (~800 nm) allows for deeper penetration into the resin than UV light [3, 4]. However, 2PP machines can cost more than £100000, due to high-intensity femtosecond lasers, which are required since the absorption cross-section of initiators for the two-photon process is very small. Moreover, the time-consuming spot-by-spot printing process, and small working distances (< 380 μm) of the focusing optics limit the overall size of fabricated objects, which makes 2PP more suitable for fabrication of nano/microstructures. Upconversion (UC) involves the sequential absorption of low energy photons (e.g. NIR) before the subsequent emission of a relatively higher energy photon (e.g. UV/visible). Lanthanide-based UC phosphors have real energy levels, so the probability of transition for a 2-photon process can be approximately one million times higher than systems that use virtual energy levels (TPA, second-harmonic generation, etc.). Hence the power of the excitation laser can be much smaller, and inexpensive diode lasers can be used [5]. It was recently demonstrated that NIR to UV/blue UC based on thulium (Tm^{3+}) and ytterbium (Yb^{3+}) co-doped sodium yttrium fluoride ($NaYF_4$) can be used for ultra-deep photopolymerization, reaching curing depths of more than 13 cm [6]. Tm^{3+} doped K_2YbF_5 crystals were demonstrated to show potential in 3D printing applications [7]. By far the most efficient UC materials are based on erbium (Er^3) doped $NaYF_4$, with the photoluminescent quantum yield (PLQY) capable of reaching values above 16% [8-10]. Here, we utilize NIR (980 nm) to green light emissions (Fig. 1 (a, b)) of $NaYF_4$:Yb^{3+},Er^{3+} phosphor for laser patterning of structures with high curing depths and aspect ratios.

2. Materials and Methods

$NaYF_4$:(20%)Yb^{3+},(3%)Er^{3+} phosphor, Eosin Y and triethanolamine (TEA) were obtained from Sigma-Aldrich, and Clear resin (FLGPCL04) was obtain from Formlabs. Laser patterning was performed using a 980 nm laser diode (OFL371, OdicForce Lasers) and a two-axis stage with a stepper motor controller (A-MCB2, Zaber Technologies). A calibrated spectrofluorometer (FLS920, Edinburgh Instruments) was used for spectral measurements, equipped with a 102 mm inner diameter integrating sphere (Jobin-Yvon) and a 980 nm laser diode (LSR980NL-3W, Lasever Inc.) used for excitation.

3. Results and Discussion

As Fig. 1 (b) shows, bulk $NaYF_4$: (20%)Yb^{3+},(3%)Er^{3+} powder exhibits prominent green (540 nm) and red (660 nm) emissions, as well as small emissions in the blue (410 nm) and UV (380 nm) regions, upon excitation with a 980 nm laser. As expected, the emission intensity increases with an increase in power of the laser. In order to utilize the emission profile of $NaYF_4$: (20%)Yb^{3+},(3%)Er^{3+} for

photopolymerzation of SLA resin (Formlabs Clear), a suitable photoinitator must be employed. Eosin Y is a photosensitizer, which exhibits maximum absorbance at 530 nm, and matches well the green emissions of $NaYF_4$: (20%)Yb^{3+},(3%)Er^{3+}, as shown in Fig (c). When used alongside a co-initiator (synergist), such as TEA, it can be effectively used as a type II photoinitiator in photopolymerization reactions. The optimal formulation of photoinitiation system was found to be 0.05 wt% Eosin Y and 2.5 wt% TEA. Whilst $NaYF_4$:(20%)Yb^{3+},(3%)Er^{3+} concentration of 5 mg/mL in Formlabs Clear resin, shows transmittance of 89% at 980 nm. This formulation was used for laser patterning of Formlabs Clear resin, resulting in curing depths of over 1 cm and aspect ratios of over 20:1, for example as shown in Fig. 1 (d).

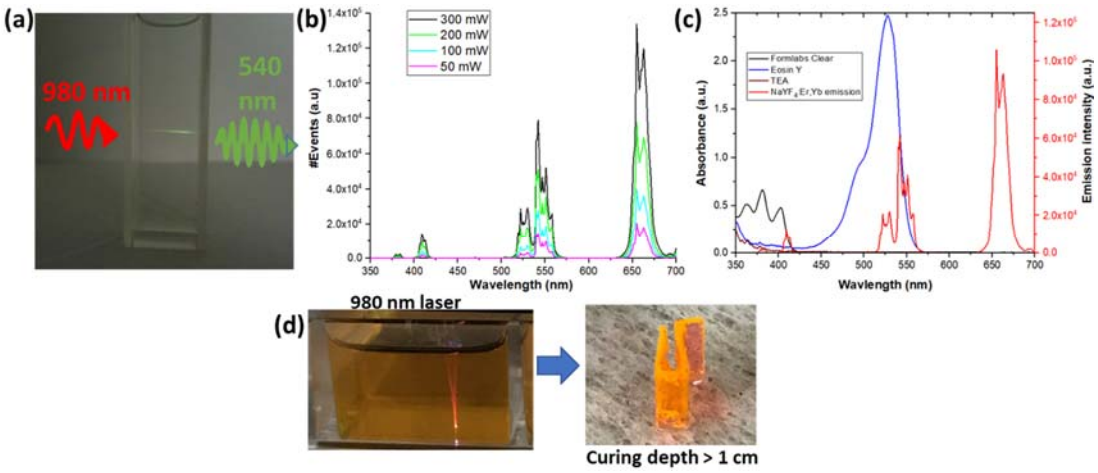

Fig. 1. (a) Illustration of NIR-green light upconversion; (b) Emission profile of bulk $NaYF_4$:(20%)Yb^{3+},(3%)Er^{3+} phosphor at different 980 nm laser excitation powers; (d) Absorption spectrum of the photoinitiation system matched with phosphor emissions; (d) Illustration of NIR-green light UC assisted laser patterning of Formlabs Clear resin.

4. Conclusion

The formulation based on NIR-green light UC allowed for patterning structures with curing depths of over 1 cm, compared to less than 1 mm achieved in traditional UV/blue light-based curing and 3D printing techniques. This method allows to transform photopolymerization from thin 2D layers to the fabrication of thick 3D layers with high aspect ratios, opening the door for new approaches, such as multi-material SLA.

Acknowledgements

This research work is supported by UK Engineering and Physical Science Research Council (EPSRC) Grant EP/T013680/1.

References

[1]. C. Weller, R. Kleer, and F. T. Piller, Economic implications of 3D printing: Market structure models in light of additive manufacturing revisited, *International Journal of Production Economics*, Vol. 164, 2015, pp. 43–56.

[2]. S. H. Park, D. Y. Yang, and K. S. Lee, Two-photon stereolithography for realizing ultraprecise three-dimensional nano/microdevices, *Laser & Photonics Reviews*, Vol. 3, Issue 1-2, 2009, pp. 1–11.

[3]. J. P. Malval et al., Enhancement of the Two-Photon Initiating Efficiency of a Thioxanthone Derivative through a Chevron-Shaped Architecture, *Chemistry of Materials*, Vol. 23, Issue 15, 2011, pp. 3411–3420.

[4]. Z. Li et al., A Straightforward Synthesis and Structure–Activity Relationship of Highly Efficient Initiators for Two-Photon Polymerization, *Macromolecules*, Vol. 46, Issue 2, 2013, pp. 352–361.

[5]. F. Auzel, Upconversion and Anti-Stokes Processes with f and d Ions in Solids, *Chemical Reviews*, Vol. 104, Issue 1, 2004, Jan. 2004, pp. 139–174.

[6]. R. Liu et al., Extremely deep photopolymerization using upconversion particles as internal lamps, *Polymer Chemistry*, Vol. 7, Issue 14, 2016, pp. 2457–2463.

[7]. J. Méndez-Ramos et al., Infrared-light induced curing of photosensitive resins through photon up-conversion for novel cost-effective luminescent 3D-printing technology, *Journal of Materials Chemistry C*, Vol. 4, Issue 4, 2016, pp. 801–806.

[8]. S. K. W. MacDougall et al., Ultra-high photoluminescent quantum yield of β-NaYF4: 10% Er3+ via broadband excitation of upconversion for photovoltaic devices, *Optics Express*, Vol. 20, Issue S6, 2012, pp. A879–A887.

[9]. C. M. S. Jones, A. Gakamsky, and J. Marques-Hueso, The upconversion quantum yield (UCQY): a review to standardize the measurement methodology, improve comparability, and define efficiency standards, *Science and Technology of Advanced Materials*, Vol. 22, Issue 1, 2021, pp. 810–848.

[10]. C. M. S. Jones et al., Optimized photoluminescence quantum yield in upconversion composites considering the scattering, inner-filter effects, thickness, self-absorption, and temperature, *Scientific Reports*, Vol. 11, 2021, pp. 13910.

(035)

Performance Evaluation of a Network Cluster Operating in the Solar-blind UV-C Band under a Non-Line-of-Sight Regime

N. Raptis [1], G. Pekridis [1], K. Krilakis [1], K. Panoliaskos [2], E. Roditi [3] and D. Syvridis [1]
[1] National and Kapodistrian University of Athens, Dept. of Informatics and Telecommunications, Optical Communications and Photonics Technology Laboratory, University Campus, Ilisia, 157 84, Athens, Greece
[2] Link S.A., Markou Mpotsari 47, 122 42, Aigaleo, Athens, Greece
[3] National and Kapodistrian University of Athens, Dept. of Physics, University Campus, Ilisia, 157 84, Athens, Greece
Tel.: +30 2107275322, +30 2107275236
E-mail: raptis@di.uoa.gr

Abstract: The favorable attributes of the solar-blind part of the ultraviolet-C band for the deployment of Non-Line-of-Sight communications systems have been studied intensely the last two decades. However, most works have focused on links. In this work, both experimental and theoretical results will be presented about a wireless network of 3 nodes operating under a regime of diffused emissions at 265 nm for covering tens of meters distances between communicating nodes. The physical and link layers have been implemented. Each node has 4 emitting sides based on Light Emitting Diodes, 3 receiving sides based on Photo-Multiplier Tubes and optical filters, and a processing unit based on a Field Programmable Gate Array fabric and an ARM processor. A physical layer rate around 7.80 kbit/s is achieved applying the fourth-order Pulse Position Modulation scheme. The link layer and some of the physical layer operations are accomplished by the processing unit.

Keywords: Non-Line-of-Sight network cluster, Ultraviolet solar-blind UV-C band, Optical scattering, Diffuse optical wireless communications, 4-PPM, Photo-multiplier tube, Light emitting diodes.

1. Introduction

The interaction between wavelengths in the Ultraviolet C-band (UV-C) between 200 and 280 nm and molecules and particles in the lower atmosphere results in intense scattering and absorption. This fact and the severe absorption by ozone in the upper atmosphere have been the keystones for several theoretical and experimental studies about short range Non-Line-of-Sight (NLOS) wireless communications systems with low background noise [1]. The main interest has been in links, though. The networking has been investigated at a simulation level [1], [2], but the experimental verification has not been sufficient so far, except a limited number of works [3]. Here, both theoretical and experimental results will be demonstrated that concern the operation of a small wireless network of 3 peer nodes. Diffused NLOS emissions take place at around 265 nm and at a low bit rate. Each node has 4 emitting sides, 3 receiving sides and a processing unit. Following the Internet protocol stack [4], the physical and the link layers are covered by the proposed implementation. In section 2, the nodes' components and functionalities are briefly described. Then, theoretical results about the network are given, whereas experimental results obtained indoors are presented in section 4. Successful diffused operation was confirmed for different scenarios that were examined. The text closes with the conclusions.

2. Node's Components and Functionalities

In terms of the hardware, each node is separated in 3 parts; the emitting, the receiving and the part with the electronics, as depicted in Fig. 1.

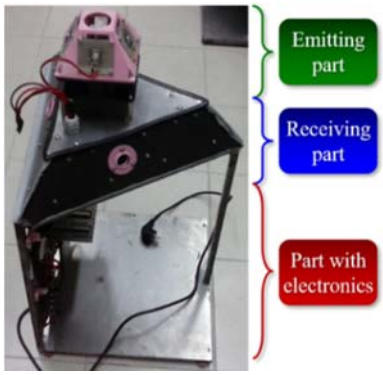

Fig. 1. Hardware of each node and separation into parts.

4 Light Emitting Diodes (LEDs) (at ~265 nm) are used per side. An optical filter plus a Photo-Multiplier Tube (PMT) followed by a Transimpedance amplifier (TIA) are used per side for signals' reception. Parts of the PMTs and TIAs circuits are placed inside the second triangular part. The elevation angles of both the emission and reception parts are fixed to 25°. Proper

circuits at the lower part of each node support the signals transmission and reception. Pulse Position Modulation of 4th order (4-PPM) is applied in the system. Above de/modulation, the 1024-bits physical layer frames dis/assembly take place, where a m-sequence of 511 bits plus a zero bit are the preamble for synchronization, 510 bits are the payload and 2 more dummy zero bits are discarded during reception. Forward Error Correction (FEC) en/de-coding processes have been specified but not included so far.

A processing kit by Terasic Technologies with a Field Programmable Gate Array (FPGA) unit and an ARM processor ([5]) controls the operation of each node and is placed at its lower part (Fig. 1). Above de/modulation, all the functions are implemented in software. For the emitting part, the 4-PPM signals that will modulate the LEDs per side are extracted through specific General Purpose Input/ Output (GPIO) pins on the platform. All the sides of a node emit the same signal. At the receiving part, each detected stream of the 3 becomes the input of a channel of the Analog to Digital Converter (ADC) on the board. The number of samples per channel of the ADC is 32768. The channel with the largest energy of the 3 is kept per interval that includes the buffer duration of 32768 samples, denoted as the channel sampling ($t_{chan.}$), plus the fixed interval of processing the samples, denoted as the processing interval ($t_{proc.}$) from now on. In the implementation, $t_{proc.}$ was set to $0.9 \times t_{chan}$. The sampling time and the number of samples per 4-PPM slot are set to $T_s = 16.05$ μsec and $N_{slot} = 4$, respectively. These give a slot duration of $T_{slot} = 64.2$ μsec, a physical layer rate $R_b \approx 7.80$ kbit/s and 16 samples per symbol for 4-PPM ([5]). Thus, each physical layer frame as 8192 samples must be detected in a 32768 samples buffer. Additionally, $t_{chan.} = 32768 \times T_s \approx 526.93$ msec. Details about the repetitive steps of summations of samples per slot duration per 32768 received samples combined with the cross-correlation operation with the m-sequence in order to achieve the synchronization at the physical layer can be found in [5].

At the link layer, the Medium Access Control (MAC) protocol is based on the Carrier Sensing Multiple Access scheme with Collision Avoidance (CSMA-CA) [4], [5]. All MAC frames have 358 bits (a segment of the 510-bits payload of each physical layer frame). MAC frames dis/assembly functions are placed at this layer. The specified types of MAC frames are the Beacon, Request-To-Send (RTS), Clear-To-Send (CTS), Data, Acknowledgement (ACK) and the General RTS (GenRTS) frame which is used as a report of presence in the network. In Fig. 2, the node's structure is depicted. The lower 2 layers of the Internet protocol stack have been implemented.

The frames succession is given in more detail for the link layer in Fig. 2. All the green arrows correspond to expected transitions either for frames emissions or receptions that represent a session of exchanged frames in which the node participates either as a transmitter or a receiver. The red arrows represent re-emissions or transitions due to collisions, errors and frames losses during a running session with the node as participant. The green-yellow arrows concern the transitions for the initiation of new sessions where a node may change role or not, even if the previous session with the node as an involved member did not end as expected.

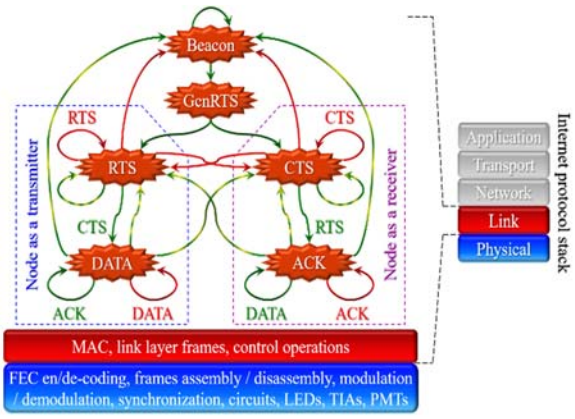

Fig. 2. Node's functionalities and operations and their position in the Internet protocol stack with focus on the link layer frames succession. FEC has not been included.

Specifically, the nodes will contend in order to access the medium. One of them will manage to emit a beacon 5 times in a row in order the rest of them to remain synchronized until the next successive beacons emission. The repeated emissions of beacons are the reason for the green arrow directed from the beacon to itself. The star with the Beacon label corresponds to either transmission or reception of the specific frame. Then, every node will try to emit a GenRTS. If a node has something to send, it will try to sense the wireless medium as idle in order to act as a transmitter, enter in the blue dashed polygon in Fig. 2 and emit a RTS to the desired recipient node. The node must receive a CTS in order to start emitting Data frames. This is represented by the green arrow from the RTS to the Data star with label CTS on it. If the node doesn't receive the required CTS, it re-emits the RTS with priority. This is represented by the red arrow from RTS to itself with an RTS label on it on the left side of Fig. 2. After a limit of 32 unsuccessful RTS re-emissions, with each re-emission represented by the same red arrow, the node will quit the attempt to emit. It will either try to get access to the medium again and initiate a new session by emitting a RTS, as implied by the green-yellow arrow from RTS to itself, or get into a reception mode, if another node manages "violently" sent a RTS, the node listened this action and must answer with a CTS, following the transition with the red arrow from RTS to CTS in Fig. 2, or try to emit 5 beacons, if the interval between two successive 5 beacons emissions ends or the node just listens to the channel for an interval. If the node manages to access the medium after a number of emissions that is lower than 32, the green-yellow arrow from RTS to itself simulate the initiation of a new session. However, after the reception of a CTS, the emission of Data frames follows. The emission of each Data frame must be followed by an ACK reception. Otherwise, the node re-emits the last Data frame. After 32 unsuccessful

emissions of the same Data frame, which corresponds to the red arrow from Data to itself with the red Data label on it, the node quits its attempt to send its data and must contend for getting access to the medium again. The node remains at the Data state when an ACK is successfully received, as declared by the green arrow from Data to itself with the ACK label on it, at the lower left part of Fig. 2. After the session of Data frames emissions finishes (or the maximum unsuccessful transmissions have happened), the node may either try to get access to the medium and act as a transmitter again by sending a RTS or become a receiver after receiving a RTS or try to emit or receive Beacon frames if a new inter-beacon interval must start. These initiations of new sessions are represented by the three respective green-yellow arrows starting from Data star in Fig. 2.

A succession of frames RTS–CTS–Data–ACK–Data–ACK and so on is conventionally expected in a link between 2 nodes. According to Fig. 2, when a node acts as a receiver, the transitions are similar to those of a transmitting node already described. The only difference is that an ACK is not emitted if a Data frame is not received successfully – that is, the responsibility to ensure the progress of the succession of frames is left to the node that initiated the session. The red arrow from ACK to itself with the ACK label at the right side of Fig. 2, suggests an unsuccessful reception of an expected Data frame. The node will remain at this state without emitting any frame waiting for the reception of the respective Data frame. After 32 unsuccessful receptions, the node saves any data that have been received during the session.

It is pointed out that before any step, a node listens to the channel independently of its role either as a transmitter or receiver and processes whatever it receives. Therefore, the protocol has an asynchronous manner and the synchronization is critical.

3. Theoretical Results

Following the nomenclature of [6], the average interval ($T_{avg.}$) for the successful emission of a MAC frame payload versus the transmission probability was estimated. The concepts in [6] have been adjusted to the current network aspect. The propagation delay for tens of meters coverage is negligible compared to the 4-PPM slot duration of 64.2 μsec. The distributed and short inter-frame spaces ([6]) are set to 0. The average time the channel is sensed busy due to a successful frame transmission is $T_s = 4\times(t_{chan.} + t_{proc.})$. The average time the channel is sensed busy during a collision is $T_c = (t_{chan.} + t_{proc.})$ and so is the empty slot time. The values are owed to the fixed intervals for the reception and processing ($t_{chan.} + t_{proc.}$) and then the transmission (again $t_{chan.} + t_{proc.}$) of any MAC frame. From [6] and the assumptions considered here, the estimated $T_{avg.}$ is shown in Fig. 3. The intervals are in the range of seconds due to the large $t_{chan.}$ and $t_{proc.}$ intervals. For a block of information which gets fragmented in a number of MAC Data frames, the RTS–CTS mechanism is applied once [4], whereas the Data frames of the same session are emitted following the Data–ACK scheme. With such a process, the effect of the large intervals for successful emissions of useful data is mitigated to some extent.

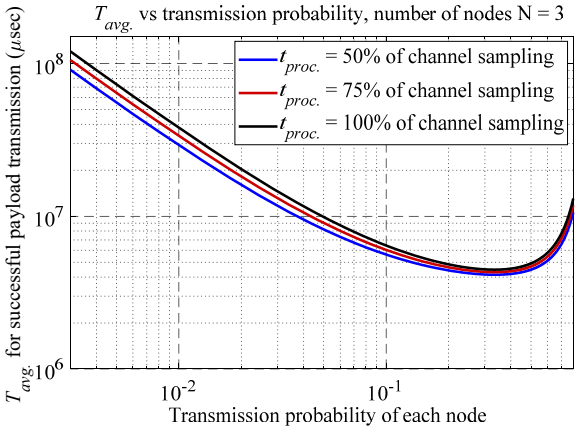

Fig. 3. Average interval for the successful emission of the payload of a MAC frame vs. the transmission probability.

4. Experimental Results

Isolating 2 of the 3 nodes, an attempt was made to relate the physical with the link layer and investigate the limits of coverage. The measurements were taken in an indoor corridor for distances between 15 m and 35 m, under 2 configurations per distance considering the alignment of the same emitting side of the nodes. Specifically, the nodes were placed under aligned beams and with beams at an angle. In the latter case, one node was turned by 35° with respect to their axis. The PMTs and TIAs gains were set per distance and kept unchanged for both cases, but were not adjusted to get the best results for both configurations at all distances. The mean number of bit errors per physical layer frame for 50 frames and the number of Cyclic Redundancy Check (CRC) errors appearances in MAC frames per session of 84 Data frames using 32 appended bits per MAC frame for CRC check were measured separately for the node that was subjected to the turning and acted as the sender of Data. All CRC errors appearances were taken into account independent of the reception of a corrupted ACK due to a re/transmission. The results are given in Fig. 4.

For the cases with not aligned nodes where the gains were not adjusted well, the errors in ACK frames were not prohibitive for the other node to receive all the Data frames of the session successfully even after retransmissions. It seems that the network coverage can be extended further by optimizing the PMTs and TIAs gains and by adding FEC coding.

The next scenario included 3 nodes. The network configuration can be seen in Fig. 5. In the right inset, node 1 is given. Nodes 1 and 2 are loosely aligned communicating under a NLOS regime. The top view of the emitting and receiving parts of Node 3 is given in the left inset. Nodes 2 and 3 have not aligned

emitting beams and receiving field of views. Node 1 is out of sight of node 3. The gains of the PMTs and the TIAs are set properly in order to ensure an operation at an as stable as possible level.

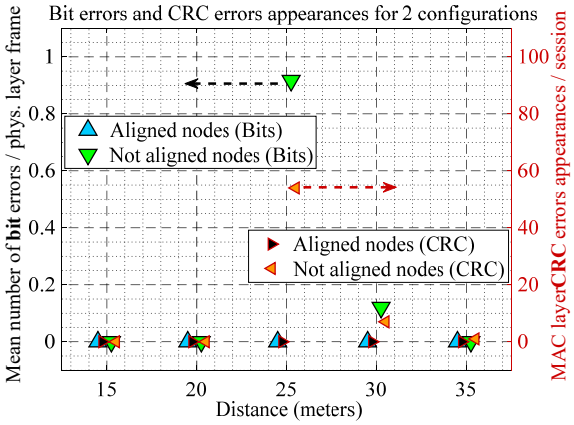

Fig. 4. Errors at physical and link layer frames vs. distance.

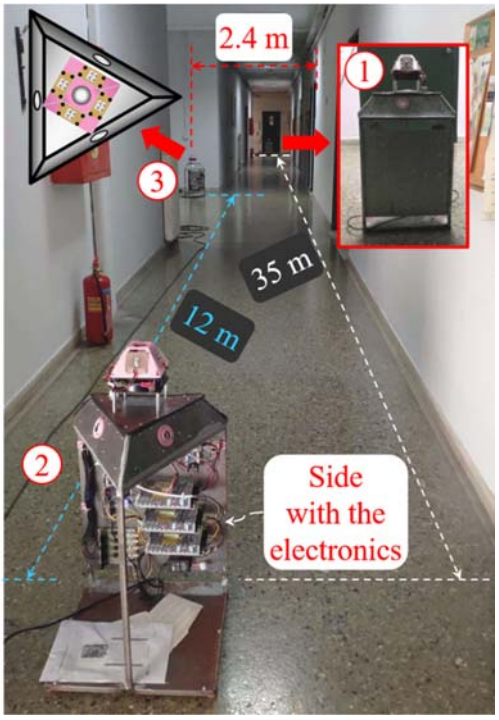

Fig. 5. Experimental setup with 3 nodes in the network.

The capabilities of the physical layer processes and the MAC protocol are investigated. Initially, the reception of physical layer frames is evaluated. Focus is given on node 3 which communicated with node 1 under a low Signal to Noise Ratio (SNR) regime. In Fig. 6, a received physical layer frame sent by node 1 is depicted as a voltage signal without the DC value in channel 0 of the ADC of node 3 for which the largest energy (of the 3) was estimated. It is noted that the corresponding receiver is on the side with the electronics. The gain of the PMT was set close to 2.12×10^7. The shot noise due to the large PMT gain is obvious. The ripple of the curve is owed to the lights that were open during the experiment. In the electrical domain, after the TIAs no additional filtering was applied at any node. However, the specific frame was received without errors. On the horizontal axis, the samples numbering begins from 0. In the inset, the same curve is zoomed in at the beginning of the entire frame at the sample 14316 which must be found.

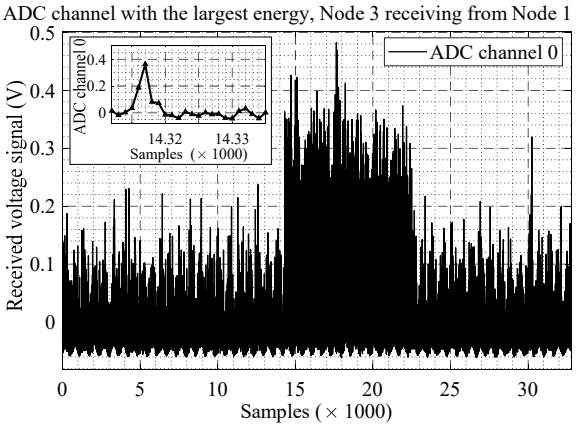

Fig. 6. Received physical layer frame in the channel of node's 3 ADC with the largest energy of the 3 channels.

In Fig. 7, the 4 (= N_{slot}) cross-correlation (C_{corr}) estimations of the m-sequence with the samples of Fig. 6 after shifting the stream by the samples mentioned in the legend and applying summations of samples per 4-PPM slot are shown. The C_{corr} vector with the largest peak value of the 4 appears in the inset graph focused around its maximum value. It will be used to find the starting position of the frame. In the current example, this vector was estimated for the case where no shifting of samples was applied. The number of C_{corr} samples (c_i) on the horizontal axis is $32768/N_{slot} + 1024 - 1 = 9215$ ([5]). The numbering begins from 0. From the inset, the position of the maximum is at 4602. The starting position of data in the buffer after summations per slot is at sample 4602 – 1023, whereas the starting position in the buffer of Fig. 6 is at (4602 – 1023) × 4 = 14316, as expected.

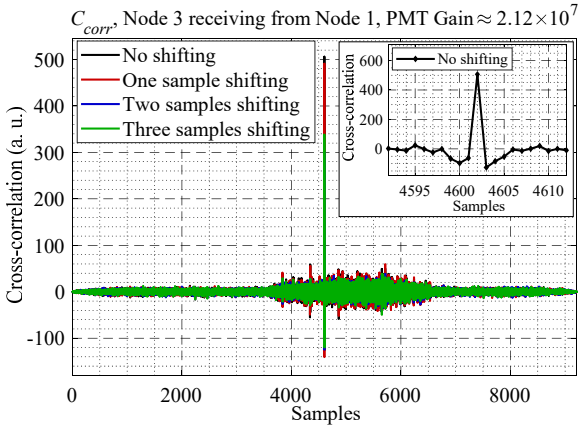

Fig. 7. Cross-correlation of the m-sequence with the samples in the ADC channel with the largest estimated energy of the 3. The estimations are after summations per slot per shifting case.

The vector $\Delta C_{corr} = c_{i+1} - c_i$ is also estimated using the best C_{corr} vector in order to avoid any false indication of signal presence given by C_{corr}. In Fig. 8, the C_{corr} in the inset of Fig. 7 is given accompanied by the respective ΔC_{corr} focused around the position of the peak value of C_{corr}. This is the expected pattern of ΔC_{corr} for a successful reception. The maximum of ΔC_{corr} must appear one sample before the maximum of C_{corr}, whereas the positions of the minimum of ΔC_{corr} and the maximum of C_{corr} must coincide. This is the process of synchronization at the physical layer. The inset red curve is the entire ΔC_{corr} with the same limits on the vertical axis as the main figure.

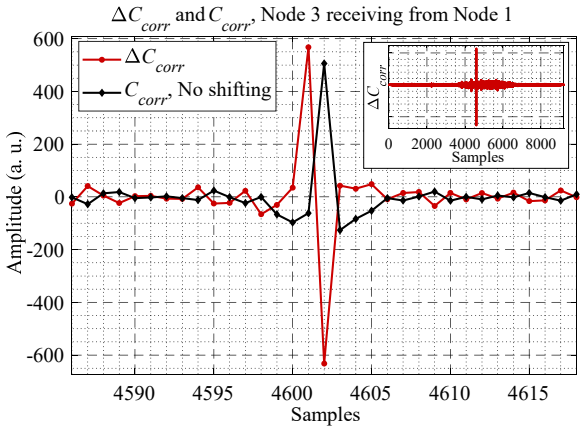

Fig. 8. C_{corr} with the largest peak value of the 4 and the respective ΔC_{corr} both focused around the position of the peak value of C_{corr}. The entire ΔC_{corr} is given in the inset.

Considering the MAC protocol, each node has a fixed IPv4 address and a link layer identity as an 8-bit integer that is used in order to be recognized in the network. The integer is refreshed each time the board is switched on. All the values are given in Table 1.

Table 1. IPv4 address (the last number due to the same mask) and link layer identity of each node as an integer.

Node's number in Fig. 5	**1**	**2**	**3**
IPv4 address (195.134.67.XX)	24	23	21
Link layer identity in the network	228	119	193

A succession of exchanged frames in the network was experimentally obtained and depicted in Fig. 9. The frames were extracted from the last part of a session where node 1 (228) was the transmitter and node 3 (193) was the receiver of Data frames. A .txt file was transformed into a bit sequence with 32 bits per character. The bit stream was fragmented in order each fragment to become the payload of each MAC frame. In the figure, 3 columns appear excluding the left one with the rows numbering. The first 2 concern the two communicating nodes and the right one has the messages printed by node 2 who listened to the channel. The frames that were received by each node and the respective answers are shown aligned in order the figure to be legible. For example, a Data frame emission and the reception messages from the other nodes are shown on the same row, whereas the ACK frame that must follow, appears on the next row along with the reception messages that were printed. The Data frames on the left column emitted for the first time by node 1 are written with purple color and so do the messages of the "well" received frame by the other two nodes on the same row. A "well" received frame means that the physical layer frame was detected inside the buffer for the receiver with the largest energy of the 3 per node. The positive number, e.g. 675 on the first row in the column of node 3 or 1282 on the same row in the last column, corresponds to the position where the preamble starts after the summations per 4-PPM slot take place during demodulation. Similarly, the ACK emissions and the messages for the "well" received frame by the other 2 nodes appear with green color. In 2 cases, on rows 5-6 and 13-14, node 3 received on time the Data frame by node 1, but errors were estimated at the link layer. A message appears with red color about non-zero CRC remainder at the second line of the cells on rows 5 and 13 in the column of node 3. These frames were rejected. As mentioned above, the node does not emit an ACK in such an instance, as indicated at rows 6 and 14 (inserted for legibility). Then, node 1 retransmitted its last Data frame due to no reception of a corresponding ACK. The 2 retransmissions are shown on rows 7 and 15 with red colors. There are also 3 incidents, on rows 2, 8 and 16, where the physical layer frame that carries an ACK was not detected in a proper position inside the receiver's buffer of node 1. The negative integer in orange color is the position of the starting point of the physical layer frame provided by the cross-correlation results. It means that the frame was found outside the buffer and earlier than expected. These frames were rejected at the link layer even if the useful part of the physical layer frame could be entirely inside the buffer. A retransmission of the last Data frame took place. This can be seen on node's 1 column, on rows 3, 9, 17 with the orange color DATA. A received frame outside the buffer means that the link is instable and the synchronization is almost lost, but even in the succession of frames in Fig. 9, the communication finished normally. It becomes apparent that the low SNR regime in the communication between nodes 1 and 3 is translated into CRC errors that appear during receptions of Data frames. It can be observed, though, that finally node 3 received and saved the file sent by node 1, as indicated by the message which is marked with the dashed blue oval rectangle on the column of node 3 for the last Data frame (row 27). Node 2 appeared fairly stable as it had both nodes in sight (Fig. 5). It received all the frames that were exchanged.

Despite some issues of instability, the principle of the network operation in its entirety was proved experimentally. Open space is left for amendments.

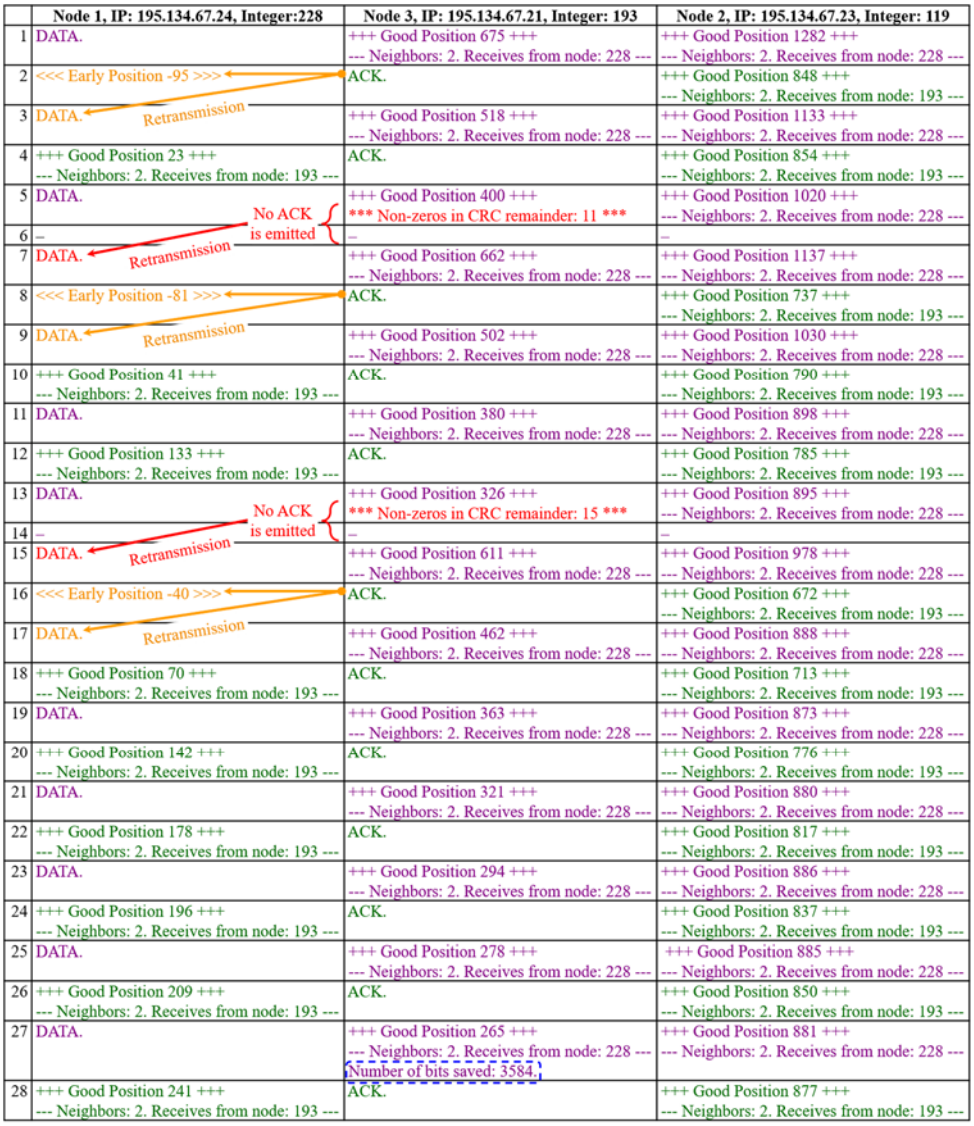

Fig. 9. Experimentally obtained part of the communication between nodes 1 and 3 with node 2 listening to the other two.

5. Conclusions

The performance of a wireless network cluster operating at 265 nm was evaluated both theoretically and experimentally. The bit rate is set to ~7.80 kbit/s under 4-PPM to encounter the large losses of the diffused links. The delays were large due to the large channel sampling and processing intervals. Moreover, the number of samples of useful data per physical layer frame is a fraction of the receiving buffers' length resulting in throughput waste. Nevertheless, successful emissions were achieved experimentally at tens of meters coverage even under no sight conditions between 2 of the nodes. Further enhancements can be applied to improve the stability of the network, ameliorate performance and allow the coverage of larger distances. Parameters optimization, e.g. the gains of PMTs and TIAs, and a FEC scheme are such measures that can be included. Therefore, the deployment of optical wireless NLOS networks in the UV-C band becomes feasible.

Acknowledgments

This research has been co-financed by the European Regional Development Fund of the European Union and Greek national funds through the Operational Program Competitiveness, Entrepreneurship and Innovation, under the call RESEARCH – CREATE – INNOVATE (project code: T1EDK-05446).

References

[1]. A. Vavoulas, H. G. Sandalidis, N. D. Chatzidiamantis, Z. Xu, and G. K. Karagiannidis, A survey on ultraviolet C-band (UV-C) communications, *IEEE Communications Surveys & Tutorials*, Vol. 21, No. 3, 2019, pp. 2111–2133.

[2]. C. Li, J. Li, Z. Xu, J. Wang, Y. Lin, J. Zhao, A. Qi, and H. Shen, Performance of the UV multinode network under the lossless contention MAC protocol, *IEEE*

Photonics Journal, Vol. 14, No. 2, 2022, Article Sequence Number: 7319207.

[3]. C. Li, J. Li, Z. Xu, and J. Wang, Research on the lossless contention MAC protocol and the performance of an ultraviolet communication network, *Optics Express*, Vol. 29, No. 20, 2021, pp. 31952–31962.

[4]. J. F. Kurose and K. W. Ross, Computer Networking, A Top-Down Approach, 6th ed., *Pearson Education, Inc.*, 2013.

[5]. N. Raptis, G. Pekridis, K. Krillakis, K. Panoliaskos, E. Roditi and D. Syvridis, Implementation and assessment of a Non-Line-of-Sight network cluster operating at the UVC wavelength band, *Proceedings of SPIE: Free-Space Laser Communications XXXIV*, Vol. 11993*,* 2022.

[6]. G. Bianchi, Performance analysis of the IEEE 802.11 distributed coordination function, *IEEE Journal on Selected Areas in Communications*, Vol. 18, No. 3, 2000, pp. 535–547.

(036)

Preparation and Investigation of a Nanostructured Tuneable Hybrid Mirror for a High-Energy Tamm Plasmon State Generation

A. Belosludtsev [1], O. Buchnev [2, 3] and A. Fedotov [2, 3]
[1] Optical Coating Laboratory, Center for Physical Sciences and Technology,
Savanoriu ave. 231, Vilnius, Lithuania
[2] Centre for Photonic Metamaterials, University of Southampton, Southampton SO17 1BJ, UK
[3] Optoelectronics Research Centre, University of Southampton, Southampton SO17 1BJ, UK
E-mail: belosludtsev@ftmc.lt, vaf@orc.soton.ac.uk;

Summary: It is reported on the experimental observation of a Tamm plasmon state in the near-IR characterised by an anomalously high energy level located in the upper half of the photonic bandgap. The hybrid mirror structure was prepared by using reactive magnetron sputtering. Afterwards, thick film of gold which was deposited at room temperature via thermal evaporation. Finally, two wire-grid nanogratings were fabricated in the Au film using focused ion beam milling. The design and operation principle of the nanostructured hybrid mirror allows its straightforward integration with functional materials for tuning the mirror's wavelength/polarisation extinction ratio.

Keywords: Tamm plasmon, Nanograting, Effective medium approach, Hybrid optical cavity, Distributed Bragg reflector.

1. Introduction

A Tamm plasmon (TP) is a localized resonant optical state, a quasi-particle, which exists at the interface between a metal and a dielectric (or semiconductor) Bragg mirror. Kaliteevski and co-workers [1] have recently pointed out that there must be an optical analogue of such states, the so-called Tamm plasmons, which correspond to optical fields confined at the surface of one-dimensional photonic crystals (i.e., Bragg reflectors) terminated by metal layers. The TP dispersion lies completely within the light cone and, therefore, in contrast to an ordinary surface plasmon polariton, a TP can be excited with both transverse electric (TE)- and transverse magnetic (TM)-polarized light at any angle of incidence. Also, unlike conventional surface plasmons, Tamm plasmons are largely insensitive to ohmic losses in metal layers.

Tamm plasmons have been experimentally demonstrated in and are currently regarded as a viable alternative to conventional surface plasmons in many applications, including optical switches, semiconductor lasers, light emission and harmonics generation, solar cells, and sensors.

The design and operation principle of the nanostructured hybrid mirror allows its straightforward integration with functional materials for tuning the mirror's wavelength/polarisation extinction ratio.

1.1. Structure Fabrication

It was prepared a multilayer coating. It consist of pairs of Nb_2O_5 (high index) and SiO_2 (low index) layers with a thickness of, respectively, 159 nm and 246 nm, which were deposited onto a 1 inch diameter and 1 mm thick double-side polished fused silica substrate using reactive magnetron sputtering. The nanograting was milled in a larger patch of the film using a focused ion beam. The slits of the nanograting were cut through the film and had various different grating width. The period of the pattern ensured that the nanograting would operate in the near-IR as a non-resonant, optically uniform anisotropic film transmitting and reflecting light without diffraction in the substrate and air.

1.2. Structure Characterization

The spectral response of the fabricated sample was characterised in reflection at normal incidence using an imaging microspectrophotometer (CRAIC Technologies) equipped with a tungsten-halogen light source, broadband linear polarizer and cooled near-IR CCD array.

For single layers and multilayer structures were measured transmittance and reflectance spectra using a Photon RT (Essent Optics) spectrophotometer.

1.3 Results and Discussion

It was recently reported [2, 3] on the first experimental demonstration of the predicted high-energy Tamm plasmon state in the near-IR and provide an insight into its microscopic nature. We also show that the appearance of such a state cannot be described in the frame of the commonly employed transfer matrix method and the effective medium approach, suggesting that the latter has limited applicability to nanostructured non-resonant metal films. The example on investigated structure and measured spectra are shown in Fig. 1.

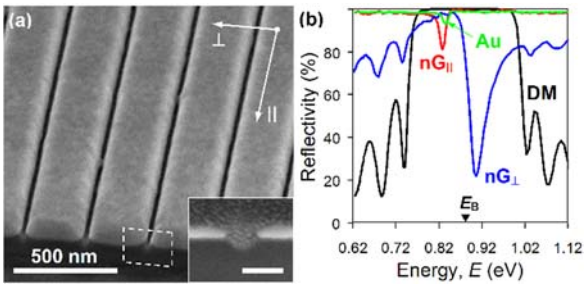

Fig. 1. (a) SEM image of a fragment of Au nanograting with the period of 300 nm fabricated on top of a dielectric mirror. (b) Reflectivity spectra measured in different areas of the sample corresponding to a pristine dielectric mirror (black, DM), mirror coated by a continuous 50 nm thick Au film (green, Au) and mirror terminated by the nanograting with its slits being parallel (red) and orthogonal (blue) to incident polarization. Figure taken from [2].

One of the way of tuning the resonances is to change the period of the nanograting. It was shown how the energy of the anomalous state changing it‘s level.

4. Conclusions

We observed experimentally and analysed numerically the appearance of an anomalous near-IR Tamm plasmon state, which emerged at the interface between a conventional, completely periodic Bragg reflector and a sub-wavelength non-resonant gold nanograting. The observed state had the energy exceeding the theoretical limit achieved in the case of a continuous semi-infinite gold layer

Acknowledgements

We would also like to acknowledge the financial support of the UK Engineering and Physical Sciences Research Council (EP/R024421/1) and European Social Fund (project No 09.3.3-LMT-K-712-19-0203) under grant agreement with the Research Council of Lithuania (LMTLT).

References

[1]. E. I. Tamm, O Vozmozhnoi Sviazi Elektronov na Poverkhnostiakh Kristalla, *Journal of Experimental and Theoretical Physics* 3, 34, 1933 (in Russian).
[2]. O. Buchnev, A. Belosludtsev, V. A. Fedotov, Observation of a High-Energy Tamm Plasmon State in the Near-IR, *ACS Applied Materials & Interfaces,* 14, 2022, pp. 13638–13644.
[3]. O. Buchnev, A. Belosludtsev, V. Reshetnyak, D. R. Evans, V. A. Fedotov, Observing and controlling a Tamm plasmon at the interface with a metasurface. *Nanophotonics,* 9, 2020, pp. 897–903.

(038)

Optical Computation of a Spin Glass Dynamics with Adaptive Optics

Marco Leonetti [1, 2], Luca Leuzzi [1], Erik Hörmann [3], Giorgio Parisi [2, 3] and Giancarlo Ruocco [1, 3]
[1] Center for Life Nano Science@Sapienza, Istituto Italiano di Tecnologia, 00161 Rome, Italia.
[2] CNR NANOTEC-Institute of Nanotechnology, Soft and Living Matter Lab, 00185 Rome, Italy
[3] Department of Physics, University Sapienza, 00185 Roma, Italy
Tel.: +393284593011
E-mail: marco.leonetti@iit.it

Summary: Spin glasses (SGs) are paradigmatic physical models whose dynamics computation is nondetermistic polynomial-time hard. Here we report on a recent implementation of the optical simulation of an SG, exploiting the N segments of a wavefront-shaping device to play the role of the spin variables, combining the interference downstream of a scattering material to realize the random couplings between the spins. In the optical SG, where interaction terms are realized simultaneously when the independent light rays interfere on the detector's surface, we demonstrate a speedup, with respect to purely in-silico simulations, scaling with N.

Keywords: Optical computation, Complex photonics, Adaptive optics, Light diffusion.

1. Introduction

Optical computing is an emerging trend in computation and it involves using a pairing of an optical layer with a traditional digital processing machine to improve performances while reducing computational costs and processing times. It promises parallel processing and high bandwidth that may be eventually performed in free space, with limited power consumption (e.g., Fourier transform performed by a lens). Optical computation is an emerging scheme in quantum transport, quantum simulation [1], and machine learning, and can be implemented on different platforms including free space, photonic chips, and optical fibers. One of the advantages brought by optics is that certain operations can be performed at the "speed of light." Indeed, we can estimate the evaluation of a matrix product as fast as a modulated light beam can pass through an opportunely tailored diffractive pattern [2].

By exploiting last-generation optical modulation devices, millions of light rays can be driven simultaneously between several states within microseconds, thus potentially providing a scalable optical platform that only needs to be built around the relevant computationally hard problem.

Spin glasses [3] serve as prototype models, capable of providing both equilibrium and off-equilibrium nontrivial phenomenology. In particular, the dynamics in an energy landscape with many equilibrium states and the origin of (multiple) relaxation times in finite dimensional systems are open questions in modern statistical mechanics. Complex systems from diverse fields fall into the spin glass universality class, e.g. brain functions, random lasers, and quantum chromodynamics. Indeed, novel methods for the calculation of the equilibrium states and of the dynamics of a spin glass system are highly sought after.

In a recent paper [4], and employing the experimental setup sketched in Fig. 1, we proposed an optical system to compute the dynamics of a given spin glass state. We paired the optical layer with a standard digital computation layer to realize an optical spin glass (OSG) dynamics simulation. We observed that the overall intensity at P given points on a screen placed downstream of a strongly scattering medium shone with N coherent light rays from a single laser can be formally written as a spin glass Hamiltonian. Thus we proposed scattering, coupled with an adaptive optical element, as an instrument to access the spin glass dynamics and employed for low-complexity simulations.

In the optical layer, the illumination state, mimicking the spin state, is controlled by a digital micromirror device (DMD). Using the superpixel method, we are able to provide individual control of the input laser wavefront through many segments, each one composed of four DMD mirrors. Each i-th segment can be then programmed into a state characterized by a phase factor $\varphi_i = \pm\pi$, equivalent to an amplitude factor of $S_i \in \{-1, +1\}$.

In this configuration, light at the back of a disordered medium can be expressed like:

$$I = EE^T = \sum_{i,j}^{N} \xi_i a_i \xi_j^T a_i^T = \\ = \sum_{i,j}^{N} |\xi_i||\xi_j| a_i a_j e^{i(\psi_i - \psi_j)} \quad (1)$$

where a_i is the input field on the i[th] modulator segment, and $\xi_i = |\xi_i| exp(i\psi_i)$ is the transmission matrix element connecting the output to the i[th] input segment.

We then rewrite the terms in the sum as follows:

$$|\xi_i||\xi_j|e^{i(\psi_i-\psi_j)} = V_{i,j} \quad (2)$$

and we study the special case of a flat input wavefront, whose electric field can only take in the +1 or -1 configuration. The state of the adaptive optical element is therefore: $a_i = S_i = [\pm 1]$.

We can express the intensity as:

$$I = \sum_{i,j}^{N} V_{i,j}\, S_i S_j \quad (3)$$

Which is the same formal dyadic expression as the Spinglass Hamiltonian.

2. Methods

With the guidance of the relations laid down in the previous paragraph, we are now able to perform a **Monte Carlo optical simulation** in the canonical ensemble on the optical system. This begins with an initialization step, and then follows the standard Metropolis rule for each updates:

1) We select a random segment S_i and we change it's state by switching its sign
2) We measure the resulting intensity at the target
3) We accept the with an acceptance probability P_{acc} given by the Metropolis choice:
$$P_{acc} = \min\{1,\ e^{\beta \Delta E}\}$$
4) If the change is refused, we restore the previous configuration is restored
5) The loop is iterated for a given number of iterations N_{iter}

The **superpixel method** allows us to modify the ON-OFF modulating nature of the DMD, which would give rise to spin states $S_i = \{0,1\}$ to a phase shift of the incident wavefront, which is used to achive the correct spin states $S_i = \{-1, +1\}$. This technique is based on the phase delays accumulated by light rays corresponding to different pixels, if light is collected from specific positions in Fourier space. The first step is to collect light thought a spatial filter (the iris in Fig.1). In such case each DMD pixel acquires a relative phase delay which depends on its position in the real space: in particular, if pixel are identified by a couple of integers $[x_i, y_i]$ (coordinates in the DMD plane), pixels with even $T = x_i + y_i$ have a constructing interference while pixels with odd T contribute with a destructive interference. We organize the DMD into superpixels composed by 2×2 DMD pixels, in which the two configurations $S_i = \{-1, +1\}$ are obtained activating only the pixels with even or odd T parameter (which are the oneslaying on either diagonal of the 2×2 groups). In order to optically merge the pixels of the same superpixel we reduce the optical resolution in order to *blur them together*. This is performed with the aforementioned iris, which is tuned on a diameter of 2.66 mm, producing an optical resolution of 32 μm. Since the DMD pixel pitch is equal to 13.68 μm, the superpixel essentially act as a single light source on the detector surface.

Noise control plays a crucial role in the simulation, as noise creates a spuriously higher temperature β_{noise} that interfere with the study of phase diagram of the spin glass. The main source of noise in our setup is the camera readout noise, which accounts for approximately 1 count per each pixel of the sensor array. Given the 10 bits dynamic range of the sensor, which allows for $1024 = 2^{10}$ intensity levels on each pixels, and the fact that the superpixel method combines the light of 4 sub-pixels for each elements, this yields a maximum signal to noise ratio (SNR) of 4096/1 per (binned) pixel.

The **simulation time** of the optical simulation was reduced choosing a fast camera, capable of achieving a full frame readout time of 277 μs. We further reduced this time by limiting the region of interest to a small square in the middle of the camera sensor. The area of such ROI should be large enough to allow us to pick a sufficient number of independent readout points, but larger areas involve longer readout times. We have decided to use a total of 69120 pixels, which allowed to reach peak readout times of around 90 μs. The exposure time is kept at its minimum possible value of 1 μs. We used the output laser intensity to regulate under- or over-exposure. The DMD is controlled by the workstation through custom-built drivers, which enables fast updates, with peak performance of 50 μs for the commutation time of two adjacent rows. This is sufficient to perform any single-spin update with the superpixel method. This time also takes into account the time for the stabilization of the micromirrors after the commutation. The digital processing, which includes the random number generation, the data handling and the Metropolis choice algorithm is handled by a standard Threadripper 2950x CPU through the MATLAB programming language, and adds a total overhaul of less than 10 μs. Overall, a complete Metropolis update takes $4.5 \cdot 10^{-4}$ s, of which $1.5 \cdot 10^{-4}$ s is the actual update of the optical system and algorithmic computations, while the rest is due to the overhaul caused by both the programming language and the input/output handling of the operating system. Such overhaul is quite consistent, accounting for more than half of the time of the simulation step, which leaves ample space for improvement. In fact, a sustained average of just above $1.5 \cdot 10^{-4}$ s should be achieved with a transition to a custom operating system and a programming language closer to the silicon layer.

3. Results

In Fig. 2, we study the simulation time, which is an important parameter to confirm the advantage of the optical setup on *in-silico* simulations, as well as the gateway to tackle simulations of very large systems that are currently too expensive to simulate. We report a measurement with a large fully connected spin glass (N = 12,100 micromirror-combined spins organized into a 110 × 110 2D square lattice). We retrieve a minimum time per step (TPS) of 10^{-4} s per step for this large optical experiment.

This TPS is barely dependent on N: see the inset in Fig. 2, where we report the TPS for the optical simulation as red circles. The TPS for the digital simulation is, instead, growing with N , as expected (Fig. 2, Inset, blue circles). The optical simulation can thus outperform the digital one at N = 12,000. Only a small portion of the full DMD has been exploited thus further advantage may be achieved by the optical measurement.

In Fig. 3, we report the self-correlation function F_{self} as a function of time, expressed in *sweeps*. One sweep is equal to *N* Monte Carlo steps, where *N* is the system size. In other words, one sweep is the time needed to perform a single update of all the spins in the system.

We then perform a best fitting on the self-correlation function using the following equation:

$$F_{self}(\tau) = (1 - A)e^{-\frac{\tau}{\tau_1}} + A\frac{C}{\tau^a}$$

in which the first term is the exponential relaxation time, while the second term comes from the power law decay appearing when approaching the glassy phase.

The A parameter represents the relative weight of the two terms; the larger it is, the more the power-law-like term is relevant. We can observe that the first order phase transition of the A parameter (smoothen by finite size effects) is observed in the optical simulation. Furthermore, it is in accordance with the predictions of the standard computer simulations.

As expected, as temperature decreases, the system moves from the paramagnetic phase towards spin glass phase. This transition is quantifiable by sharp transition in a number of key observables:

- The weight A of the power-law decay contribution in the critical region (Fig. 3C)
- The correlation time τ_1 (Fig. 3D)
- The power-law decay exponent a in the critical region (Fig. 3E)
- In addition, we have studied the weight A of the power-law decay contribution in the critical region (Fig. 3C)

Critical slowing down of the dynamics, which is a symptom of a system with many uncorrelated local minima of the free energy landscape.

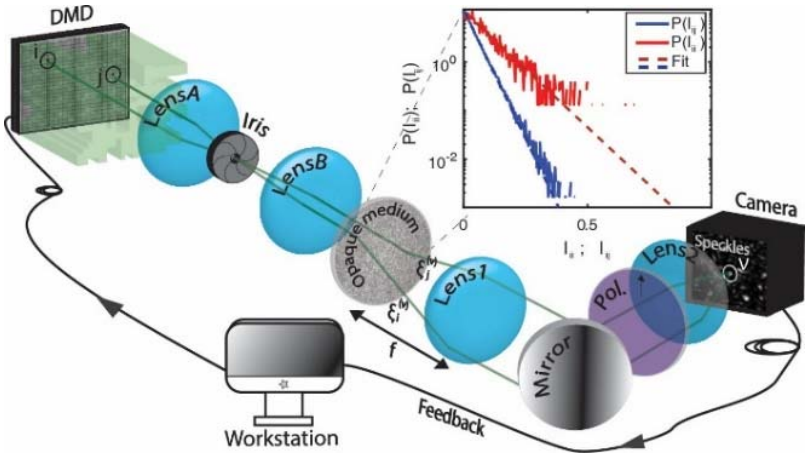

Fig. 1. A sketch of the experimental setup. Light modulated by a digital micromirror device, in the State S in the superpixel mode, impinges on an opaque medium and thus each light ray is independently de-phased and attenuated. Transmitted light is measured on the camera. Intensity measure on a target is described from an equation identical to the SG Hamiltonian, where the role of the J_{ij} matrix is played by the scattering matrix of the opaque medium.

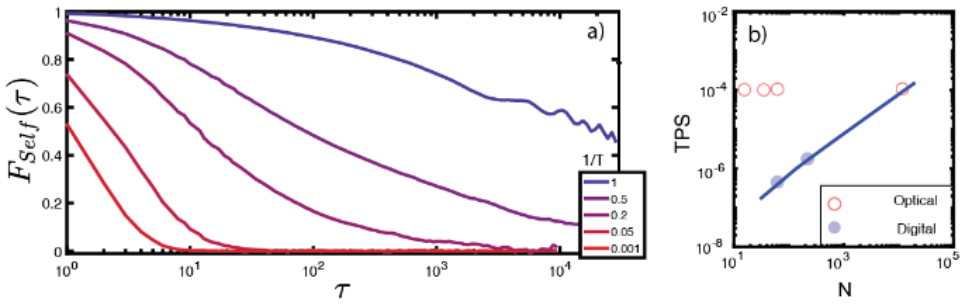

Fig. 2. Optical Supremacy. In a) we report the F-Self (dynamical self-similarity of S at different time with temporal distance τ) of a large scale simulation with N=12000. In b) it is reported the time per step (TPS) as a function of the number of segments /spins N, for the optical and digital simulation.

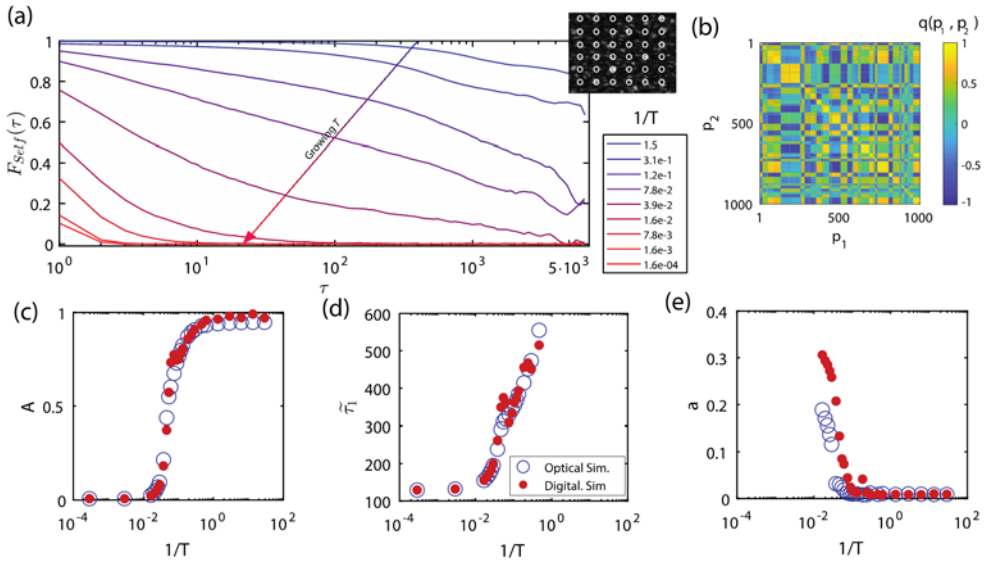

Fig. 3. Results for $P = 36$, $N = 225$. (*A*) The F_{self} as a function of τ indicating the sweeps. The *Inset* reports the image on the camera, with white circles highlighting the target positions. In *B*, we report the degree of similarity obtained for clusterized states resulting many optimizations at zero temperature. The phase space results clusterized in many states. In *C–E*, we report, respectively, *A*, τ_1, and *a* as a function of 1/T, comparing the results from the digital simulation (red full dots) with those of the optical simulation (open blue symbols). In *D*, τ_1 is reported only in the region where the exponential contribution results a reasonable interpolation, while, in *E*, *a* is reported only in the critical region.

4. Conclusions

This work has proven the viability of simulating the dynamics of a system with N spins and N2 couplings with random couplings and exhibiting a spin glass phase at low-temperature. This approach has several advantages:

- **Scalability**: it allows to simulate very large systems with a fixed calculation speed O(1), because the calculation is performed instantaneously by the interference of the light beam, which enables the calculation of the energy difference without explicitly solving the O(N) coupling terms;
- **Flexibility**: by varying the constraints density, we are able to investigate both a ferromagnetic-like ordering, which allows to retrieve the transmission matrix patterns, and a spin glass state, in which loss of memory, critical slowdown, and other critical phenomena occur. This is achieved by changing the number of optical targets over which the intensity is summed;
- **Generalizability**: the superpixel method opens a breath of possibilities for generalization. We are able to simulate both variables taking multiple discrete state and complex continuous phasors. In the multiple discrete variables configuration, as long as the number of targets per spin is below the critical $\alpha_c(T)$ value of memory retrieval, the analysis of the ferromagnetic Mattis-like states allows reconstruction of the transmission matrix elements of the random opaque medium through the states ***S*** visited in the optical simulation, as memories learned in a neural network.

References

[1]. N. C. Harris, et. al., Quantum transport simulations in a programmable nanophotonic processor, *Nature Photonics,* Vol. 11, 2017, pp. 447.

[2]. N. H. Farhat et. al., Optical implementation of the Hopfield model, *Applied Optics*, 24, 10, 1985, pp. 1469-1475.

[3]. M. Mezard, G. Parisi, M. Virasoro, Spin glass theory and beyond: An Introduction to the Replica Method and Its Applications, *World Scientific Publishing Company,* 1987.

[4]. M. Leonetti, L. Leuzzi, E. Hormann, G. Parisi and G. Ruocco, Optical computation of a spin glass dynamics with tunable complexity, *Proceeding of the National Academy of Science*, Vol. 118, No. 21, 2021, e2015207118.

(039)

Bulk Dirac Semimetal for the Exploration of Terahertz OptoelectronicDevices

Tony Mathew Blessan, C. Venkateswaran and N. Yogesh
Department of Nuclear Physics, University of Madras (Guindy Campus), Chennai -600025, India
E-mail: phy.yogesh@gmail.com

Summary: By making use of the symmetrically coupled terahertz (THz) surface plasmon polariton (SPP) modes in bulk Dirac semimetal (BDS), we have demonstrated sub-wavelength waveguiding in a curved BDS geometry and the possibility of all optical logic gates at terahertz frequencies recently. In this contribution, we further demonstrate how our findings will work with 3-D integrated terahertz photonic circuits so that the exploration of THz optoelectronic devices are possible with BDS.

Keywords: Bulk Dirac semimetal (BDS), Sub-wavelength waveguiding, THz logic gates, Surface Plasmon Polariton (SPP).

1. Introduction

Surface Plasmon Polariton (SPP) are the quanta of quasi-interaction between electromagnetic (e-m)wave and plasmons (collective excitations ofelectrons) at the interface between plasmonic materialand a dielectric. At optical frequencies, bulk metals shows negative dielectric permittivity and they exhibit plasmonic response. For the formation of SPP resonance at optical frequencies one can, not only usebulk metals but also the artificial e-m structures including metamaterials. However, for the terahertz (THz) range (0.1 THz-10 THz), the availability of natural materials with plasmonic response is limited. To overcome this limitation, researchers are exploring the option of employing bulk Dirac semimetals (BDS) such as Cd_3As_2 [1], Na_3Bi and $ZrTe_5$. In our previous study, we have reported how the curved geometries of BDS sustain THz SPPs using Kretschmann–Raether and Otto configurations [2]. Moreover in our latest report, we demonstrated the possibility of SPP waveguiding and all optical THz logical gates with BDS [3]. In this contribution, we further demonstrate how the THz sub-wavelength waveguiding and THz logic gate are possible with BDS system using a three-dimensional integrated photonic circuit design numerically.

1.1. Bulk Dirac Semimetal

The Dirac semimetal is an unusual material in which the nodes of the bulk electronic states are protected against the gap formation by crystalline symmetry leading to high carrier mobility and dramatically reduced intrinsic Ohmic losses. We observe that that BDS is a promising candidate for THz plasmonic applications in the regime (0.5 THz – 2 THz) bytheoretically analyzing its dielectric response. The dielectric function of BDS is expressed through

$$\varepsilon_r(\omega) = \varepsilon_\infty + \frac{i\sigma(\omega)}{\omega\varepsilon_0},$$

where $\sigma(\omega)$ is obtained from Kubo formalism [4]. We can infer from Fig. 1 that BDS is an excellent candidate for supporting SPP at (0.1 THz – 2 THz) regime because the real and imaginary part is considerably small.

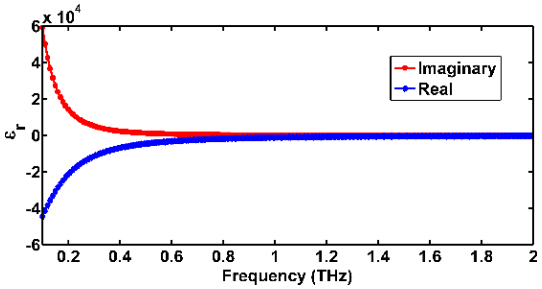

Fig. 1. Complex dielectric permittivity of BDS.

2. THz SPP Waveguiding in Curved BDS Geometry

It is known that when the separation between two adjacent BDS sheets is smaller than the skin depth, SPP at each BDS boundaries can interact together to form a coupled propagating (symmetric or anti-symmetric) SPP mode. In our preceding work [2, 3], detailed analysis of THz SPP sustainment in single and multilayer BDS curved geometries have been examined and concluded why symmetrically coupled THz SPP mode are preferred over anti-symmetric SPP mode. Here we extend our analysis to 3-D BDS geometries. Firstly, BDS-Air-BDS multilayer with optimized air gap (***g***) of 50 μm between two BDS slabs of height 850 μm and optimized thickness as 7 μm as shown in Fig. 2(a) is

modelled with scattering boundary conditions in all three directions and solved using COMSOL RF module with boundary mode analysis. The corresponding H_z field profile at 1.9THz given in Fig. 2(b) shows the sustainment of SPP mode. When a perturbation is introduced in the form of a macrobend (radius of curvature is 500 µm) as shown in Fig. 2(c), SPP still sustains along the bend. The corresponding H_z field profile at 1.9 THz givenin Fig. 2(d) ascertain that symmetric SPP can evade bends efficiently without much losses as it is confinedwithin BDS walls.

3. Plasmonic Terahertz Logic Gates

The waveguiding feature (Fig. 2) shown inparallel BDS system with circuit miniaturization can be extended to the realization of logic gates as it is an essential component for the empowerment of THz optoelectronics. Considering the evading nature of symmetric mode SPP in macrobend geometry, one can very well reach out its application to logic gate. Fig. 3(a) shows the geometry of XOR gate in the form of Y-structure whose input arms are separated by 136 µm and the continuing arm of length 600 µm serves as an output. When coupled SPP modes ineach input arm are in phase, constructive interference occurs and when they are 180° out of phase with each other, destructive interference takes place which cancels out the output signal in the detection port. To support the Y configuration, SiO_2 substrate ($\varepsilon_r = 4.2$)of dimension $1500\mu m \times 600\mu m \times 50\mu m$ is placed at the bottom. The norm of magnetic field strength ($|\vec{H}|$) patterns shown in Fig. 3(b), 3(c) and 3(d) demonstrateXOR gate at frequency 1.192 THz. The output transmission level less than 50 % can be marked as a threshold for OFF state. Interestingly, the destructive interference of coupled SPP modes correspond to low transmission level of 15.60 % at 1.192 THz. Table 1 shows the truth table for XOR gate at 1.192 THz.

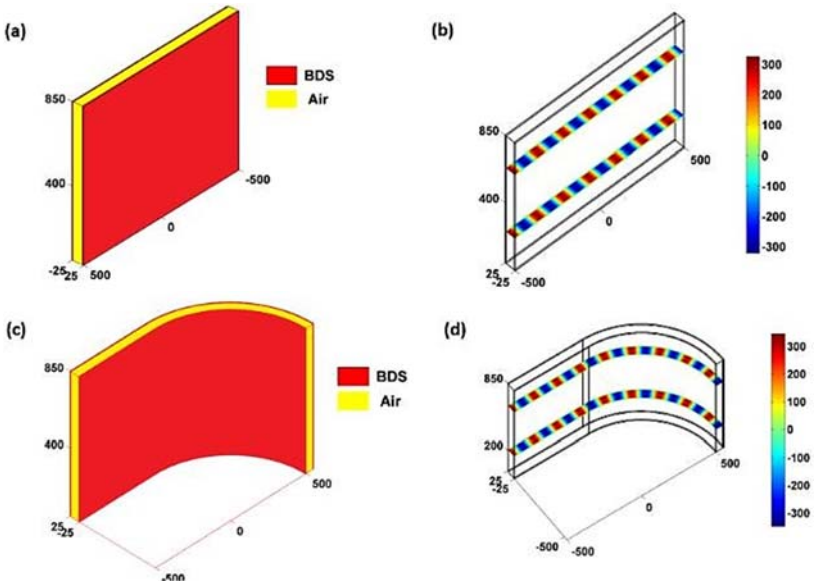

Fig. 2. BDS-Air-BDS configuration a) Straight 3-D geometry; b) corresponding H_z field map at 1.9 THz; c) Macrobend 3-D geometry; d) corresponding H_z field map at 1.9 THz.

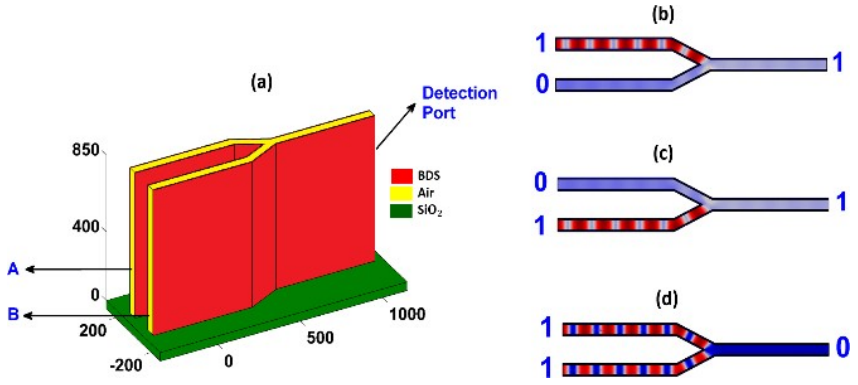

Fig. 3. (a) 3-D Logic gate designed formed by parallel BDS structure; (b)-(d) represent norm of $\vec{H}$ field patternsfor XOR gate at 1.192 THz.

Table 1. Truth table for XOR gate.

Input		Output (S21%)
A	**B**	**XOR (1.192 THz)**
0	0	0
1	0	62.90
0	1	62.91
1	1	15.60

4. Conclusion

To conclude, with the advent of operating room temperature BDS [5], the reported sub-wavelength 3-D curved BDS waveguide and plasmonic logic gate at THz waveband opens up a new horizon for designing BDS based THz optoelectronics devices.

Acknowledgements

This work was funded by the Department of Science and Technology, Ministry of Science and Technology,India (DST/INSPIRE/04/2015/002420).

References

[1]. Z. Wang, H. Weng, Q. Wu, X. Dai and Z. Fang, Three-dimensional Dirac semimetal and quantum transport in Cd_3As_2, *Phys. Rev. B*, Vol. 88, Issue 125427, 2013, pp. 1-6.

[2]. T. M. Blessan and N. Yogesh, Terahertz surface plasmon polariton resonances and microparticle sensing in bulk Dirac semimetal with spatially perturbed geometries, *J. Opt. Soc. Am. B*, Vol. 38, Issue 8, 2021, pp. 2261-2266.

[3]. T. M. Blessan, C. Venkateswaran and N. Yogesh, All- optical terahertz logic gates based on coupled surface plasmon polariton subwavelength waveguiding in bulk Dirac semimetal, *Optik*, Vol. 257, Issue 168795, 2022, pp. 1-9.

[4]. T. Zhao and Z. Wu, Cherenkov terahertz radiation from Dirac Semimetals surface plasmon polaritons excited by an electron beam, *Chinese Phys. B*, Vol. 29, Issue 034101, 2020, pp. 1-10.

[5]. Z. Dai, M. Manjappa, Y. Yang, T. C. W. Tan, B. Qiang, S. Han, L. J. Wong, F. Xiu, W. Liu and R. Singh, High Mobility 3D Dirac Semimetal (Cd_3As_2) for Ultrafast Photoactive Terahertz Photonics, *Adv. Funct. Mater.*, Vol. 31, Issue 2011011, 2021, pp. 1-9.

(040)

Laser Processing by Ultrafast Bursts of Pulses

A. Žemaitis, M. Gaidys, P. Gečys and M. Gedvilas
Department of Laser Technologies (LTS), Center for Physical Sciences and Technology (FTMC), Savanoriu Ave. 231, 02300 Vilnius, Lithuania
E-mail: andrius.zemaitis@ftmc.lt

Summary: State-of-the-art femtosecond laser producing various temporal schemes of light pulses was utilised to explore the processing efficiency of metals. The comparison of burst, biburst, and single-pulse ablation efficiencies was performed for beam-size-optimised regimes, showing the real benefits of laser milling and drilling processing methods. Highly-efficient ultrafast laser processing was achieved for 1030 nm laser wavelength: 8.8 $\mu m^3/\mu J$ for copper drilling, 5.6 $\mu m^3/\mu J$ for copper milling, and 6.9 $\mu m^3/\mu J$ for steel milling.

Keywords: GHz burst, Biburst, Ablation efficiency, Ultrafast laser, Drilling, Milling.

1. Introduction

Laser micro-machining by ultrafast light pulses is an attractive technique due to the confined laser-matter interaction area and pulse duration being shorter than electron-phonon thermalisation time, which results in high processing quality [1]. Nevertheless, the demands on high throughput and quality come from the laser-based manufacturing industry, resulting in constantly evolving laser technology. To keep up with global technological progress, laser source manufacturers put a lot of effort to produce high average power lasers with pulse repetition rates in the range of MHz and even GHz in the burst working regime. It is known that the average power of ultrafast lasers doubles every three years, following famous Moor's law [2]. Pulse repetition rates in the range of MHz or GHz allows division of high pulse energy and induce heat accumulation and low energy losses for more efficient processing [3–5]. All of the efforts are focused on making laser production faster and keeping laser technology as the preferred method for precision material processing. To exploit the full potential of laser ablation, the processing efficiency has to be optimised.

The ablation efficiency can be specified as the volume of the material removed per laser energy, for example, $\mu m^3/\mu J$. The ablation efficiency is calculated by [6]:

$$\eta_E = \frac{\delta}{2F_0} \ln^2\left(\frac{F_0}{F_{\text{th}}}\right), \quad (1)$$

where δ is the effective energy penetration depth, F_0 is the peak fluency and F_{th} is the ablation threshold. Peak fluency F_0 depends on the laser beam radius $w(z)$:

$$F_0 = \frac{2E_{\text{p}}}{\pi w^2(z)}. \quad (2)$$

where E_{p} is the pulse energy and z is the sample focus position. Therefore, by adjusting the distance between the focusing lens and sample surface the ablation efficiency can be optimised [7, 8]. The beam size optimisation technique allows simultaneous improvement of ablation efficiency and ablation rate leading to superior surface quality.

In this work state-of-the-art femtosecond laser with the possibility to produce bibursts with repetition rates of 64.5 MHz or/and 4.88 GHz was used to process copper and steel samples [9]. Variations in the number of pulses per burst in traditional burst regimes and in the biburst mode were used to investigate ablation efficiency and quality of processed samples. Burst, biburst, and single-pulse ablation efficiencies were compared for beam-size-optimised regimes, revealing the true benefits and drawbacks of milling and drilling processing methods. Research of ablation quality in terms of the resulting surface roughness after laser processing was performed as well.

2. Experiment

A solid-state industrial-grade laser (Pharos, Light Conversion) capable of producing light pulses of $\tau = 210$ fs duration at $\lambda = 1030$ nm wavelength was utilised in the laser processing experiments (Fig. 1 a). A galvanometer scanner (Intelliscan 14, Scanlab) coupled with an F-theta lens with a focal distance of 100 mm were used to scan and focus the laser beam, while the beam waist location and precise sample positioning were performed by linear *Z*- and *XY*-stages. The cutting-edge technology laser had four modes of operation: 1) the traditional pulsed operation with a pulse repetition rate of $f_{\text{P}} = 100$ kHz; 2) MHz burst – producing burst of pulses with an intra-burst repetition rate of $f_{\text{MHz}} = 64.68$ MHz; 3) GHz burst – producing burst of pulses with an intra-burst repetition rate of $f_{\text{GHz}} = 4.88$ GHz; 4) Biburst – burst in the burst operation, where a set of 4.88 GHz burst pulses can be burst again at 64.5 MHz (Fig. 1 b). The laser source was always operating at a repetition rate of $f_{\text{B}} = 100$ kHz A maximum average optical power on the sample surface was $P_{\text{ave}} = 7.3$ W, which was always kept constant during the experiments.

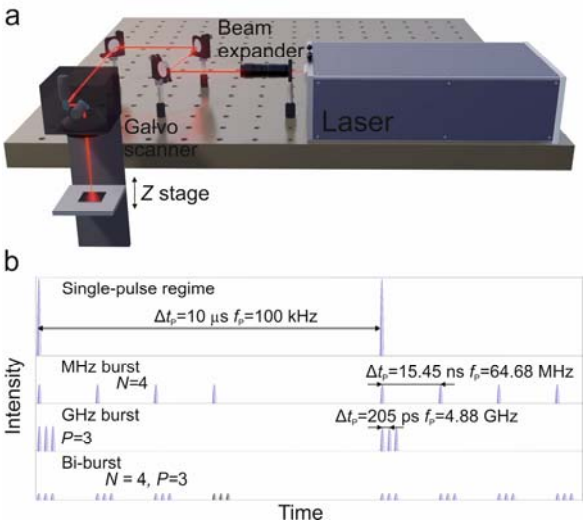

Fig. 1. (a) Laser processing setup. (b) Operational modes of ultrafast laser.

To calculate laser milling efficiency rectangular cavities with dimensions of 2 × 1 mm^2 were engraved into stainless steel (1.4301) and copper (purity of 99.9%) plates. Rectangles were scanned multiple times to be measurable in depth by stylus profiler (Dektak 150, Veeco) and to have situation closer to the real life application, were multiple scans are needed to reach desired depth. The bidirectional scanning of parallel lines separated by hatch distance was used. Hatch distance was kept constant of 10 μm. The depth and surface roughness R_a of the milled cavities were measured by the stylus profiler. In the case of laser drilling, different number single-pulses or bursts ranging from 1 to 1000 were shot into the one spot to have a situation closer to real percussion drilling. Volume of the removed material was measured by 3D optical profiler (S neox, Sensofar).

3. Results and Discussion

Ablation efficiencies were measured for single-pulse, MHz-, GHz- and biburst laser operation modes. Beam size optimisation method was applied for various pulse numbers per burst for drilling of craters (Fig. 2) and milling of rectangular cavities.

In the case of MHz burst processing of copper, the strong dependence of odd and even number of pulses per burst was clearly visible for both crater ablation and cavity milling. The highest ablation efficiency for MHz burst crater drilling was 8.8 μm^3/μJ for $N = 3$ pulses per burst and was higher than conventional mode efficiency by 15 %. For cavity milling, the highest ablation efficiency was 5.6 μm^3/μJ for $N = 3$ pulses per MHz burst and was higher than single-pulse mode efficiency by 8 %.

In the case of GHz burst processing the ablation efficiency for copper milling decreased by ~90 % compared to conventional mode processing. For GHz burst copper drilling the efficiency was also significantly reduced by 80 – 90 % depending on the number of pulses per burst compared to the single-pulse drilling. The ultrashort pulse laser-matter interaction caused plasma and particle shielding, which partially blocked the incoming laser pulses, resulting in a substantial efficiency decrease for GHz burst processing.

For the biburst milling of copper and steel the ablation efficiency values were not much different from the GHz burst milling being, about three times less efficient than single-pulse milling. High ablation efficiency values were measured for copper biburst drilling, which at the certain number of pulses per burst combination, exceeded the value of the single-pulse drilling. The difference of biburst drilling and milling efficiencies was huge, at a certain combination of pulse per burst copper drilling had the efficiency more than 12 times higher than milling. Due to the recoil vapour pressure, heat-induced melt is expelled out of the crater during drilling, while during milling melt flows back on the processed area and does not contribute to material removal.

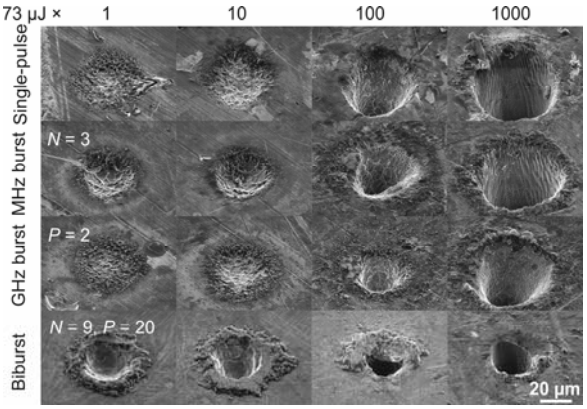

Fig. 2. Laser drilling in copper by conventional and burst modes of femtosecond pulses. Numbers in columns represent quantity single-pulses or bursts per irradiation spot. Energy of single pulse or burst was always 73 μJ.

4. Conclusions

The study of laser ablation efficiency for processing of copper and steel by MHz and GHz bursts of pulses was performed. The novel biburst mode showed promising results in the copper drilling experiments. High laser processing efficiency was achieved: 8.8 μm^3/μJ for copper drilling, 5.6 μm^3/μJ for copper milling, and 6.9 μm^3/μJ for steel milling.

Acknowledgements

This project has received funding from European Regional Development Fund (project No. 01.2.2-LMT-K-718-03-0050) under grant agreement with the Research Council of Lithuania (LMTLT).

References

[1]. K. Sugioka and Y. Cheng, Ultrafast lasers — reliable tools for advanced materials processing, *Light: Science & Applications,* Vol. 3, 2014, p. e149.

[2]. R. Weber and T. Graf, The challenges of productive materials processing with ultrafast lasers, *Advanced Optical Technologies,* Vol. 10, No. 4–5, 2021, pp. 239–245.

[3]. C. Kerse, H. Kalaycıoğlu, P. Elahi, et al., Ablation-cooled material removal with ultrafast bursts of pulses, *Nature,* Vol. 537, 2016, pp. 84–88.

[4]. K. Mishchik, G. Bonamis, J. Qiao, et al., High-efficiency femtosecond ablation of silicon with GHz repetition rate laser source, *Optics Letters*, Vol. 44, No. 9, 2019, pp. 2193–2196.

[5]. A. Žemaitis, P. Gečys, M. Barkauskas, G. Račiukaitis, and M. Gedvilas, Highly-efficient laser ablation of copper by bursts of ultrashort tuneable (fs-ps) pulses, *Scientific Reports,* Vol. 9, No. 1, 2019, p. 12280.

[6]. G. Račiukaitis, M. Brikas, P. Gečys, B. Voisiat, and M. Gedvilas, Use of High Repetition Rate and High Power Lasers in Microfabrication: How to Keep the Efficiency High? *Journal of Laser Micro/ Nanoengineering,* Vol. 4, No. 3, 2009, pp. 186–191.

[7]. A. Žemaitis, M. Gaidys, M. Brikas, P. Gečys, G. Račiukaitis, and M. Gedvilas, Advanced laser scanning for highly- efficient ablation and ultrafast surface structuring: experiment and model, *Scientific Reports*, Vol. 8, November 2018, p. 17376.

[8]. A. Žemaitis, M. Gaidys, P. Gečys, G. Račiukaitis, and M. Gedvilas, Rapid high-quality 3D micro-machining by optimised efficient ultrashort laser ablation, *Optics and Lasers in Engineering,* Vol. 114, 2019, pp. 83–89.

[9]. A. Žemaitis, M. Gaidys, P. Gečys, M. Barkauskas, and M. Gedvilas, Femtosecond laser ablation by bibursts in the MHz and GHz pulse repetition rates, *Optics Express,* Vol. 29, No. 5, 2021, pp. 7641–7653.

(041)

Highly Sensitive Plasmonic Sensor Device made of Au Nanoantennas on SiO_2 Nanopillar Arrays

P. Venugopalan[1] and S. Kumar[2]
[1] Faculty of Engineering, New York University, Saadiyat Island, Abu Dhabi, UAE
[2] Department of Mechanical Engineering, New York University, Brooklyn, USA
E-mail: pv33@nyu.edu

Summary: We report on plasmonic sensors based on arrays of metallic nanoantennas with a higher sensitivity and enhanced figure of merit (FOM). In the proposed sensor, each gold nanoantenna is on the top of a SiO_2 nanopillar which is placed on a quartz substrate. The role of the nanopillar is to substantially decrease the spatial overlap between the substrate and the enhanced fields generated at plasmon resonance. The refractive index sensitivity of the sensor device, which is the resonance wavelength shift per refractive index unit due to the change in the surrounding material, was numerically obtained as 557 nm/RIU, while the FWHM was calculated around 10 nm with a FOM of 55. The proposed sensor has a great potential for sensing and detection applications.

Keywords: Plasmonic lattice resonance, Plasmonic sensors, Sensitivity.

1. Introduction

Plasmonic nano antennas have recently gained much popularity due to their ability to localise and confine electromagnetic fields in nano regimes, achieved by the coupling of localised surface plasmon resonances (LSPR) [1]. Amongst the other designs, bow tie nano antennas, made of two gold triangles in a tip to tip configuration, provides much stronger electric field confinement and enhancement because of the near-field coupling across the gap and the lightning rod effect [2]. Periodic arrays of metal nano antennas can generate plasmonic lattice resonances (PLR) owing to the coupling between the localised surface plasmons of the metal nano antennas and the diffracted waves from the periodic array. The coupling generates enhanced electric field around the nanostructures that can be employed in plasmonic sensors which rely on the shifts of their lattice resonant wavelength induced by a change in the refractive indices of the ambient media. The performance of a sensor based on such periodic metal arrays is determined by the figure of merit (FOM) which is the ratio of the sensitivity to the full width at half maximum (FWHM). However, substrate supported nano structures suffer from an intrinsic drawback that a fraction of the electromagnetic field around the structure is coupled to the substrate due to its high refractive index [3]. This weakens the intensity of the lattice resonance and thus its FWHM.

In this work, we propose a plasmonic sensor device that overcomes the substrate effect by lifting the nano antenna array by using dielectric nanopillar arrays. Our sensor design consists of arrays of gold (Au) nano antennas placed on top of SiO_2 nanopillars which are in turn placed on a glass substrate. The lifting of the nano antennas provides a more uniform dielectric environment to the metallic nanoantenna arrays. PLRs generated by the proposed design is more sensitive to the ambient medium, thereby improving the performance of the sensor device.

2. Methods

Fig. 1 shows the plasmonic system under investigation consisting of an array of Au nano antennas on the top of a quartz substrate (n_s = 1.46). SiO_2 nanopillar has a diameter of 200 nm (d) and height of 500 nm (h_1). We fixed the geometry of nano antennas, height as 50 nm (h_2), length and width as 140 nm and 150 nm respectively and gap distance as 5 nm, P is the period of the arrays in x and y directions. The refractive index of the ambient media vary from 1.0 to 1.3.

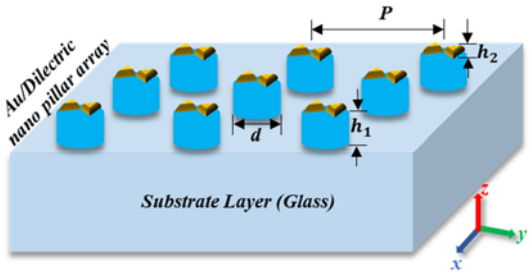

Fig. 1. Schematic of the periodic arrays of Au nano antennas on SiO_2 nanopillars, placed on a quartz substrate.

Three-dimensional finite difference time domain (3D-FDTD) method implemented in a commercial software from Lumerical Inc. (Canada) was used to carry out the simulations. The geometry of nano antenna arrays was described by using Cartesian coordinates with the x and y axis in the plane and with z axis perpendicular to the plane of the arrays. The mesh size was 2 nm × 2 nm × 2 nm in all the simulations. Perfectly matched layers (PML) were used as absorbing boundary condition for z-axis to prevent counterfeit reflections and periodic Bloch boundary conditions in x and y axes. Electromagnetic fields in the proximity of the nano antennas were calculated assuming plane wave illumination, with wavelengths varying between 500 nm and 1000 nm.

The FDTD calculations were carried out for TE (transverse electric) polarization of the electric field, i.e. the incident E-field being polarized along the axis of the nano antennas. Optical constants of gold and SiO_2 were taken from literature [4].

3. Results and Discussions

PLRs generated by the coupling between the LSPR and the diffraction from the periodic arrays, can be very sensitive to the changes of different structural parameters. In this section, we show how the period of the Au nano antenna arrays can control the intensity and position of the PLR wavelength.

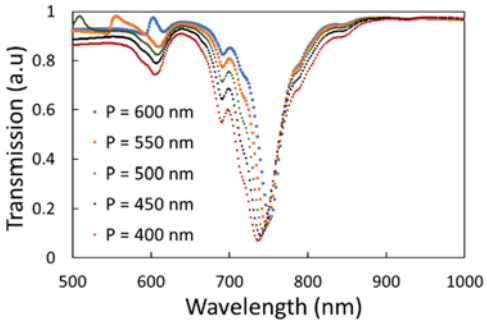

Fig. 2. The simulated transmission spectra of Au nano antennas on SiO_2 nanopillar arrays for different periods, P.

Fig. 2 shows the transmission spectra of Au nano antennas on SiO_2 nanopillars for different array periods. When the array period is increased, the PLR wavelength position is red shifted as is seen in Fig. 2. This is because of the red shifting of the wavelengths of surface diffraction waves, which is proportional to the period of the arrays and the refractive index of the surrounding medium [5]. As the wavelength of the diffraction waves are shifted, coupling between the diffracted waves and localized surface plamons becomes weak and thus increasing the transmitted intensity at the lattice resonances.

Fig. 3 shows the transmission spectra of the proposed sensor in different media environments. Since the wavelength position of the surface diffraction waves moves to red as per the diffraction theory [6], when the refractive index of the medium environment increases, lattice resonant wavelength linearly shifts towards red. Thus the change of the refractive index of the medium environment can be detected by monitoring the transmittance near the resonance wavelength. It can be seen that, when the refractive index of the medium environment increases from 1 to 1.3, the PLR wavelength almost shifts linearly from 750 nm to 917 nm. The sensitivity of the proposed structure, which is defined as the PLR wavelength shift per refractive index unit (RIU) of the structure is thereby calculated as 557 nm/RIU. Furthermore, it can be seen from Fig. 3 that the FWHM of the PLR is about 10 nm. Figure of merit FOM) is calculated as the ratio of sensitivity to FWHM and is thus obtained as 55, which is higher than the previously reported periodic nanoparticle arrays [7].

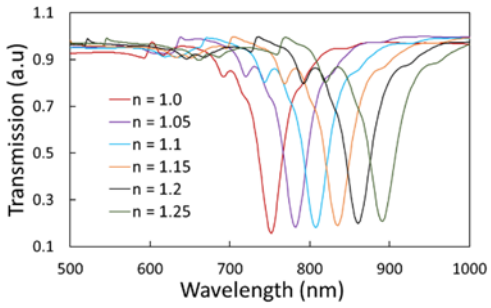

Fig. 3. The simulated transmission spectra of Au nano antennas on SiO_2 nanopillar arrays in different ambient media for a period of 600 nm.

4. Conclusions

In conclusion, a highly sensitive plasmonic sensor device is proposed consisting of Au nanoantennas on SiO_2 nanopillars arrays with a reduced FWHM of the plasmonic lattice resonance of 10 nm (for n = 1.3, P = 600 nm. d= 200 nm, h_1 = 500 nm, h_2 = 50 nm). The calculated refractive index sensitivity of the structure is 557 nm/RIU, which is higher than that (365 nm/RIU) of the previously reported metal arrays. The high sensitivity together with a small FWHM of this device may provide potential advantages in the application of sensors.

References

[1]. P. Bharadwaj, B. Deutch and L. Novotny. Optical Antennas, *Advances in Optics and Photonics*, Vol. 1, Issue 3, 2009, pp. 438-483.

[2]. D. P. Fromm, A. Sundaramurthy, P. J. Schuck, G. Kino, and W. E. Moerner, Gap-Dependent Optical Coupling of Single "Bowtie" Nanoantennas Resonant in the Visible, *Nano Letters*, Vol. 4, Issue 5, 2004, pp. 957-961.

[3]. E. Martinsson, M. A. Otte, M. M. Shahjamali, B. Sepulveda, and D. Aili, Substrate effect on the refractive index sensitivity of silver nanoparticles, *Journal of Physical Chemistry C,* Vol. 118, Issue 42, 2014, pp. 24680-24687.

[4]. P. B. Johnson and R. W. Christy, Optical Constants of the Noble Metals, *Physical Review B,* Vol. 6, 1972, pp. 4370-4379.

[5]. S. M. Sadeghi, R. R. Gutha, and W. J. Wing, Turning on plasmonic lattice modes in metallic nanoantenna arrays via silicon thin films, *Optics Letters,* Vol. 41, Issue 14, 2016, pp. 3367-3370.

[6]. M. Meier, A. Wokaun, and P. Liao, Enhanced fields on rough surfaces: dipolar interactions among particles of sizes exceeding the Rayleigh limit, *Journal of Optical Society of America B*, Vol. 2, Issue 6, 1985, pp. 931-949.

[7]. A. I. Kuznetsov, A. B. Evlyukhin, M. R. Gonçalves, C. Reinhardt, A. Koroleva, M. L. Arnedillo, R. Kiyan, O. Marti, and B. N. Chichkov. Laser Fabrication of Large-Scale Nanoparticle Arrays for Sensing Applications, *ACS Nano,* Vol. 5, Issue 6, 2011, pp. 4843-4849.

(043)

Temporal Talbot Effect in Birefringent Optical Filters for Multiplying Pulse Repetition Rates

Youcef Driouche [1,2], Rachid Hamdi [1,2], Leila Graini [1], Abderezzaq Halassi [1] and Badr-Eddine Benkelfat [2]
[1] Université 8 mai 1945 Guelma, Laboratoire des Télécommunications, BP 401, Guelma 24000, Algeria
[2] SAMOVAR, Télécom SudParis, Institut Polytechnique de Paris, 91120 Palaiseau, France
E-mail: driouche.youcef@univ-guelma.dz

Summary: We propose a pulse rate multiplier based on the temporal Talbot effect using a phase-only birefringent optical filter. The Opto-geometrical parameters of the filter are obtained by an optimization algorithm to achieve the desired spectral response. Preliminary results show excellent agreement with those anticipated by theory.

Keywords: Periodic quadratic phase birefringent filter, Temporal Talbot effect, Pulse repetition rate multiplication.

1. Introduction

Since the first description in 1981 by T. Jannson and J. Jannson [1] of the temporal Talbot effect (TTE) by propagating a temporal pulse train in the first-order dispersion approximation, this phenomenon has become attractive in various applications, such as sub-harmonic clock recovery, optical passive amplification and optical real-time discrete Fourier transformer [2-4]. Besides these applications, pulse repetition rate multiplication (PRRM) techniques induced by TTE have drawn attention throughout the years, because of their simple all-passive realization, with much lower complexity than other PRRM methods. Most importantly, this technique depends on a phase-only filtering process, which can conserve most energy spectrum available from the input signal [5].

In this work, for the first time to the best of our knowledge, we present a new type of pulse repetition rate multiplier based on TTE using birefringent optical filters, which naturally have a periodic quadratic phase and a flattened transmittance. An optimization algorithm is used to determine the Opto-geometrical parameters of the filter. Preliminary results show extremely high fidelity in multiplying a 10 GHz input pulse rate by a factor m without affecting the individual pulse characteristics.

2. Filter Design, Results and Discussion

When a periodic train of optical pulses with a repetition period T_{rep} (or equivalently f_{rep} is the frequency repetition rate), propagate through a continuous quadratic phase filter satisfying the temporal Talbot condition,

$$\ddot{\Phi} = \frac{s}{m}\frac{T_{rep}^{\,2}}{2\pi} \qquad (1)$$

with s and m are mutually prime integer numbers and $\ddot{\Phi}$ is the first-order dispersion coefficient, a copy of the original temporal sequence reappears but with a frequency repetition rate multiplied by a factor m [6]. It's worth noting that the TTE may be achieved with periodic phase filtering as well [7]. This property allows us to take advantage of the periodic nature of the transfer function of the birefringent optical filter. Specifically, our filter should have a free spectral range (FSR) of $m \cdot f_{rep}$, a first-order dispersion coefficient satisfying the TTE condition given by Eq. (1) for each period, and a flattened transmittance.

Fig. 1 illustrates the proposed design of the N-stages birefringent phase filter. The filter consists of N-hybrid stages placed between an input polarizer (P) parallel to the laboratory x-axis and an analyzer (A) oriented at an angle φ_p. Each stage is composed of a birefringent plate (BP) as the identical section associated with a liquid-crystal cell (LCC) as the variable section [8]. The slow (S) and fast (F) axes of each section are parallel to each other and orientated at an angle φ_i (i = 1,2,….N).

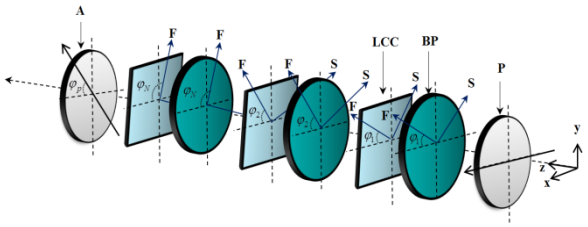

Fig. 1. The configuration of the N-stages birefringent periodic phase filter.

Assuming we have a periodic sequence of Gaussian laser pulses with a repetition period T_{rep} = 100 ps, (f_{rep} = 10 GHz), each pulse has an FWHM pulse duration of 5 ps. We design a birefringent filter to increase this repetition rate by a factor of m = 4 (with s = 1) to generate a pulse train with a frequency repetition rate of f_{rep} = 40 GHz.

Referring to the procedure shown in our previous work [8], and relying on optimization algorithms, for instance, the Genetic Algorithm, the absolute angles and the phase shifts introduced by the LCCs for each stage have to be determined. For our case of $m = 4$, 12 stages-filter of Rutile (Titanium dioxide, TiO2) birefringent plates having a birefringence of 0.25 at $\lambda = 1550$ nm associated with liquid crystal cells (LCC) are required.

The results obtained for the amplitude and phase responses of the proposed filter with the input and output pulse train are depicted in Fig. 2. As shown in Fig. (2a), the amplitude response has a flattened transmittance with a negligible normalized power loss of 0.08 and a peak-to-peak amplitude ripple of 0.08. Fig. (2b) shows the periodic quadratic phase with an FSR of $m \cdot f_{rep}$ (40 GHz) and a first-order dispersion coefficient $\ddot{\Phi} = 397.8874 \text{ps}^2$.

Fig. (2c) represents the normalized temporal intensity for the input and output Gaussian pulse train before and after propagating through the birefringent optical filter. As predicted by theory, the output pulse train is a distortionless replica of the input pulse train in terms of shape and FWHM pulse duration of 5 ps, but with four times the original frequency repetition rate and a perfect 1/4 less intensity.

Since the FSR depends upon the factor m, and in order to obtain higher multiplication factors, more stages are needed to cover the entire operation bandwidth and ensure high-fidelity results with minimal errors.

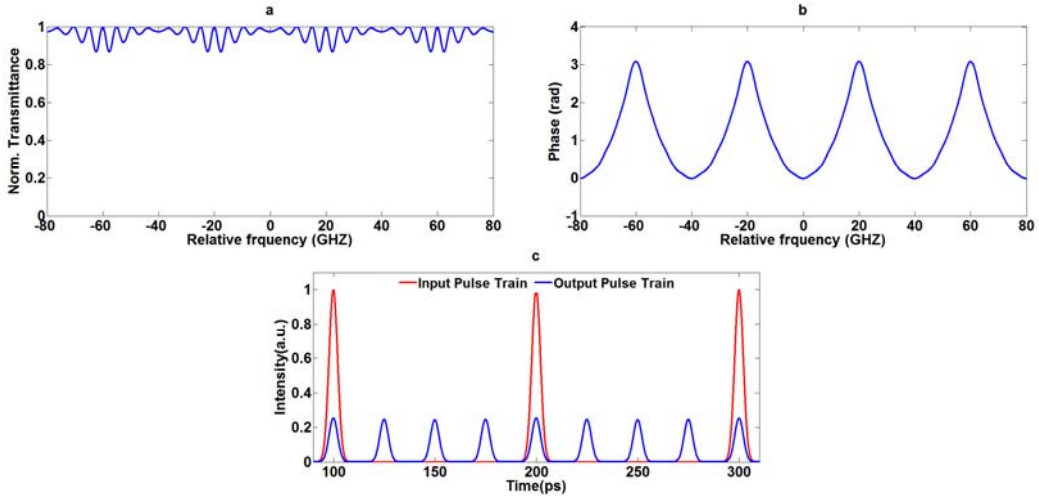

Fig. 2. PRRM by the designed 12-stages birefringent filter. (a) Amplitude response; (b) Phase response; (c) The output pulse train with a multiplication factor of $m = 4$. The frequency repetition rate of the input pulse train is 10 GHz. The frequency repetition rate of the output pulse train is 40 GHz.

3. Conclusions

In this work, we have demonstrated, for the first time to the best of our knowledge, a pulse repetition rate multiplier based on TTE using a birefringent optical filter. The filter has a periodic quadratic phase and a flattened transmittance. An optimization algorithm is used to determine the Opto-geometrical parameters of the 12-stages filter. Preliminary results show extremely high fidelity in multiplying a 10 GHz input pulse rate by a factor $m = 4$ to achieve an output pulse train of 40 GHz without affecting the individual pulse characteristics.

References

[1]. T. Jannson and J. Jannson, Temporal self-imaging effect in single-mode fibers, *J. Opt. Soc. Am*, Vol. 71, Issue 11, 1981, pp. 1373-1376.

[2]. R. Maram, L. R. Cortés, and J. Azaña, Sub-harmonic periodic pulse train recovery from aperiodic optical pulse sequence through dispersion-induced temporal self-imaging, *Opt. Express*, Vol. 23, Issue 3, 2015, pp. 3602-3613.

[3]. J. Jeon, R. Maram, J. V. Howe, and J. Azaña, Programmable passive Talbot optical waveform amplifier, *Opt. Express*, Vol. 26, Issue 6, 2018, pp. 6872-6879.

[4]. H. Chi, S. Hu, Y. Zhai, B. Yang, Z. Cao, J. Ou, and S. Yang, Real-time discrete Fourier transformer with complex-valued outputs based on the inverse temporal Talbot effect, *Opt. Express*, Vol. 28, Issue 14, 2020, pp. 20543-20552.

[5]. R. Maram, L. R. Cortés, J. V. Howe and J. Azaña, Energy-Preserving Arbitrary Repetition-Rate Control of Periodic Pulse Trains Using Temporal Talbot Effects, *Journal of Lightwave Technology*, Vol. 35, Issue 4, 2017, pp. 658-668.

[6]. J. Azaña and M. A. Muriel, Temporal self-imaging effects: Theory and application for multiplying pulse repetition rates, *IEEE J. Sel. Top. Quantum Electron*, Vol. 7, Issue 4, 2001, pp. 728-744.

[7]. J. Caraquitena, M. Beltrán, R. Llorente, J. Martí, and M. A. Muriel, Spectral self-imaging effect by time-domain multilevel phase modulation of a periodic

pulse train, *Opt. Lett*, Vol. 36, Issue 6, 2011, pp. 858-860.

[8]. A. Halassi, R. Hamdi, D. F. Bendimerad, B.-E. Benkelfat. A novel synthesis approach for birefringent filters having arbitrarily amplitude transmittances, *Optics Communications, Elsevier,* Vol. 369, 2016, pp. 12-17.

(044)

Tests and Developments of a NIR laser CO_2 Sensor based on Dense-pattern Multipass Gas Cell

F. Defossez, J. Jacquemin, R. Vallon, B. Parvitte, V. Zeninari
Université de Reims Champagne Ardenne, CNRS, GSMA UMR 7331, 51100 Reims, France
Tel.: +33 326913395, fax: +33 326913147
E-mail: raphael.vallon@univ-reims.fr

Summary: We report on test and development of a NIR laser CO_2 sensor using new compact dense-pattern multipass cell. This 34m pathlength open multipass cell has been developed thanks to a homemade ray tracing software able to simulate gaussian beam propagation allowing to avoid spot overlapping. This cell was used with a DFB laser emitting at 2.004 µm to perform TDLAS (Tunable Diode Laser Spectroscopy) measurements on CO_2. The sensor was validated during a massive CO_2 release test campaign which took place in an urban site dedicated to military training (CENZUB). This experiment organized by INERIS, aimed to collect measurements about heavy gases dispersion in an urban environment by deploying several analyzers on the site. During this experiment our spectrometer was set near an EVM multi-parameters sensor and measurements cross-comparison shows agreements.

Keywords: Multipass cell, Herriott cell, TDLAS, CO_2 measurements, in-situ.

1. Introduction

In a global warming context, concentrations of greenhouse gases like CO_2 and CH_4 are crucial information requires for modelisation. Since few years some efforts are produced to measure sub-ppm concentrations with robust and compact sensors. One suitable method to realize such sensor is the so called Tunable Diode Laser Spectroscopy (TDLAS). TDLAS take advantage of gases spectral absorption properties, to carry out molecules selective detection and quantification. According to the HITRAN database [1] and the Beer-Lambert law (Eq. 1), this method allows sensitives concentrations measurements down to a ppm level without any calibrations.

$$T(\sigma) = exp\left(-\frac{lNC}{\pi} \times \left(\sum_{i}^{N} s_i \times f_i(\sigma)\right)\right) \quad (1)$$

T is the transmission as a function of wavenumber σ, *l* the absorption length, *C* the species mixture ratio, s_i the spectral line intensity and f_i the lineshape.

Atmospheric molecules like CO_2 show strong absorption features in the mid-infrared spectral range induce by their fundamental rovibrational transition. Thus, mid-infrared laser sources are often a good choice to perform sensitive absorption spectrum measurements. Active research has led to many improvement of mid-infrared laser technologies, which are mostly based on Optical Parametric Oscillator (OPO) or Quantum Cascade Laser (QCL). Both technologies allows to cover wavelength from 3 µm to 12 µm with optical power reaching few watts. But near infrared lasers are mature and robust technologies and easy to couple to an optical fiber. However, as molecules spectral lines intensities are weaker than in the mid-infrared range, sensitivity must be improve by using multipass cell. Such system, based on NIR DFB laser and a new multipass cell has been developed and test during a massive CO_2 release test campaign, on CENZUB site, managed by INERIS.

2. Dense-pattern Multipass Gas Cell

Herriott multipass cells are robust and suitable for on-field measurements. However, because of its elliptical spot pattern, the number of pass without spot overlapping is limited. Moreover, because of a poor mirror surface filling, long path cells need large volume. One improvement should be performed by using astigmatic mirrors, thus leading to Lissajou spot pattern which filled the full mirror surfaces. However, if these cells allow to reach long pathlength the price to be paid is a high sensitity to the position and the beam input angle. Moreover, due to large number of reflexions, these cells are particulary sensitive to mirror surface contaminations.

Recently, several improvements of the classical Herriott multipass, commonly called dense-pattern multipass cell have been reported [2]. These Herriott-like multipass cells take advantage of spherical aberrations induced by spherical mirror, to achieve a better spreading of the light spot on the mirrors surfaces. Thus, the number of pass can be increase without spot overlapping. One common method use to perform geometrical optics simulation is ABCD matrix formalism. However, ABCD matrix which works well to treat with paraxial optics and allows to simulate gaussian beam propagation, cannot be used in this case. Therefore a model has been developed to simulate a beam propagation and deduced, according to beam injection parameters, a reflexion spot pattern. As spot overlapping leads to interference fringes on spectrum measurements, chief ray tracing is not satisfying and beam width has to be consider. In order to carefully design our multipass cell, our model take

into account for gaussian beam (Fig. 1). This model enabled to realize a 12 cm long open multipass cell with an effective pathlength of 34 m. This multipass cell was injected by a NIR DFB laser emitting at 2.004 µm to perform CO_2 concentrations measurements.

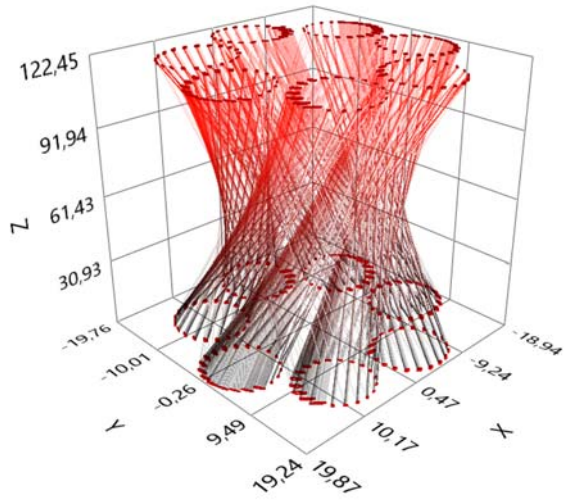

Fig. 1. Homemade software simulation of gaussian beam propagation through a 7-circles dense-pattern multipass cell.

3. NIR Laser Spectrometer Set-up

DFB (Distributed FeedBack) laser, because of their great spectral quality are well suitable source for high resolution spectrum measurements, especially for concentration measurements [3]. Indeed these lasers benefit for narrow linewidth of few megahertz and can be tune over several wavenumbers, at frequencies up to few kilohertz by current modulation, enabling high spectral and temporal resolution which are required to improve S/N ratio and therefore measurements sentivity. Such laser was used to build a CO_2 sensor [3]. As depicted on the sketch (Fig. 2.) we used a DFB laser emitting at 2.004 µm in order to measure the R20 line from the $(00^00)_1 \rightarrow (20^01)_2$ CO_2 band at 4992,516 cm^{-1}. The laser beam was split in two arm thanks to a 50/50 beamsplitter towards two InGaAs photodiodes. One arm is used to monitor the wavelength temporal evolution thanks to a reference confocal Fabry-Perot cavity while the second arm contain the 34 m pathlength multipass cell. The DFB wavelength was tuned over 1 cm^{-1} thanks to a 13 Hz frequency sawtooth modulated current. Photodiode signal are samples at 10 kS/s thanks to a 16 bit resolution acquisition card controlled by a LabVIEW software.

This laser spectrometer was used to perform on-field CO_2 measurements during a massive release test campaign, managed by French National Institute for Industrial Environment and Risks (INERIS) in a dedicated urban site of a military training camp (CENZUB). This experiment which was carried out to validate heavy gases dispersion model in urban environment, was performed by deploying several analyzers on site. Concentrations from 400 ppm to 5 % has been measured and cross comparison of our concentrations measurement with that of reference analyzer show good agreements.

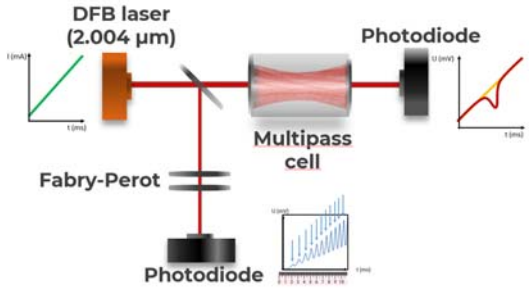

Fig. 2. Sketch of the experimental setup.

4. Conclusion

A gaussian beam ray tracing model was developed to simulate gaussian beam propagation in a dense-pattern multipass cell, allowing to build a 34m pathlength cell free of interference fringe. This cell was used with a DFB laser diode emitting at 2.004 µm to perform on-field CO_2 concentrations measurements during a massive release test campagn and cross comparison of our results with that of reference analyzers show good agreements.

Acknowledgements

This work is supported by the INTERREG V France-Wallonie-Vlaanderen program through the project SAFESIDE

We are grateful to INERIS for inviting the consortium of SAFESIDE to participate in their massive CO_2 release campaign on CENZUB site

References

[1]. I. E. Gordon, L. S. Rothman, R. J. Hargreaves et al., The HITRAN2020 molecular spectroscopic database, *Journal of Quantitative Spectroscopy and Radiative Transfer,* Vol. 277, 2022, 107949.

[2]. Y. Cao, Z. Xu, X. Tian, G. Cheng, C. Liu, Y. Zhang, Generalized calculation model of different types of optical multi-pass cells based on refraction and reflection law, *Optics & Laser Technology*, Vol. 139, 2022, 106958.

[3]. A. Moriaux, R. Vallon, C. Cilindre, B. Parvitte, G. Liger-Belair, V. Zéninari, Development and validation of a diode laser sensor for gas-phase CO2 monitoring above champagne and sparkling wines, *Sensors and Actuators B: Chemical,* Vol. 257, 2018, pp. 745-752.

(047)

Birefringent Pulse Shaper Using Non-identical Crystals

Youcef Driouche [1,2], Rachid Hamdi [1,2], Leila Graini [1], Abderezzaq Halassi [1] and Badr-Eddine Benkelfat [2]
[1] Université 8 mai 1945 Guelma, Laboratoire des Télécommunications, BP 401, Guelma 24000, Algeria
[2] SAMOVAR, Télécom SudParis, Institut Polytechnique de Paris, 91120 Palaiseau, France
E-mail: driouche.youcef@univ-guelma.dz

Summary: We present a new simple method to synthesize a temporal pulse shaper using non-identical birefringent crystals. The shaper configuration consists of *N* crystal with appropriate length and orientation placed between a polarizer and an analyzer. The Opto-geometrical shaper parameters are achieved by an optimization algorithm. This shaper is capable of generating several desired output pulse profiles with high efficiency and fidelity in both picosecond and femtosecond regimes.

Keywords: Birefringent pulse shaper, Laser pulse shaping, Non-identical birefringent crystals.

1. Introduction

Various birefringent shapers have been reported to generate desired pulse profiles, such as saw-tooth, parabolic, or flat-top pulses [1, 2]. Those shapes are required in wide different fields, for instance, wavelength conversion based on self-phase modulation using a saw-tooth pulse that is more efficient than a Gaussian pulse, also, by applying parabolic pulse train as pump signal to create nonlinear time-lens [3, 4]. Recently, we have demonstrated a technique to synthesize birefringent pulse shaper based on the resolution of a nonlinear system deduced from Jones matrix formalism in the time domain. The shaper consists of *N* identical crystals, generating *N+1* sub-pulses to create interference at the output polarizer to obtain the target output profile [5]. Unfortunately, this technique has two major drawbacks. Firstly, the large number of crystals complicates the optical setup and likely leads to errors in the orientation angles of the shaper's crystals. Secondly, the temporal equidistance between the sub-pulses resulting from the identical length of the crystals restricts the degree of freedom in the synthesis procedure.

This paper reports a novel method to synthesize a birefringent shaper based on non-identical crystals. The shaper generates 2^N sub-pulses to produce any temporal pulse shapes, which is achieved by optimizing the amplitude of each sub-pulse and the specific time delay between any two successive pulses. This technique will overcome the disadvantages aforementioned in our previous work with only three crystals.

2. Synthesis Procedure

In the general case of *N*-stages non-identical birefringent crystals (BC), and relying on the Jones matrix formalism, the polarized output electric field component A_{out} along the transmission axis of the analyzer can be described as,

$$\begin{pmatrix} A_{out} \\ 0 \end{pmatrix} = P_A R(\theta_p)\{R(-\theta_N)R(\eta_N)R(\theta_N)\} \ldots \{R(-\theta_1)R(\eta_1)R(\theta_1)\} P_x \begin{pmatrix} A_{in} \\ 0 \end{pmatrix} \quad (1)$$

Here, $P_x = \begin{pmatrix} 1 & 0 \\ 0 & 0 \end{pmatrix}$ and $P_A = \begin{pmatrix} 1 & 0 \\ 0 & 0 \end{pmatrix}$ are the Jones matrix of the polarizer and analyzer, respectively, $R(\eta_i) = \begin{pmatrix} e^{j\eta_i/2} & 0 \\ 0 & e^{-j\eta_i/2} \end{pmatrix}$, is the birefringent matrix of the i^{th} stage with $\eta_i = \omega T_i$ denotes to the phase delay and ω is the pulsation.

$R(\varphi_i) = \begin{pmatrix} \cos\theta_i & \sin\theta_i \\ -\sin\theta_i & \cos\theta_i \end{pmatrix}$, is the rotation matrix, whose absolute angle is θ_i.

For simplicity, we rewrite Eq. (1) in terms of the relative angles φ_i instead of dealing with the absolute angles θ_i, note that, $\varphi_i = \theta_i - \theta_{i-1}$ and $\varphi_p = \theta_p - \theta_N$. Eq. (1) become,

$$\begin{pmatrix} A_{out} \\ 0 \end{pmatrix} = P_A \{R(\varphi_p)R(\eta_N)\}\{R(\varphi_N)R(\eta_{N-1})\} \ldots \{R(\varphi_2)R(\eta_1)\} R(\varphi_1) \begin{pmatrix} A_{in} \\ 0 \end{pmatrix} \quad (2)$$

The general form of Eq. (2) is given as,

$$\begin{pmatrix} A_{out} \\ 0 \end{pmatrix} = \begin{pmatrix} 1 & 0 \\ 0 & 0 \end{pmatrix} \begin{pmatrix} \cos\varphi_p e^{-j\eta_N} & \sin\varphi_p \\ -\sin\varphi_p e^{-j\eta_N} & \cos\varphi_p \end{pmatrix} \prod_{i=2}^{N} \begin{pmatrix} \cos\varphi_i e^{-j\eta_{i-1}} & \sin\varphi_i \\ -\sin\varphi_i e^{-j\eta_{i-1}} & \cos\varphi_i \end{pmatrix} \begin{pmatrix} A_{in}\cos\varphi_1 \\ -A_{in}\sin\varphi_1 \end{pmatrix} \quad (3)$$

Applying the matrix product in Eq. (3), we find an exponential series form of the output electric field,

$$A_{out} = A_{in}\sum_{i=0}^{k} A_i e^{-j\Gamma_i} = A_{in}\left(A_0 + A_1 e^{-j\Gamma_1} + \ldots + A_k e^{-j\Gamma_k}\right) \quad (4)$$

where $k = 2^N - 1$, A_i are real amplitudes depend upon the relative angles, and Γ_i are the new phase shifts resulting from a combination between the phase shifts introduced by each stage, which are arranged according to the order of the output sub-pulses.

Taking the inverse Fourier transform of Eq. (4), we obtain the temporal output electric field,

$$e_{out}(t) = e_{in}(t) * \sum_{i=0}^{k} A_i \delta(t - \Delta T_i) = \sum_{i=0}^{k} A_i e_{in}(t - \Delta T_i) \quad (5)$$

where (*) denotes to the convolution product and ΔT_i are the time delays between the output sub-pulses depending on each crystal's time delay, with $\Delta T_0 = 0$ Once the target output profile $s(t)$ is defined, A_i and ΔT_i can be achieved using the genetic algorithm. The error function is chosen as follows,

$$F_{err} = \left(\frac{1}{M}\sum_{n=0}^{M}\left|s(t) - e_{out}(t, A_i, \Delta T_i)\right|^2\right)^{1/2} \quad (6)$$

where M is the number of time points.

3. Shaper Design, Results and Discussions

For a comparison purpose with our previous work, the schematic diagram shown in Fig. 1 fits perfectly with our case. Fig. 1 illustrate the case of three stages of non-identical BC introducing different phase shifts $\eta_1 > \eta_2 > \eta_3$, placed between a polarizer and an analyzer. The time interval between the sub-pulses $T_1 > T_2 > T_3$ and their amplitudes depend upon the thickness and the orientation $\theta_1, \theta_2, \theta_3$ of each crystal. The polarizer is parallel to the x-axis while the analyzer makes an angle θ_p with it.

To prove the robustness of our new synthesis method, we chose the same temporal input pulse of our previous work [5], which has a Sech^2 shape with a full width at half maximum pulse duration of 6.5 ps, operating at the wavelength of 532 nm.

Fig. 2 depicts the results obtained by the new synthesis method generating a parabolic pulse profile with a 30 ps time duration. As can be seen, the output pulses match perfectly with the ideal shape. Instead of using eight stages of identical crystals as used in [5], we only use three stages of Yttrium Orthovanadate (YVO4) crystals: 14.44, 6.82 and 5.53 mm, oriented at the optimal absolute angles -128.95°, 33.26°, and -107.69°, respectively, with the absolute angle of the analyzer found to be -68.93°.

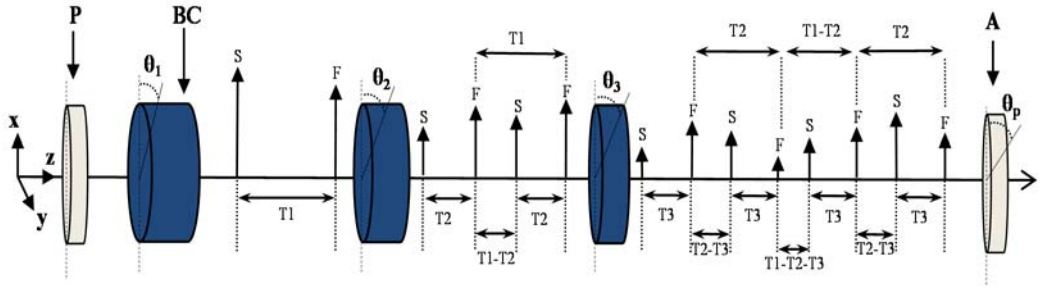

Fig. 1. Structure of three stages of non-identical BC F: Impulse polarized parallel to the fast axis of the crystal S: Impulse polarized parallel to the slow axis of the crystal P: Polarizer, A: Analyzer.

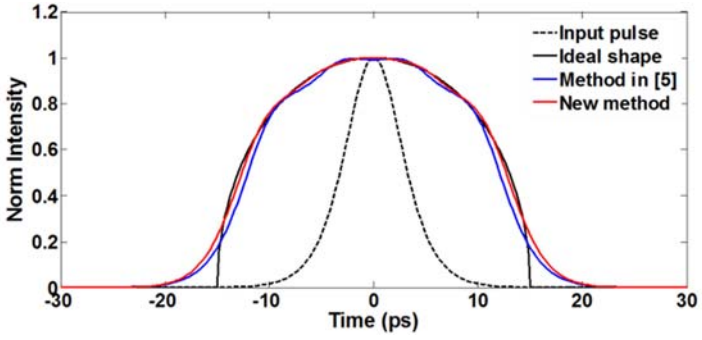

Fig. 2. The normalized intensity of the parabolic output pulse profile calculated by the new synthesis method.

4. Conclusions

In this work, we have proposed a new synthesis method for temporal pulse shaping based on non-identical BC. The genetic algorithm was used to find the Opto-geometrical shaper parameters. The high effectiveness of the new method has been assessed in terms of simplicity, fidelity, and lower values of the number of stages for the parabolic target shape compared to our previous technique.

References

[1]. F. Liu, S. Huang, S. Si, G. Zhao, K. Liu, and S. Zhang, Generation of picoseconds pulses with variable temporal profiles and linear polarization by coherent pulse stacking in a birefringent crystal shaper, *Optic Express*, Vol. 27, Issue 2, 2019, pp. 1467-1478.

[2]. I. Will, Generation of flat-top picosecond pulses by means of a two-stage birefringent filter, *Nucl. Instr. And Meth*, Vol. 594, Issue 2, 1995, pp. 119-125.

[3]. F. Parmigiani, M. Ibsen, T. T. Ng, L. Provost, P. Petropoulos and D. J. Richardson, An Efficient Wavelength Converter Exploiting a Grating-Based Saw-Tooth Pulse Shaper, *IEEE Photonics Technology Letters,* Vol. 20, Issue 17, 2008, pp. 1461-1463.

[4]. R. Maram and J. Azaña, Spectral self-imaging of time-periodic coherent frequency combs by parabolic cross-phase modulation, *Opt. Express*, Vol. 21, Issue 23, 2013, pp. 28824-28835.

[5]. A. Halassi, Y. Driouche, R. Hamdi, and B.-E. Benkelfat, Generalized temporal synthesis method for a birefringent laser pulse shaper, *J. Opt. Soc. Am. A*, Vol. 37, Issue 11, 2020, pp. C15-C19.

(051)

1DPhC-based Resonant Cavity for Optical Fiber Sensing

J. Durisova [1], T. Mizera [1], R. Kanok [2], P. Hlubina [2], D. Pudis [1, 3], P. Gaso [1] and D. Jandura [1]
[1] Dept. of Physics, Faculty of Electrical Engineering and Information Technology, University of Žilina, Univerzitná 1, 010 26 Žilina, Slovakia
[2] Department of Physics, Technical University Ostrava, 17. Listopadu 2172/15, 708 00 Ostrava-Poruba, Czech Republic
[3] University Science Park of the University of Zilina, Zilina, Slovakia
Tel.: + 4215132312
E-mail: jana.durisova@feit.uniza.sk

Summary: Photonic crystals (PhCs) are low-loss dielectric systems characterized by a periodic modulation of the refractive index along one or more spatial directions. They can be designed and constructed to generate photonic band gaps (PBGs) by changing either the geometry or materials of the periodic structure, what prevents from the propagation of electromagnetic waves of specific wavelengths inside the PhCs along specific directions. Moreover, the PhCs with the PBGs enable to sustain surface electromagnetic waves at certain frequencies within the PBG. This paper describes an idea of creating a liquid analyte sensor based on a one-dimensional (1D) photonic crystal - dielectric mirror - integrated on the optical fiber end face and creating a resonant cavity with the reversed structure. This geometry produces the evident resonances within the PBG spectral region which are sensitive to refractive index changes inside the resonant cavity.

Keywords: Photonic crystal, Analyte sensor, Lab-on-a-chip.

1. Introduction

Dielectric structures composed of alternating layered media, referred to as the one-dimensional photonic crystals (1DPhCs) or the Bragg reflectors, are interesting for their optical properties [1]. Due to a periodic modulation of the refractive index, regions of forbidden light frequencies – the photonic band gap (PBG) – exist and light is not allowed to propagate through the structure. 1DPhCs show up a high reflectivity and are widely used as reflective coatings and filters [2]. 1DPhCs can be also used as planar waveguides, and the guided waves can be used in sensing applications [3]. Moreover, the Bloch surface waves (BSWs) propagating along the interface of the 1DPhC and external medium are widely used in sensing [4, 5].

Here we proposed the 1DPhCs as a part of a Fabry-Pérot resonant cavity. Such an arrangement produces resonances inside the PBG of 1DPhC what could be attractive for optical sensing. Moreover, we proposed the integration of such structure on optical fiber end face what promotes the structure for Lab-on-a-chip (LOC) application where photonic detection principles are currently very attractive [6].

2. Experimental and Results

The multilayer 1DPhC structure under study consists of six SiO_2/TiO_2 bilayers and a termination layer of TiO_2 [5]. The 1DPhC is deposited on a glass substrate. The used structure shows app. 80% spectral reflectance in the range from 500 to 600 nm (Fig. 1).

Key experimental procedure was to integrate the 1DPhC structure on a single mode optical fiber (SMF) end face. For direct integration, the 1DPhC structure deposited on a glass substrate was cleaved to a small sample of area of 0.5 x 0.5 mm^2. For the sticking the samples at the end facet of SMF we used our experiences with polydimethylsiloxane (PDMS). The SMF was sticked to the glass side of the sample using PDMS under special care about the perpendicularity to the sample surface. The sample was cured for 24 hours.

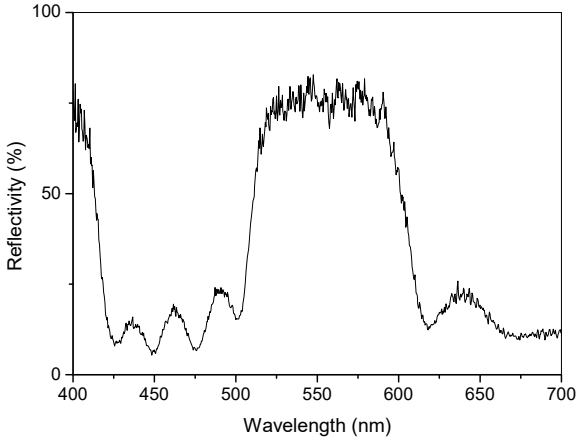

Fig. 1. Spectral reflectance of used SiO_2/TiO_2 mirror on glass substrate.

We investigated the spectral transmission on such a doubled 1DPhC structure with thin air cavity. Fig. 2 shows the experimental setup using excitation with the SMF. A halogen lamp, MI-150 Edmund, was used as a white light source. The white light was coupled to a SMF, where the 1DPhC structure was binded to the other end. The fiber with structure was placed on a micromechanical stage. The output SMF integrated with the same 1DPhC at the end was placed on the

second micromechanical stage. The samples were approached close to each other (a necessary condition is very small spacing *d* between the samples). The output light from SMF was analysed by a compact spectrometer, USB 2000 Ocean Optics.

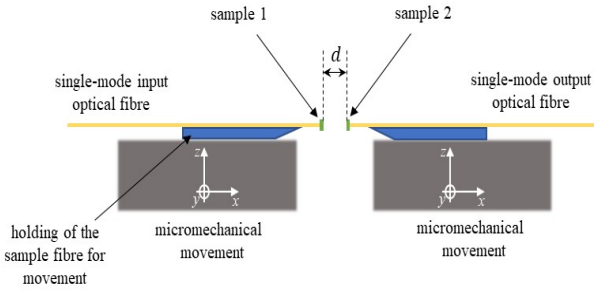

Fig. 2. Experimental setup for spectral transmission measurements of 1DPhC integrated on SMFs.

First, we verified the existence of peaks within the photonic band gap of the 1DPhC structure formed by air cavity between the two structures. The spectral transmission (Fig. 3) shows evident spectral band gap corresponding to Bragg reflection of 1DPhC structure modulated by resonance peaks given by air cavity between the structures. The air cavity of length of app. 6.5 µm produces free spectral range (FSR) λ_{FSR} = 46 nm, what can be confirmed by a separation of peaks in the measured spectral transmittance in the spectral band gap from 500 to 620 nm.

If isopropyl alcohol is dripped into the gap between the samples, the λ_{FSR} changes to 33 nm what agrees with the corresponding refractive index 1.377. A comparison of the transmission spectrum of air and isopropyl spectrum is shown in Fig 3.

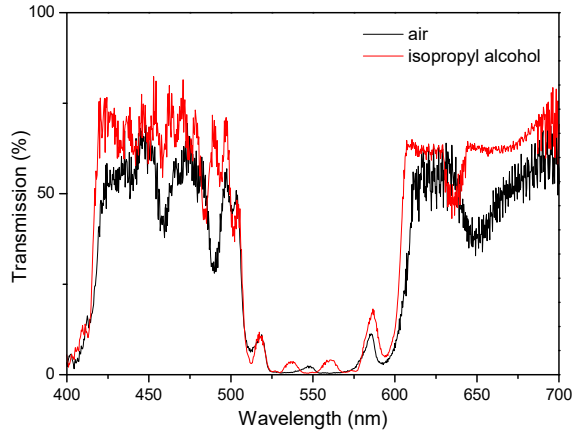

Fig. 3. Spectral transmission of air and isopropyl alcohol

Since the idea is to use this arrangement as a sensor in LOC arrangement, we designed the chip with two SMFs with 1DPhC at the end face, and inlet and outlet for different liquid analyte delivery. The proposed LOC arrangement is shown in Fig. 4.

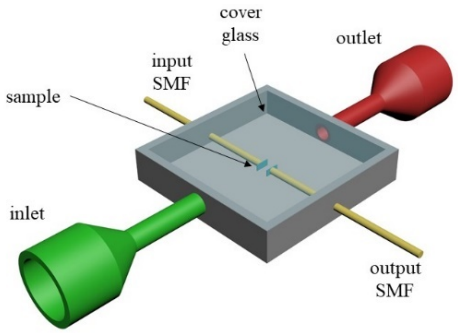

Fig. 4. Design of LOC with integrated SMF with 1DPhC.

4. Conclusions

We proposed the 1DPhC-based resonant cavity employing optical fibers and producing evident resonances inside the PBG of the 1DPhC. Such an arrangement is attractive for highly resolved optical sensing and with integration on SMF it promotes the structure for LOC applications.

Acknowledgements

This work was supported by grant agency of Ministry of Education, Science, Research and Sport of the Slovak Republic project VEGA 1/0363/22, and APVV 20-0264. This publication was realized with support of Operational Program Integrated Infrastructure 2014 - 2020 of the project: Innovative Solutions for Propulsion, Power and Safety Components of Transport Vehicles, code ITMS 313011V334, co-financed by the European Regional Development Fund. This work was also supported by Student Grant System (SP2022/25) and by project Support for Science and Research in the Moravia-Silesia Region 2020 (RRC/02/2020).

References

[1]. Z. Saleki et al., Optical properties of a one-dimensional photonic crystal containing a graphene-based hyperbolic metamaterial defect layer, *Appl. Optics,* 56, 2017, pp. 317-323.
[2]. U. Ahmed et al., Investigation of spectral properties of DBR-based photonic crystal structure for optical filter application, *Crystals,* 12, 2022, p. 409.
[3]. R. Kanok et al., Efficient optical sensing based on phase shift of waves supported by a One-dimensional photonic crystal, *Sensors,* 21, 2021, p. 6535.
[4]. P. Hlubina et al., High performance liquid analyte sensing based on Bloch surface wave resonances in the spectral domain, *Optics and Laser Technol.,* 145, 2022, 107492.
[5]. M. Gryga et al., One-dimensional photonic crystal for Bloch surface waves and radiation modes based sensing, *Optical Materials Express,* 9, 2019, pp. 4009–4022.
[6]. T. N. Ackermann et al., Plug and measure – a chip-to-world interface for photonic lab-on-a-chip applications, *Lab on a Chip,* 16, 2016, pp. 3220-3226.

(052)

Anti-squeezing Noise in Continuous-variable Quantum Communication

V. C. Usenko, A. Nag Oruganti and I. Derkach
Department of Optics, Faculty of Science, Palacky University,
17. listopadu 12, 77146 Olomouc, Czech Republic
Tel.: + 420585634248, fax: + 420585634002
E-mail: usenko@optics.upol.cz

Summary: Signal squeezing is known to improve robustness and efficiency of continuous-variable quantum communication, particularly quantum key distribution. However, squeezed states are never pure in practice as losses in the process of generation and collection of squeezed states unavoidably lead to reduction of squeezing and effective increase of anti-squeezing excess noise. We address the role of such noise in continuous-variable quantum key distribution, assuming either trusted or untrusted anti-squeezing noise. We show that the trusted anti-squeezing noise can even somewhat limit the information leakage and allows for analytical expression for the bounds on the leakage in the limit of infinite anti-squeezing. However, such noise reduces the quality of parameter estimation having a negative impact on the protocols. On the other hand, untrusted anti-squeezing noise limits the secure distance of the protocols and requires high-purity squeezed states. Our results are essential for implementation of squeezed-state quantum communication with realistic impure squeezed states.

Keywords: Quantum communication, Quantum key distribution, Quantum noise, Continuous variables, Squeezed states.

1. Introduction

Continuous-variable (CV) optical quantum communication and, particularly, quantum key distribution (QKD) are a feasible alternative to well-known discrete-variable QKD protocols. Contrary to the challenging direct photodetection of ideally single-photon states, used in the latter, CV QKD offers high-speed low-noise and highly efficient quadrature homodyne detection of quadrature-modulated generally multipohoton light, broadly used in classical optical communication. Being feasible already using coherent states of light [1], CV QKD can be improved in terms of achievable distances, secret key rates or robustness to channel noise by the use of signal squeezing [2], which is an essentially nonclassical phenomenon manifesting itself on the sub-shot-noise fluctuations of one of the field quadratures. To comply with the uncertainty principle, an orthogonal quadrature is inclined to the above-shot-noise fluctuations, hence being noisier than that of a coherent or vacuum state of light and being referred to as an anti-squeezed quadrature. Importantly, anti-squeezing noise unavoidably appears in the process of generation of squeezed states due to intrinsic losses in an optical parametric oscillator, which reduce squeezing and lead to higher anti-squeezing variance than that of a pure state. If $V_s \leq 1$, where 1 is the shot-noise level, is the squeezed quadrature variance, then the anti-squeezed quadrature has the variance of $1/V_s + \Delta V$, where ΔV is the anti-squeezing noise and the state is not pure for any $\Delta V > 0$. We study the role of such phase-sensitive anti-squeezing noise in CV QKD, assuming trusted and untrusted preparation scenarios.

2. CV QKD with Noisy Squeezed States

In order to analyse the role of anti-squeezing noise in CV QKD we consider the generalized squeezed-state protocol in which the trusted sender Alice generates a generally noisy squeezed states containing anti-squeezing noise and applies Gaussian quadrature modulation. Alice then sends the modulated states through a generally lossy and noisy quantum channel, which is assumed to be fully controlled by an eavesdropper Eve, who is capable of collective Gaussian eavesdropping attacks, which were shown optimal against Gaussian protocols. After the channel the states are measured by the remote trusted party Bob, who performs homodyne detection, generally randomly switching between measuring either of the complementary quadratures, and obtains the respective data.

In order to analyze the security of the scheme we design an equivalent entanglement based scheme by using the generalized squeezed-state scheme [3] and adding another squeezed mode on a strongly unbalanced beamsplitter similarly to adding trusted preparation noise in the analysis of coherent-state protocol [4]. We assess the security of the scheme in terms of the lower bound on the secret key rate, which generally reads

$$K = I_{AB} - \chi_{BE}, \qquad (1)$$

where I_{AB} is the mutual classical (Shannon) information shared between the trusted parties and χ_{BE} is the Holevo bound, which upper limits the information accessible to an eavesdropper. While the calculation of the mutual information I_{AB} is

straightforward from the variances and correlations between the data at Alice and Bob, the evaluation of χ_{BE} is more involved and is based on the calculation of von Neumann entropies of the state shared between Alice and Bob before and after Bob's measurement (see details on the security analysis of CV QKD in [4]). Positivity of the lower bound (1) indicates the possibility to establish the secret key distribution and results in security regions in terms of the tolerable channel attenuation and noise, which define the applicability of the protocol.

3. Role of the Anti-squeezing Noise

In order to assess the role of the anti-squeezing noise in the squeezed-state protocol described above, we assume either trusted or untrusted noise hence either trusting the source of squeezing, possessed by Alice, or assuming that it is controlled by the malicious Eve.

3.1. Trusted Anti-squeezing Noise

In the case of trusted anti-squeezing noise being a part of the trusted preparation, which is the typical assumption in CV QKD, and a channel with fixed transmittance (typical for fiber links), the noise is even slightly helpful for the trusted parties and allows analytical derivation of the Holevo bound, upper bounding the information leakage, in the limit of infinitely strong anti-squeezing noise. If the channels are fluctuating, however (which is typical for the atmospheric channels where turbulence effects lead to transmittance fluctuations also referred to as fading), presence of even trusted anti-squeezing noise leads to appearance of untrusted channel noise, concerned with fading [5], and limits applicability of squeezed-state CV QKD, requiring squeezed states with high purity or even reduced squeezing [6].

3.2. Untrusted Anti-squeezing Noise

In the stricter assumption of untrusted anti-squeezing (meaning that an eavesdropper controls the squeezer), the presence of such noise significantly limits the achievable key rates, secure distances and robustness to channel noise, the latter shown in Fig. 1. Therefore, for a squeezing source to be untrusted, high level of purity of squeezed states is required.

We also consider finite-size effects concerned with the estimation of parameters in CV QKD [7] and show that the parameter estimation is undermined by the presence of anti-squeezing noise even if it is trusted, hence limiting the efficiency of the protocols.

4. Conclusions

Our results set the bounds on anti-squeezing noise for practical squeezed-state CV QKD and represent a challenging task of high squeezed-state purity requirement for practical implementation of the protocols.

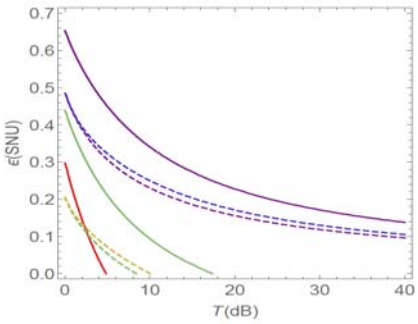

Fig. 1. Maximum tolerable channel noise for strong (-10 dB, solid) and weak (-3 dB, dashed) pure squeezing (purple) and with untrusted anti-squeezing noise of 0.5 shot-noise units (SNU, green) and 1 SNU (red). Blue line: 10 SNU trusted anti-squeezing noise.

Acknowledgements

Authors acknowledge support from the grant 21-44815L of the Czech Science Foundation.

References

[1]. F. Grosshans et al. High-rate quantum cryptography using Gaussian-modulated coherent states, *Nature*, Vol. 421, 2003, pp. 238-241.

[2]. R. García-Patron, N. J. Cerf. Continuous-Variable Quantum Key Distribution Protocols Over Noisy Channels, *Phys. Rev. Lett.*, Vo. 102, 2009, p. 130501; L.S. Madsen, V.C. Usenko, M. Lassen, R. Filip, U.L. Andersen. Continuous variable quantum key distribution with modulated entangled states, *Nature Communications*, Vol. 3, 2012, p. 1083.

[3]. V. C. Usenko, R. Filip, Squeezed-state quantum key distribution upon imperfect reconciliation, *New Journal of Physics*, Vol. 13, 2011, p. 113007.

[4]. V. C. Usenko, R. Filip, Trusted noise in continuous-variable quantum key distribution: a threat and a defense, *Entropy*, Vol. 18, 2016, p. 20.

[5]. V. C. Usenko, B. Heim, C. Peuntinger, C. Wittmann, C. Marquardt, G. Leuchs, R. Filip, Entanglement of Gaussian states and the applicability to quantum key distribution over fading channels, *New J. Phys.*, Vol. 14, 2012, p. 093048.

[6]. I. Derkach, V. C. Usenko, R. Filip, Squeezing-enhanced quantum key distribution over atmospheric channels, *New J. Phys.*, Vol. 22, 2020, p. 053006.

[7]. L. Ruppert, V. C. Usenko, R. Filip, Long-distance continuous-variable quantum key distribution with efficient channel estimation, *Phys. Rev. A*, Vol. 90, 2014, p. 062310.

(054)

Development of Efficient Clad-pumped Fiber Optical Amplifiers for Telecommunication Systems

J. Grube [1], A. Supe [2], K. Zakis [2], S. Olonkins [3], A. Udalcovs [2], R. Murnieks [2], U. Senkans [2], D. Prigunovs [2,3], L. Gegere [2,3], E. Elsts [1], I. Lukosevics [1], O. Ozolins [2], S. Spolitis [2], V. Bobrovs [2]
[1] Institute of Solid State Physics, University of Latvia, 8 Kengaraga street, Riga, Latvia
[2] Institute of Telecommunications, Riga Technical University, Azenes street 12, Riga, Latvia
[3] AFFOC Solutions, Kalnciems, Latvia
Tel.: + 371 2829486, fax: + 371 67132778
E-mail: jurgis.grube@cfi.lu.lv

Summary: Cladding-pumped erbium (Er^{3+}) and ytterbium (Yb^{3+}) co-doped amplifiers (EYDFAs) mostly are used in high output power optics and fiber laser systems. In this research, we consider this type of amplifier applicability for optical communications systems considering the typical output power and wavelength range used in communications systems. The proposed EYDFA simulation model and experimental setup are based on a commercial double-clad Er^{3+}/Yb^{3+} co-doped fiber (EYDF) whose parameters are experimentally obtained and used in the EYDFA simulation model to analyze its performance in a data transmission system. We investigate the wavelength dependence of the EYDFA absolute gain and gain uniformity for different EYDF lengths in the range of 2–7 m. A COMSOL Multiphysics model of cladding pumping coupler has also been developed to optimize the pumping efficiency considering angles between different fibers and different numbers of electromagnetic modes.

Keywords: Coupler, Double-clad doped fiber amplifiers, Fiber optic transmission systems, Side pumping, COMSOL Multiphysics.

1. Introduction

Recently, cladding-pumped doped fiber amplifiers have attracted significant interest for applications in space-division multiplexed (SDM) multicore optical fiber systems providing the data transmission capacity increase in a cost-effective way [1].

This research is aimed to solve the problem of developing a new optical fiber amplifier for optical transmission systems. In particular, the focus of this work is on the investigation of Er^{3+}/Yb^{3+} co-doped fiber amplifiers (EYDFAs) pumped with cost-efficient multimode light sources for use in wavelength division multiplexed (WDM) transmission systems to increase optically transparent path length.

2. Experimental Results and Discussion

The proposed EYDFA simulation model operation is directly related to the EYDF and the pump source optical parameters. Accordingly, the first step is characterization of Er^{3+}/Yb^{3+} co-doped double-clad fiber: Scanning electron microscopy (SEM) measurements, optical microscopy, optical absorption measurements and multimode LED spectral measurements. At the same time, we have performed simulations of cladding pumping suitable coupler to clarify how radiation from pumping is coupled to the active fiber core using COMSOL Multiphysics software.

The EYDF cross-section images are obtained using Eclipse LV150N microscopic. As it can be seen in Fig. 1 the doped fiber has a flower-shaped inner cladding. The overlap factor is obtained by analyzing the dimensions of the obtained EYDF cross-section images to identify the area of core and flower shaped inner cladding, shown in Fig. 1. A total of 8 different crossings are selected from the cross-section image (the maximum and minimum diameters) all crossing the center. All sub-results (pixel grayscale values versus diameter) are averaged to minimize the image noise, as well as to account for fiber`s imperfections. Using this approach, four regions can be distinguished two outer/inner cladding boundaries and two inner cladding/core boundaries.

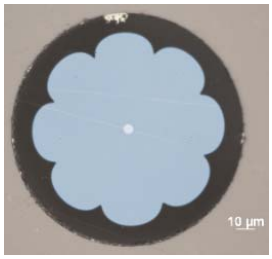

Fig. 1. Double-clad EYDF cross-section image.

COMSOL Multiphysics model is also developed and used to assess the pumping efficiency for different side pumping angles and different numbers of electromagnetic modes [2, 3]. The obtained results show that the highest pumping efficiency, above 75%, is achieved for 5–14 modes when two fibers representing the pump source and the signal source

form a 10-degree angle between their central axes. The search for the optimal number of modes corresponds to the development trend in optical coupler technology where the multimode pumping by light-emitting diode (LED) replaces the classical scheme with a single-mode pumping by a laser diode (LD). In Fig. 2, ten (10) modes are injected into a multimode pump fiber. The pump signal initially propagates almost parallel to the direction of the fiber, but entering the double-clad fiber starts to reflect from the outer coating.

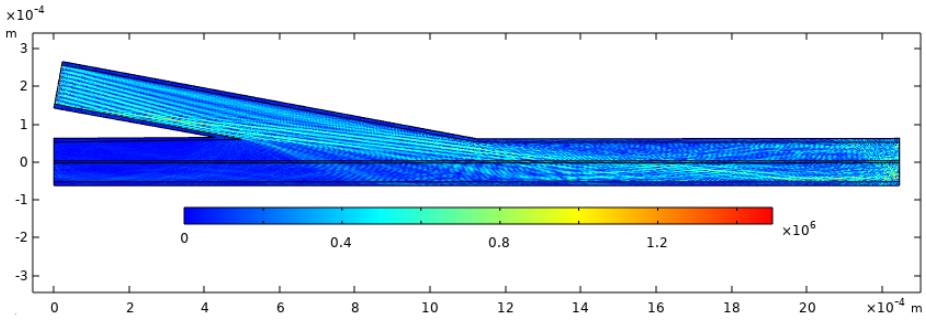

Fig. 2. The 2-dimensional coupler model in COMSOL Multiphysics forms a 10º angle between the pumping and the signal-carrying fiber with and ten electromagnetic modes injected in the pumping fiber.

The mathematical amplifier model has been created in the VPIphotonics Design Suite TM. The main purpose of mathematical modeling is to determine possible gain characteristics and provide baseline values of fiber length and pump parameters for the experimental amplifier setup [4]. To obtain a per-channel gain of the experimental EYDFA, we use the input signal formed by filtering a wideband amplified spontaneous emission (ASE) noise (covering optical C and L bands with a 10-dB bandwidth of 1526–1630 nm) [5]. For pumping a diode centered around 975 nm is used. The absorption around 975 nm is attributed to the optical transition of Yb^{3+}: $^2F_{7/2} \rightarrow {}^2F_{5/2}$. From simulations it is concluded that the length of EYDF in the range of 2–7 m produces an optical signal output power reasonable for fiber optic communications systems. Accordingly, the wavelength dependence of EYDFA absolute gain and gain uniformity for different fiber lengths in the range up to 7 m has been experimentally analyzed.

Additionally, we observe that the first meter or so of the EYDF glows in green when the pump source is active, shown in Fig. 3. Such glow originates from the Er^{3+} upconversion luminescence, indicating low pump conversion efficiency. The effect is diminished when connecting the input signal that returns most of the exciting Er^{3+} ions to the ground state by amplifying the C band.

4. Conclusions

The experimental and simulation results of the overall level of amplification and the envelope of the gain spectrum show the best agreement when the EYDF is 5 meters long. This length also provides signal gain > 21 dB and the gain ripple is less than 12 dB in the wavelength range 1534–1565 nm.

Also, a successful two-dimensional model simulating electric and magnetic fields in a coupler with COMSOL Multiphysics software was developed, which shows that the optimum number of pumping modes lies in the range of 5 to 14 modes, which is similar to the previously reported results but obtained by different methods.

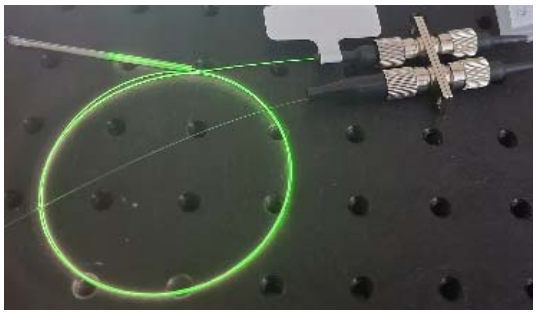

Fig. 3. Green luminescence of the EYDF while pump is active. A purple tinge is also visible due to some pump light leaking from the fiber that is picked up by the camera. The fusion splice protection sleeve had its steel rod removed to avoid potential thermal expansion effects.

Acknowledgments

This work has been supported by the European Regional Development Fund project No.1.1.1.1/18/A/068. The Institute of Solid State Physics, University of Latvia as a Center of Excellence has received funding from the European Union's Horizon 2020 Framework Programme H2020-WIDESPREAD-01-2016-2017-TeamingPhase2 under grant agreement No. 739508, project CAMART^2.

References

[1]. N. Yoshikane and T. Tsuritani, Recent Progress in Space-Division Multiplexing Optical Network

Technology, in *Proceedings of the International Conference on Optical Network Design and Modeling (ONDM' 2020)*, Castelldefels, Barcelona, Spain, 2020, pp. 1-4.

[2]. A. Supe et al., Recent Developments in Cladding-Pumped Doped Fiber Amplifiers for Telecommunications Systems, in *Proceedings of the 22nd International Conference on Transparent Optical Networks (ICTON' 2020)*, 2020, pp. 1-6.

[3]. E. Elsts et al., Fibre Optical Coupler Simulation by Comsol Multiphysics Software, *Latvian Journal of Physics and Technical Sciences*, (accepted)

[4]. A. Supe et al., Cladding-Pumped Erbium/Ytterbium Co-Doped Fiber Amplifier for C-Band Operation in Optical Networks, *Applied Sciences*, 11, 4, 2021, 1702.

[5]. K. Zakis et al., Cladding-pumped Er/Yb Co-Doped Fiber Amplifier for Multi-Channel Operation, *Journal of Lightwave Technology*, (submitted)

(055)

Optomechanical Inertial Sensing and Displacement Interferometry

F. Guzman [1], A. S. Hines [1], A. Nelson [1, 2] and Y. Zhang [1, 2]
[1] Texas A&M University, Aerospace Engineering & Physics, College Station, TX 77843, USA
[2] College of Optical Sciences, University of Arizona, AZ 85721, USA
Tel.: + 1-979-845-0124, fax: +1-979-845-6051
E-mail: felipe@tamu.edu

Summary: We present our research work on the development of novel optomechanical inertial sensing technologies, primarily targeting low frequency acceleration sensing. Our devices utilze laser interferometric displacement sensing to read out the motion of their test mass. We will show some compact laser interferometer topologies that we are developing with the goal of realizing integrated portable units.

Keywords: Optomechanics, Laser interferometry, Instrumentation, Fiber-optics, Metrology.

1. Introduction

Gravitational acceleration provides unique measurement opportunities to identify natural and man-made phenomena at global scales with signatures that are extremely difficult to mask due to their nature. Such gravitational observations are currently conducted with commercial gravimeters and gravity gradiometers that consist of complex mechanical structures operating large, inertially sensitive test masses and cumbersome displacement readout.

We are currently developing highly compact, portable, and cost-effective optomechanical inertial sensors of high sensitivity, building upon advances in the area of optomechanics. These technologies consist of low-loss and highly stable monolithic mechanical oscillators that we combine with miniaturized laser interferometric displacement sensors, enabling us to achieve extremely high performances in acceleration sensing in small form factors.

To this end, it is necessary to develop various subsystems that are building blocks, each contributing to the implementation of these kinds of instruments. We will discuss our work on the fabrication of low-loss mechanical resonators, and the development of compact monolithic laser interferometer heads, fiber-based multi-color fiber interferometers, and new measurement concepts targeting smaller footprints and higher integration into photonic platforms. This includes some of the error and noise sources that affect these types of measurement systems.

2. Optomechanical Accelerometers

The accelerometers we are developing consist of a mechanical resonator with a linearly oscillating test mass. Displacement oscillations are readout optically and converted to accelerations according to the transfer function given in equation 1 [1-3].

$$\frac{x(\omega)}{a(\omega)} = -\frac{1}{\omega_0^2 - \omega^2 + i\frac{\omega_0}{Q}\omega} \qquad (1)$$

Thermal noise dominates in the low frequency regime while gas damping dominates at higher frequencies. The thermal acceleration noise floor is given by equation 2 [1].

$$a_{th}(\omega) = \sqrt{\frac{4k_BT}{m\omega}[\omega_o\Gamma_v + \omega_o^2\phi(\omega)]} \qquad (2)$$

This noise floor is inversely proportional to the mQ product of the resonator, where m is the mass and Q the mechanical quality factor. Therefore, we aim to maximize the mQ-product to achieve low acceleration noise floors, while realizing a compact and lightweight system. Our resonators are made from monolithic fused silica, a low loss material for operation near room temperature (Figs. 1 and 2). We are also working to develop and fabricate Si-based resonator systems for operation at cryogenic temperatures (Fig. 2). Our models consist of resonators for both low and high frequency fundamental oscillation modes. These could be applied for absolute gravimetry and inertial sensing, respectively. Geometries are optimized to minimize loss [1]. We have demonstrated mechanical quality factors, Q, of 4.77×10^5 with our fused silica resonators.

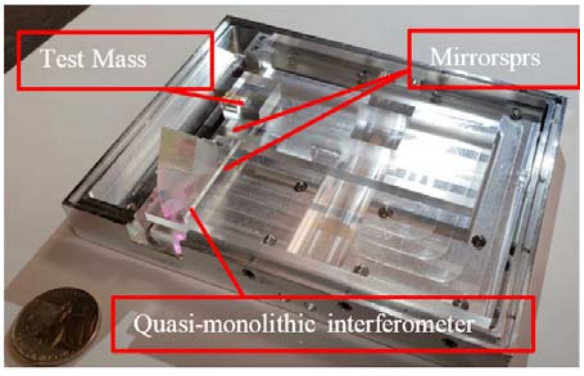

Fig. 1. The combination of our low frequency fused silica resonator and quasi-monolithic interferometer design in a prototype mount.

3. Displacement Interferometers

In addition to the resonators, we aim to improve optical readout sensitivity. We have three models for optical readout, depending on resonator size. This includes the development of a compact quasi-monolithic heterodyne interferometer for integration with our lower frequency systems (Fig. 1 and Fig. 3), the use of a Fabry-Perot cavity formed with optical fiber [3] for our smaller, higher frequency systems, and a new method under consideration that will use Si_3N_4 ring resonator waveguides to allow for further miniaturization and on-chip integration.

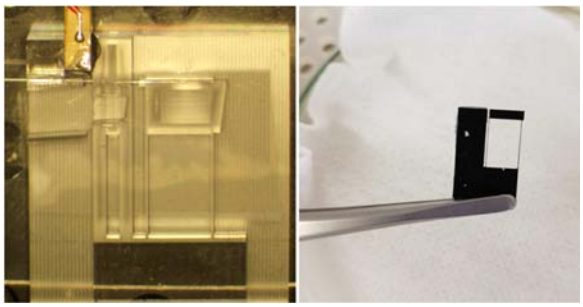

Fig. 2. (Left) 700 Hz fused silica resonator with Fabry-Perot fiber optic readout. (Right) Si resonator sample prototype etched using the Cryo-Si etch DRIE method. Optimization of the etching process is still underway. In this sample, a layer of black-Si can be seen where the mask etched away.

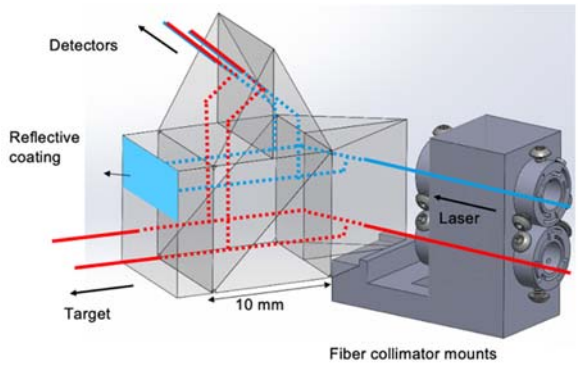

Fig. 3. Our quasi-monolithic heterodyne displacement interferometer design, including a measurement and reference interferometer for subtraction of common optical path noise and periodic errors. See Fig. 1 for integration with the resonator design.

Furthermore, we have developed data processing algorithms for further reduce the displacement noise in our heterodyne interferometers. This process reduces noise that results from non-linear optical pathlengths, laser frequency, and temperature fluctuations [4]. This is intended to prevent the readout noise from becoming a limiting factor and to improve readout sensitivity. Preliminary measurements taken with our 5 Hz resonator and a heterodyne interferometer benchtop prototype are shown in Fig. 4. The signal above 100 mHz is consistent with the New High Noise Model (NHNM). Acceleration sensitivity is on the order of 10^{-7} m $s^{-2}/\sqrt{Hz}$ near 1 Hz. Results appear limited by readout noise below 100 mHz.

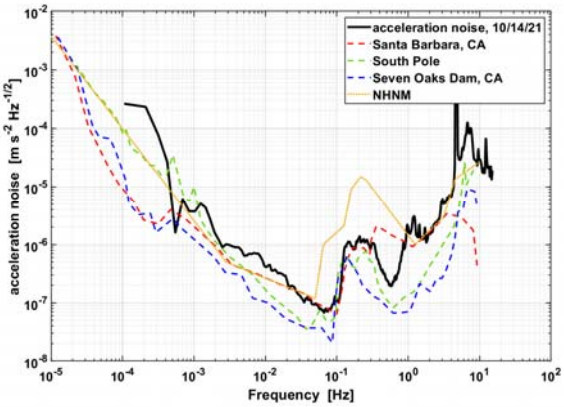

Fig. 4. The measured acceleration noise floor of our 5 Hz system compared to the New High Noise Model.

These systems aim for low loss highly sensitive accelerometers that are compact and portable. We will present on the technology concepts and recent laboratory results, as well as improvement strategies we have developed to enhance the overall performance of our instruments.

4. Conclusions

The co-development of low-loss mechanical resonators and dedicated sensitive and compact laser interferometers show a clear path toward achieving a new type of highly sensitive and portable inertial sensors, capable of addressing a wide variety of scientific and industrial applications.

Acknowledgements

We acknowledge support from our sponsors: NGA: HMA04762010016, NSF: PHY-2045579, ECCS-1945832, and NASA: 80NSSC20K1723.

References

[1]. A. Hines, L. Richardson, H. Wisniewski, and F. Guzmán, Optomechanical inertial sensors, *Applied Optics* 59, 22, 2020, pp. G167–G174.
[2]. R. Middlemiss, A. Samarelli, D. Paul, J. Hough, S. Rowan, and G. Hammond, Measurement of the Earth tides with a MEMS gravimeter, *Nature,* 531, 2016, 614.
[3]. F. Guzmán, L. M. Kumanchik, J. R. Pratt, and J. M. Taylor, High sensitivity optomechanical reference accelerometer, *Applied Physics Letters,* 104, 2014.
[4]. Y. Zhang, A. Hines, G. Valdes, F. Guzmán, Investigation and mitigation of noise contributions in a compact heterodyne interferometer, *Sensors,* 21, 2021, 5788.

(056)

Machine Learning Methods applied to Vibrational Spectroscopy: New Horizons

D. Sharma [1,2] and N. Jaggi [3]
[1] Department of Higher Education, Government of Haryana, India
[2] Shaheed Udham Singh Government College, Matak-Majri, Haryana, India
[3] National Institute of Technology, Kurukshetra, Haryana, India
Tel.: + 91-8813965077
E-mail: bhargava.dp@gmail.com

Summary: Machine Learning Methods have revolutionized almost every sphere of research over the last decade. Vibrational Spectroscopy is also not an exception to this. This keynote presentation explores the emerging horizon where the Machine Learning and Vibrational Spectroscopy meet. Machine learning methods are being used by the spectroscopists for functional group identification, spectrum prediction, spectrum-based structure recognition and explanatory analysis of spectroscopic data. Algorithms are being written to generate the data set with an artificial neural network that may be used to predict spectroscopic properties of interest. Since its advent, vibrational spectroscopy has been widely used to characterize the properties of test samples in various biomedical and engineering fields. Many of these tasks require the analysis of recorded vibrational signals to extract information, which can be achieved using machine learning. Broadly speaking, any task that analyses a signal for fetching the information can be regarded as a potential application of artificial intelligence. The conventional artificial intelligence methods adopt a knowledge-based analytical approach which has various limitations. However, new learning-based approach when implemented using specific machines has provided us with different machine learning methods which when combined with the previous spectroscopic techniques will open new routes for novel research.

Keywords: Machine learning, Vibrational spectroscopy, Spectroscopic data, Functional group identification, Optical computing, Artificial intelligence.

1. Introduction

Spectroscopic techniques have served as a major tool for determining the molecular structures and predicting the mechanism of various physical and chemical processes. No sphere of life is left unbenefitted by its applications. With recent exponential progress in material science, the demand for quick and accurate spectrum prediction and spectrum-based structure recognition has increased and spectroscopy is being extensively used for this purpose. Vibrational spectroscopy is particularly useful owing to its multiple detection methods and a high sensitivity to the local environment enabling high spatial and temporal resolution of structural details. Prediction and interpretation of vibrational spectra commonly adopt a trial-and-error method to correlate an experimental spectrum with a (series of) probable microstructure(s). This conventional methodology requires deep chemical intuition and broad experience to "guess "the most probable microstructures, followed by expensive calculation, mostly at the first-principles level, of vibrational spectra of the "guessed "microstructures. However, the past decade has witnessed a rapid growth of machine learning for a variety of applications, such as image classification and machine translation. Broadly defined, ML algorithms use example training data to "learn" a model that can be used to make predictions or decisions, without the need for explicit programming of the model. ML has been applied to a wide variety of problems and efforts have been made to formalize best practices for these studies. More specifically, ML has been applied to both infrared (IR) absorption and Raman vibrational spectroscopy including functional group identification.

2. Redefining Spectral Studies using Machine Learning

2.1. Spectrum Prediction

Machine learning (ML) has greatly advanced the application of quantum and chemical physics for determining electronic structures energetics, reaction activities, drug discovery and materials design. Extensive ML efforts have been reported for correlating spectral features with molecular structures. For example, photoionization, X-ray absorption (XAS), UV- visible, infrared (IR), and nuclear magnetic resonance (NMR) spectra can now be predicted by ML models based on either detailed geometrical structure (i.e., 3D coordinates) or abstract structural descriptors only containing atomic connectivities. The latter approach however, is not capable of capturing fine spectroscopic variations due to subtle differences in local environments, thereafter limiting their practical applications. ML- accelerated molecular dynamics has been used to simulate IR spectra of water clusters and small molecules, with results comparable to density functional theory (DFT) results. ML models to predict IR signals of the hydroxyl stretch in condensed phase water clusters.

Either of these ML models requires only a marginal computational cost to obtain results at the same level of accuracy as DFT calculations. It has been demonstrated that the accuracy of ML models can reach the same level as the data set on which they are trained; the accuracy can be further improved based on datasets of higher accuracy by transfer- learning or Δ-machine learning techniques.

2.2. Spectrum based Structure Recognition

Compared to the process of spectrum prediction from known structures, spectrum-based structure recognition is more important and of greater practical interest. In principle, one can straightforwardly calcu-late spectral responses from known structures, while the reverse pro- cess is in general more difficult. Efforts to construct ML models to ex- tract structural features from IR or NMR spectra of small collections of molecules can be traced back to the 1990s . The spectrum- structure correlations then obtainable were not very plausible, because each functional group examined was based on only a mere dozens of small molecules. The “shallow ”neural networks (NNs) used in previous work likewise had restricted ability to incorporate multiple spectral data for analysis. The recent development of NN algorithms, especially those with deep and complex hidden layers, has brought opportunities to establish the complex correlations inherent in multiple spectroscopic fields from large and reliable datasets. For example, the DP4-AI system developed very recently aids in the interpretation of NMR spectra based on characteristic chemical shifts .

3. Developing ML Techniques for Vibrational Spectroscopy

Developing ML techniques for vibrational spectroscopy is actually challenging. Many key vibrational spectral signals arise collectively from displacements of several atoms around an equilibrium configuration (i.e. vibrational modes or phonons). In addition, delocalized molecular structures, e.g., conjugated functional groups, and long-range chemical connectivities/interactions are involved in vibrational spectra. Moreover, spectral intensities are determined by quantum selection rules, leading to different spectral features of the same mode when mea-sured by different techniques. These challenges, on the other hand, give us advantageous and complementary means for structure recognition. For example, IR and Raman spectra are often used complementarily for improving structure characterization. ML models can predict vibrational spectra of known structures at a computational cost that is three orders of magnitude lower than first-principles calculations while maintaining the same level of accuracy. More importantly, based on IR and Raman spectra, the models can recognize the existence of functional groups in a molecule at accuracies of around 99 % . The recognition accuracy can be significantly improved by interrelating information extracted from both IR and Raman spectroscopies and even further by involving other spectroscopic or non-spectroscopic characteristics. The established ML protocols trained with small molecules can be transferred to larger ones, suggesting a bright future for fast and precise spectrum prediction and intelligent structure recognition in various important applications, such as detection of structural variations/fluctuations in chemical re-actions, automatic identification of interstellar molecules, or real-time recognition of molecular groups in biomedical diagnosis.

4. Conclusions

Application of Machine Learning Techniques to Spectroscopic problems is going to introduce a completely new dimension to the research in the field of spectroscopy.

Acknowledgements

The patronage of Hon’ble Director General Higher Education, Haryana Sh. Rajiv Rattan, IAS and the financial support provided by the Department of Higher Education, Government of Haryana (India) is wholeheartedly acknowledged and appreciated.

References

[1]. Butler, K. T., Davies, D. W., Cartwright, H., Isayev, O., Walsh, A., Machine Learning for Molecular and Materials Science, *Nature,* 559, 7715, 2018, pp. 547–555.

[2]. Janet, J. P., Kulik, H. J., Machine Learning in Chemistry, *American Chemical Society*, Washington, USA, 2020.

[3]. Artrith, N., Butler, K. T., Coudert, F.-X., Han, S., Isayev, O., Jain, A., Walsh, A., Best Practices in Machine Learning for Chemistry, *Nat. Chem*., 13, 6, 2021, pp. 505–508.

[4]. Lussier, F., Thibault, V., Charron, B., Wallace, G. Q., Masson, J.-F., Deep Learning and Artificial Intelligence Methods for Raman and Surface-Enhanced Raman Scattering, *TrAC Trends in Analytical Chemistry,* 124, 2020, 115796.

[5]. K. T. Schütt, S. Chmiela, O. A. von Lilienfeld, et al., Machine Learning Meets Quantum Physics, Lecture Notes in Physics, Vol. 968, *Springer*, 2020.

Sponsored by:

physicsworld

IFSA Publishing

chemosensors
an open access journal by MDPI

IOP
Institute of Physics

hv photonics

ISBN 978-84-09-40460-5